UNIVERSITEIT VAN PRETORIA
UNIVERSITY OF PRETORIA
YUNIBESITHI YA PRETORIA
Faculty of Natural and Agricultural Sciences

Cellulose-metal organic framework nanocomposite adsorbent films for water remediation

By

Lebogang Manamela

(17226199)

Submitted in fulfilment of the requirements for the degree

Doctor of Philosophy in Chemistry

In the Faculty of Natural & Agricultural Sciences

University of Pretoria

October 2024

Declaration

I, Lebogang Manamela (17226199), declare that the thesis, which I hereby submit for the degree Doctor of Philosophy in Chemistry, at the University of Pretoria, is my own work and has not previously been submitted by me for a degree at this or any other tertiary institution.

Signature: ……

Date: ……..

Dedication

This work is dedicated to my son, Amogelang, my mother, Nkwe Onicia Manamela, and the Manamela family, and my father Ludwick Mologadi Matomo John Mabotja and the Mabotja family.

Acknowledgements

I would like to acknowledge the following people and departments:

- I would like to express my gratitude to God Almighty for granting me the strength and ability to begin and end this academic journey.
- I would like to express my gratitude to my supervisor, Prof N Nombona

  for her invaluable guidance, support, and encouragement throughout this journey.
- I want to express my gratitude to my parents and family for their emotional and financial support throughout this journey.
- I want to extend my appreciation to my colleagues from the Nombona research group for their moral and emotional support, as well as for creating a welcoming and supportive atmosphere for research.
- I would like to acknowledge the Laboratory for Microscopy and Microanalysis for allowing me to use their instruments for SEM and EDX analysis.
- I would like to thank the National Metrology Institute of South Africa for the XPS measurements.
- I would like to acknowledge Tshwane Municipality for providing the industrial-domestic wastewater.
- I would like to thank Dr Samuel A. Iwarere from the Department of Chemical Engineering at the University of Pretoria for assisting with cost analysis calculations.
- I would like to thank the University of Pretoria, Faculty of Natural and Agricultural Sciences, Department of Chemistry for giving me the opportunity and environment to pursue Doctor of Philosophy in Chemistry.
- I would like to thank NRF for giving me financial support.

Research outputs

PUBLICATIONS

Cellulose Acetate Supported MOF-5/Crystalline Nanocellulose Composite Film as an Adsorbent Material for Methylene Blue Removal from Aqueous Solutions
Lebogang Manamela and Nolwazi Nombona, ACS Omega, Volume 9, Issue 36, pages 37418-38315,

PREPARED MANUSCRIPTS

- Adsorption of methylene blue on water-stable Cu-BDC MOF/cellulose composite film
  Lebogang Manamela and Nolwazi Nombona
  Target Journal: Chemosphere
- Ni-BDC and crystalline nanocellulose-based adsorbent films for methylene blue removal
  Lebogang Manamela and Nolwazi Nombona
  Target Journal: Microporous and Mesoporous Materials

CONFERENCE PRESENTATIONS

- Synthesis of MOF adsorbents for wastewater remediation, Lebogang Manamela and Nolwazi Nombona, 10th Nanoscience's Young Researcher's symposium, University of the Witwatersrand, South Africa, 2020/21 {Virtual, poster presentation}
- Evaluation of cellulose acetate supported MOF/crystalline nanocellulose nanocomposite as an adsorbent for methylene blue removal from water, Lebogang Manamela and Nolwazi Nombona, National Young Chemists' Symposium, 2022 {Virtual, Poster presentation}
- Evaluation of cellulose acetate supported MOF-5/crystalline nanocellulose nanocomposite as an adsorbent for methylene blue removal from water, Lebogang Manamela and Nolwazi Nombona, SACI 44th National Convention, Stellenbosch, 8-13 January 2023 {Oral presentation}

- Evaluation of cellulose acetate supported MOF/crystalline nanocellulose nanocomposite as an adsorbent for methylene blue removal from water. Lebogang Manamela and Nolwazi Nombona, 4th International Conference on Materials Science and Engineering, Singapore 13-15 March 2023 {virtual oral presentation}
- Evaluation of cellulose acetate supported MOF-5/crystalline nanocellulose nanocomposite as an adsorbent for methylene blue removal from water, Lebogang Manamela and Nolwazi Nombona, 7th Green and Sustainable Chemistry Conference, Dresden, 22-24 May 2023 {Poster presentation}

Abstract

This study evaluates the effectiveness of adsorbent films for the adsorptive removal of organic dyes, particularly methylene blue (MB) from aqueous solutions. The adsorbent films consist of solvothermally synthesized metal-organic framework (MOF)/crystalline nanocellulose (CNC) composites, supported on a cellulose acetate (CA) substrate. Three adsorbent films were fabricated, i.e. CA-supported MOF-5/CNC (**1**), CA-supported Cu-BDC/CNC (**2**), and CA-supported Ni-BDC/CNC (**3**). This composition results in water-stable adsorbent films, which are recyclable with minimized secondary contamination. The successful preparation of the adsorbent films was verified by several characterization techniques such as X-ray diffraction (XRD), Fourier transform infrared spectroscopy (FTIR), scanning electron microscopy (SEM), energy dispersive X-ray (EDX), thermogravimetric analysis (TGA), Brunauer-Emmett-Teller (BET) analysis and X-ray photoelectron spectroscopy (XPS). Batch adsorption experiments were carried out for the decontamination of MB from aqueous solutions under different conditions including varying pH, contact time, initial MB concentration, and temperature. The optimum adsorption conditions were at pH 11, at 360 minutes, at an initial MB concentration of 6 mg/L, and at 25 °C. Under these conditions, the adsorbent films achieved adsorption capacities between 2.79 - 4.29 mg/g, with corresponding maximum % removals between 77 - 85 %. The adsorption isotherms and kinetic models revealed multilayer chemical adsorption on the surface of film **1** as indicated by the experimental results which were best described by the Freundlich isotherm and pseudo-second-order kinetic models. On the surfaces of films **2** and **3**, the isotherms and kinetic models revealed monolayer chemical adsorption according to the Langmuir isotherm and pseudo-second-order kinetic models. Thermodynamic parameters showed the adsorption processes were exothermic in nature and feasible. The films showed good recyclability, after five adsorption cycles, film **1** maintained 76% of its original adsorption capacity, film **2** maintained 73%, and film **3** 67%. The films showed pH-dependent selectivity, demonstrating preferential affinity for anionic methyl orange (MO) at acidic pH and a preference for cationic MB at alkaline pH. The practical applicability of the adsorbent films was assessed in the treatment of real textile industry effluent where the films achieved

between 20 - 45 % effluent removal. The economic assessment of the adsorption processes was conducted by considering the cost of chemicals and the energy cost of the adsorption process. The adsorption costs for films were calculated to be between USD 43.60 and 53.00. These findings suggest that cellulose derivatives and MOFs have the potential to perform synergistically to result in stable, recyclable, versatile, and cost-effective adsorbents for the removal of organic dyes from polluted water.

Table of contents

List of abbreviations

MOF	Metal-organic framework
CNC	Crystalline nanocellulose
CNF	Cellulose nanofibers
BNC	Bacterial nanocellulose
CA	Cellulose acetate
MB	Methylene blue
MO	Methyl orange
BDC	Benzenedicarboxylic acid
XRD	X-ray diffraction
FTIR	Fourier transform infrared
UV-Vis	Ultraviolet-Visible
SEM	Scanning electron microscopy
EDX	Energy dispersive X-ray
TGA	Thermogravimetric analysis
BET	Brunauer-Emmett-Teller
XPS	X-ray photoelectron spectroscopy
TOCNF	TEMPO-oxidised Cellulose nanofibers

LIST OF FIGURES

LIST OF TABLES

CHAPTER 1

1.0 INTRODUCTION

1.1 Background

Organic dyes are compounds capable of absorbing light and imparting color to materials. Primarily composed of carbon structures, these compounds typically have conjugated systems that allow for electron delocalization, enabling them to absorb light and produce vibrant colors. They can be categorized based on their chemical structures and chromophores, which are groups of atoms and electrons in organic compounds that interact with light to generate color [1]. Azo dyes are organic compounds distinguished by one or more azo groups (R-N=N-R') [2]. These synthetic dyes are crucial in industries such as food and textiles, accounting for 60-70% of all dyes used. Examples of azo dyes include methyl orange, Congo red, and methylene blue [3]. Another class of dyes, identified by the anthraquinone structural unit are the anthraquinone dyes, known for their stability and vivid colors [4]. These dyes are primarily used in the textile and ink industries.

Other categories of organic dyes include nitroso and nitro dyes, characterized by NO and NO_2 functionalities. The indigo structure defines indigo dyes; and phthalocyanine dyes, recognized by their macrocyclic ring, are often complexed with metals [4]. Each class of organic dyes is characterized by unique properties that make them useful in various applications. Overall, organic dyes play a significant role in industries and everyday life. In the textile industry, these dyes are essential for coloring clothes and fabrics [5], while the food industry uses specific dyes as colorants for food and beverages [6]. In biomedical research, organic dyes are used to visualize cells and tissues [6], and in solar cells, such as dye-sensitized solar cells, organic dyes are used to generate energy from the sunlight [7]. The cosmetics industry employs dyes in lipstick and nail polish to achieve vibrant colors while other industries utilize organic dyes for functions such as color-coding printing and coating paper [8].

Despite their benefits, the use of organic dyes contributes to environmental pollution, particularly in water bodies. The dye industry ranks among modern civilization's top three most polluting sectors [9]. Each year, the textile industry releases approximately 200,000 tons of organic dye waste to the environment, mainly due to the dyes' inability to fully adhere to fabrics, leading to significant pollution [10]. The textile industry accounts for 55% of dye pollution, while the dye, paint, and pulp industries contribute 21%, 8%, and 9%, respectively [11].

These industries discharge effluents into the environment, causing water bodies to become polluted, and threatening both aquatic and terrestrial life. Moreover, organic dyes are highly toxic and capable of causing cancer and other severe health issues in humans and animals [12 – 14]. Azo, nitro, and anthraquinone dyes can induce mutations and are known to be genotoxic, cytotoxic, and capable of damaging DNA [12 – 13]. Some organic dyes, such as phthalocyanines, contain heavy metals, which, when released into the environment and consumed by humans and animals, can lead to kidney failure, neurotoxicity, brain damage, and gastrointestinal diseases [14]. In addition to their harmful effects on humans and animals, organic dyes negatively impact the environment by altering the pH, chemical composition, and water turbidity. The presence of these dyes in water blocks sunlight penetration, ultimately affecting vital underwater processes such as algae photosynthesis [15].

As highlighted above, organic dyes are crucial to the economy however, when improperly discharged, they pose significant risks to humans, animals, and the environment. Therefore, it is essential to implement measures to decontaminate dye-containing waste. Numerous studies have investigated methods for removing organic dyes from aqueous solution, which include flocculation, coagulation, membrane filtration, photodegradation, and adsorption [15 – 16]. However, some of these methods have drawbacks, for instance, flocculation and coagulation have high operational costs and produce sludge. Membranes, while effective, require significant energy input to pump water through the membrane. Photodegradation is less effective in highly polluted water because the high turbidity and suspended solids obstruct the light required for the process to occur, and this technique can also generate toxic and harmful intermediate compounds [17 – 19].

In this study, adsorption was selected as the preferred decontamination method due to its advantages over the other techniques. Adsorption features a simple setup and operates without energy input. Many adsorbents are inexpensive, making the process cost-effective. A significant benefit of adsorption is the ability to modify the adsorbent surface to enhance selectivity towards the target pollutant, thereby improving the efficiency and overall effectiveness of the adsorbent [18 – 19]. In the design and development of effective and efficient adsorbent for water remediation, nanomaterials have emerged as promising candidates due to their high surface area, modifiable surface chemistry, and controllable porosity, collectively improving the removal of contaminants from water. Metal-organic frameworks (MOFs), a class of materials consisting of a metal ion or a cluster of metal ions, referred to as nodes, coordinated to an organic ligand to form one-dimensional (1D), two-dimensional (2D), or three-dimensional (3D) structures, have been used in water treatment for the removal of contaminants from water. MOFs are characterized by high surface area, abundant active sites, and tunable surface chemistry making them ideal adsorbents for organic dyes and many other pollutants [20]. Figure 1.1 shows a general structure of a 3D MOF, highlighting the network connection of nodes and organic linkers.

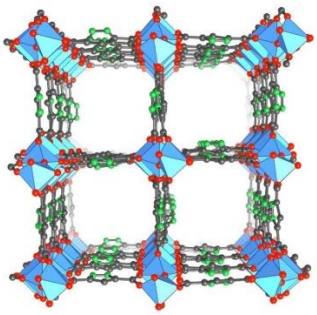

Figure 1.1: Structure of a metal-organic framework network array (image retrieved from: https://www.eurekalert.org/multimedia/892666).

Liu *et al*. (2024) reported the simultaneous removal of the azo dyes Congo red and methylene blue from aqueous solutions using a UiO-66 MOF adsorbent, achieving a maximum adsorption capacity of 585 mg/g for Congo red removal and ~150 mg/g for methylene blue [21]. This adsorbent contains Zr-O coordination providing good structural stability which is favorable in the adsorption of organic dyes from aqueous solutions.

Mogharbel *et al*. (2023) showed that the Fe_3O_4@Ag-MOF adsorbent achieved an adsorption capacity of 856.06 mg/g for the removal of the triphenylmethane dye Gentian violet from aqueous solutions. The Fe_3O_4@Ag-MOF adsorbent showed good reusability for five cycles [22].

MOFs typically exist in powder form, to enhance the practical use of MOF-based adsorbents and to reduce secondary contamination, MOFs are supported on polymeric substrates [23]. This approach results in adsorbent films that are easy to handle and use [23 – 27]. Most MOFs have poor wetting stability and aggregate in aqueous solution resulting in a reduced overall surface area [28]. Composite formation with mechanically stable materials can reinforce MOFs and make them useful in water purification.

Several support materials have been used for MOFs employed in water purification and these include polyethylene glycol (PEG), polyacrylonitrile (PAN), and polyethyleneimine (PEI). PEG demonstrated an adsorption capacity of 747.4 mg/g when used as a support for NH_2-MIL-125(Ti) MOF for the removal of methylene blue [29]. The adsorbent could be easily handled and recovered from aqueous solutions for recycling. Abundant, cheaper, and biodegradable supports such as cellulose have gained popularity for their green nature. Cellulose acetate (CA), a cellulose derivative, has the capacity to improve the practical application of MOFs by supporting MOF particles in their structure, resulting in a film-like material that can be recycled. This capability was demonstrated when CA@Ti-MIL-NH_2 was used for the adsorptive removal of paracetamol, demonstrating good reusability [30]. Nanocellulose (NC) materials such as crystalline nanocellulose (CNC), bacterial nanocellulose (BNC), and cellulose nanofibers (CNF) can minimize the aggregation of MOFs when employed as MOF/NC composites. Zhu *et al*. (2022) used CNFs to disperse ZIF-8 MOFs resulting in a porous functional filter for water purification. [31]. NC materials are mechanically stable and can impart stability to MOFs in aqueous solutions [32].

1.2 Problem statement

The discharge of organic dyes into water bodies, primarily from the textile industry continues to be a global environmental issue. The presence of organic dyes in ecosystems poses risks to both wildlife and human health. These dyes disrupt aquatic ecosystems by blocking sunlight and hindering photosynthesis, while also posing severe health risks to humans including cancer and kidney diseases. Addressing this challenge requires the development and implementation of effective dye removal technologies to mitigate ecological and health impacts.

1.3 Research aims and objectives

This study aims to develop and evaluate the effectiveness of metal-organic frameworks embedded in cellulose as adsorbent materials for the removal of a model organic dye (methylene blue) from aqueous solution. The study will focus on optimizing the synthesis of the MOF/NC composite, characterizing the structural and chemical properties, and assessing its adsorption capacity and efficiency in removing methylene blue from aqueous solution. The end goal is to advance water purification technologies.

1.3.1 Objectives

a) To synthesize MOF-5, Cu-BDC, and Ni-BDC using a solvothermal technique and characterize the MOFs. The characterization techniques used in this work include X-ray diffraction (XRD), Fourier transform infrared spectroscopy (FTIR), scanning electron microscopy (SEM), energy dispersive X-ray (EDX), and thermogravimetric analysis (TGA).
b) To synthesize CNC using sulfuric acid hydrolysis and characterize the CNC.
c) To synthesize MOF/CNC composites using a solvothermal process and characterize the composites.
d) To fabricate CA-supported MOF/CNC adsorbent films through a drop-casting method and characterize the composites.
e) To determine the adsorption capacity of the CA-supported MOF/CNC adsorbent films as a function of adsorption parameters.

f) To investigate the adsorption mechanisms of the adsorption films using isotherm and kinetic models.

g) To determine the recyclability of the adsorbent films, the cost-effectiveness, and their ability to remove real industry dye effluents.

1.4 Research hypothesis

The research project hypothesizes that embedding metal-organic frameworks onto cellulose derivatives will enhance the adsorption capacity for removing organic dyes from aqueous solution compared to pristine MOF due to the synergistic effect of MOFs high surface area and the hydrophilic nature of cellulose.

1.5 Thesis layout

This thesis comprises five chapters. Chapter 1 introduces the study, providing background information and an overview. It highlights the significance of the study by establishing the problem statement, motivation, and objectives. Chapter 2 is a literature review that offers a comprehensive overview of the topic, providing context and background. It examines the current state of research, analyzing trends, patterns, and key publications, and discusses advancements in materials and methodologies used in the study.

Chapter 3 presents the first manuscript titled "Cellulose Acetate Supported MOF-5/Crystalline Nanocellulose Composite Film as an Adsorbent Material for Methylene Blue Removal from Aqueous Solutions." It begins with an introduction to organic dye pollution and the effectiveness of MOF-5, CNC, and CA in purification, followed by the motivation for using CA-supported MOF-5/CNC adsorbent film for MB adsorption. The chapter details the experimental work, listing all chemicals, instruments, and equations used, as well as the synthesis methodology, characterization, and MB adsorption procedure. The results and discussion section provides a detailed analysis of measurements and results, evaluating the efficiency and practical applicability of the adsorbent film. It also discusses the economic feasibility by considering the costs of chemicals and energy consumption.

The chapter compares the adsorption performance of the adsorbent with other reported adsorbents.

Chapters 4 and 5 follow a similar structure to Chapter 3 but focus on the adsorbents CA-supported Cu-BDC/CNC and CA-supported Ni-BDC/CNC, respectively. The final chapter, Chapter 6, concludes the study by acknowledging the performances and synthesis techniques of the adsorbents. It compares the performances of the adsorbent films, identifies the best-performing adsorbents, and provides possible explanations. The chapter also highlights the successes of the study and offers future recommendations.

1.7 References

1. Yaneva, Z.; Ivanova, D.; Nikolova, N.; Toneva, M. Organic dyes in contemporary medicinal chemistry and biomedicine. I. From the chromophore to the bioimaging/bioassay agent. *Biotechnol. Biotechnol. Equip*. 2022, DOI:10.1080/13102818.2022.2039077.

2. Khan, A.; Ju, P.; Han, Z.; Ni, C. A comprehensive review on adsorptive removal of azo dyes using functional materials. *Aqua Water Infrastruct. Ecosyst. Soc.* 2024, DOI: 10.2166/aqua.2024.292.

3. Eltaboni, F.; Bader, N.; El-Kailany, R.; Elsharif, N.; Ahmida. A. Chemistry and Applications of Azo Dyes: A Comprehensive Review. *J. Chem. Rev.* 2022, DOI:10.22034/JCR.2022.349827.1177.

4. Benkhaya, S.; M' rabet, S.; El Harfi, A. A review on classifications, recent synthesis and applications of textile dyes. *Inorg. Chem. Commun*. 2020, DOI: 10.1016/j.inoche.2020.107891.

5. Pizzicato, B.; Pacifico, S.; Cayuela, D.; Mijas, G.; Riba-Moliner, M. Advancements in Sustainable Natural Dyes for Textile Applications: A Review. *Molecules* 2023, 28, DOI:10.3390/molecules28165954.

6. Di Salvo, E.; Lo Vecchio, G.; De Pasquale, R.; De Maria, L.; Tardugno, R.; Vadalà, R.; Cicero, N. Natural Pigments Production and Their Application in Food, Health and Other Industries. *Nutrients* 2023, 15, DOI:10.3390/nu15081923.

7. Brągoszewska, E.; Bogacka, M.; Bogacka, M.; Wajda, A. Enhancing the efficiency of photovoltaic cells through the usage of dye concentrators. *Front. Energy Res.* 2024, DOI: 10.3389/fenrg.2024.1399020.

8. Valli, N.-C.; Rakshi, A.-D.; Sandhya, S.; Britlin D.-J.-N.; Nellore, J. Developments in treatment technologies of dye-containing effluent: A review. *Case Stud. Chem. Environ. Eng.* 2023, DOI:10.1016/j.cscee.2023.100339.

9. Centobelli, P.; Abbate, S.; Nadeem, S.-P.; Garza-Reyes, J.-A. Slowing the fast fashion industry: An all-round perspective. *Curr. Opin. Green Sustain. Chem.* 2022, DOI: 10.1016/j.cogsc.2022.100684.

10. Miah, L. Impact of textile dyeing effluent on environment; a study based on Bangladesh. *IJAEM* 2022, DOI: 10.35629/5252-041013181324.

11. Adesanmi, B.-M.; Hung, Y.; Paul, H.; Huhnke, C.-R. Comparison of dye wastewater treatment methods: A review. *GSCARR* 2022, DOI:10.5281/zenodo.6331586.

12. Farias, N.-O.; Albuquerque, A.-F.; dos Santos, A. Is natural better? An ecotoxicity study of anthraquinone dyes. *Chemosphere* 2023, DOI:10.1016/j.chemosphere.2023.140174.

13. Alzain, H.; Kalimugogo, V.; Hussein, K. A Review of Environmental Impact of Azo Dyes. *Int. J. Res. Rev.* 2023, DOI: 10.52403/ijrr.20230682.

14. Islam, T.; Repon, M.-R.; Islam, T.; Sarwar, Z.; Rahman, M.-M. Impact of Textile Dyes on Health and Ecosystem: A Review of Structure, Causes, and Potential Solutions. *Springer Berlin Heidelberg* 2023, DOI:10.1007/s11356-022-24398-3.

15. Al-Tohamy, R.; Ali, S.-S.; Li, F. A critical review on the treatment of dye-containing wastewater: Ecotoxicological and health concerns of textile dyes and possible remediation approaches for environmental safety. *Ecotoxicol. Environ. Saf.* 2022, DOI:10.1016/j.ecoenv.2021.113160.

16. El-Gaayda, J.; Titchou, F.-E.; Oukhrib, R. Natural flocculants for the treatment of wastewaters containing dyes or heavy metals: A state-of-the-art review. *J. Environ. Chem. Eng.* 2021, DOI:10.1016/j.jece.2021.106060.

17. Groeneveld, I.; Kanelli, M.; Ariese, F.; van Bommel, M.-R. Parameters that affect the photodegradation of dyes and pigments in solution and on substrate – An overview. *Dye Pigment* 2023, DOI:10.1016/j.dyepig.2022.110999.

18. Badran, A.-M.; Utra, U.; Yussof, N.-S.; Bashir, M.-J.-K. Advancements in Adsorption Techniques for Sustainable Water Purification: A Focus on Lead Removal. *Separations* 2023, DOI:10.3390/separations10110565.

19. Algarni, T.-S.; Al-Mohaimeed, A.-M. Water purification by adsorption of pigments or pollutants via metaloxide, *J. King Saud. Univ. Sci.* 2022, DOI: 10.1016/j.jksus.2022.102339.

20. Motshekga, S.-C.; Oyewo, O.-A.; Makgato, S.-S. Recent and Prospects of Synthesis and Application of Metal-Organic Frameworks (MOFs) in Water Treatment: A Review. *J. Inorg. Organomet. Polym.* 2024, DOI:10.1007/s10904-024-03063-x.

21. Liu, Y.; Yan, A.; Ding, L.; Wei, J.; Liu, Y.; Niu, Y.; Qu, R. Simultaneous and ultrafast removal of anionic and cationic dyes from aqueous solution by Zr-based MOFs hybridized by attapulgite and adsorption performance research. *Colloids Surfaces A Physicochem. Eng. Asp.* 2024, DOI:10.1016/j.colsurfa.2023.132643.

22. Mogharbel, R.-T.; Alkhamis, K.; Felaly, R.; El-Desouky, M.-G.; El-Bindary, A.-A.; El-Metwaly, N.-M.; El-Bindary, M.-A. Superior adsorption and removal of industrial dye from aqueous solution via magnetic silver metal-organic framework nanocomposite. *Environ. Technol.* 2023, DOI: 10.1080/09593330.2023.2178331.

23. Xiao, C.; Tian, J.; Chen, Q.; Hong, M. Water-stable metal–organic frameworks (MOFs): rational construction and carbon dioxide capture. *Chem. Sci.* 2024, DOI: 10.1039/D3SC06076D.

24. He, Y.; Wang, Y.; Shi, J.; Lu, X.; Liu, Q.; Liu, Y.; Zhu, T.; Wang, D.; Yang, Q. Incorporating metal−organic frameworks into substrates for environmental applications. *J. Chem. Eng.* 2022, DOI: 10.1016/j.cej.2022.136866.

25. Yu, B.; Liu, Y.; Li, Z.; Liu, Y.; Rao, P.; Li, G. Durable substrates incorporated with MOFs: Recent advances in engineering strategies and water treatment applications. *J. Chem. Eng.* 2023, DOI: 10.1016/j.cej.2022.140840.

26. Yu, S.; Pang, H.; Huang, S.; Tang, H.; Wang, S.; Qiu, M.; Chen,Z.; Yang, H.; Song, G.; Fu, D.; Hu, B.; Wang, X. Recent advances in metal-organic framework membranes for water treatment: A review. *Sci. Total Environ.* 2021, DOI: 10.1016/j.scitotenv.2021.149662.

27. Yang, C.; Xue, Z.; Wen, J. Recent Advances in MOF-Based Materials for Remediation of Heavy Metals and Organic Pollutants: Insights into Performance, Mechanisms, and Future Opportunities. *Sustainability* 2023, DOI:10.3390/su15086686.

28. Yu, L.; Nie, Z.; Xie, S.; Jiang, L.; Xia, B.; Li, M.; Cheng, C.; Duan, J.; Antonietti, M.; Chen, S. Bioinspired inhibition of aggregation in metal-organic frameworks (MOFs). *iScience*, 2023, DOI: 10.1016/j.isci.2023.106239.

29. Yao, P.; Liu, Y.; Tang, X.; Lu, S.; Li, Z.; Yao, Y. Synthesis of reusable NH2-MIL-125(Ti)@polymer monolith as efficient adsorbents for dyes wastewater remediation. *Green Chem. Eng.* 2023, DOI: 10.1016/j.gce.2022.06.004.

30. Emam, H.-E.; El-Shahat, M.; Abdelhameed, R.-M. Observable removal of pharmaceutical residues by highly porous photoactive cellulose acetate@MIL-MOF film. *J. Hazard. Mater.* 2021, DOI: 10.1016/j.jhazmat.2021.125509.

31. Zhu, W.; Han, M.; Kim, D.; Zhang, Y.; Kwon, G.; You, J.; Jia, C.; Kim, J. Facile preparation of nanocellulose/Zn-MOF-based catalytic filter for water purification by oxidation process. *Environ. Res.* 2022, DOI:10.1016/j.envres.2021.112417.

32. Tao, Y.; Du, J.; Cheng, Y.; Lu, J.; Min, D.; Wang, H. Advances in Application of Cellulose-MOF Composites in Aquatic Environmental Treatment: Remediation and Regeneration. *Int. J. Mol. Sci.* 2023, DOI: 10.3390/ijms24097744.

CHAPTER 2

2.0 LITERATURE REVIEW

2.1 Water pollution

Water pollution is the contamination of water bodies such as rivers, lakes, oceans, and groundwater due to human activity or natural phenomena. It occurs as a result of harmful substances such as chemicals and microorganisms being released into these ecosystems, leading to a decline in water quality. Human activities that cause water pollution include untreated sewage, industrial wastes, and agricultural run-off [1]. Natural forms contributing to water pollution include volcanic eruptions, fluorine salts, and microbiological contamination. The type of water pollution can be categorized into point-source and non-point-source water pollution [2 – 3].

Point-source water pollution occurs when contaminants are released into water bodies from a single, identifiable source, such as through a pipe or channel from factories, sewage treatment plants, power plants, and agricultural run-off [4 – 5]. Due to its identifiable nature, this type of pollution can be manageable and regulated efficiently. Common pollutants associated with this pollution include heavy metals, organic dyes, pesticides, and pharmaceutical wastes [4 – 5]. The second category, non-point-source, refers to water pollution that does not originate from a single, identifiable source, however, comes from multiple, widespread sources making it challenging to control and regulate [6 – 7]. Non-point-source water pollution includes pesticides from agricultural run-off, street debris from urban run-off, and pathogens from animal waste or improperly maintained septic systems [7].

Table 2.1 lists pollutants and their sources, categorized under point-source and non-point-source water pollution.

Table 2.1: Point-source and non-point-source water pollutants

Point-source water pollution		**Non-point-source water pollution**	
Source	Pollutants	Source	Pollutants
Industrial facility	Heavy metals, Organic dyes, pharmaceuticals, etc.	Agricultural run-off	Pesticides, herbicides, fertilizers, etc.
Wastewater treatment plants	Nutrients	Urban run-off	Oil, debris, grease
Power plants	Particulate matter	Forestry activity	Nutrients
Oil refineries	Ammonia, sulfides	Atmospheric deposition	Nitrogen and sulfur compounds

Water pollution is a significant environmental issue with devastating consequences on the ecosystem, wildlife, and human health. Contamination of water can disrupt the natural balance of aquatic ecosystems. This can occur when excessive nutrients from fertilizers and agricultural runoff deposit in water bodies, triggering algal bloom which in turn depletes oxygen in water, threatening aquatic life [8]. Crucial aquatic habitats such as coral reefs and wetlands can be damaged, reducing biodiversity and disturbing the ecosystem [9]. Pollutants pose a threat to aquatic organisms, causing them to migrate, which disrupts the balance of the aquatic ecosystem and interferes with the food chain [8 – 9]. Pollutants may also lead to health complications, including reproductive complications and death [9 – 11].

2.1.1 Water purification techniques

Contaminated water brings about serious chronic and water-borne diseases such as cholera, hepatitis, and gastrointestinal infections in humans [1, 12]. These negative

impacts imposed by pollutants on the environment, animals, and humans highlight the need to decontaminate pollutants at the point source of pollution.

To improve the quality of freshwater, several treatment technologies have been employed. These treatment technologies are divided into three categories; chemical, physical, and biological treatment, as shown in table 2.2.

Table 2.2: Water purification technologies.

Chemical techniques	**Physical techniques**	**Biological techniques**
Coagulation and Flocculation	Membrane filtration	Anaerobic digestion
Photodegradation	Distillation	Activated sludge process
Adsorption	UV radiation	Biofiltration

Chemical techniques for water purification employ chemical agents or chemical reactions for the removal of pollutants from water for safe consumption and environmental discharge. Several chemical techniques have been employed for decontamination of a wide range of pollutants from water. Coagulation and flocculation are two processes that are used together for waste decontamination. Coagulation occurs when chemical species called coagulants are added to polluted water to neutralize the charge on suspended particles, reducing repulsion and allowing the suspended particles to clump into larger aggregates [13]. Coagulants that are typically used for this role are aluminum sulfate, iron chloride, and polymers. The subsequent step, flocculation, follows when the small, destabilized clumps are aggregated into larger and easily removable flocs through gentle mixing. These larger flocs are removed through physical techniques such as filtration and sedimentation.

Photodegradation is a chemical purification technique that uses a photocatalyst exposed to light, usually UV or visible light, for water purification [14]. During this technique, a photocatalyst such as titanium oxide, zinc oxide, or silver nanoparticles, is exposed to light, leading to the excitation of electrons from the highest occupied molecular orbital (HOMO) to the lowest unoccupied molecular orbital (LUMO), resulting in electron/hole (e^-/h^+) pairs. The e^- and h^+ migrate to the surface of the photocatalyst reacting with oxygen

and water molecules to produce reactive oxygen species such as hydroxyl radicals (•OH), superoxide radicals (O_2^-•), and hydrogen peroxide (H_2O_2), capable of degrading pollutants into less harmful substances [14].

Adsorption is a chemical technique that involves the adhesion of pollutants onto the surface and the pores of a solid material, thereby recovering pollutants from water. During this process, the adsorbent is the solid material, and it attracts the adsorbate, which is the pollutant being removed from water [15]. This process occurs through surface interactions whereby the pollutants in water come into contact with the adsorbent and adhere to the surface through chemical interactions such as electrostatic interactions and these adsorbents are called chemisorbents. Adsorption can also occur through physical interactions such as through van der Waals forces and such adsorbents are referred to as physisorbents. Common adsorbents include activated carbon, zeolites, and clay.

Physical techniques for water purification involve the use of physical processes to decontaminate pollutants from water. A physical method used for the purification of water is membrane filtration, which is a technology that employs a semi-permeable membrane to selectively allow substances to pass through while blocking others on the basis of their sizes and shapes [16 – 18]. Membranes are classified based on their pore sizes, as shown in table 2.3.

Table 2.3: Membrane classification

Membrane	**Pore size**
Microfiltration Membrane	100 nm – 10 μm
Ultrafiltration Membrane	10 – 100 nm
Nanofiltration Membrane	1 – 10 nm
Reverse osmosis Membrane	0.1 – 1 nm

Microfiltration is typically a pretreatment technique for other membrane filtration processes. Microfiltration employs membranes with pore diameters between 100 nm to 10 μm, useful for the removal of large colloids and bacteria [18]. Ultrafiltration uses membranes with pore diameters in the range of 10 – 100 nm to separate pollutants such

as viruses, colloidal particles, and macromolecules from water [18]. Nanofiltration uses membranes with pore sizes between 1 and 10 nm for softening and purifying water by removing organic molecules and multivalent ions such as calcium (Ca^{2+}) and magnesium (Mg^{2+}) ions [18]. Reverse osmosis membranes have pore sizes between 0.1 to 1 nm, capable of purifying water from monovalent ions such as Na^{+}, dissolved salts, and organic species [18]. This technique practically removes all contaminants from water.

Distillation is a physical technique for removing contaminants by heating polluted water at temperatures above the boiling point, leading to evaporation [19]. The resulting water vapor is condensed through cooling, yielding purified water. This method is useful for the removal of salts and heavy metals from aqueous solutions. UV radiation is useful for disinfecting water by killing or inactivating microorganisms [20]. This technique is not useful for removing particles from water.

Biological purification methods leverage natural processes to treat and purify water. These approaches utilize microorganisms, plants, or other biological systems to clean water [21]. One example is anaerobic digestion, where microorganisms break down organic material in an oxygen-free environment, resulting in the production of biogas as a byproduct [21]. Another method is the activated sludge process, which requires oxygen to facilitate the decomposition of organic matter into a sludge that can be readily separated from water [22]. Biofiltration is a biological purification technique that involves passing polluted water through a filter containing a layer of microorganisms that break down organic matter into less toxic substances [23].

2.2 Composite and bio-based adsorbents in water purification

Adsorption has been reported as the most effective method for water purification applications, offering several advantages such as ease of operation, no energy input, and cost-effectiveness [15]. The use of composite adsorbent materials further enhances the potential for adsorption. Adsorption using composites has demonstrated high adsorption efficiencies, with the ability to remove contaminants by up to 100 % [15].

Another advantage of adsorption and composite adsorbents is their versatility, leading to more selective and tunable adsorbents that are favorable for a wide range of applications. This technology can decontaminate trace contaminants from aqueous solutions, and using composites improves the limit of detection [24].

Composite adsorbents are characterized by their high surface area, high porosity, tunable surface chemistry, and abundant adsorption active sites. These properties enable excellent performance in removing pollutants such as organic dyes, heavy metals, and pharmaceutical wastes [25].

Biosorbents are biological adsorbents derived from natural materials such as plants, bacteria, and fungi, capable of adsorbing and accumulating contaminants from water onto their surfaces [26 – 27]. These adsorbents are progressively favored over traditional adsorbents due to their non-toxic nature, environmental friendliness, biodegradability, and recyclability [28 – 29]. Bio-based adsorbents are grouped into several categories as shown in table 2.4.

Table 2.4: Biosorbent classifications

Bio-sorbent categories	**Examples**
Agricultural waste	Rice husk, sawdust, corncob, sugarcane bagasse, etc.
Biopolymers	Chitosan, cellulose, and its derivatives
Biochar	Rice husk, softwood, sewage sludge
Fruit and vegetable wastes	Peels

Adsorbents based on agricultural waste, which include rice husks, sawdust, and corncobs are capable of removing pollutants such as heavy metals and dyes from water. A low-cost agricultural waste biosorbent, sugarcane bagasse, showed a removal percentage of 81.90 % for direct red 28 dye in aqueous solutions [26]. Biopolymers such as cellulose and chitosan have demonstrated good capabilities in the adsorptive removal of pollutants from wastewater. Salama (2023) showed that using a cellulose derivative yields a sustainable and environmentally friendly biosorbent for the removal of anionic methyl

orange (MO) and cationic methylene blue (MB) dyes from water [27]. This novel biosorbent produced maximum adsorption efficiencies of 135 and 106 mg/g for MB and MO, respectively. Biochar-based sewage sludge presents an environmentally friendly and efficient method for the removal of pollutants from water, as demonstrated by Ravindiral *et al.* (2023) achieving adsorption efficiencies of 99.32% and 94.28% for the decontamination of Acidic Blue 210 and Acidic Blue 7 from aqueous solutions [28]. Fruit and vegetable wastes make useful and environmentally friendly adsorbents. Banana peels used by Yhon *et al*. (2023) showed removal efficiencies of 20.11 mg/g for MB adsorption [29]. These findings show that bio-based adsorbents are increasingly used as replacements for traditional adsorbents due to their non-toxic nature, effectiveness, and environmental friendliness.

Many biosorbents face significant challenges in water treatment applications, including limited understanding of molecular-level interactions with contaminants and poor reusability. Cellulose offers a distinct advantage as a biosorbent platform due to its well-defined adsorption mechanisms, extensively studied at the molecular level. This in-depth understanding facilitates targeted chemical and physical modifications, such as grafting, crosslinking, and functionalization, to improve adsorption capacity, selectivity, and reusability. By exploiting these properties and versatility for modification, cellulose-based materials hold potential to overcome the limitations of traditional biosorbents and provide more effective and sustainable solutions for water decontamination.

2.3 Cellulose

2.3.1 Structure, properties and applications

Structure

Polysaccharides have become a significant focus in material science, with cellulose standing out as the most studied polymer due to its abundance, with plants producing approximately 10^{11} tons of cellulose annually [30]. Cellulose is a linear polymer and polysaccharide, with the chemical formula $(C_6H_{10}O_5)_n$, and structural characterization reveals it comprises ~ 45% carbon, 6% hydrogen, and 48% oxygen. This polysaccharide

is a homopolymer, consisting of hundreds to thousands of D-anhydroglucopyranose units connected by β(1→4) glycosidic linkages forming between the C1 and C4 carbon atoms of adjacent glucose units, with the C1 anomeric carbon in the β-configuration [31]. Each glucose unit rotates approximately 180 degrees relative to the next, creating a repeating cellobiose disaccharide unit. The D-anhydroglucopyranose ring exists in a pyranose form, adopting the $^{4}C_{1}$ conformation. The length of a cellulose chain varies depending on its source and extraction method [30 - 31]. Hydrogen bonds between adjacent glucose units hold the linear chains together, forming cellulose bundles known as microfibrils. These microfibrils are critical components of the plant cell wall, providing stability and rigidity [30].

Properties

Cellulose makes up 90% of cotton, 40-50% of wood, and 57% of hemp [32]. This organic polymer is hydrophilic, durable, biodegradable, possesses a high surface area, and is insoluble in water and most solvents due to hydrogen bonds between its chains [33].

A cellulose chain contains three equatorially positioned hydroxyl groups located at positions C2, C3, and C6, which are susceptible to chemical modification, and they influence cellulose chemical reactivity [34]. Due to these hydroxyl groups, cellulose materials exhibit two types of hydrogen bonding: intermolecular, which links cellulose chains within a microfibril, and intramolecular, occurring among hydroxyl groups on a single cellulose strand [34].

Intramolecular hydrogen bonds form between the hydroxyl groups at C2, C3, and C6, and the endocyclic oxygen of adjacent glucose units of a single cellulose strand, while intermolecular hydrogen bonds occur between the hydroxyl group at C3 of one cellulose chain and the C6 hydroxyl group of an adjacent chain [33 – 34], as shown in figure 2.1. Intramolecular hydrogen bonds maintain the rigidity of the cellulose chains, enhancing crystallinity and strengthening the mechanical properties. The ordered regions of intra- and intermolecular hydrogen bonds compact the cellulose chains, limiting the accessibility and reactivity of the hydroxyl groups, and reducing solubility [33 – 34].

Cellulose stiffness is also a consequence of hydrogen bonding as well as the chair conformation of the glucose subunits. The terminals of the cellulose chain are different in the sense that one end, C1, has a hydroxyl group forming part of an aldehyde group which has a reducing activity, enhancing chemical reactivity [35]. The other end has an unmodified hydroxyl group at C4, known as the nonreducing end [35].

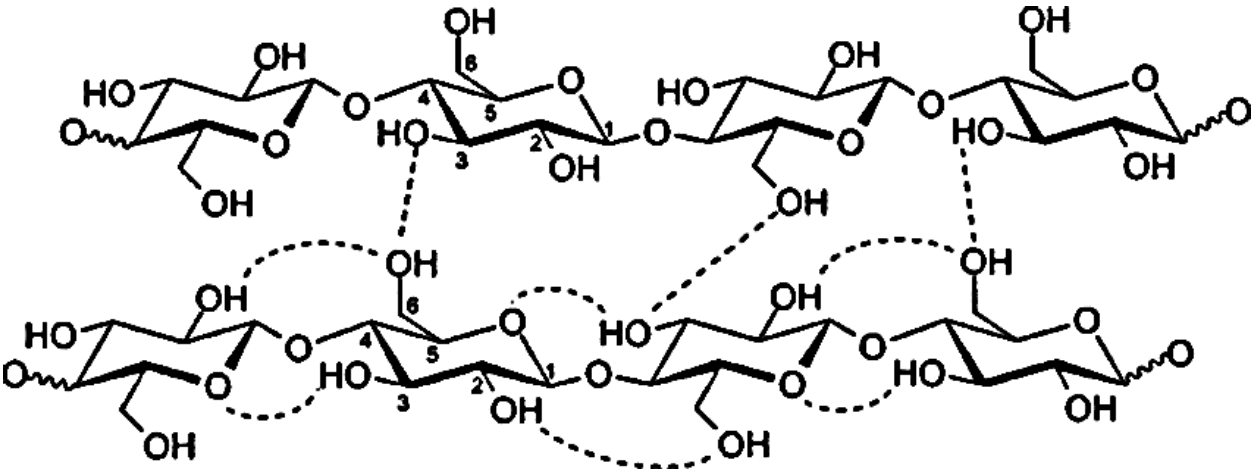

Figure 2.1: Intra- and intermolecular hydrogen bonding of cellulose (Pinkert, 2009).

As previously stated, cellulose is a linear chain made of glucose units linked by glycosidic bonds. These linear chains are held together by hydrogen bonding, which gives rise to the supramolecular structure of cellulose. Determined by the intra- and intermolecular hydrogen bonding in cellulose, the supramolecular structure of cellulose contributes to the unique properties of cellulose and its structure. Intermolecular hydrogen bonding interactions which cause cellulose chains to align themselves side by side strengthen and stabilize the structure of cellulose and give rise to the other important aspect of the supramolecular structure of cellulose, which is cellulose microfibrils [36].

Microfibrils are cellulose bundles that result when cellulose chains align themselves side by side, in a parallel manner, as a result of hydrogen bonding. These structures occur when aligned cellulose chains further aggregate into thicker and larger structures. The robust intra- and intermolecular hydrogen bonds maintain the integrity of the microfibrils, preventing them from separating and forming a highly organized and strong network with significant mechanical strength [36 – 37]. Microfibrils may further interact with each other

through additional hydrogen bonding resulting in macrofibrils, also known as cellulose fibre [36]. The collective hydrogen bonding at various organizational levels contributes to the macroscopic properties of cellulose, such as its strength, stability, and insolubility in water and other solvents [37]. These properties are essential for the structural integrity of plant cell walls, where microfibrils and macrofibrils play a crucial role.

The supramolecular structure of cellulose consists of a complex arrangement of individual cellulose chains, leading to a hierarchical organization. This organization results in the formation of two distinct regions within cellulose fibres: the crystalline and amorphous regions as shown in figure 2.2. The crystalline regions are characterized by a high level of organization and molecular order due to their repetitive pattern, which is maintained by hydrogen bonding between adjacent cellulose chains. These regions are stable and rigid, contributing to the mechanical stability and stiffness of cellulose-based materials, thereby enhancing their strength. The strong intermolecular hydrogen bonds make the crystalline regions of cellulose fibres relatively insoluble in water, providing resistance to environmental factors [38]. Additionally, the highly organized nature of these regions makes cellulose resistant to enzyme degradation, ensuring a longer lifespan for cellulose materials in moist environments [38].

In contrast, the amorphous regions of cellulose fibres exhibit structural disorder. Unlike the crystalline regions, these areas lack a regular repeating pattern and have cellulose chains arranged in a disordered and random manner [38 – 39]. The amorphous regions are very flexible and deform easily, which makes cellulose beneficial for applications requiring materials that can bend or stretch without breaking. However, these regions are more susceptible to enzyme degradation, and breaking down cellulose fibres in these areas is relatively simple. The less restrictive nature of the structure of the amorphous region of the cellulose fibres makes them vulnerable to water absorption, leading to moisture affecting the mechanical properties of cellulose materials [38].

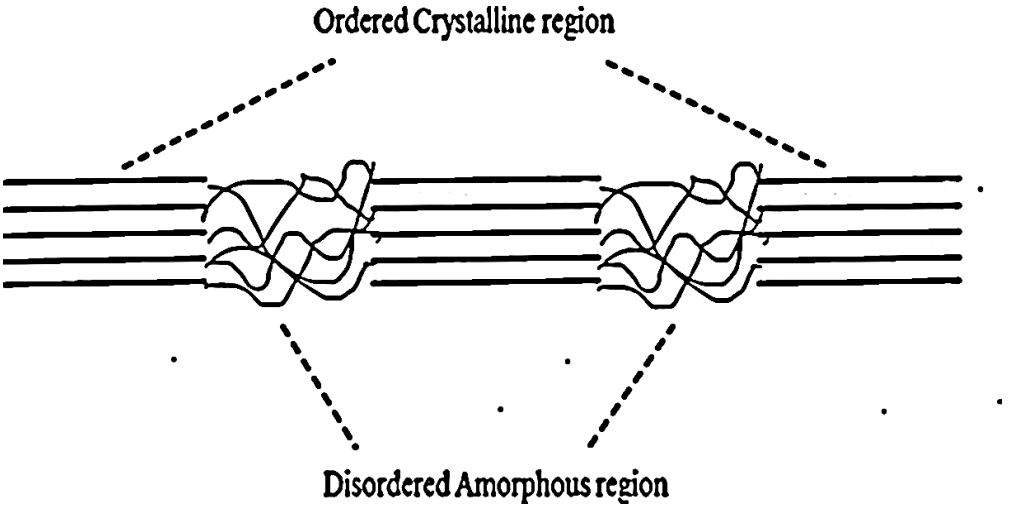

Figure 2.2: Illustration of amorphous and crystalline regions of cellulose fibers [40]

Control on how to balance between the amorphous and crystalline regions of cellulose fibres allows for tailoring of the cellulose material based on the desired applications. When cellulose is employed for structural applications, it will be beneficial if the proportion of crystalline regions is higher than amorphous regions. Conversely, if cellulose is employed for flexible materials' application, it will make sense to tailor the supramolecular structure to have a higher ratio of amorphous regions. Furthermore, a higher proportion of amorphous regions in cellulose will result in a more biodegradable material [41].

The polymorphs of cellulose play a role in the supramolecular structure of cellulose. Different arrangements of cellulose chains result in four cellulose polymorphs: cellulose I-IV, as shown in table 2.5 [41].

Table 2.5: Cellulose polymorphs

Polymorph	**Cellulose chains arrangement**	**Allomorphs**
Cellulose I	Parallel	Cellulose I_α and I_β
Cellulose II	Anti-parallel	
Cellulose III	Parallel and anti-parallel	Cellulose III_I and III_{II}
Cellulose IV	Parallel	Cellulose IV_I and IV_{II}

Cellulose I is the native form of cellulose, and cellulose II is the regenerated form of cellulose I. These two polymorphs, shown in figure 2.3, are the most common forms of cellulose. They differ based on the orientation of the cellulose chains in the crystal structure [42].

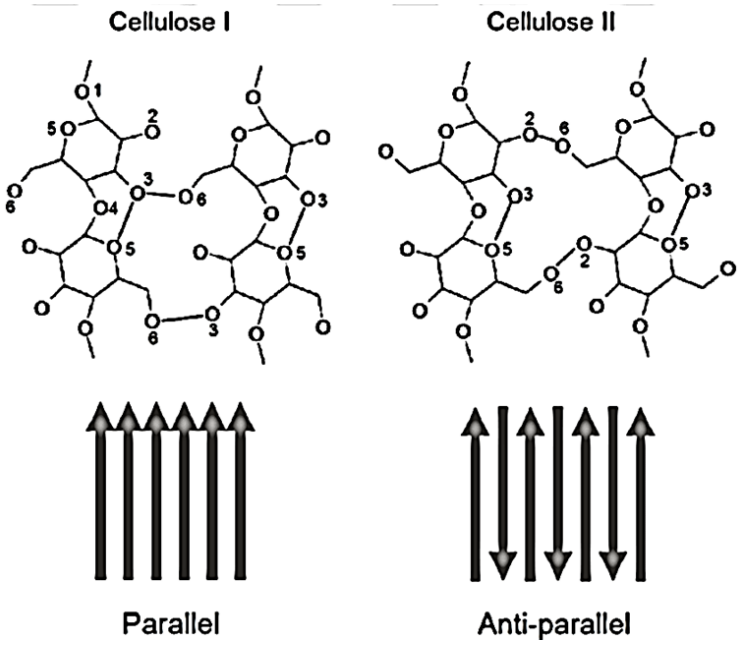

Figure 2.3: The parallel chains of cellulose I vs. antiparallel chains of cellulose II (Serizawa. 2021).

Cellulose I has a parallel arrangement of cellulose chains, resulting in intermolecular hydrogen bonding occurring between hydroxyl groups at C3 of one cellulose chain and C6 of the adjacent cellulose chain while cellulose II has the carbon chains in its crystal structure arranged in an antiparallel manner, resulting in intermolecular hydrogen bonding of this cellulose to occur between the hydroxyl group on C3 and the oxygen atom of the adjacent cellulose chains [41].

The glucopyranose ring structure in cellulose I is parallel to the plane in which hydrogen bonding occurs between cellulose chains, referred to as the b-c plane of cellulose. The chains of cellulose I situated in crystalline regions exist in two allomorphs: cellulose I_α and cellulose I_β, differing based on their crystalline structure and properties [41]. Cellulose I_α exhibits a triclinic crystalline structure, while cellulose I_β has a monoclinic crystalline structure. These differences arise from the varying arrangements and hydrogen bonding

patterns of the cellulose chains within the crystal lattice. Cellulose I_α is mainly a product of bacterial synthesis and is mostly found in algae, and is less stable, while cellulose I_β is primarily produced by higher plants and marine life and has high stability [41].

Swelling native cellulose or treating it with alkali leads to cellulose II. These processes disrupt hydrogen bonding in cellulose I and allow the chains to reorganize themselves in an anti-parallel fashion, resulting in cellulose II. Compared to cellulose I, it is less stable in water. Intramolecular hydrogen bonding in cellulose II is similar to that of native cellulose. However, intermolecular hydrogen bonding is more complex because, despite the backbone of the two adjacent chains having similar conformations, the hydroxymethyl C6 conformations differ [33 – 37]. At the origin of the chains, the hydroxymethyl group has a gauche-trans conformation and forms the intermolecular hydrogen bonds between hydroxyl groups at C6 and C2 of respective cellulose chains; meanwhile, at the center of the chain, the C6 group adopts a trans-guache conformation leading to hydrogen bond occurring between hydroxyl groups at C6 and C3 [41]. This cellulose is amorphous as it lacks long-range order, leading it to be water-soluble.

Immersing cellulose I in ammonia or amine solution leads to its impregnation and expansion, forming a complex structure. Other solvents often used for this impregnation are N'-methylmorpholine-N-oxide or dimethyl sulfoxide. Washing the swollen cellulose fibrillar structure leads to the cellulose material shrinking and converting to cellulose III polymorph [41 – 42]. This polymorph can also be obtained when cellulose I is subjected to high temperature and pressure. The transformation of cellulose I alters the crystal structure and results in the cellulose chains adopting a different arrangement. The cellulose III obtained from cellulose I is referred to as cellulose III_I, and similarly, if it is obtained from cellulose II, it is referred to as cellulose III_{II}, as shown in figure 2.4 [35 – 37].

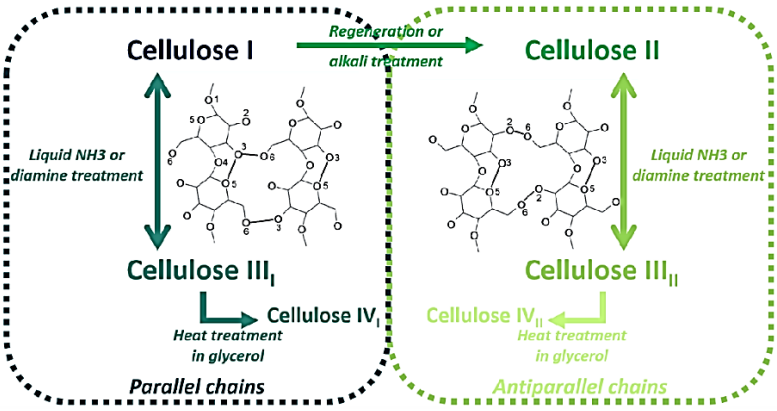

Figure 2.4: Cellulose IIII vs Cellulose IIIII (Gasper. 2019).

Despite cellulose III$_I$ being synthesized from cellulose I, the hydrogen bonding pattern is different, however, it exhibits cellulose chains closely packed parallel to each other with no staggering of the hydroxyl groups at the C6 in the direction of the cellulose chain. The intermolecular hydrogen bonds occur between hydroxyl groups at C3 of one cellulose chain and C6 of the other cellulose chain. Distinct from cellulose III$_I$, cellulose III$_{II}$ has chains arranged anti-parallel to each other, similar to cellulose II. This antiparallel arrangement rearranges the hydrogen bonds, making it distinct from cellulose III$_I$. The cellulose IV polymorph is obtained by subjecting regenerated cellulose fibres such as cellulose II to water baths while stretching them. Its lattice structure resembles that of cellulose I. Its allomorphs, cellulose IV$_I$ and IV$_{II}$, originate from cellulose I and II, respectively, as highlighted in figure 2.4 [41 – 42].

Applications

Cellulose has diverse applications across various industries. It is a crucial raw material for paper production, where it is extracted from wood through chemical pulping, a process that removes lignin and other components, leaving cellulose fibres suitable for making paper. These fibres form the structural framework of paper, enhancing its strength and durability [43]. In the textile industry, cellulose is utilized in the form of cotton fibre, which is obtained from cellulose present in cotton plants. Cotton is widely used in textile

manufacturing for producing clothing, tents, and bedding sheets. Furthermore, cotton has an absorbency of 25-30 times its weight [44].

Native cellulose plays a crucial role in the bioenergy industry as it can be converted into biofuels for renewable energy generation [45]. It serves as a feedstock for bioethanol production, which involves breaking down cellulose into individual sugars through enzymatic hydrolysis, followed by fermentation to produce bioethanol. Additionally, burning cellulosic biomass generates energy. Ongoing research is exploring the potential of cellulose for producing biofuels beyond bioethanol [45].

In the food industry, native cellulose is incorporated into foods to increase fibre content and can be used as a fat substitute. Due to its biodegradability, cellulose is also utilized in packaging, producing biodegradable bags [46].

Further research into native cellulose has shown its potential as an adsorbent in water treatment technologies. Hadid *et al.* (2021) reported the sorption properties of native cellulose and its derivatization for MB removal [47]. Further studies by Mostafa et al. (2023), showed that introducing new functional groups on native cellulose improves adsorption efficiency. Research into cellulose derivatives for water purification shows promise with improved adsorption capacity [48].

2.3.2 Cellulose derivatives

Cellulose derivatives can be produced through chemical and physical modifications of cellulose. One common method is esterification, where the hydroxyl groups on the cellulose chain are replaced with ester groups by treating cellulose with a carboxylic acid or an acid catalyst [40]. This process typically yields cellulose acetate, a widely used cellulose derivative. Another modification method is etherification, which involves replacing the hydroxyl groups with ether groups, resulting in derivatives such as methylcellulose and ethyl cellulose. Moreover, carboxymethylation is the introduction of carboxymethyl groups to the cellulose chain, producing carboxymethyl cellulose [49].

Treating cellulose fibrils with a strong acid such as H_2SO_4, a process known as acid hydrolysis, breaks the glycosidic bonds in the amorphous regions, resulting in shorter

cellulose segments. The products of cellulose hydrolysis include crystalline nanocellulose and cellulose nanofibers [50]. Chemical modification of native cellulose can also be achieved through oxidation, using 2,2,6,6-tetramethylpiperidine-1-oxyl radical (TEMPO)-mediated oxidation, which produces oxidized fibres that disperse individually in water [51].

Physical modification procedures, which do not alter the chemical composition of cellulose, include mechanical swelling, surface adsorption, and grinding. These methods produce regenerated forms of cellulose (cellulose II) and result in derivatives such as cellulose nanofibers, crystalline nanocellulose, and microcrystalline cellulose [33, 50, 52 - 53].

Nanocellulose (NC) materials are significant derivatives obtained from both chemical and physical treatments [50]. Nanocellulose materials are advanced derivatives of cellulose, often referred to as cellulose at the nanoscale. The breakdown of long cellulose fibers into smaller components results in nanocellulose materials with nanoscale dimensions. These materials exhibit superior properties compared to native cellulose, making them highly versatile and promising for various applications. They have a higher surface area, allowing contaminants easy access during adsorption processes, and possess improved mechanical strength and enhanced chemical stability due to their crystalline nature [53].

Nanostructured materials are produced by subjecting native cellulose to chemical, physical treatment, or microbial fermentation. The three primary forms of nanocellulose are bacterial nanocellulose (BNC), cellulose nanofibrils (CNF), and crystalline nanocellulose (CNC), as shown in table 2.6. These materials are utilized in water purification, biomedical applications, optoelectronics, and flexible electronics.

Table 2.6: Nanocellulose classification

Nanocellulose	**Source**	**Main treatment**
Bacterial nanocellulose	Microorganisms	Bacterial fermentation
Cellulose nanofibers	Plant	Mechanical fibrillation
Crystalline nanocellulose	Plant	Acid hydrolysis

2.3.3 Bacterial nanocellulose

Bacterial nanocellulose is a type of nanocellulose that is produced by certain bacteria through fermentation. This form of nanocellulose possesses distinct properties compared to plant-derived cellulose. BNC materials consist of 3D nanoporous fibers with diameters ranging from 30-50 nm, which are thinner than plant-based nanocellulose fibers [49 – 50, 53 – 54]. Additionally, BNC is free of lignin and hemicellulose, components commonly found in plant-based cellulose, resulting in higher purity and crystallinity [54]. BNC's ability to retain water within its structure makes it highly desirable for biomedical applications. Furthermore, BNC is non-toxic and biocompatible, expanding its potential applications. The fine fibers produced through bacterial synthesis exhibit a high degree of polymerization, leading to a mechanically robust material. Another key feature of this high surface area material is its versatility, which allows it to be modified for specific applications [53].

BNC can be produced by various bacterial species, including *Acetobacter*, *Azotobacter*, and *Pseudomonas*, through a fermentation process involving inoculation, fermentation, and harvesting [54]. Inoculation involves introducing bacteria into a culture medium containing carbon sources, typically glucose, and other nutrients. During fermentation, the bacteria oxidize glucose, resulting in the formation of cellulose. The final step involves harvesting and purifying the synthesized cellulose to obtain BNC.

BNC has found applications in numerous fields, its biocompatibility and water retention capabilities make it valuable for biomedical applications. In the food industry, BNC serves as a thickening agent and as a capsule for bioactive compounds. Its excellent mechanical properties make it suitable as a reinforcing component in nanocomposites [54]. BNC has been reported in water purification technologies as a mechanical support structure because of its porosity and high surface area as in the case of hybrid aerogels of BNC and MoS_2 [55]. A study by Radhakrishnan *et al*. (2022) showed that when Pd/Graphene oxide/BNC (Pd/GO/BNC) was used as a composite adsorbent, the hydroxyl groups on the surface of BNC were responsible for the removal of pollutants from water [56]. Table 2.7 shows a few adsorbents that incorporate BNC as a support material.

Table 2.7: Bacterial nanocellulose composite adsorbent material.

Material	**Pollutant**	**Adsorption efficiency**	**Reference**
BNC/MoS_2	Methylene blue	96 %	[55]
	Cr^{6+}	88 %	
Pd/GO/BNC	Methyl orange	99.3 %	[56]
PEI/BNC	Congo red	515.46	[57]
Keratin/DCNC	Crystal violet	1166.67	[58]
BNC-GO-NBC	Rhodamine B	0.1150	[59]
	Acridine Orange	0.1749	
BNC@MOF	Congo Red	3518.6	[60]

BNC has insufficient adsorption sites and needs to be modified to increase surface functionality. Polymers such as polyethyleneimine (PEI) have been used to impart amine groups on BNC to remove anionic dyes such as Congo red [57]. BNC can be derivatized to dialdehyde cellulose nanocrystal (DCNC), this together with keratin forms a biocomposite that can remove Cd^{2+} and Crystal violet from water [58]. A composite of graphene oxide (GO) and BNC results in a mechanically stable nanobiocomposite (NBC) called BNC-GO-NBC which has a combination hydrophilic and hydrophobic properties, promoting π-π interactions and hydrogen bonding to boost the adsorption of Rhodamine B and Acridine orange [59]. MOFs have been incorporated into BNC forming BNC@MOF composites that show ultra-high adsorption for Congo red [60].

2.3.4 Cellulose nanofibers

The morphology and properties of cellulose nanofibers (CNF) vary depending on the cellulose source. CNF fibers typically have widths from 4 to 50 nm and lengths between 0.5 and 2 µm, resulting in a high aspect ratio. Measuring the mechanical properties of CNF is challenging due to their small size, but previous studies have shown that CNF possesses high mechanical stability, making it an excellent support material in

composites. Additionally, its high strength and light weight make it suitable for this purpose.

CNF is characterized by a high surface area, biocompatibility, biodegradability, and thermal stability, making it ideal for various applications, including water purification, either alone or as part of a composite [61].

CNF is naturally synthesized from plant cell walls. During purification, non-cellulose components such as hemicellulose, lignin, and pectin are removed, leaving only cellulose. These non-cellulose materials inhibit fibrillization, the formation of cellulose fibers, and thus hinder CNF formation. CNF synthesis methods can be categorized into three types: mechanical, chemical, and enzymatic [51, 61].

Mechanical treatments to produce CNF include high-pressure homogenization, microfluidization, and grinding. High-pressure homogenization breaks down cellulose into nanofibers under pressure, shearing and reducing the fibers to nanoscale dimensions. The cellulose suspension is passed through the homogenizer 10 to 15 times to ensure complete disintegration. This method has been used to synthesize uniform CNFs with an average diameter of 27 ± 8 nm and a yield of 81% [51].

Increasing pressure and the number of cycles in the high-pressure homogenization synthesis of CNF improves the aspect ratio and dispersion stability of the CNFs [61]. Moreover, the mechanical properties and hydrophilicity also improve. Combining ultrasonication with high-pressure homogenization has been reported to yield high-quality CNF [51, 61 – 62].

Microfluidization is similar to high-pressure homogenization, but instead of using a high-pressure chamber, cellulose suspensions are forced through microchannels with diameters between 200 to 400 µm. This process leads to the fragmentation of cellulose microfibers into cellulose nanofibers (CNFs). CNFs produced via microfluidization tend to have uniform sizes compared to those obtained from high-pressure homogenizers. This method produces CNFs with diameters between 2 nm to 6 nm with crystallinity increasing as the number of microfluidization cycles is increased. However, both high-pressure

homogenization and microfluidization are energy-intensive and are prone to clogging [51, 61].

Another mechanical method for synthesizing CNFs is the grinding method, also known as ultrafine friction grinding. This technique involves subjecting cellulose materials to high-speed grinding and shearing. The grinding method offers advantages such as high efficiency, large capacity, lower energy consumption, and is not prone to clogging. Reports indicate that this method produces CNFs with high crystallinity (81%), excellent thermal stability (above 350°C), and improved dispersion stability. Additionally, the CNFs produced have been shown to enhance the mechanical stability of composites [61 – 62].

Chemical methods for CNF synthesis include acid hydrolysis, oxidation, and solvent-assisted treatments. Acid hydrolysis involves using a strong acid to decompose cellulose microfibers into CNFs. The standard procedure involves adding cellulose to a strong acid solution and quenching with water. Previous studies have demonstrated that strong acids effectively break down the amorphous regions of cellulose fibers, leaving behind the crystalline regions that can be isolated to produce CNFs. This method has been employed to generate CNFs with high crystallinity, high aspect ratio, and significant thermal stability [61 – 62].

The second chemical treatment method is cellulose oxidation, essential for breaking down cellulose into cellulose nanofibers. A well-known procedure is 2,2,6,6-tetramethylpiperidine-1-oxyl (TEMPO)-assisted oxidation, which selectively oxidizes primary hydroxyl groups into carboxyl groups with TEMPO catalyzing the reaction. Common oxidizing agents include NaClO or $NaClO_2$, typically used in alkaline conditions with NaBr [63 – 64]. The process begins by mixing cellulose with TEMPO under alkaline conditions, then adding oxidizing agents to form cellulose fibrils with carboxyl groups. These fibrils are fibrillated into CNF through homogenization.

TEMPO-mediated oxidation combined with mechanical treatments such as counter-collision can produce high-quality CNFs with widths between 15.1 nm and 22 nm [61 – 62]. The degree of carboxylic group functionalization can be controlled by varying the concentration of oxidizing agents and catalysts [64]. Cellulose oxidation is a reliable

technique for producing high-quality CNF materials, allowing control over properties such as crystallinity, thermal stability, and nanofiber size.

CNFs exhibit great potential as adsorbents for removing contaminants from aqueous solutions. CNF has a high surface area, which enhances its ability to effectively capture contaminants. The material surface hydroxyl groups can adsorb pollutants, and further functionalization of these groups can increase selectivity and affinity for specific contaminants, making CNF highly effective for adsorption. Additionally, CNF's biodegradability makes it environmentally friendly for adsorption applications. Despite their small size, CNF materials are mechanically strong and chemically stable, preventing collapse in aqueous environments and enabling their use as reinforcements in composite adsorbents [51, 61, 63]. Moreover, CNF is cheap and sustainable. These properties have led researchers to explore CNF's potential as an adsorbent for removing contaminants from water [62].

CNF has shown excellent performance in adsorbing heavy metals and inorganic contaminants from water. Ultrafine CNF prepared through chemical, physical or a combination of the two methods has demonstrated good performance in this regard. These methods produce CNF aerogels with high adsorption efficiencies for lead, copper, and zinc [65].

CNF materials are effective adsorbents for organic dye removal from water, as shown in Table 2.8. CNF decorated with carboxylic groups through oxidation of bleached cellulose pulp from bagasse (TPC-CNF) showed improved affinity for methylene blue (MB), achieving a maximum adsorption capacity of 502 mg/g compared to 409 mg/g for TEMPO-oxidized CNF (T-CNF) [68]. This novel functionalization route yielded an effective adsorbent with high MB affinity. Porosity enhances adsorption by allowing contaminants to reach internal active sites. 3D porous CNF-based hydrogels (CNF-HG) functionalized with acrylic acid and acrylamide demonstrated promise for MB removal due to their porous structure, enabling diffusion to inner surfaces and access to more active sites [69]. These hydrogels exhibited good cellular compatibility and low toxicity, preventing secondary contamination in water purification technologies.

Melanized-cationic cellulose nanofiber (melanized-C-CNF) demonstrated effective removal of organic dyes, particularly crystal violet, with good recyclability [70]. Composite formation of CNF with other adsorbents can enhance adsorption performance through synergistic effects. CNF/carbon nanomaterial hybrid aerogels achieved maximum adsorption capacities of 1178.5 mg/g for MB and 505 mg/g for Congo red (CR), surpassing the capacities of the individual parent materials and unlocking the potential for effective dye removal from water [71].

Table 2.8: Cellulose nanofiber composite adsorbent materials.

Material	**Pollutant**	**Adsorption capacity**	**Reference**
TPC-CNF	methylene blue	502 mg/g	[68]
TEMPO-oxidized CNF	methylene blue	409 mg/g	[68]
PAMPS-CNF	methylene blue	4535 mg/g	[69]
melanized-C-CNF	crystal violet dye	425.53 mg/g	[70]
CNF/carbon	methylene blue	1178.5 mg/g	[71]
CNF/carbon	Congo red	505 mg/g	[71]

2.3.5 Crystalline nanocellulose

Crystalline nanocellulose (CNC) is characterized by widths between 2-30 nm and lengths extending to several hundred nm. These materials are produced by isolating cellulose crystallites from cellulose sources through hydrolysis with strong acids like sulfuric acid, which degrades the amorphous regions of cellulose fibrils. These regions act as defects, and their removal leads to the breakdown of fibrils, allowing for the isolation of nanocrystals.

CNC can be derived from various cellulose sources such as microcrystalline cellulose, rice straw, hardwood pulp, and softwood pulp [61 – 62]. During hydrolysis, the strong acid degrades the most accessible parts of the cellulose fibrils, starting with the amorphous

regions, followed by the reducing end, and finally the crystalline section. Controlling the degree of hydrolysis requires careful management of acid concentration, reaction time, and temperature [61]. Longer reaction times result in complete hydrolysis, while shorter times maintain a higher degree of polymerization with undispersed fibrils. The purified CNC, obtained through dialysis, forms nanoscale rod-like particles known as CNC nanowhiskers. While sulfuric acid is commonly used, other acids like hydrochloric, phosphoric, and hydrobromic acid can also be effective. Sulfuric acid hydrolysis breaks the glycosidic bonds in the amorphous regions and can esterify crystalline surface hydroxyl groups to sulfate groups, enhancing crystallinity and functionalizing CNC with sulfate groups.

Research indicates that nanocellulose materials are effective adsorbents for removing methylene blue, other organic dyes, heavy metals, biological contaminants, oil, and various organic compounds (including phenols and organic solvents) from the environment [61 – 62]. These materials exhibit high adsorption efficiencies and can be reused multiple times for adsorption without compromising structural integrity. The effective use of CNC in composites as adsorbent materials is shown in table 2.9.

Table 2.9: Crystalline nanocellulose composites as adsorbent materials for water purification.

Material	**Pollutant**	**Adsorption capacity**	**Reference**
Graphene-CNC	Aspirin	99 mg/g	[72]
	acetaminophen	76.34 mg/g	
Cu-BTC/CNC aerogel	Congo Red	43 mg/g	[73]
MIP-NC	Pb^{2+}	27.55 mg/g	[74]
	Hg^{2+}	161.31	
MCNC	Doxycycline	61.2 mg/m^2 (70 %)	[75]
PAA-CNC	diclofenac	396.8 mg/g	[76]

Ogunleye *et al.* (2023) incorporated CNC into graphene resulting in an adsorbent that did not aggregate in water [72]. Furthermore, CNC serves as a scaffold, reinforcing the adsorbent while increasing the surface area, improving the adsorption of aspirin from 61.73 mg/g to 99 mg/g and acetaminophen from 20.41 to 76.34 mg/g. CNC when used in combination with MOFs has been found to overcome limitations inherent with powdered MOFs such as Cu-BTC, which include difficulty in handling and mass transfer limitations. Trapping Cu-BTC in a CNC aerogel to obtain a Cu-BTC/CNC aerogel for the removal of Congo red resulted in a sufficiently good adsorption efficiency of 43 mg/g [73].

Molecularly imprinted polymers (MIPs) based on CNC form a mechanically stable and higher surface area adsorbent. MIP-NC had adsorption capacities of 27.55 mg/g and 161.31 mg/g for the removal of Hg^{2+} and Pb^{2+}, respectively [74]. A one-pot synthesis approach was used to prepare a functionalized magnetic cellulose nanocrystal (MCNC) composite adsorbent. The presence of CNC enhanced the efficiency due to the high surface area and presence of carboxyl, sulfate, and phenyl groups, leading to the adsorbent achieving 61.2 mg/m^2 (70 %) for doxycycline removal [75]. A hydrogel prepared by forming a composite of CNC and poly(acrylic acid) (PAA), CNC/PAA, demonstrated good adsorption efficiency for diclofenac (396.8 mg/g). The presence of CNC resulted in a mechanically stable adsorbent with abundant hydroxyl and sulfate groups to facilitate adsorption [76].

2.3.6 Cellulose acetate

Cellulose acetate, CA, is a synthetic derivative of cellulose and is considered the most important ester of cellulose, having some of its surface hydroxyl groups replaced with acetate groups [77], as shown in figure 2.5. The esterification of surface hydroxyl groups is achieved by reacting cellulose with acetic acid or acetic anhydride in the presence of sulfuric acid, and the degree of substitution affects the properties of CA. The most common form of CA has acetate groups substituting 2-2.5 hydroxyl groups out of 3 and is soluble in most common solvents rendering it simple to process into 2D or 3D materials. CA can be processed into various forms such as films, fibres, membranes, and beads,

allowing it to be applied in applications such as textiles, water purification, and medical industries [77 – 79].

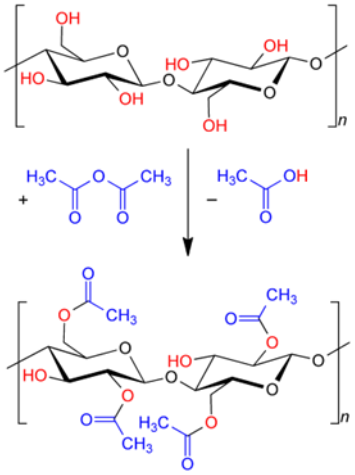

Figure 2.5: Esterification of cellulose to form cellulose acetate (https://commons.wikimedia.org/wiki/File:Formation_of_Cellulose_acetate_V1.png)

The transparency or opacity of cellulose acetate can vary based on the synthetic method and extent of substitution. This variability is significant when CA is utilized for optical applications. Additionally, its flexibility, solubility, and relatively low melting point are advantageous for processing in diverse applications.

CA is well-suited for water purification purposes such as adsorption and membrane technologies due to its strong tensile strength and resistance to water damage. For water purification, CA is mainly used in the manufacturing of membranes [78]. Cellulose acetate has been applied in reverse osmosis, ultrafiltration, and nanofiltration, performing well for the separation of contaminants from water [78 – 79]. The performance of CA in water purification can be improved by decorating CA membranes with inorganic materials such as metal oxides and metal nanoparticles, including TiO_2, Fe_3O_4, MOFs, and zeolites. Functionalization with these materials can minimize fouling, improving permeability and selectivity [79].

CA has been used as a substrate for adsorbents in wastewater purification technologies. This is due to the hydrophilic nature of CA that maximizes interaction with water, speeding up the adsorption of contaminants. Furthermore, the biocompatibility of CA makes it eco-

friendly, and safe for water applications, and its porous structure aids in maximizing adsorption efficiency [78 – 79].

Most adsorbents are in powdered form, making them difficult to handle and separate after adsorption. This can lead to secondary contamination. CA has been used as a support material for powdered adsorbents such as MOFs and these composites have shown high selectivity for pollutants and demonstrated good reusability [80], as shown in table 2.10.

The presence of CA in CA/metal-organic framework-derived porous carbon (MOFDPC) promoted the reusability of the adsorptive membrane while achieving a high removal efficiency of 98.2% for MB removal [81]. UiO-66 was combined with Fe_3O_4 and functionalized with third-generation hyperbranched poly(amidoamine) dendrimer (PAMAM), to form a composite with good chemical stability and good adsorption efficiency. The composite was electrospun on CA, resulting in a reusable adsorbent that achieved an adsorption capacity of 940.76 mg/g, maintaining 80.76 % of the adsorption capacity after 4 adsorption cycles [82]. A chitosan-decorated CA adsorbent showed great structural stability in water, as evidenced by its performance over eight adsorption cycles of chromium ion removal in water [79]. The structural stability, thermal resilience, and adsorption efficiency make CA composite adsorbents highly promising materials for water pollution treatment.

Table 2.10: Cellulose acetate as a substrate for adsorbent materials.

Adsorbent	**Pollutant**	**Efficiency**	**Reference**
CA/MOFDPC	MB	98.2%	[81]
CA/Fe_3O_4/UiO-66	MB	940.76 mg/g	[82]
CA/Chitosan	Cr^{6+}	51.6 mg/g	[79]
CA/MOF-DPC	MB	41.36 mg/g	[80]

2.4 Metal-organic frameworks

2.4.1 Introduction, properties and applications

Metal-organic frameworks (MOFs) are crystalline structures that can be one-dimensional (1D), two-dimensional (2D), or three-dimensional (3D). These frameworks are formed by the covalent bonding of metal ions or clusters with organic linkers/ligands. MOF materials are highly ordered, crystalline materials, characterized by a regular arrangement of metal ion nodes and organic ligands in a repeating pattern, resulting in high surface area and clearly defined pores and channels. MOFs are known for their high surface area, porosity, numerous active chemical reaction sites, and customizable surface chemistry [82]. More than 86 different metal ions have been identified as suitable for constructing MOFs, and over a thousand organic ligands have been reported to be capable of forming MOFs. The selection of metal ions and corresponding organic ligands determines the diversity of MOFs, resulting in various frameworks with distinct pore structures, surface areas, and properties [82]. Common metal ions used in MOF synthesis include zinc, zirconium, iron, nickel, and copper, which act as coordination centers. Frequently used organic ligands include 1.4-benzene dicarboxylic acid (terephthalic acid), bipyridine and its derivatives, 2,5-dihydroxyterephthalic acid, benzene-1,3,5-tricarboxylic acid (BTC), and 2-aminobenzenedycarboxylic acid [82 – 87].

The careful selection of metal ions and organic ligands allows for the regulation of pore sizes, making MOFs suitable for a wide range of applications. Due to their high porosity and organized channels, MOFs can form host-guest interactions with various substances, molecules, and particles [83]. These materials are used in catalysis, photodegradation, and other processes due to the catalytic activity exhibited by metal centers in MOFs with accessible coordination sites [83 – 84]. Their large surface area makes them ideal for adsorption in gas capture, storage, and water purification [82 – 83]. MOFs are used in catalysis, drug delivery, environmental sensing, and gas sensing. MOFs have also found application in membrane technologies due to their functionalizable adsorption-active sites [82 – 83]. Additionally, their high surface area and tunable surface chemistry have led MOFs to be used for energy storage applications.

2.4.2 MOF synthesis strategies

Several strategies are used for the synthesis of MOFs, the choice is governed by the desired structure, properties, and intended application of the MOF material. Table 2.11 shows different synthetic strategies used for MOFs.

Table 2.11: Synthesis strategies for MOFs

Procedure	Temperature	Solvent usage	Speed
Solvothermal	Moderate to High (120–250°C)	High (organic solvents)	Slow
Hydrothermal	Moderate (100–200°C)	High (water-based)	Slow
Ionothermal	High (150–300°C)	Low (ionic liquid as solvent)	Moderate
Microwave-assisted	Moderate to High (120–250°C)	Moderate to High	Very fast
Slow evaporation	Ambient to Moderate (20–80°C)	High (organic solvents)	Very slow
Diffusion	Ambient to Moderate (20–80°C)	High (multi-solvent system)	Slow

The most common synthesis strategy is the solvothermal/hydrothermal method, which is shown in figure 2.6. During this process, the building blocks (the metal ion source and the organic ligand) are reacted in a closed vessel at high temperature and pressure [88]. The solvent, ligand, and metal are combined and heated under pressure above the boiling point of the solvent. Temperature ranges for these reactions are between 50 ^{o}C and 260 ^{o}C, or higher. The elevated temperatures are required for forming bonds of the framework as well as ensuring proper crystallization. Varying the synthesis temperature has been observed to have an impact on the morphology of the MOF crystal. Shen *et al*. (2022) synthesized Ni-based MOFs at different temperatures (60 – 120 ^{o}C) and found the MOF prepared at 80 ^{o}C to have a larger specific surface area, a cross-network structure, and

was the best performing MOF for the selected application i.e. supercapacitor [85]. Kamal *et al*. (2020) used the solvothermal synthetic procedure for MOFs and found the washing procedure as the drawback of this method and they developed an optimized washing method [86]. The best solvents for MOF synthesis are high boiling points such as N'N' dimethylformamide (DMF), diethylformamide (DEF), water, methanol, and ethanol.

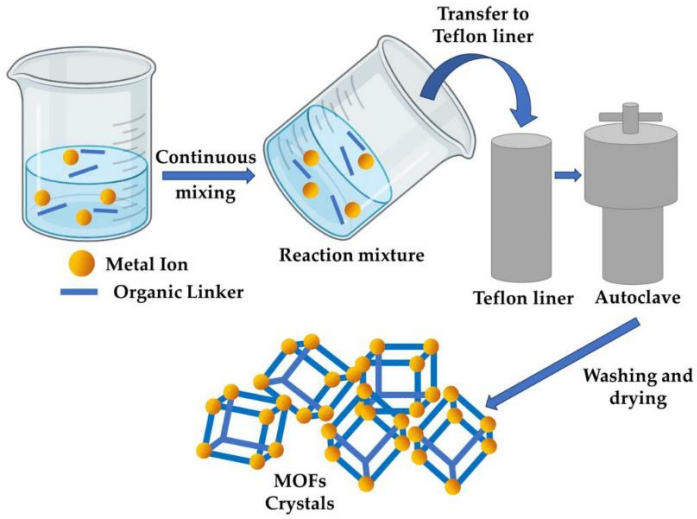

Figure 2.6: A depiction of the solvo/hydrothermal synthesis process for MOF crystals [88].

Ionothermal synthesis is classified as a subcategory of solvo/hydrothermal synthesis. This synthesis method involves the use of ionic liquids as substitutes for solvents, and it is more environmentally friendly. Azbell *et al*. (2023) showed that combining an organic linker with a low-melting metal dihalide or hydrate salt without the addition of a solvent yields high-quality MOFs. The authors concluded that the MOFs synthesized under ionothermal conditions have properties comparable to those of MOFs synthesized by the traditional solvothermal procedure. This environmentally friendly method is more sustainable and scalable compared to traditional techniques, capable of reducing organic solvent usage [87].

MOFs can be produced through microwave-assisted methods. This technique is rapidly evolving, and its main advantage is its ability to fast-track the synthesis of MOF crystals. Microwaves are used to irradiate the reaction mixture of the metal source and the organic linker, accelerating the chemical reaction and leading to faster nucleation and crystal

growth [89]. The target MOF structure and properties dictate the optimization of parameters, such as temperature, reaction time, and microwave power [82]. The synthesized MOF is isolated by centrifugation or filtration, and the resulting powder is washed and dried to produce the MOF crystal. This procedure synthesizes MOFs with high purity and better-defined crystals, as a result of the uniform heating during the irradiation process [82, 89]. Better control over the crystallite size is found with this method. Additionally, the presence of a modulator, which is small organic molecules such as carboxylic acids and amines, is added to the preparation method to control morphology, porosity, and other properties of MOFs, increasing MOF yield and crystal size [90].

MOFs can be synthesized through slow evaporation and diffusion methods [91]. These are two closely related synthesis techniques. The benefits that come with these methods are that they require no energy input and are conducted at room temperature. The slow evaporation method ensures controlled formation of the crystal structure. The first step of this procedure is choosing a metal precursor and the organic ligand, followed by dissolving them together in the solvent of choice and stirring to ensure the mixture is homogeneous, as shown in figure 2.7. The homogeneous mixture is left to slowly evaporate leaving behind crystals when the critical concentration is reached [90]. The critical concentration is the concentration that favors nucleation and crystal growth. The solvent for this procedure is a mixture of low boiling point solvents.

During diffusion, the metal salt and the organic ligand are dissolved in separate solvents. Polar solvents are used for the metal source and less polar solvents are used to dissolve organic ligands. The two solutions are layered on top of each other with the metal solution at the bottom and the ligand solution added at the top, separated by an intermediate layer, usually a less polar solvent to retard mixing. The metal ion and the organic ligand slowly diffuse to the intermediate layer and mix and self-assemble into the desired MOF.

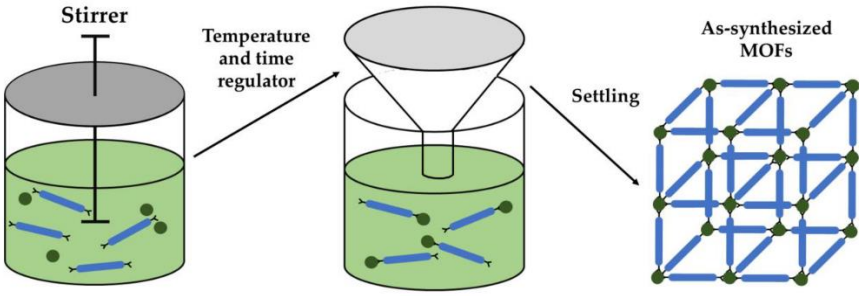

Figure 2.7: An illustration of the slow evaporation method [88]

The challenges in MOF synthesis, such as limited control over their shape and size, the high energy demands of traditional methods, the reliance on potentially harmful solvents, and the difficulty of scaling up production, have driven the exploration of innovative synthetic approaches. Future research will likely focus on developing greener and more sustainable methods, including the use of alternative solvents and renewable energy sources. Simultaneously, advancements in techniques like microwave-assisted synthesis and 3D printing will allow greater control over the MOF structure. Furthermore, the integration of high-throughput screening methods with the power of artificial intelligence and machine learning will accelerate the discovery of new MOFs and optimize their synthesis conditions. These combined efforts will unlock the full potential of MOFs for diverse applications.

2.4.3 Copper-based MOFs as adsorbents for water purification

Copper-based MOFs consist of copper ions or clusters that serve as the node, coordinated to an organic ligand referred to as the linker. The choice of the ligand and its coordination with copper determine the structure of the MOF and its properties [92 – 96]. There is a wide range of structural diversity with copper as the node, which can be coordinated with many different organic ligands. This structural diversity results in several copper-based MOFs with different properties such as crystallite size, pore size, morphology, shape, and surface chemistry. This results in copper-based MOFs being useful in many applications including water purification, gas sensing, gas storage, catalysis, and drug delivery [92].

Copper-based MOFs have been reported to be useful in the adsorptive removal of contaminants from aqueous media. The success of these MOFs in water purification is attributed to their notable characteristics such as high surface area, high porosity, availability of abundant adsorption active sites, tunable surface chemistry, and pore structure [92 – 97]. As a result, these materials have been used as adsorbents for the removal of contaminants such as organic dyes, heavy metals, volatile organic compounds, and pharmaceutical wastes [96 – 102]. The working principle of the adsorption of contaminants on the surface of the Cu-MOF adsorbent involves several mechanisms. The adsorption process can occur through physical adsorption, chemical adsorption, or a synergistic combination of both mechanisms, as shown in table 2.12.

Table 2.12: Adsorption mechanisms for Cu-based MOFs

Physical adsorption	**Chemical adsorption**
Pore filling	$\pi - \pi$ interaction
Size exclusion	hydrogen bonding
Van der Waals interactions	coordination interaction
	Lewis acid-base interactions

Examples of physical methods of adsorption are pore-filling, size exclusion, and van der Waals interactions. Pore-filling results when contaminants in aqueous solutions become trapped in the pores of the MOF and are ultimately removed from these solutions. Depending on the target contaminant, the pore structures of the materials can be tailored to have specific sizes and shapes, for better adsorption of contaminants from aqueous solutions [96 – 97]. Size exclusion also involves tailoring the pore structures and occurs when the size and shape of the pore are engineered to exclude certain substances from passing while allowing others to pass through. With this procedure, contaminants are excluded from passing through and only pure water is allowed to pass through, resulting in decontamination [97].

Van der Waals interactions are physical interactions that MOFs use for the adsorption of contaminants. This mechanism involves intermolecular interactions between MOFs and

the contaminants, aiding in adsorption. This form of interaction occurs due to the polarization of the electron distribution of the MOF and the pollutant [103]. Cu-MOFs have shown great capabilities for the removal of pollutants from water, as illustrated in table 2.13.

Table 2.13: Cu-MOFs for the removal of pollutants from water.

Adsorbent	**Pollutant**	**Efficiency**	**Reference**
Cu-BTC-Th	Pb^{2+}	732.86 mg/g	[96]
Cu-DPA	Cr^{6+}	96.7 %	[98]
	Cd^{2+}	99.5 %	
	Pb^{2+}	99.5 %	
Cu-BTC	Pb^{2+}	958.37 mg/g	[99]
Cu-BDC	Sunset Yellow FCF	80 %	[100]
	Tartrazine	90 %	
	Orange II	93%	
	Methyl orange	85%	
Cu-BTC@Algal/Fe_3O_4	Rhodamine B	200 mg/g	[101]
2D Cu(II)-MOF	Methylene blue	96.5 %	[102]
	Methyl orange	95.3 %	
	methyl red	93.0%	

Zhong et al. (2022) developed a copper-based MOF by functionalizing Cu-BTC with 4-thioureidobenzoic acid (Th), resulting in Cu-BTC-Th [96]. 4-thioureidobenzoic acid was introduced to selectively adsorb Pb^{2+} from aqueous solutions. The functionalization significantly enhanced Pb^{2+} adsorption capacity from 634.09 mg/g to 732.86 mg/g. The addition of Th boosted the electrostatic attractions between Cu-BTC-Th and Pb^{2+}, contributing to increased adsorption capacity. However, the primary mechanism for the adsorption process was identified as the ion exchange of Cu^{2+} for Pb^{2+}, followed by electrostatic interactions due to the strong affinity of $-NH_2$ and -C=S groups on the surface of Cu-BTC-Th for Pb^{2+}ions.

Haso *et al*. (2022) synthesized copper (II) diphenylamine MOF for the simultaneous adsorptive removal of Cr^{6+}, Cd^{2+}, and Pb^{2+} ions in aqueous solutions [98]. The adsorbent reported a maximum removal efficiency of 96.7 %, 99.5 %, and 99.5 % respectively for these heavy metals, demonstrating the potential of this adsorbent to effectively remove toxic heavy metals from aqueous solutions simultaneously, indicating its practical applicability. Lee and Choi (2022) fabricated Cu-BTC MOF adsorbents *via* a solvothermal procedure for the removal of Pb^{2+} ions from aqueous media [99]. The major driving force for this adsorption was determined to be ion exchange between the Cu^{2+} of the Cu-BTC and Pb^{2+} contaminant, achieving the highest adsorption capacity of 958.37 mg/g.

Copper-based MOFs have been used as adsorbents in the removal of organic dyes from aqueous solutions. Chernomorova *et al*. (2023) evaluated the performance of copper benzenedicarboxylate (Cu-BDC) for the removal of sunset yellow FCF, tartrazine, orange II, and methyl orange, with the adsorbent observed to perform better than traditional materials such as activated carbon [100]. The high organic dye recovery exhibited by Cu-BDC showed that this MOF has the potential to be applied efficiently as a reusable adsorbent for the removal of organic dyes from contaminated aqueous solutions.

The incorporation of Cu-BTC MOF onto Alginate-coated nano-iron oxide combined with copper-based solvothermal conditions resulted in a novel, environmentally friendly composite, Cu-BTC@Algal/Fe_3O_4 whose adsorptive performance was reasonable for the removal of Rhodamine B (RhB) dye from wastewater [101]. This study coupled adsorption with photocatalysis, achieving an adsorption capacity of 200 mg/g and 97 % RhB removal. Raza *et al*. (2021) synthesized a 2D copper-based MOF with aminobenzoic acid as the organic linker at room temperature under solvothermal conditions [102]. Both techniques yielded identical MOFs as confirmed by several characterization techniques. The MOF was applied for the removal of methylene blue, methyl orange, and methyl red from contaminated water. The adsorbent achieved a high adsorption rate of the organic dyes as within the first minute of the adsorption process, >90 % of the organic dyes were adsorbed. Mechanisms responsible for this adsorption process were electrostatic attractions, hydrogen bonding, $\pi - \pi$ interactions, and coordination interactions. The

synergistic effect of all these mechanisms was responsible for the adsorption of the organic dyes by the copper-based MOF.

2.4.4 Zinc-based MOFs as adsorbents for water purification

Most Zn-based MOFs use ZnO or ZnO clusters as their metal nodes. Coordination of these Zn metal nodes with different organic ligands results in MOFs having a variety of pore sizes and pore shapes [103 - 107]. This further extends the surface area, stability, and other general properties of these materials. The properties of Zn-based MOFs, or any MOF, can be expanded through calcination, and this expands the scope of application of these materials. [103 – 104].

Zn-based MOFs have been used for the adsorptive removal of heavy metals from contaminated water, and some studies are listed in table 2.14.

Table 2.14: Zn-MOF adsorbents for water purification

Adsorbent	**Pollutant**	**Efficiency**	**References**
IUST-2	Pb^{2+}	97 %	[107]
	Hg^{2+}	87 %	
PUC7	W^{6+}	476.2 mg/g	[108]
	V^{5+}	460.8 mg/g	
Zn-AHMT	Hg^{2+}	802.8 mg/g	[109]
Zn(BDC)	Aniline blue	55.34 mg/g	[110]
	Orange II	10.01 mg/g	
	Methylene blue	2.63 mg/g	
Zn(CPA)(DMF)	Methylene blue	92.5 %	[111]

Hossiene and Tadjarodi (2023) synthesized $Zn_2(DPTTZ)(OBA)_2$, referred to as IUST-2, through a solvothermal procedure, using 2,5-di(4-pyridyl) thiazolo [5,4-d] thiazole (DPTTZ) and 4,4-oxy bis(benzoic acid) (OBA) as organic ligands [107]. Upon evaluation of the adsorption performance, the Zn-based MOF achieved 97 % and 87 % removal of

Pb^{2+} and Hg^{2+} ions in aqueous solution, respectively. Zn-based MOFs demonstrate good reusability as this study showed that upon desorbing $Zn_2(DPTTZ)(OBA)_2$ with EDTA.2Na solution, it further attained good adsorption efficiencies, highlighting its reliability and economic nature.

A highly luminescent and porous Zn-based MOF, PUC7, was synthesized in a mixture of DMF and methanol using 1,2-di(4-pyridyl) ethylene and 2-aminoterephthalic acid as the organic ligand. The MOF was used to detect W^{6+} and V^{5+} ions and achieved low detection limits of 0.17 µM and 0.22 µM, for W^{6+} and V^{5+} ions, respectively [108]. The recyclable MOF further displayed efficient removal of these heavy metal ions from aqueous solutions, achieving 476.2 mg/g and 460.8 mg/g adsorption capacity for W^{6+} and V^{5+} ions, respectively.

Zeng *et al*. (2021) evaluated Zn-AHMT, a Zn-based MOF, with 3-amino-3-hydrazine-5-mercapto-1,2,4-triazole (AHMT) as the organic linker for the removal of Hg^{2+} from aqueous solutions. The adsorbent achieved an adsorption capacity of 802.8 mg/g through chelation between Hg^{2+} and $-NH_2$ and ion exchange between Hg^{2+} and -SH [109]. This adsorbent was further reported to selectively adsorb Hg^{2+} ions in an aqueous solution containing Hg^{2+}, Ni^{2+}, Co^{2+}, Mg^{2+}, Mn^{2+}, Al^{3+}, and Cr^{3+} ions.

A Zn-based MOF with terephthalic acid (BDC) as the organic linker was evaluated for the adsorption of aniline blue (AB), orange II (O(II)), and methylene blue (MB). The adsorbent, Zn(BDC) MOF, achieved adsorption capacities of 55.34 mg/g, 10.01 mg/g, and 2.63 mg/g for the adsorption of AB, O(II), and MB, respectively [110]. The Zn(BDC)-MOF demonstrated strong stability after undergoing five adsorption-desorption cycles, maintaining its functional groups and framework without any alterations showing Zn-MOFs as effective adsorbents. Another Zn-based MOF with a 2.5-bis(4'-carboxyphenyl) aniline ligand displayed good performance when used for the removal of MB from aqueous solutions, achieving a removal efficiency of 92.5 % [111]. The same adsorbent further adsorbed nitrobenzene in DMF at a limit of 2.09×10^{-5} mol/L while exhibiting high selectivity and sensitivity for Hg^{2+} and Cr^{6+} ions highlighting the versatility and practical applicability of Zn-based MOFs. Zn-based MOFs have photocatalytic activity, due to their

metal component. This property improves adsorption efficiency upon light irradiation [91, 105].

These studies highlight the effectiveness, versatility, and reliability of Zn-based MOF materials for the removal of organic dyes from aqueous solutions. Zn-based MOFs are highly effective for the adsorptive removal of contaminants from water due to their unique properties and structural characteristics. These MOFs exhibit excellent adsorption/desorption properties, ensuring good reusability and cost-effectiveness. Reused Zn-based MOFs maintain high adsorption efficiencies, making them a promising solution for water purification.

2.4.5 Nickel-based MOFs as adsorbents for water purification

Nickel-based MOFs have nickel ions or clusters coordinated with organic ligands that serve as anchors or connectors.

Owing to the coordination environment at the nodes, Ni-based MOFs have been reported to exhibit catalytic activity. The coordination environment enables the MOF material to engage in Lewis acid-base reactions with certain molecules to facilitate catalysis [112 – 113]. Additionally, these materials can catalyze various reactions through redox and coordination processes, demonstrating their versatility and effectiveness as catalysts [114 – 116]. Furthermore, the magnetic properties of Ni ions provide an opportunity to impart magnetism to the MOF structure, making them suitable for applications such as magnetic sensing. The functional groups on the organic linkers can serve as additional catalytic active sites.

Ni-based MOFs have been reported as adsorbents for the removal of contaminants from aqueous systems. Adsorption mechanisms involved in this decontamination procedure mainly stem from the Ni environment in the node. In a typical adsorption process, the Ni ions serve as the adsorption active centers. Ni ions facilitate the adsorption of contaminants through several mechanisms such as coordination interactions whereby, the contaminant acts as the ligand and forms a coordination complex with the metal ion [117]. Additionally, the Ni^{2+} ion's positive charge density attracts anionic contaminants

through electrostatic interactions, also, the metal ion may act as a Lewis acid and interact with contaminants that are capable of behaving as Lewis bases through Lewis acid-base interactions [118]. The Ni ions are also capable of facilitating the adsorption process through ion exchange reactions [119].

The organic ligands contribute to the adsorption performance and can serve as adsorption active sites, capable of interacting with a wide variety of contaminants in aqueous solutions through a wide range of adsorption mechanisms [117]. Almost all organic linkers have benzene rings in their structures, unlocking the capacity to interact with contaminants that have benzene rings through $\pi - \pi$ interaction [116 – 117]. Organic linkers can be functionalized with functional groups with different charge densities to alter the surface charge of Ni-based MOFs, enabling them to interact with contaminants through electrostatic attractions. Certain functional groups such as -NH_2, -OH, and -COOH can facilitate hydrogen bonding between the MOF and the adsorbates, leading to enhanced adsorption [117, 120 – 121]. All these adsorption mechanisms aid in selectivity during the adsorption process.

Ni-based MOFs have been reported to effectively remove heavy metals and other contaminants from aqueous solutions, as demonstrated in table 2.15.

Table 2.15: Ni-based adsorbents for the adsorption of pollutants from water.

Adsorbent	**Pollutant**	**Efficiency**	**References**
Ni-MOF-74	Pb^{2+}	370.37 mg/g	[120]
Ni-MBI	Hg^{2+}	328.8 mg/g	[121]
Ni-BDC MOF@GO	Methylene blue	222 mg/g	[122]
Ni-MOF	Coomassie brilliant blue.	19.9 mg/g	[123]

Ni-MOF-74 consisting of 2,5-dihydroxyterephthalic acid as the organic linker evaluated for the adsorptive removal of Pb^{2+} ions from aqueous solutions demonstrated good adsorption capabilities [120]. The adsorbent achieved an adsorption capacity of 370.37 mg/g through chemisorption. The performance exhibited by Ni-MOF-74 was attributed to

the presence of surface hydroxyl groups as they increase adsorption active sites. A Ni-based MOF with 2-mercaptobenzimidazole (MBI) as the organic linker had an adsorption capacity of 328.8 mg/g for the removal of Hg^{2+} ions in aqueous solution. The bimetallic MOF, Zn/Ni-MOF, showed a higher adsorption capacity of 744.4 mg/g, indicating the synergistic benefits of the two metals for Hg^{2+} removal [121].

Ahsan et al. (2020) enhanced a Ni-based MOF by integrating it with graphene oxide and carbon nanotubes to create a nanocomposite hybrid material, which was tested for its ability to adsorb MB from water [122]. This hybrid nanocomposite demonstrated strong interactions with MB due to the synergistic effects of its components. It had an adsorption capacity of 222 mg/g which was significantly higher than that of the individual parent materials. The high adsorption capacity was attributed to the increased surface area of the MOF in the nanocomposite, as well as the unique morphological properties of the MOFs within the composite. Addai et al. (2024) developed a mesoporous Ni-based MOF using 2-methylimidazole as the organic linker for the adsorptive removal of Coomassie brilliant blue from aqueous solutions [123]. This adsorbent achieved an adsorption capacity of 19.9 mg/g with physisorption determined as the primary adsorption mechanism.

These studies illustrate the properties of Ni-based MOFs that make them effective in water purification technologies. Their versatility enables them to absorb contaminants through multiple mechanisms, allowing for the removal of a wide range of pollutants.

2.5 Nanocellulose and MOF (CelluMOF) Composites

MOF materials make good adsorbents based on their remarkable properties which include high surface area, high porosity, and abundant adsorption active sites. However, their practical application as adsorbents in water purification technologies is limited by several shortcomings, such as aggregation, poor hydrolytic stability, poor handling, and processibility [82 – 83]. The combination of MOFs with other materials to mitigate these shortcomings can result in an ideal adsorbent for the removal of contaminants from water.

Nanocellulose has notable properties that can complement those of MOFs during adsorption, such as hydrolytic and mechanical stability. Furthermore, nanocellulose materials can assist MOFs by preventing aggregation in aqueous media, thereby maximizing MOF surface area. This will result in a composite adsorbent that will be stable and perform favorably in adsorption processes [124 – 125].

CelluMOF composites can be fabricated using *ex-situ* growth methods, meaning the MOF is synthesized prior to the formation of the composite. An example is the direct mixing procedure, which involves combining the pre-synthesized MOF with nanocellulose. This preparation method utilizes ultrasonication and stirring to reduce aggregation and precipitation of the MOF within the composite [124 – 125]. The other fabrication method is referred to as an *in-situ* growth procedure where synthesis is a one-pot method or a layer-by-layer process [124 – 125]. The advantage of the *ex-situ* preparation procedure is the loading of MOFs can be controlled, and the advantages of the *in-situ* procedure are that the loading of MOFs is uniform, and MOF aggregation is minimized.

CelluMOF composites have been shown to be effective for the adsorption of pollutants from water as shown in table 2.16.

Table 2.16: CelluMOFs as adsorbents in water purification

Adsorbent	**Pollutant**	**Efficiency**	**Reference**
CelloZIF-8	Co^{2+}	328 mg/g	[126]
CelloZIF-8	Methylene blue	100 %	[127]
MIL-100(Fe)@CP	Paracetamol	37.88 mg/g	[128]
Cu-BTC/CNF	Congo red	39 mg/g	[129]

CelloZIF-8, a combination of TEMPO-oxidized cellulose nanofibers (TOCNF) and ZIF-8 MOF, showed a good adsorption capacity of 328 mg/g for the removal of Co^{2+} ion in aqueous solution with good reusability, highlighting the synergy of cellulose and MOFs as adsorbents [126]. TOCNF and ZIF-8 CelloMOF further showed 100 % adsorptive removal of methyl blue from aqueous solution, stressing the benefits of using CelluMOFs for water remediation [127]. Fe(III)-based metal-organic framework-coated cellulose

paper (MIL-100(Fe)@CP) showed CelluMOFs as useful adsorbents with an adsorption capacity of 37.88 mg/g for the removal of paracetamol from water [128]. Cu-BTC/CNF had an adsorption capacity of 39 mg/g for the removal of Congo red from aqueous solutions [129]. The use of nanocellulose aerogel (CNF) provided a matrix to trap the Cu-BTC to increase adsorption.

The research highlights the synergetic effect of combining MOFs with nanocellulose materials for enhanced adsorption performance. MOFs have exceptional properties making them promising candidates for water purification; however, their practical application are hindered by limitations including poor hydrolytic stability, aggregation and poor handling and processing. Nanocellulose materials offer compelling solutions to these challenges including high mechanical strength, improved adsorption through the presence of functional groups and biocompatibility. These collectively can enhance the performance of MOFs. These studies also show CelluMOF composites as effective adsorbents for water purification, where MOF participates actively in the adsorption process and the nanocellulose boosts their practical application by improving general stability and eliminating aggregation of the particles.

This review highlighted the issue of water pollution and explored various remediation strategies, emphasizing the role of biosorbents in water purification. While acknowledging the potential of various biosorbents, the review established cellulose as a preferred candidate due to its favorable properties. Recognizing the exceptional adsorption capabilities of MOFs, the review focused on the synergistic potential of combining MOFs with cellulose derivatives, forming CelluMOFs. However, several knowledge gaps remain that hinder the widespread application of CelluMOFs in water purification. Understanding the long-term stability of MOFs in diverse aquatic environments, including variations in pH and temperature, and developing efficient and sustainable methods for regenerating used CelluMOFs are important. Furthermore, developing scalable and cost-effective methods for synthesizing high-quality CelluMOF composites is crucial for large-scale water treatment applications. An assessment of the overall economic feasibility of using CelluMOFs in water treatment is necessary, considering factors such as energy consumption, material costs, and regeneration costs. Finally, testing of CelluMOF-based

water treatment systems in real-world environments is needed to evaluate their performance, durability, and environmental impact. Addressing these knowledge gaps is necessary for unlocking the full potential of CelluMOFs as sustainable and effective solutions for water purification.

2.6 References

1. Lin L, Yang H, Xu X. Effects of Water Pollution on Human Health and Disease Heterogeneity: A Review. *Front Environ Sci*. 2022;10(June). doi:10.3389/fenvs.2022.880246

2. Hou L, Zhou Z, Wang R, Li J, Dong F, Liu J. Research on the Non-Point Source Pollution Characteristics of Important Drinking Water Sources. *Water (Switzerland)*. 2022;14(2): doi:10.3390/w14020211

3. Lei P, Shrestha RK, Zhu B, et al. A bibliometric analysis on nonpoint source pollution: Current status, development, and future. *Int J Environ Res Public Health*. 2021;18(15). doi:10.3390/ijerph18157723

4. Xu H, Gao Q, Yuan B. Analysis and identification of pollution sources of comprehensive river water quality: Evidence from two river basins in China. *Ecol Indic*. 2022;135:108561. doi:10.1016/j.ecolind.2022.108561

5. Bak MP, Kroeze C, Janssen ABG, Strokal M. Modelling future coastal water pollution: impacts of point sources, socio-economic developments & multiple pollutants. *Environ Res Lett*. 2024;19(6). doi:10.1088/1748-9326/ad489c

6. Tomczyk N, Naslund L, Cummins C, Bell E V., Bumpers P, Rosemond AD. Nonpoint source pollution measures in the Clean Water Act have no detectable impact on decadal trends in nutrient concentrations in U.S. inland waters. *Ambio*. 2023;52(9): doi:10.1007/s13280-023-01869-6

7. Wang M, Chen L, Wu L, Zhang L, Xie H, Shen Z. Review of Nonpoint Source Pollution Models: Current Status and Future Direction. *Water (Switzerland)*. 2022;14(20). doi:10.3390/w14203217

8. Igwaran A, Kayode AJ, Moloantoa KM, Khetsha ZP, Unuofin JO. Cyanobacteria Harmful Algae Blooms: Causes, Impacts, and Risk Management. *Water Air Soil Pollut*. 2024;235(1): doi:10.1007/s11270-023-06782-y

9. Dulsat-Masvidal M, Ciudad C, Infante O, Mateo R, Lacorte S. Water pollution threats in important bird and biodiversity areas from Spain. *J Hazard Mater*. 2023;448(January):130938. doi:10.1016/j.jhazmat.2023.130938

10. Li Y, Wang M, Chen X, et al. Multi-pollutant assessment of river pollution from livestock production worldwide. *Water Res*. 2022;209(August 2021):117906. doi:10.1016/j.watres.2021.117906

11. Chen M, Yue Y, Bao X, et al. Microplastics as Contaminants in Water Bodies and Their Threat to the Aquatic Animals: A Mini-Review. *Animals*. 2022;12(20): doi:10.3390/ani12202864

12. Babuji P, Thirumalaisamy S, Duraisamy K, Periyasamy G. Human Health Risks due to Exposure to Water Pollution: A Review. *Water (Switzerland)*. 2023;15(14): doi:10.3390/w15142532

13. El-taweel RM, Mohamed N, Alrefaey KA, et al. A review of coagulation explaining its definition, mechanism, coagulant types, and optimization models; RSM, and ANN. *Curr Res Green Sustain Chem*. 2023;6(January):100358. doi:10.1016/j.crgsc.2023.100358

14. Al-Nuaim MA, Alwasiti AA, Shnain ZY. The photocatalytic process in the treatment of polluted water. *Chem Pap*. 2023;77(2): doi:10.1007/s11696-022-02468-7

15. Maftouh A, El Fatni O, El Hajjaji S, Jawish MW, Sillanpää M. Comparative Review of Different Adsorption Techniques Used in Heavy Metals Removal in Water. *Biointerface Res Appl Chem*. 2023;13(4). doi:10.33263/BRIAC134.397

16. Omar NMA, Othman MHD, Tai ZS, et al. Overcoming challenges in water purification by nanocomposite ceramic membranes: A review of limitations and technical solutions. *J Water Process Eng*. 2024;57(September 2023):104613. doi:10.1016/j.jwpe.2023.104613

17. Iqbal A, Cevik E, Mustafa A, Qahtan TF, Zeeshan M, Bozkurt A. Emerging developments in polymeric nanocomposite membrane-based filtration for water

purification: A concise overview of toxic metal removal. *Chem Eng J*. 2024;481(January):148760. doi:10.1016/j.cej.2024.148760

18. Aziz S, Mazhar AR, Ubaid A, et al. A comprehensive review of membrane-based water filtration techniques. *Appl Water Sci*. 2024;14(8): doi:10.1007/s13201-024-02226-y

19. Bartzis V, Sarris IE. Advanced Technology for Desalination and Water Purification. *Water (Switzerland)*. 2024;16(8): doi:10.3390/w16081094

20. Kim HJ, Yoon HW, Lee MA, Kim YH, Lee CJ. Impact of UV-C Irradiation on Bacterial Disinfection in a Drinking Water Purification System. *J Microbiol Biotechnol*. 2023;33(1): doi:10.4014/jmb.2211.11027

21. Abouee Mehrizi E, Ebrahimi AA, Saadati H, et al. Investigating the effectiveness of anaerobic digestion in the treatment of sugarcane industry wastewater: A systematic review and meta-analysis. *Case Stud Chem Environ Eng*. 2023;8(May):100414. doi:10.1016/j.cscee.2023.100414

22. Roman MD, Sava C, Iluțiu-Varvara DA, et al. Biological Activated Sludge from Wastewater Treatment Plant before and during the COVID-19 Pandemic. *Int J Environ Res Public Health*. 2022;19(18). doi:10.3390/ijerph191811323

23. Pachaiappan R, Cornejo-Ponce L, Rajendran R, Manavalan K, Femilaa Rajan V, Awad F. A review on biofiltration techniques: recent advancements in the removal of volatile organic compounds and heavy metals in the treatment of polluted water. *Bioengineered*. 2022;13(4): doi:10.1080/21655979.2022.2050538.

24. Thorat, M.-N.; Jagtap, A. & Dastager, S.G. Fabrication of bacterial nanocellulose/polyethyleneimine (PEI-BC) based cationic adsorbent for efficient removal of anionic dyes. J Polym Res 28, 354 (2021). https://doi.org/10.1007/s10965-021-02702-y.

25. Kolya, H.; Kang, C.-W. Next-Generation Water Treatment: Exploring the Potential of Biopolymer-Based Nanocomposites in Adsorption and Membrane Filtration. *Polymers (Basel)* 2023, DOI:10.3390/polym15163421.

26. Praipipat, P.; Ngamsurach, P.; Libsittikul, N.; Kaewpetch, C.; Butdeesak, P.; Nachaiperm, W. Cationic oxides and dioxides of modified sugarcane bagasse beads with applications as low-cost sorbents for direct red 28 dye. *Sci. Rep*. 2024, DOI:10.1038/s41598-024-51934-7.

27. Salama, A. Novel cellulose derivative containing aminophenylacetic acid as sustainable adsorbent for removal of cationic and anionic dyes. *Int. J. Biol. Macromol*. 2023, DOI:10.1016/j.ijbiomac.2023.126687.

28. Ravindiran, G.; Sundaram, H.; Rajendran, E.-M.; Ramasamy, S.; Nabil, A.-Z.; Ahmed, B. Removal of azo dyes from synthetic wastewater using biochar derived from sewage sludge to prevent groundwater contamination. *Urban Clim*. **2023**, DOI:10.1016/j.uclim.2023.101502.

29. Yhon, J.; Mendoza, J.; Osorio, E.; Domínguez, M.-P. Continuous Removal of Dyes from Wastewater Using Banana-Peel Bioadsorbent: A Low-Cost Alternative for Wastewater Treatment. *Sustain*. **2023**, DOI:10.3390/su15139870.

30. Deng, Y., Zhu, T., Cheng, Y. et al. Recent Advances in Functional Cellulose-Based Materials: Classification, Properties, and Applications. Adv. Fiber Mater. (2024). https://doi.org/10.1007/s42765-024-00454-0.

31. Cheng W, Zhu Y, Jiang G, et al. Sustainable cellulose and its derivatives for promising biomedical applications. Prog Mater Sci. 2023;138(May):101152. doi:10.1016/j.pmatsci.2023.101152.

32. Muhammad Khusairy Bin Bakri, Md Rezaur Rahman, Faisal Islam Chowdhury, Chapter 1 - Sources of cellulose, Editor(s): Md Rezaur Rahman, Fundamentals and Recent Advances in Nanocomposites Based on Polymers and Nanocellulose, Elsevier, 2022, DOI: 10.1016/B978-0-323-85771-0.00012-9.

33. Magalhães, S.; Fernandes, C.; Pedrosa, J.-F.-S. Eco-Friendly Methods for Extraction and Modification of Cellulose: An Overview. *Polymers (Basel)*. 2023, DOI: 10.3390/polym15143138.

34. Wohlert, M.; Benselfelt. T.; Wågberg, L.; Furó. I.; Berglund, L.-A.; Wohlert, J. Cellulose and the role of hydrogen bonds: not in charge of everything. *Cellulose*. 2022, DOI:10.1007/s10570-021-04325-4.

35. Mafa, M.-S.; Pletschke, B.-I.; Malgas S. Defining the frontiers of synergism between cellulolytic enzymes for improved hydrolysis of lignocellulosic feedstocks. *Catalysts*. 2021**,** DOI:10.3390/catal11111343.

36. Lu, S.; Du, B.; Khan, S.-A.; Huang, S. Laser-Inscribable, Moisture-Responsive Cellulosic Supramolecular Structures with Tunable Broadband Coloration. *Adv. Funct. Mater*. 2024, DOI:10.1002/adfm.202406902.

37. Chen, Q.; Chen, Y.; Wu, C. Probing the evolutionary mechanism of the hydrogen bond network of cellulose nanofibrils using three DESs. *Int. J. Biol. Macromol*. 2023, DOI:10.1016/j.ijbiomac.2023.123694.

38. Thandavamoorthy, R.; Devarajan, Y.; Kaliappan, N. Antimicrobial, function, and crystalline analysis on the cellulose fibre extracted from the banana tree trunks. *Sci. Rep*. 2023, DOI:10.1038/s41598-023-42160-8.

39. Muhammad Khusairy Bin Bakri, Md Rezaur Rahman, Faisal Islam Chowdhury, Chapter 1 - Sources of cellulose, Editor(s): Md Rezaur Rahman, Fundamentals and Recent Advances in Nanocomposites Based on Polymers and Nanocellulose, Elsevier, 2022, DOI: 10.1016/B978-0-323-85771-0.00012-9.3

40. Acharya S, Liyanage S, Abidi N, Parajuli P, Rumi SS, Shamshina JL. Utilization of cellulose to its full potential: A review on cellulose dissolution, regeneration, and applications. Polymers (Basel). 2021;13(24). doi:10.3390/polym13244344.

41. Chen, T.; Li, J.; Xu, J. Effect of Acetylation of Two Cellulose Nanocrystal Polymorphs on Processibility and Physical Properties of Polylactide/Cellulose Nanocrystal Composite Film. *Molecules*. 2023, DOI:10.3390/molecules28124667.

42. Rathinavelu, R.; Paramathma, B.-S; Divkaran, D.; Siengchin, S. Physicochemical, thermal, and morphological properties of microcrystalline cellulose extracted from

Calotropis gigantea leaf. *Biomass Convers. Biorefinery*. 2023, DOI:10.1007/s13399-023-04370-y.

43. Verma J, Petru M, Goel S. Cellulose based materials to accelerate the transition towards sustainability. Ind Crops Prod. 2024;210(September 2023):118078. doi:10.1016/j.indcrop.2024.118078.

44. Begum HA, Tanni TR, Shahid MA. Analysis of Water Absorption of Different Natural Fibers. J Text Sci Technol. 2021;07(04):152-160. doi:10.4236/jtst.2021.74013

45. Atiku, Y.-M.; Abdulsalam, S.; Mohammed, J.; Ahmed, S.-I. Conversion of Cellulosic Biomass to Bioethanol through Fermentation Using Native Microorganisms: A Review. *J. Appl. Sci. Environ. Manag*. 2023, DOI:10.4314/jasem.v27i8.7.

46. Jiang, Z.; To, N. Recent Advances in Chemically Modified Cellulose and Its Derivatives for Food Packaging Applications: A Review. *Polymers (Basel)* 2022, DOI:10.3390/polym14081533

47. Hadid, M.; Noukrati, H.; Ben, H.; Barroug, A.; Sehaqui, H. Phosphorylated cellulose for water purification: a promising material with outstanding adsorption capacity towards methylene blue. *Cellulose* 2021, DOI: 10.1007/s10570-021-04012-4.

48. Mostafa, A.-G.; Gaith, E.-A.; Akl, M.-A. Aminothiol supported dialdehyde cellulose for efficient and selective removal of Hg(II) from aquatic solutions. *Sci. Rep*. 2023, DOI:10.1038/s41598-023-46082-3.

49. Ho, N.-A.-D.; Leo, C.-P. A review on the emerging applications of cellulose, cellulose derivatives and nanocellulose in carbon capture. *Environ. Res*. 2021, DOI:10.1016/j.envres.2021.111100.

50. Aziz, T.; Farid, A.; Haq, F. A Review on the Modification of Cellulose and Its Applications. *Polymers (Basel)* 2022, DOI:10.3390/polym14153206.

51. Silvestre, G.-H.; Pinto, L.-O.; Bernardes, J.-S.; Miwa, R.-H.; Fazzio, A. Disassembly of TEMPO-Oxidized Cellulose Fibers: Intersheet and Interchain Interactions in the Isolation of Nanofibers and Unitary Chains. *J. Phys. Chem. B*. 2021, DOI: 10.1021/acs.jpcb.1c01928.

52. Ho, N.-A.-D.; Leo, C.-P. A review on the emerging applications of cellulose, cellulose derivatives and nanocellulose in carbon capture. *Environ. Res*. 2021, DOI:10.1016/j.envres.2021.111100.

53. Kaur, P.; Sharma, N.; Munagala, M. Nanocellulose: Resources, Physio-Chemical Properties, Current Uses and Future Applications. *Front Nanotechnol*. 2021, DOI:10.3389/fnano.2021.747329.

54. Taokaew, S. Bacterial Nanocellulose Produced by Cost-Effective and Sustainable Methods and Its Applications: A Review. *Fermentation*. 2024, DOI:10.3390/fermentation10060316.

55. Ferreira-Neto, EP, Ullah S, Da Silva TCA, et al. Bacterial Nanocellulose/MoS2Hybrid Aerogels as Bifunctional Adsorbent/Photocatalyst Membranes for in-Flow Water Decontamination. *ACS Appl Mater Interfaces*. 2020;12(37): doi:10.1021/acsami.0c14137.

56. Radhakrishnan, A.; Jaabir, M.; Jeyachandran, S.; Thrini, K.; Vijaya A.; Murugesan, A. Nanocelluloses for Removal of Organic Dyes from Wastewater. In: Barhoum, A. (eds) Handbook of Nanocelluloses. *Springer*, 2022, DOI:10.1007/978-3-030-62976-2.

57. Thorat, M.N., Jagtap, A. & Dastager, S.G. Fabrication of bacterial nanocellulose/polyethyleneimine (PEI-BC) based cationic adsorbent for efficient removal of anionic dyes. J Polym Res 28, 354 (2021). https://doi.org/10.1007/s10965-021-02702-y.

58. Peiravi-Rivash O, Mashreghi M, Baigenzhenov O, Hosseini-Bandegharaei A. Producing bacterial nano-cellulose and keratin from wastes to synthesize keratin/cellulose nanobiocomposite for removal of dyes and heavy metal ions from waters and wastewaters. Colloids Surfaces A Physicochem Eng Asp. 2023;656(PA):130355. doi:10.1016/j.colsurfa.2022.130355.

59 Walling B, Bharali P, Ramachandran D, et al. In-situ biofabrication of bacterial nanocellulose (BNC)/graphene oxide (GO) nano-biocomposite and study of its

cationic dyes adsorption properties. Int J Biol Macromol. 2023;251(July):126309. doi:10.1016/j.ijbiomac.2023.126309.

60. Yan Z, Jiang S, Meng L, et al. Self-supporting and hierarchical porous membrane of bacterial nanocellulose@metal-organic framework for ultra-high adsorption of Congo red. Int J Biol Macromol. 2024;277(P2):134277. doi:10.1016/j.ijbiomac.2024.134277.

61. Kurniawan, T.-W.; Sulistyarti, H.; Rumhayati, B.; Sabarudin, A. Cellulose Nanocrystals (CNCs) and Cellulose Nanofibers (CNFs) as Adsorbents of Heavy Metal Ions. *J. Chem*. 2023, DOI:10.1155/2023/5037027.

62. Qi, Y.; Guo, Y.; Liza, A.-A. Nanocellulose: A Review on Preparation Routes and Applications in Functional Materials. *Springer* 2023, DOI:10.1007/s10570-023-05169-w.

63. Araya-Chavarría, K.; Rojas, R.; Ramírez-Amador, K.; Sulbarán-Rangel, B.; Rojas, O.; Esquivel-Alfaro, M. Cellulose Nanofibers as Functional Biomaterial from Pineapple Stubbles via TEMPO Oxidation and Mechanical Process. *Waste and Biomass Valorization* 2022,DOI: 10.1007/s12649-021-01619-3.

64. Xu, H.; Sanchez-Salvador, J.-L.; Balea, A.; Blanco, A.; Negro, C. Optimization of reagent consumption in TEMPO-mediated oxidation of Eucalyptus cellulose to obtain cellulose nanofibers. *Cellulose* 2022, DOI: Optimization of reagent consumption in TEMPO-mediated oxidation of Eucalyptus cellulose to obtain cellulose nanofibers.

65. Syeda, H.-I.; Muthukumaran, S.; Baskaran, K. Shape-memory cellulose nanofiber/polyglutamic acid-based aerogels as novel adsorbents for the removal of heavy metals from aqueous solutions. *J. Water Process Eng*. 2024, DOI:10.1016/j.jwpe.2024.104780.

66. Fiol, N.; Tarrés, Q.; Vásquez, M.-G. Comparative assessment of cellulose nanofibers and calcium alginate beads for continuous Cu(II) adsorption in packed

columns: the influence of water and surface hydrophobicity. *Cellulose* 2021, DOI: 10.1007/s10570-021-03809-7.

67. Guccini, V.; Yu, S.; Meng, Z.; Kontturi, E.; Demmel, F.; Salazar-Alvarez, G. The Impact of Surface Charges of Carboxylated Cellulose Nanofibrils on the Water Motions in Hydrated Films. *Biomacromolecules* 2022, DOI: 10.1021/acs.biomac.1c01517.

68. Abou-Zeid, R.-E.; Salama, A.; Al-Ahmed, Z.-A.; Awwad, N.-S.; Youssef, M.-A. Carboxylated cellulose nanofibers as a novel efficient adsorbent for water purification. *Cellul. Chem. Technol*. 2020, DOI: 10.35812/CelluloseChemTechnol.2020.54.25.

69. Oyarce, E.; Cantero-López, P.; Roa, K. Removal of highly concentrated methylene blue dye by cellulose nanofiber biocomposites. *Int. J. Biol. Macromol*. 2023, DOI:10.1016/j.ijbiomac.2023.124045.

70. Tran-Ly, A.-N.; De France, K.-J.; Rupper, P. Melanized-Cationic Cellulose Nanofiber Foams for Bioinspired Removal of Cationic Dyes. *Biomacromolecules* 2021, DOI: 10.1021/acs.biomac.1c00942.

71. Yu, Z.; Hu, C.; Dichiara, A.-B.; Jiang, W. Gu, J. Cellulose nanofibril/carbon nanomaterial hybrid aerogels for adsorption removal of cationic and anionic organic dyes. *Nanomaterials* 2020, DOI:10.3390/nano10010169.

72. Ogunleye DT, Akpotu SO, Moodley B. Crystalline Nanocellulose Anchored on Reduced Graphene Oxide for the Removal of Pharmaceuticals from Aqueous Systems: Adsorbent Characterization and Adsorption Performance. ChemistrySelect. 2023;8(4): doi:10.1002/slct.202202533.

73. Shaheed N, Javanshir S, Esmkhani M, Dekamin MG, Naimi-Jamal MR. Synthesis of nanocellulose aerogels and Cu-BTC/nanocellulose aerogel composites for adsorption of organic dyes and heavy metal ions. Sci Rep. 2021;11(1). doi:10.1038/s41598-021-97861-9.

74. Liu S. Preparation of nanocellulose grafted molecularly imprinted polymer for selective adsorption Pb(II) and Hg(II). Chemosphere. 2023;316(October 2022):137832. doi:10.1016/j.chemosphere.2023.137832.

75. Soliman AIA, Díaz Baca JA, Fatehi P. One-pot synthesis of magnetic cellulose nanocrystal and its post-functionalization for doxycycline adsorption. Carbohydr Polym. 2023;308(October 2022):120619. doi:10.1016/j.carbpol.2023.120619.

76. Tie L, Ke Y, Gong Y, Zhang W xian, Deng Z. Nanocellulose fine-tuned poly(acrylic acid) hydrogel for enhanced diclofenac removal. Int J Biol Macromol. 2022;213(June). doi:10.1016/j.ijbiomac.2022.06.051.

77. Adegoke, K.-A.; Oyedotun, K.-O.; Ighalo, J.-O.; Cellulose derivatives and cellulose-metal-organic frameworks for CO_2 adsorption and separation. *J. CO_2 Util*. 2022, DOI:10.1016/j.jcou.2022.102163.

78. Islam, M.-D.; Uddin, F.-J.; Rashid, T.-U.; Shahruzzaman, M. Cellulose acetate-based membrane for wastewater treatment—A state-of-the-art review. *Mater. Adv*. 2023, 4.

79. Xiong, J.; Hu, Q.; Wu, J. Structurally stable electrospun nanofibrous cellulose acetate/chitosan biocomposite membranes for the removal of chromium ions from the polluted water. *Adv. Compos. Hybrid Mater.* 2023, DOI:10.1007/s42114-023-00680-x.

80. Tahazadeh S, Karimi H, Mohammadi T, Emrooz HBM, Tofighy MA. Fabrication of biodegradable cellulose acetate/MOF-derived porous carbon nanocomposite adsorbent for methylene blue removal from aqueous solutions. J Solid State Chem. 2021;299(February). doi:10.1016/j.jssc.2021.122180.

81. Tahazadeh S, Mohammadi T, Tofighy MA, Khanlari S, Karimi H, Motejadded Emrooz HB. Development of cellulose acetate/metal-organic framework derived porous carbon adsorptive membrane for dye removal applications. *J Memb Sci*. 2021;638(May):119692. doi:10.1016/j.memsci.2021.119692

82. Heidari Y, Noroozian E, Maghsoudi S. Electrospun nanofibers of cellulose acetate/metal organic framework-third generation PAMAM dendrimer for the removal of methylene blue from aqueous media. *Sci Rep*. 2023;13(1). doi:10.1038/s41598-023-32097-3.

82. Darabdhara, J.; Ahmaruzzaman, M. Recent developments in MOF and MOF based composite as potential adsorbents for removal of aqueous environmental contaminants. *Chemosphere* 2022, DOI:10.1016/j.chemosphere.2022.135261

83. Naser, S.-A.-E.; Badmus, K.-O.; Khotseng, L. Synthesis, Properties, and Applications of Metal Organic Frameworks Supported on Graphene Oxide. *Coatings* 2023 DOI:10.3390/coatings13081456.

84. He, Y.; Wang, Y.; Shi, J. Incorporating metal–organic frameworks into substrates for environmental applications. *Chem. Eng. J*. 2022, DOI:10.1016/j.cej.2022.136866.

85. Shen, W. Guo, X. Pang, H. Effect of Solvothermal Temperature on Morphology and Supercapacitor Performance of Ni-MOF. *Molecules*. 2022, DOI:10.3390/molecules27238226.

86. Kamal, K.; Bustam, M.-A.; Ismail, M.; Grekov, D. Optimization of Washing Processes in Solvothermal Synthesis of Nickel-Based MOF-74. *Mater. J*. 2020, DOI:10.3390/ma13122741.

87. Azbell, T.-J.; Pitt, T.-A.; Bollmeyer, M.-M.; Cong, C.; Lancaster, K.-M.; Milner, P.-J. Ionothermal Synthesis of Metal-Organic Frameworks Using Low-Melting Metal Salt Precursors. *Angew. Chem. Int. Ed. Engl*. 2023, DOI:10.1002/anie.202218252.

88. Gatou MA, Vagena IA, Lagopati N, Pippa N, Gazouli M, Pavlatou EA. Functional MOF-Based Materials for Environmental and Biomedical Applications: A Critical Review. Nanomaterials. 2023;13(15). doi:10.3390/nano13152224.

89. Phan, P.-T.; Hong, J.; Tran, N.; Le, T.-H. The Properties of Microwave-Assisted Synthesis of Metal–Organic Frameworks and Their Applications. *Nanomaterials* 2023, DOI:10.3390/nano13020352.

90. Vakili R, Xu S, Al-Janabi N, Gorgojo P, Holmes SM, Fan X. Microwave-assisted synthesis of zirconium-based metal organic frameworks (MOFs): Optimization and gas adsorption. Microporous Mesoporous Mater. 2018;260(August 2017). doi:10.1016/j.micromeso.2017.10.028.

91. Zaamouchi, I.; Kaci, M.-M.; Zidane, Y.; Belaid, S.; Bouacida, S.; Benmerad, B. The impressive photocatalytic performance of Zn-MOF as a novel photocatalyst for the effective purification of dyes under solar exposure. J. Mol. Struct. 2024, DOI:10.1016/j.molstruc.2023.137070.

92. Sun, Y.; Jiang, X.; Liu, Y. Recent advances in Cu(II)/Cu(I)-MOFs based nano-platforms for developing new nano-medicines. *J. Inorg. Biochem*. 2021, DOI:10.1016/j.jinorgbio.2021.111599.

93. Zhang, Y.; Gao, Z.; Liu, W. Synthesis of copper-based metal-organic framework for sensing nitroaromatic compounds. *Inorg. Chem. Commun*. 2021, DOI:10.1016/j.inoche.2021.109017.

94. Al-Harbi, S.-A.; Almulaiky, Y.-Q. Copper-based metal-organic frameworks (BDC-Cu MOFs) as supporters for α-amylase: Stability, reusability, and antioxidant potential. *Heliyon* 2024, DOI:10.1016/j.heliyon.2024.e28396.

95. Abdulkadhim, A.-H.; Husein K.-S.-M.; Al-Saedi H.-F. Microwave-assisted synthesis and development of novel penicillinoate@copper metal-organic frameworks as a potent antibacterial agent. *Front Chem*. 2023, DOI:10.3389/fchem.2023.1331933.

96. Zhong, J.; Zhou, J.; Xiao, M. Design and syntheses of functionalized copper-based MOFs and its adsorption behavior for Pb(II). *Chinese Chem. Lett*. 2022, 33.

97. Shah, A.-H.; Abideen, Z.-U.; Maqsood, S. Porous Cu-based metal organic framework (Cu-MOF) for highly selective adsorption of organic pollutants. *J. Solid State Chem*. 2023, DOI:10.1016/j.jssc.2023.123935.

98. Haso, H.-W.; Dubale, A.-A.; Chimdesa, M.-A.; Atlabachew, M. High Performance Copper Based Metal Organic Framework for Removal of Heavy Metals From Wastewater. *Front. Mater*. 2022, DOI:10.3389/fmats.2022.840806.

99. Lee, J.-Y.; Choi, J.-H. Copper-based metal-organic framework for highly efficient adsorption of lead ions from aqueous solution. *Mater. Res. Express* 2022, DOI:10.1088/2053-1591/ac93ea.

100. Chernomorova, M.-A.; Khrabrova, N.-S.; Zhinzhilo, V.-A.; Uflyand, I.-E. The Use of Copper Terephthalate for the Determination and Separation of Organic Dyes via Solid-Phase Extraction with Spectrophotometric Detection. *Appl. Sci*. 2023, DOI:10.3390/app13053063.

101. Hemdan, M.; Ragab, A.-H.; Gumaah, N.-F.; Mubarak, M.-F. Sodium alginate-encapsulated nano-iron oxide coupled with copper-based MOFs (Cu-BTC@Alg/Fe_3O_4): Versatile composites for eco-friendly and effective elimination of Rhodamine B dye in wastewater purification. *Int. J. Biol. Macromol*. 2024, DOI:10.1016/j.ijbiomac.2024.133498.

102. Raza, H.; Yildiz, I.; Yasmeen, F. Synthesis of a 2D copper(II)-carboxylate framework having ultrafast adsorption of organic dyes. *J. Colloid Interface Sci*. 2021, 602.

103. Li, M.; Zhang, Z.; Yu, Y. Recent advances in Zn-MOFs and their derivatives for cancer therapeutic applications. *Mater. Adv*. 2023, 4.

104. Roy, D.; Kumar, P.; Soni, A.; Nemiwal, M. A versatile and microporous Zn-based MOFs as a recyclable and sustainable heterogeneous catalyst for various organic transformations: A review (2015-present). *Tetrahedron*. 2023, DOI:10.1016/j.tet.2023.133408.

105. Ye, X.; Xiong, M.; Yuan, K. Synthesis and Characterization of a Novel Zinc-Based Metal-Organic Framework Containing Benzoic Acid: A Low-Toxicity Carrier for Drug Delivery. *Iran J. Pharm. Res*. 2023, DOI:10.5812/ijpr-136238.

106. Ren, Q.; Wei, F.; Chen, H.; Chen, D.; Ding, B. Preparation of Zn-MOFs by microwave-assisted ball milling for removal of tetracycline hydrochloride and Congo red from wastewater. *Green Process Synth*. 2021, 10.

107. Karbalaee, H.-A.; Tadjarodi, A. Novel Zn metal–organic framework with the thiazole sites for fast and efficient removal of heavy metal ions from water. *Sci Rep*. 2023, DOI:10.1038/s41598-023-38523-w.

108. Kumar, A.; Arya, K.; Mehra, S.; Kumar, A.; Mehta, S.-K.; Kataria, R. Detection and sorption of heavy metal ions in aqueous media using Zn-based luminescent metal-organic framework. *Sep. Purif. Technol*. 2024, DOI:10.1016/j.seppur.2023.125875.

109. Zeng, B.; Wang, W.; He, S. Facile synthesis of zinc-based organic framework for aqueous Hg (II) removal: Adsorption performance and mechanism. *Nano Mater. Sci*. 2021, 3.

110. Elsherbiny, A.-S.; Rady, A.; Abdelhameed, R.-M.; Gemeay, A.-H. Efficiency and selectivity of cost-effective Zn-MOF for dye removal, kinetic and thermodynamic approach. *Environ. Sci. Pollut. Res*. 2023, 3.

111. Li, J.; Sun, C.; Wen, C. A stable multifunctional Zn(II) based metal-organic framework for sensitive detection of Hg(II), Cr(VI), nitrobenzene and adsorption of methylene blue. *J. Environ. Chem. Eng*. 2022, DOI:10.1016/j.jece.2022.107880.

112. Xu, B.; Zhang, Y.; Pi, Y.; Shao, Q.; Huang, X. Research Progress of Nickel-Based Metal-Organic Frameworks and Their Derivatives for Oxygen Evolution Catalysis. *Chinese J. Inorg. Chem*. 2021**,** DOI:10.3866/PKU.WHXB202009074.

113. Liu, X.; Yang, H.; Diao, Y. Recent advances in the electrochemical applications of Ni-based metal organic frameworks (Ni-MOFs) and their derivatives. *Chemosphere* 2022, DOI:10.1016/j.chemosphere.2022.135729.

114. Amri, F.; Kasim, W.; Rochliadi, A.; Patah, A. Facile one-pot microwave-assisted synthesis of rod-like and hexagonal plate-like AgNP@Ni-BTC composites for a

potential salivary glucose sensor. *Sensors and Actuators Reports*. 2023, DOI:10.1016/j.snr.2023.100141.

115. Zheng, S.-Q.; Lim, S.-S.; Foo, C.-Y. Solvothermal synthesis of nanostructured nickel-based metal–organic frameworks (Ni-MOFs) with enhanced electrochemical performance for symmetric supercapacitors. *J. Mater. Sci*. 2023, 58.

116. Wu, L.-Z.; Zhou, X.-Y.; Zeng, P.-C.; Huang, J.-Y.; Zhang, M.-D.; Qin, L. Hydrothermal synthesis of Ni(II) or Co(II)-based MOF for electrocatalytic hydrogen evolution. *Polyhedron* 2022, DOI:10.1016/j.poly.2022.116035.

117. Mguni, L.-L.; Yao, Y.; Ren, J.; Liu, X.; Hildebrandt, D. Modulated synthesized Ni-based MOF with improved adsorptive desulfurization activity. *J. Clean Prod*. 2021, DOI:10.1016/j.jclepro.2021.129196.

118. Helal A, Fettouhi M, Arafat ME, Khan MY, Sanhoob MA. Nickel based metal-organic framework as catalyst for chemical fixation of CO2in oxazolidinone synthesis. J CO2 Util. 2021;50(February):101603. doi:10.1016/j.jcou.2021.101603.

119. S. Sharma, A.V. Desai, B. Joarder, S.K. GhoshA Water-Stable Ionic MOF for the Selective Capture of Toxic Oxoanions of Se-VI and As-V and Crystallographic Insight into the Ion-Exchange Mechanism Angewandte Chemie-International Edition., 59 (20) (2020),10.1002/anie.202000670

120. Lou, J.; Fu, Q.; Yu, L. Highly effective removal of Pb^{2+} from wastewater by -based metal organic framework. *J. Solid State Chem*. 2022, DOI:10.1016/j.jssc.2022.123535.

121. Yu, J.; Jiang, X.; Zhou, Z. A novel mercapto-functionalized bimetallic Zn/Ni-MOF adsorbents for efficient removal of Hg(II) in wastewater. *J. Environ. Chem. Eng*. 2024, DOI:10.1016/j.jece.2024.113258.

122. Ahsan, M.-A.; Jabbari, V.; Imam, M.-A. Nanoscale nickel metal organic framework decorated over graphene oxide and carbon nanotubes for water remediation. *Sci. Total Environ*. 2020, DOI:10.1016/j.scitotenv.2019.134214.

123. Addai FP, Liu Y, Wu J, et al. High-performance petal-like nickel organic framework for efficient dye sequestration. J Water Process Eng. 2024;57(November 2023):104622. doi:10.1016/j.jwpe.2023.104622.

124. Abdelhamid, H.-N.; Mathew, A.-P. Cellulose–metal organic frameworks (CelloMOFs) hybrid materials and their multifaceted Applications: A review. *Coord. Chem. Rev*. 2022, DOI:10.1016/j.ccr.2021.214263.

125. Esmailzadeh, F.; Taheri-Ledari, R.; Kashtiaray, A.; Soltani, S.-S.; Mashayekhan, S.; Maleki, A. Sustainable celloMOF cargoes for regenerative medicine and drug delivery therapies: A review. *Ind. Crops Prod*. 2024, DOI:10.1016/j.indcrop.2024.118293.

126. Nasser Abdelhamid H, Sultan S, Mathew AP. Binder-free Three-dimensional (3D) printing of Cellulose-ZIF8 (CelloZIF-8) for water treatment and carbon dioxide (CO2) adsorption. Chem Eng J. 2023;468(April 2023):143567. doi:10.1016/j.cej.2023.143567

127. Nasser H, Sultan S, Mathew AP. for water treatment and carbon dioxide (CO 2) adsorption Zn ZIF-8 Hmim @ TOCNF 3D Printing ZnO @ TOCNF 3D Printing 3D Hmim @ TOCNF 3D ZnO @ TOCNF Zn. 2025;468(April 2023).

128. Yılmaz Ş, Zengin A, Şahan T. Effective utilization of Fe(III)-based metal organic framework-coated cellulose paper for highly efficient elimination from the liquid phase of paracetamol as a pharmaceutical pollutant. Environ Technol Innov. 2021;24:101799. doi:10.1016/j.eti.2021.101799

129. Shaheed N, Javanshir S, Esmkhani M, Dekamin MG, Naimi-Jamal MR. Synthesis of nanocellulose aerogels and Cu-BTC/nanocellulose aerogel composites for adsorption of organic dyes and heavy metal ions. Sci Rep. 2021;11(1). doi:10.1038/s41598-021-97861-9

CHAPTER 3

ACS OMEGA

http://pubs.acs.org/journal/acsodf
Article

Cellulose Acetate Supported MOF-5/Crystalline Nanocellulose Composite Film as an Adsorbent Material for Methylene Blue Removal from Aqueous Solutions

Lebogang Manamela and Nolwazi Nombona*

Cite This: *ACS Omega* 2024, 9, 37621−37635
Read Online

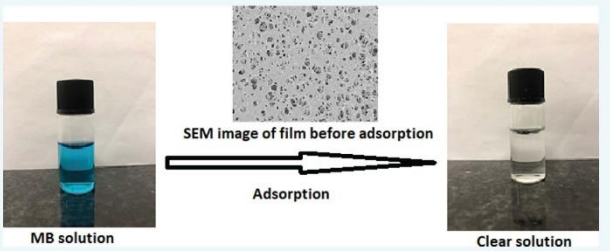

ABSTRACT: In this study, a novel, low-cost, and efficient adsorbent film was fabricated by a solvothermal method. The adsorbent film was developed to be hydrolytically stable, not vulnerable to aggregation in aqueous environments, and not prone to secondary contamination. The adsorbent consists of cellulose acetate (CA) as a support embedded with a MOF-5/crystalline nanocellulose (CNC) composite material. The CA-supported MOF-5/CNC film was characterized using a variety of techniques, including X-ray diffraction, thermal gravimetric analysis, scanning electron microscopy, X-ray photoelectron spectroscopy, and Fourier transform infrared spectroscopy, which revealed hydroxyl and carbonyl functional groups on the adsorbent film. The film was evaluated for the adsorptive removal of methylene blue (MB) from an aqueous solution. Adsorption was characterized by a rapid increase in MB adsorption during the first hour with equilibrium achieved within 4−5 h into the adsorption process. The maximum adsorption capacity was determined to be 4.29 mg/g and the maximum dye removal efficiency was 77%. The MB adsorption process best fitted the Freundlich isotherm and pseudo-second-order kinetic models. Thermodynamic studies showed that the adsorption was exothermic and feasible. The adsorbent film showed admirable regeneration ability, demonstrating its cost-effectiveness and its potential as a promising material for wastewater treatment.

INTRODUCTION

The textile industry has been listed as one of the emerging contributors of CO_2 emissions and, unfortunately, the textile sector is also among the largest contributors of wastewater with an annual worldwide dyestuff production of over 7×10^5 tons.[1,2] One of the ways in which dye effluents enter waterbodies such as rivers and lakes is due to the inability of dye mixtures to completely attach to intended textiles.[3] Synthetic dyes are toxic by nature,[4] stable,[5] and pose a risk to the environment and human health.[6,7]

The removal of organic dyes from aquatic systems is crucial in eliminating harmful effects from reduced sunlight penetration caused by dye pollution, which often leads to a decrease in photosynthesis. Methylene blue (MB) is frequently used in the textile industry to print cotton and dye leather. Several dye removal techniques have been reported and these include membrane separation,[8] coagulation/flocculation,[9] and ozonation.[10] The most preferred method among these has been physical adsorption using solid materials, as it is highly efficient in the removal and treatment of contaminants in wastewater.[11−13] This low-cost technology is a separation process that concentrates molecules (contaminants) on the surface of a solid adsorbent.[14] Various materials have been employed as adsorbents with activated carbon being the most common commercial adsorbent.[15−17] Despite being the most established adsorbent, activated carbon is expensive and has high

Received: February 6, 2024
Revised: July 1, 2024
Accepted: August 9, 2024
Published: August 27, 2024

https://doi.org/10.1021/acsomega.4c01150
ACS Omega 2024, 9, 37621−37635

reactivation costs, and this suggests the need for cheaper, efficient, and reusable adsorbents.[18−21]

Metal−organic frameworks (MOFs) are reported to play an important role in the adsorption of organic pollutants due to their high surface area, high porosity, and biocompatibility.[22−24] Zr-based MOFs have been reported to have high adsorption capacities for the removal of organic dyes.[12,25−27] These MOFs are stable in aqueous media and can withstand harsh chemical environments, moisture and temperature changes.[28] However, their high cost of synthesis makes them uneconomical as adsorbents for organic dye removal; as a result, there is a need for cheaper MOF alternatives. One of the major challenges that cheaper MOFs encounter when applied in water remediation technologies is poor hydrolytic stability.[29] To increase water stability, high oxidation metals have been incorporated in the MOF structure with linker groups such as pyrazole to increase the metal-linker bonding strength.[30] Coating of the MOFs' internal or external surface with hydrophobic materials has also been shown to increase hydrolytic stability.[31] It was previously demonstrated that the external surface hydrophobization of MOFs has the potential to lower surface area and enhance water stability.[32] Ding et al. developed a polymerization approach to coat the surface of HKUST-1, ZIF-67, and MIL-125 with 2,2,2-trifluoroethyl methacrylate and 3-methacryloxypropyltrimethoxysilane to synthesize water-stable MOF composites without significant change of their pore features.[33] The incorporation of styrene to MOFs has been shown to improve the hydrolytic stability of MOFs, and their performance[34] hence, it is important to fabricate a MOF-based material with hydrolytic stability without compromising functionality. While these modifications improve hydrolytic stability, they do not address potential aggregation, which might minimize surface area for adsorption and cause secondary contamination. To manage these challenges, MOFs have been embedded in membrane support materials,[22,35−37] and they have been incorporated in the matrix of polymeric materials.[38] This approach was found to address secondary contamination; however, MOF particles could still aggregate on the membrane support.[22,37] Aggregation on polymer membrane supports occurs due to the attraction of MOF particles to one another coupled with poor MOF adhesion to most polymers. Duan et al. reported MOF aggregation on polymeric membrane surfaces when using an adsorption-filtration technique for MOF immobilization, resulting in secondary contamination.[22]

This study explores the use of MOF-5 as an adsorbent material for the removal of MB from aqueous solutions. MB was selected as a model contaminant, as it is frequently used in the textile industry and is an abundant pollutant in the aquatic system. Its cationic nature enables it to interact and penetrate the negatively charged cellular membranes of marine animals and human beings and this can lead to bioaccumulation of MB, which can cause illnesses such as cancer.[39] In this work, MOF-5 was used as an active material for the adsorptive removal of MB from water due to its relatively high surface area, which provides active sites for adsorption, it is cheaper compared to most MOFs, can be used multiple times for adsorption, and can be tailored to have high affinity for cationic dyes. The drawbacks of using MOFs for water remediation are that they have low water stability, they aggregate in aqueous solution, are sensitive to acidic/alkaline environments, and are hard to recycle. The functionalization of MOFs with various materials has been shown to overcome some of these challenges. To maximize the strength of the adsorbent, crystalline nanocellulose (CNC) was combined with MOF-5 to form a powdered-crystalline composite (MOF-5/CNC) for improved hydrolytic stability. The MOF-5/CNC was embedded in a cellulose acetate (CA) matrix to form an adsorbent film (CA-supported MOF-5/CNC) to avoid secondary contamination when it was applied for the adsorptive removal of MB from water. The multi-component film also acts to eliminate aggregation suffered by MOFs and renders the film recyclable. The impact of initial concentration, pH, contact time, and temperature on the adsorption process was examined. The adsorption isotherms and adsorption kinetics were evaluated by using models.

EXPERIMENTAL SECTION

Materials. Acetone (99.9%), *N*,*N*-dimethylformamide (DMF, 99.9%), chloroform (CH_3Cl, 99%), and sulfuric acid (H_2SO_4, 98%) were purchased from Radchem. Zinc nitrate hexahydrate ($Zn(NO_3)_2{\cdot}6H_2O$, 98%), microcrystalline cellulose (MCC, 11 wt %), CA (39.3−40.3%), MB (98%), and terephthalic acid (BDC, 99%) were purchased from Sigma-Aldrich.

Synthesis of a CA-Supported MOF-5/CNC Adsorbent Film. Pristine MOF-5 was prepared following a reported method.[40] Briefly, 6.5 g of zinc nitrate hexahydrate and 1.2 g of BDC were dissolved in 180 mL of DMF, and the mixture was stirred for 30 min. Thereafter, the mixture was heated in an oven at 105 °C for 24 h. After being cooled to room temperature, the white powder was washed with DMF and repeatedly washed with chloroform. The product, MOF-5, was vacuum-dried at 60 °C for 12 h.

CNC was synthesized using a reported procedure.[41] MCC (1 g) was added to 30% H_2SO_4 under vigorous stirring for 1 h. Distilled iced water was used to quench the mixture, and the solution was sonicated for 10 min followed by centrifugation for 30 min. The aqueous supernatant was discarded, and fresh distilled water was added to the pellet, followed by ultrasonication before further centrifugation. This washing process was repeated until the pH of the supernatant was neutral. The resulting pellet was freeze-dried to yield powder CNC.

14.7 wt % MOF-5/CNC was synthesized by adding 1.2 g of BDC to 90 mL of DMF. The mixture was stirred for 10 min, and CNC (50 mg) was added to the reaction mixture. In a separate reaction vessel, 5 g of $Zn(NO_3)_2{\cdot}6H_2O$ was added to 90 mL of DMF. The mixtures were stirred separately for 15 min, followed by ultrasonication for 15 min. The mixtures were combined, and the resulting mixture was stirred for 15 min, followed by ultrasonication for 15 min and heating at 50 °C under vigorous stirring for 2 h. The solution was cooled to room temperature and centrifuged to isolate the solid material. The product was washed with DMF and vacuum-dried at 60 °C for 6 h to yield MOF-5/CNC.

The synthesized MOF-5/CNC composite was supported on CA by dissolving 7.5 g of CA in 76 mL of DMF followed by stirring for 18 h at room temperature.[42] The solution was degassed with nitrogen at room temperature overnight. In a separate reaction vessel, MOF-5/CNC in DMF was stirred and sonicated for 10 min. Thereafter, 3.3 mL of CA solution was added to the reaction vessel, and the resulting mixture was stirred vigorously for 1 h, followed by sonication for 30 min to obtain a viscous gel. The gel was drop-cast on a glass slide until a thickness of 0.2 mm was obtained. The coated glass slide was placed in a water bath at 6 °C for 4 h. The coated glass slide

https://doi.org/10.1021/acsomega.4c01150
ACS Omega 2024, 9, 37621−37635

was removed from the water bath, and another glass slide was placed on top of the newly formed mat; subsequently, a force of 50 N was exerted on the film for 30 min. The film was air-dried overnight.

Adsorption Experiments. Solutions of MB (1−6 mg/L) were prepared from a 400 mg/L stock solution. The adsorbent mats (7 mm × 15 mm) were immersed in 3 mL of MB solutions and agitated in a bath shaker for 6 h. The adsorption behavior of the material at different parameters, such as contact time, solution pH, temperature, and initial MB concentration, was investigated. The percentage of MB removal was calculated using eq 1 and adsorption capacity, q_e, was calculated using eq 2:

$$\%\text{MB removal} = \frac{C_i - C_e}{C_i} \times 100\% \tag{1}$$

$$q_e = \frac{C_i - C_e}{m} \times V \tag{2}$$

where C_i is the initial concentration of MB solution (mg/L), C_e is the equilibrium concentration of MB solution (mg/L), q_e is the equilibrium adsorption capacity (mg/g), V is the volume of the solution (mL), and m is the mass of the adsorbent (g).

To assess the reusability of the film, recyclability tests were performed. The adsorbent film was removed from the MB solution after an adsorption cycle and immersed in methanol to desorb the dye. The desorption solvent (methanol) was shaken for 4 h, and the film was removed to air-dry for 1 h, ready for the next adsorption cycle.

Adsorption Isotherms. Adsorption isotherms were used to establish the effectiveness of the adsorption process and assess the affinity of the adsorbent for the adsorbates, thus describing the interactions between the adsorbent and the adsorbates. In this study, the adsorbents were analyzed using Langmuir and Freundlich isotherms. The Langmuir isotherm operates under the assumption that the adsorption process is monolayer adsorption and occurs on a homogeneous surface while the Freundlich isotherm assumes the adsorption process is multilayer and occurs on a heterogeneous surface. Equations 3 and 4 show the linearized Langmuir and Freundlich adsorption isotherm models, respectively:

$$\frac{1}{q_e} = \frac{1}{K_L q_{max}} \times \frac{1}{C_e} + \frac{1}{q_{max}} \tag{3}$$

$$\log(q_e) = \log(K_F) + \left(\frac{1}{n}\right)\log(C_e) \tag{4}$$

From the equations, q_{max} is the maximum adsorption capacity of the adsorbent (mg/g), and K_L is the Langmuir constant, which is related to adsorption affinity. The larger the values of K_L, the stronger the interactions between the adsorbent and adsorbate. K_F is the Freundlich isotherm constant. The gradient of the linear form of the equation, $1/n$, is a function of the strength of the adsorption process. The normal adsorption process occurs when $\frac{1}{n} > 1$. When $\frac{1}{n} > 1$, cooperative adsorption is taking place. R_L is a separation factor and is calculated using eq 5 below:

$$R_L = \frac{1}{1 + K_L C_i} \tag{5}$$

where K_L is the Langmuir constant and C_i is the initial adsorbate concentration. The adsorption nature is not favored when $R_L > 1$, linear when $R_L = 1$, favorable when $0 < R_L < 1$, and irreversible when $R_L = 0$.

Adsorption Kinetics. Adsorption kinetics provide a platform to understand the adsorption mechanisms, such as mass transfer and chemical reactions during adsorption. In this study, the kinetic data obtained was analyzed by pseudo-first-order and pseudo-second-order models, using eqs 6 and 7, respectively:

$$\ln(q_e - q_t) = \ln(q_e) - k_1 t \tag{6}$$

$$\frac{1}{q_t} = \frac{1}{K_2 q_e^2} + \frac{1}{q_e} t \tag{7}$$

where q_e is the adsorption capacity at equilibrium, q_t (mg/g) is the adsorption capacity at time t, t (minutes) is the contact time, k_1 is the first-order equilibrium constant, and k_2 is the second-order equilibrium constant. The diffusion mechanisms of the adsorption process were studied using the intraparticle diffusion rate equation, eq 8:

$$q_t = k_{id} t^{1/2} + I \tag{8}$$

where k_{id} is the intraparticle diffusion rate constant (mg/g·min$^{-1/2}$) and I is the thickness of the boundary layer. The Bangham diffusion model was studied to understand the adsorption mechanism using eq 9:

$$\text{loglog}\left(\frac{C_i}{C_i - q_t}\right) = \log\left(\frac{k_b m}{2.303 V}\right) + \alpha \log(t) \tag{9}$$

where k_b and α are constants. The pore diffusion model, the Boyd model, was employed to identify the rate-limiting step using eq 10:

$$B_t = -0.4977 - \ln(1 - F) \tag{10}$$

where F represents the fraction of MB adsorbed at any time t (min) and is calculated by eq 11:

$$F = \frac{q_t}{q_e} \tag{11}$$

Statistical Test. The nonlinear chi-square (χ^2) statistic test was performed in addition to the correlation coefficient (R) to discriminate the best model fit to the experimental data. A small χ^2 value demonstrates similarity between the modeled and experimental data, while a larger χ^2 demonstrates disparity. χ^2 was calculated using eq 12:

$$\chi^2 = \Sigma \frac{(q_e - q_{ecal})^2}{q_{ecal}} \tag{12}$$

where q_e is the experimental equilibrium adsorption capacity and $q_{e,cal}$ is the model equilibrium adsorption capacity.

Characterization Techniques. X-ray diffraction (XRD) analysis was conducted by using a Bruker D2 PHASER-e diffractometer using Cu-Kα radiation (0.15418 nm). Scanning electron microscopy (SEM) and energy-dispersive X-ray spectroscopy (EDX) were carried out on a cross-beam 540 FEG SEM microscope from Zeiss. UV−vis absorption measurements were conducted on a CARY 100 BIO UV−vis spectrophotometer. Fourier transform infrared spectroscopy (FTIR) spectroscopy was done on a Brunker Alpha Fourier transform spectrometer with platinum attenuated total reflectance sampling accessory. Thermal gravimetric analysis

https://doi.org/10.1021/acsomega.4c01150
ACS Omega 2024, 9, 37621−37635

(TGA) was done using an SDT Q600 V20.9 Build 20 Module DSC-TGA Standard. N_2 absorption/desorption isotherms were acquired using autosorb iQ model:7, ASiQWin version 5.2× at −196 °C, operating within a relative pressure (P/P_o) range of 0−1.0. Prior to measurement, the samples were predegassed at 130 °C for 18 h under vacuum. The Brunauer−Emmett−Teller (BET) and Barrett−Joyner−Halenda models were utilized to determine surface area and pore volume. X-ray photoelectron spectroscopy (XPS) was conducted on a Thermo model: ESCAlab 250Xi using a monochromatic Al Kα X-ray source.

RESULTS AND DISCUSSION

Material Characterization. *XRD.* Figure 1a illustrates the reference XRD pattern of MOF-5; Figure 1b shows the XRD pattern of the synthesized MOF-5 with peaks matching the reference XRD. The synthesized MOF-5 pattern is also consistent with the previously reported MOF-5 diffraction pattern.[43] The diffraction pattern exhibits peaks at 2-theta = ~8.5°, 9.9°, 14.9°, 15.8°, 17.8°, and 19.3°, which are characteristic of MOF-5 confirming successful synthesis of the material.[43−45] The crystallite size of MOF-5 was calculated using the Scherrer equation, shown in eq 13:

$$D = \frac{K\lambda}{\beta\cos\theta} \tag{13}$$

where D is the crystallite size, K is the Scherrer constant with a value of 0.9, β is the full width at half-maximum, and θ is the peak position. The size was calculated using peaks at 2θ positions 9.9°, 14.9°, 17.8°, and 19.3° and an average of 30.82 nm was considered the crystalline size of MOF-5.

Figure 1c shows the XRD pattern of CNC. This XRD pattern was observed to be consistent with previous reports and in line with JCPDC file no. 03-0226.[46,47] The diffraction pattern exhibited peaks at 2-theta = 15.2°, 16.7°, 22.6°, and 34.4°. These peaks are indexed as (110), (110), (200), and (004), respectively. Figure 1d depicts the MOF-5/CNC composite. This diffraction pattern exhibits a mixture of peaks from both the MOF-5 diffractogram and the CNC diffractogram, which is desired, as it suggests that the two materials coexist within the composite. The figure displays peaks at 2-theta = 9.9°, 14.9°, and 28°, which belong to MOF-5; and the peaks at 15.2° and 22.6° belong to CNC. This observation suggests that the phase and the crystal structure of the individual materials are maintained during the formation of the composite. No new phases or crystal structures were observed when the two materials were combined. Figure 1e shows the XRD pattern of the highly amorphous CA material, with no well-defined peaks. The XRD pattern of the CA-supported MOF-5/CNC (Figure 1f) displayed broad peaks at 10° and 22.8°, which are characteristic of CA and the MOF-5/CNC nanocomposite.

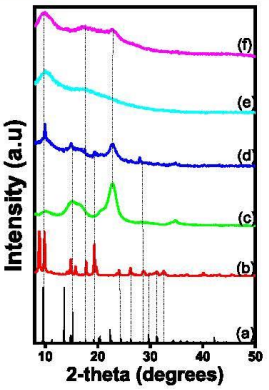

Figure 1. XRD patterns of (a) reference MOF-5, (b) MOF-5, (c) CNC, (d) MOF-5/CNC, (e) CA, and (f) CA-supported MOF-5/CNC.

FTIR. The synthesized materials were characterized by using FTIR spectroscopy. Figure 2a shows the CNC spectrum with functional group vibrations consistent with previous reports for CNC.[41,46,47] The peak at 1634 cm^{-1} is due to C═O stretching while the vibrations of the C−O−C pyranose ring are responsible for the peaks at 1430, 1374, and 1313 cm^{-1}. The peak observed at 892 cm^{-1} is because of glycosidic C_1−H deformation within the ring, which is characteristic of glycosidic linkages linking glucose monomers in the cellulose polymer. The FTIR spectra of MOF-5 (Figure 2b) show two peaks at 1381 and 1573 cm^{-1} due to asymmetric and symmetric stretching of carboxylate groups, respectively. The peak observed at 450 cm^{-1} is due to Zn−O stretching. The peaks observed at 743 and 815 cm^{-1} are due to C−H vibrations of the benzene ring. This FTIR spectrum coincides with MOF-5 spectra from previously reported studies confirming the successful synthesis of the material.[43,45] Figure 2c shows the spectrum of the MOF-5/CNC composite with peaks characteristic of CNC at 1648, 1310, and 1024 cm^{-1}. The peaks characteristic of MOF-5 are observed at 1583, 1364, 819, and 742 cm^{-1}. Figure 2d,e shows the FTIR spectra of CA and the adsorbent film, respectively. The peak at 1737 cm^{-1} in Figure 2d is due to carbonyl (C═O) stretching, and the peaks at 1028 and 1219 cm^{-1} are due to C−O−C symmetrical and asymmetrical vibrations, respectively. For the adsorbent film only peaks arising from CA are exhibited, this has been previously observed for CA nanocomposites.[42] The carbonyl (C═O) stretch in Figure 2e was shifted to 1740 cm^{-1}, indicating interaction between the MOF-5/CNC and the CA.

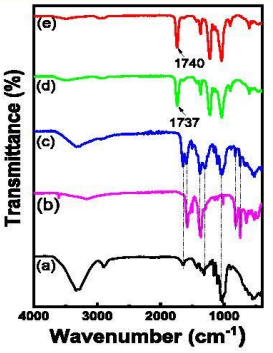

Figure 2. FTIR spectra of (a) CNC, (b) MOF-5, (c) MOF-5/CNC, (d) CA, and (e) CA-supported MOF-5/CNC.

https://doi.org/10.1021/acsomega.4c01150
ACS Omega 2024, 9, 37621−37635

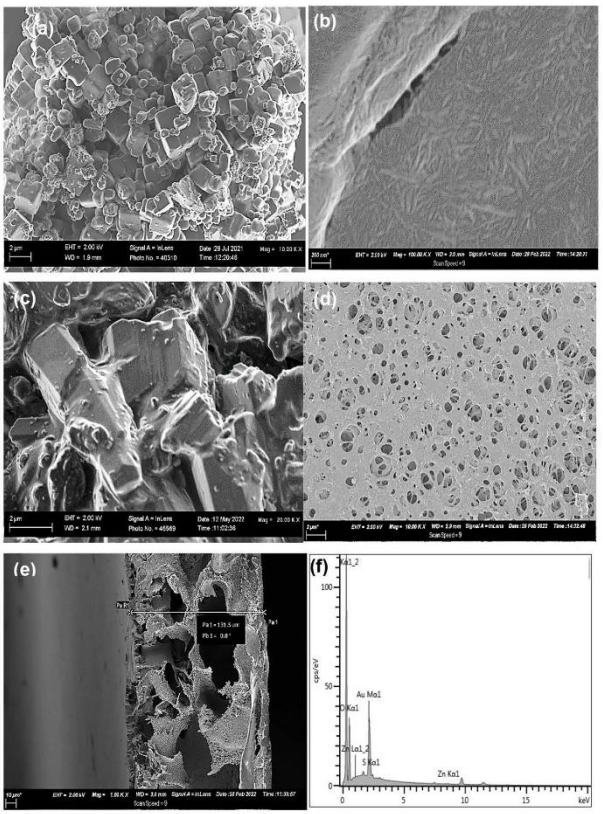

Figure 3. SEM images of (a) MOF-5, (b) CNC, (c) MOF-5/CNC, (d) CA-supported MOF-5/CNC film surface, (e) CA-supported MOF-5/CNC film cross-section, and (f) EDX spectrum of CA-supported MOF-5/CNC film.

SEM. The surface morphology of the materials was studied by using SEM. Figure 3a shows MOF-5 as mostly cubic crystals with particle sizes under 2 μm, consistent with previous reports.[40,43−45] The SEM image of CNC showed rod-like structures or nanowhiskers, which was the expected morphology.[46−48] The nanowhiskers have lengths of ca. 300 nm with diameters between 10 and 20 nm. The SEM image of MOF-5/CNC (Figure 3c) shows that the cubic crystals of MOF-5 were maintained; however, they appear to be coated with a thin layer of CNC. Figure 3d,e shows the SEM micrographs of the CA-supported MOF-5/CNC surface and cross-section, respectively. The surface of the adsorbent film is porous, and the adsorbent exhibits an irregular cross-section structure of dense skin layers and finger-like microcavities, which has been reported for CA-supported materials and membranes.[42,49] The film was synthesized via phase inversion, which results in a porous top layer and a finger-like sublayer. The film was measured to be 131.5 μm thick. Figure 3f shows the EDX spectrum of the film, and the elements observed, Zn and S, are from MOF-5 and CNC further confirming the successful synthesis of the adsorbent film.

TGA. TGA was used to assess the thermal stability of the adsorbent film. For all the materials (Figure 4a−d), the weight loss at 100 °C was attributed to loss of adsorbed water, and weight loss due to the removal of DMF occurred between 150 and 260 °C. The decomposition of the MOF-5 framework is

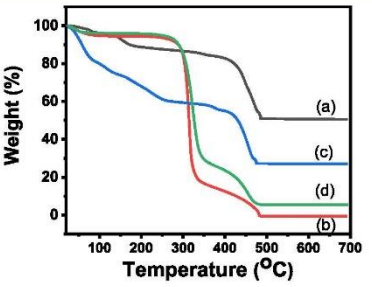

Figure 4. TGA curves of prepared (a) MOF-5, (b) CNC, (c) MOF-5/CNC, and (d) CA-supported MOF-5/CNC film.

https://doi.org/10.1021/acsomega.4c01150
ACS Omega 2024, 9, 37621−37635

shown in Figure 4a with weight loss in the range of 410−500 °C corresponding to the decomposition of the bridge between the Zn_4O carboxylate and the BDC ligand leaving a 51% zinc metal weight content. The CNC TGA curve shown in Figure 4b exhibits a second mass loss between 260 and 320 °C due to the pyrolysis of cellulose and hemicellulose. Further breakdown of the intermediates occurred beyond 340 °C until all the organic material was completely degraded. Figure 4c shows the weight loss of MOF-5/CNC. The weight loss between 410−500 °C is due to the decomposition of the composite, and 27% of zinc metal remains. The TGA curve of the CA-supported MOF-5/CNC film (Figure 4d) is slightly similar to the CNC curve since CA is a derivative of cellulose. Decomposition of the MOF-5 framework occurred between 360 and 500 °C, revealing a 5% zinc metal content.

BET and XPS. Figure 5 shows the N_2 adsorption−desorption isotherm of the adsorbent film. It can be observed that a type I

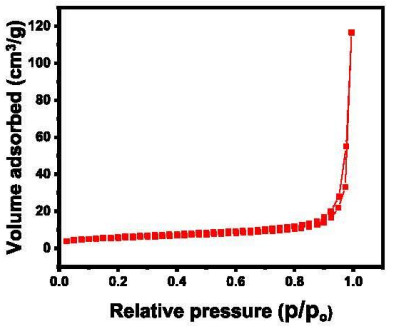

Figure 5. N_2 adsorption/desorption isotherm for the CA-supported MOF-5/CNC film.

adsorption−desorption isotherm was exhibited, and the specific surface area was determined to be 19.87 m^2/g. This renders the adsorbent microporous with a pore volume of 0.27 cm^3/g and a pore diameter of 1.17 nm. The elemental distribution of the adsorbent surface was studied by XPS. The presence of the O and C elements and their electronic state in the film are shown in Figure 6a. Figure 6b shows the deconvoluted carbon region depicting five peaks at 284.9, 284.2, 286.2, 286.2, and 287.5 eV assigned to sp^3-hybridized C−C, sp^2-hybridized C−C, C−O, and C═O bonds, respectively. The oxygen deconvoluted into two peaks at 531.9 and 532.9 eV (Figure 6c) assigned to C−O and C═O respectively.

Effect of pH on Adsorption of MB. The point of zero charge (pH_{pzc}) was used to determine the pH at which the net surface charge of the adsorbent film is zero. Figure 7 shows the plot of pH vs pH_i for the adsorbent and this study helps in understanding the surface chemistry involved during adsorption when the film interacts with MB. The figure shows the pH_{pzc} of the film to be 7.0. This means that the surface of the adsorbent film has a net positive charge in acidic pH and a net negative charge in alkaline pH.

Figure 8a shows the effect of pH on equilibrium adsorption capacity (q_e), and Figure 8b shows the effect of pH on % MB removal. pH has been observed to be a controlling parameter in the adsorption of MB.[50] The adsorption efficiency generally increases with increasing pH because, at an acidic pH, the surface of the adsorbent is positively charged, resulting in electrostatic repulsions between the cationic adsorbent and the cationic MB, minimizing adsorption. In addition, at low pH, there are excess H^+ ions that compete with the cationic MB dye for adsorption sites making adsorption unfavorable. This is true at pH 5; however, there is an anomaly at pH 3. The error limit of pH 3 is within the error limit of pH 5, and as a result, the actual adsorption behavior is valid from pH 5 and above. At pH > pH_{pzc}, the negatively charged adsorbent is electrostatically attracted to the cationic MB, and this favors adsorption. This adsorbent is versatile, as it has the ability to adsorb cations or anions depending on the application. In this study, the analyte of interest is cationic, and the highest adsorption efficiency was observed at pH 11.

Effect of Contact Time on MB Adsorption. The optimized contact time was determined at optimum pH and at initial concentrations (1−6 mg/L). Figure 9 shows the effect of contact time on the adsorption capacity and percentage of MB removal. Adsorption occurred in three phases; the first hour was the initial phase, where adsorption took place at a relatively high rate as illustrated by the sharp increase in equilibrium adsorption capacity and percentage removal. Similar behavior has been observed for dyes on biosorbents.[51] This occurs because of the availability of vacant active sites on the adsorbent film. The second phase occurs when contact time increases to 4−5 h; at this stage, adsorption happens at a lower rate due to the gradual saturation of active sites on the surface of the adsorbent film, and adsorption equilibrium is reached after 5 h. The adsorption capacity at equilibrium was 4.29 mg/g, and this corresponds to a percentage removal of 77.4%.

Effect of Initial Concentration on MB Adsorption. The dependence of equilibrium adsorption capacity and % MB removal on initial MB concentration was studied at pH 11, contact time of 6 h, at 25 °C. Figure 10a shows the equilibrium adsorption capacity increases (q_e) linearly with initial concentration from 0.75 to 4.29 mg/g, while the % MB removal (Figure 10b) decreases in a parabolic fashion from 75 to 71.6%. The increasing MB adsorption at higher initial concentrations was influenced by mass transfer, these conditions result in the saturation of active sites causing a reduction in % MB removal. From these results, the initial concentration of 6 mg/L was considered as the optimal concentration.

Effect of Temperature on MB Adsorption. The influence of temperature on q_e and % MB removal was investigated under the optimized conditions, which include the initial concentration of 6 mg/L. When the temperature was increased from 25 to 45 °C equilibrium adsorption efficiency decreased from 4.29 to 3.02 mg/g (Figure 11a) and the % MB removal dropped from 71 to 51% (Figure 11b). The results show that MB interacts less with the adsorbent film as the temperature increases. This decrease in activity implies that the adsorption process was exothermic in nature.

Adsorption Isotherms. Langmuir's and Freundlich's adsorption isotherm models were used to determine the adsorption parameters for the adsorption process. Figure 12 illustrates the linear plots, and Table 1 lists the resulting parameters along with correlation coefficients (R^2) and nonlinear chi-square (χ^2) values. This study provides insight into the adsorbate and adsorbent surface interaction during the adsorption process. The Langmuir isotherm model, shown in Figure 12a, assumes the surface of the adsorbent is

https://doi.org/10.1021/acsomega.4c01150
ACS Omega 2024, 9, 37621−37635

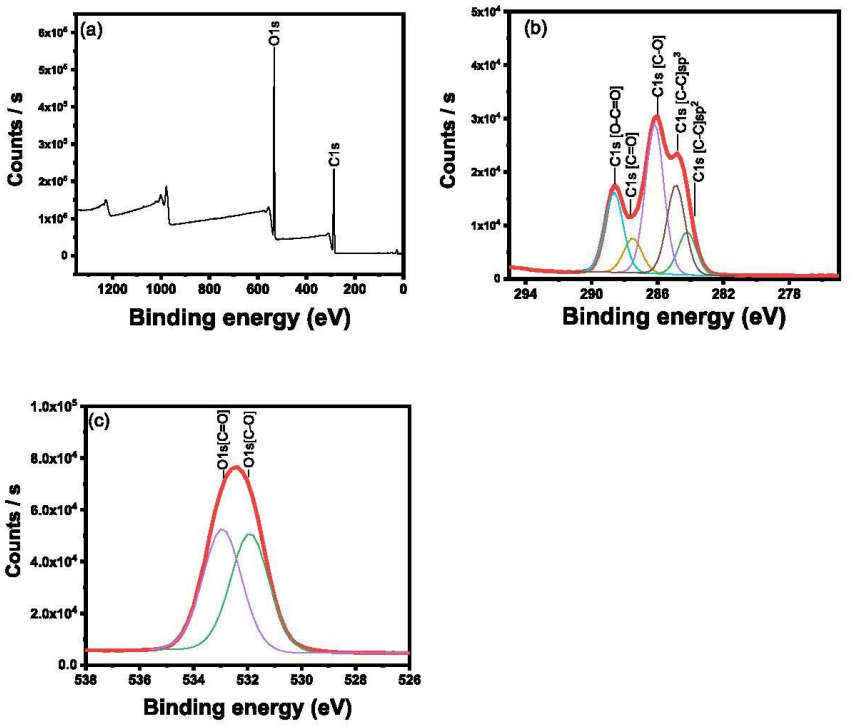

Figure 6. (a) XPS survey and (b) C 1 s and (c) O 1 s spectra of the CA-supported MOF-5/CNC adsorbent film.

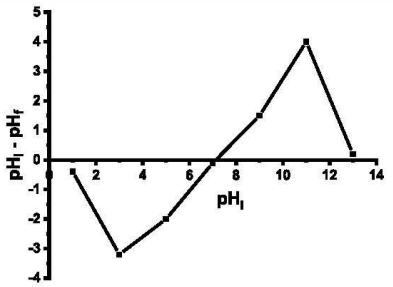

Figure 7. Plot of ΔpH vs pH_i.

homogeneous, and the maximum adsorption process occurs when monolayer coverage is achieved.[51] From Table 1, the R^2 value of the isotherm was 0.9738 and the χ^2 value was 0.011. The Langmuir constant, K_L, is dimensionless and represents the affinity of the adsorbent for the adsorbate. The K_L value in this study was 0.25, which is relatively high, suggesting that the interaction between the adsorbate and the adsorbent's surface is strong, implying that the adsorption process is favorable. The maximum adsorption capacity, q_{max} was calculated to be 13.23 mg/g and the separation factors, R_L, for all the initial concentration values, as illustrated by Figure 12c, was between 0 and 1 indicating a favorable adsorption process. The Langmuir model showed a decent fit of the experimental data; however, the maximum monolayer capacity overestimated (13.23 mg/g) the experimentally determined equilibrium capacity value of 4.29 mg/g. The Freundlich isotherm model assumes adsorption occurs on heterogeneous active sites with varying surface energies while following a multilayer coverage (Figure 12b). The R^2 value of the isotherm was 0.9674, and the χ^2 value was 0.031. From this curve, the heterogeneity factor, $1/n$, was between 0 and 1, indicating favorable adsorption. The Freundlich constant K_F was determined to be 2.77, and the equilibrium solid phase concentration was calculated using eq 14 to be 4.39 mg/g, which was closer to the experimental value (4.29 mg/g):

$$q_e = K_F C^{1/n} \tag{14}$$

The Freundlich constant presented a higher value compared to that of the Langmuir constant; this suggests that the adsorption mechanism may be described by the Freundlich isotherm. This indicates that the adsorption of MB on CA-supported MOF-5/CNC may conform to a mechanism involving multilayer coverage on a heterogeneous surface. Similar results have been observed on cellulose-based adsorbents for MB removal, showing better fitting with Freundlich isotherm.[52−54]

Adsorption Kinetic Models. Kinetic studies were used to investigate the potential rate-controlling step, as well as the adsorption mechanism. The adsorption kinetics are governed,

https://doi.org/10.1021/acsomega.4c01150
ACS Omega 2024, 9, 37621−37635

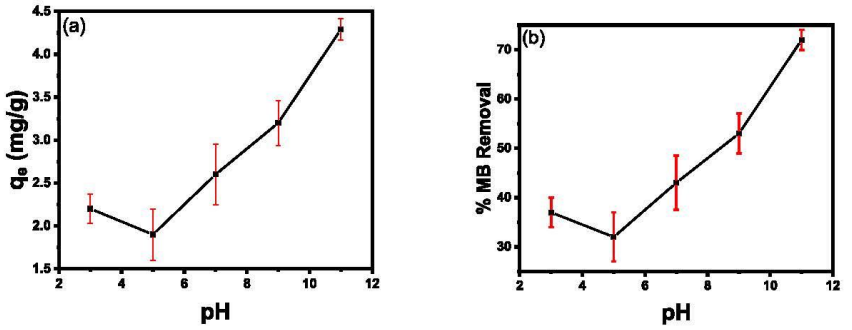

Figure 8. (a) Equilibrium adsorption capacity vs pH, and (b) % MB removal vs pH.

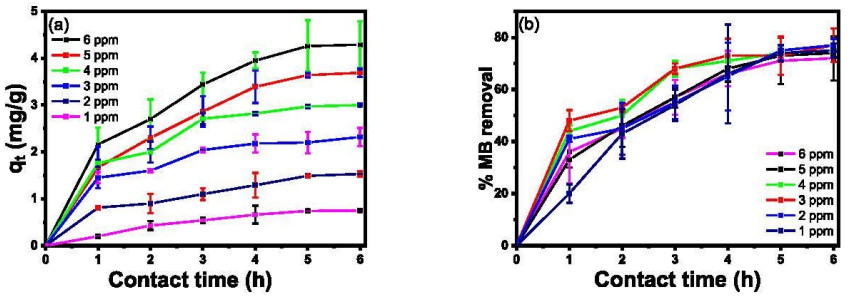

Figure 9. (a) Effect of contact time on adsorption capacity at initial concentrations of 1−6 mg/L, and (b) effect of contact time on percentage MB removal at initial concentrations of 1−6 mg/L.

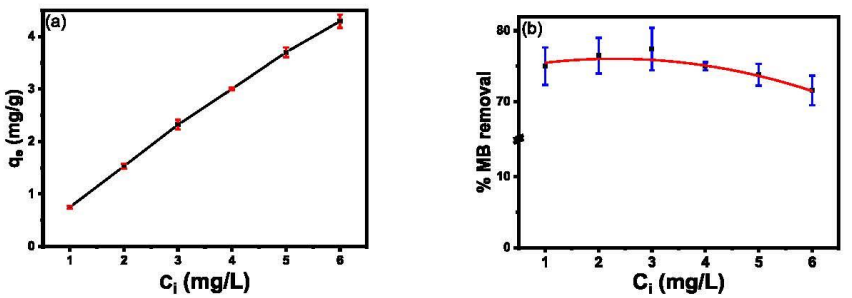

Figure 10. Plots of (a) equilibrium adsorption capacity vs initial concentration and (b) % MB removal vs initial concentration.

among various steps, by reaction processes and diffusion.[55] The adsorption data were fitted to the linearized pseudo-first-order kinetic model, and Figure 13a shows it was not applicable over the whole contact time and the calculated q_e was determined to be 13.21 mg/g. In most cases, the first order applies to the initial phase of the adsorption process and not to the rest of the contact time.[50,56] Figure 13b shows the experimental data fitting favorably over the whole adsorption range for the pseudo-second-order kinetic model. The calculated q_e from the pseudo-second-order model was determined to be 5.65 mg/g, which was closer to the experimentally obtained q_e (4.29 mg/g). The adsorption reaction can be described by pseudo-second-order kinetics with chemical interactions dominating the adsorption process.[57,58] The kinetic parameters and corresponding R^2 and χ^2 values are listed in Table 1. Adsorption can proceed through various pathways, including external diffusion, intraparticle diffusion, and pore diffusion.[58] The intraparticle and/or pore diffusion typically influence the overall rate of the adsorption process. Figure 13c−e shows the fitting of experimental data for the diffusion models. The Weber−Morris plot (q_t vs $t^{1/2}$) in Figure 13c shows that the plot is linear with $R^2 > 0.9$ and $\chi^2 < 0.05$, indicating that intraparticle diffusion is a possible pathway for MB adsorption. For this model the linear fit has to pass through the origin; this suggests that intraparticle diffusion is not the only controlling mechanism in this

https://doi.org/10.1021/acsomega.4c01150
ACS Omega 2024, 9, 37621−37635

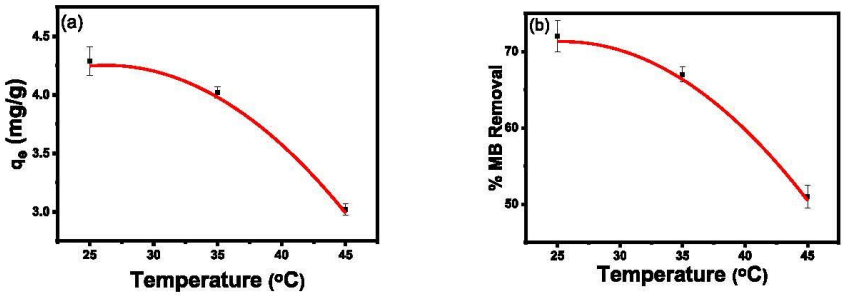

Figure 11. Effect of temperature on (a) equilibrium adsorption capacity and (b) % MB removal.

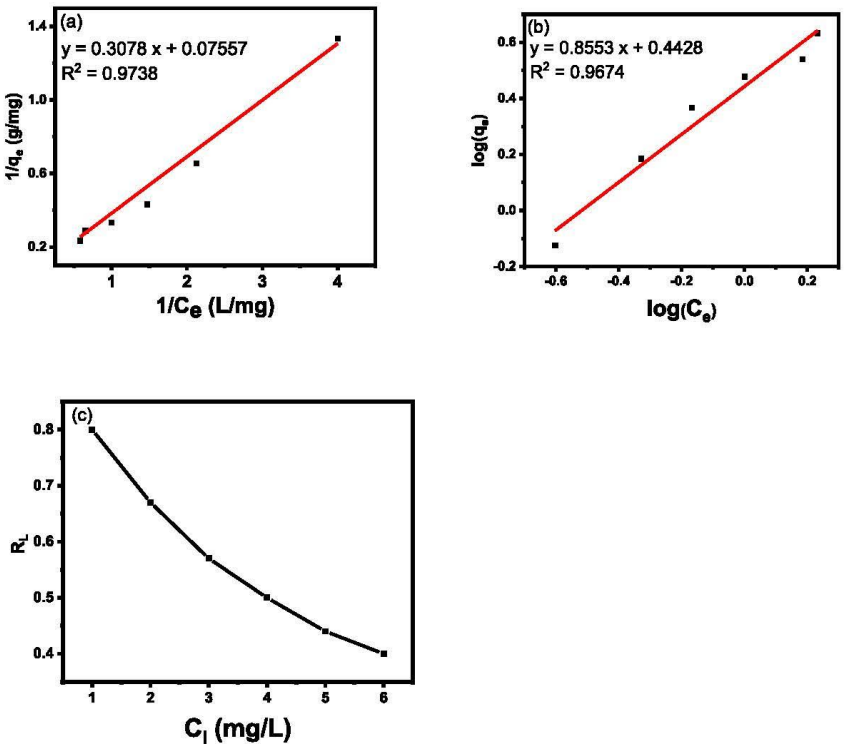

Figure 12. (a) Langmuir and (b) Freundlich isotherms of MB adsorption onto CA-supported MOF-5/CNC, and (c) R_L values from the Langmuir isotherm.

Table 1. Parameters for MB Adsorption on a CA-Supported MOF-5/CNC Film

Langmuir	Freundlich	pseudo-first-order	pseudo-second-order	intraparticle diffusion model	Bangham model	pore diffusion
q_{max} (mg/g) 13.23	q_e (mg/g) 4.39	q_e (mg/g) 13.21	q_e (mg/g) 5.65	k_{id} 0.2073	K_B 0.098	1st segment slope 0.008
						2nd segment slope 0.04
K_L (L/mg) 0.25	K_F (mg/g) 2.77	k_1 0.00005	k_2 0.0021			1st intercept −0.31
R^2 0.9738	R^2 0.9674	R^2 0.9201	R^2 0.9864	R^2 0.9709	R^2 0.9726	2nd intercept −7.67
X^2 0.011	X^2 0.031	X^2 0.036	X^2 0.023	X^2 0.028	X^2 0.044	

https://doi.org/10.1021/acsomega.4c01150
ACS Omega 2024, 9, 37621−37635

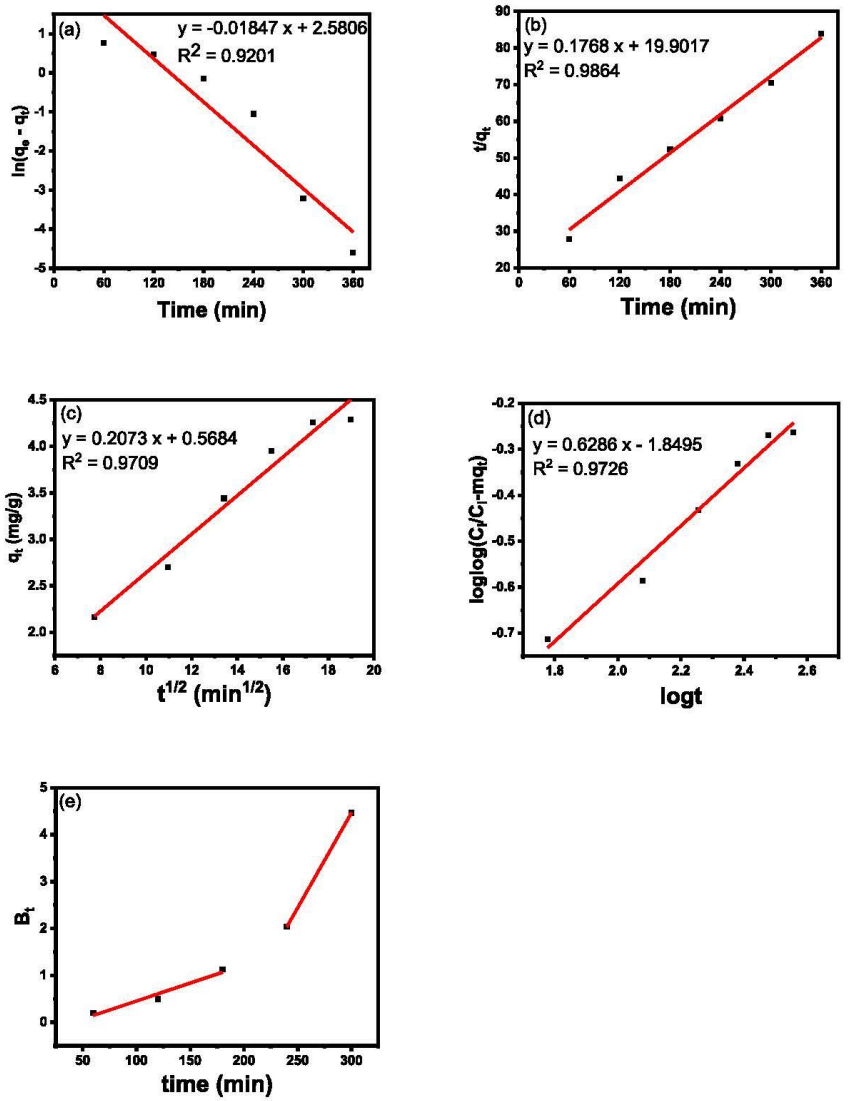

Figure 13. (a) Pseudo-first-order, (b) pseudo-second-order, (c) intraparticle, (d) pore diffusion, and (e) Boyd model plots of the experimental data for MB adsorption on the CA-supported MOF-5/CNC adsorbent film.

adsorption study but that the adsorption is a combination of multiple adsorption processes.[55,58] The intercept of the Weber–Morris plot has been reported to serve as an indicator of the thickness of the boundary layer, i.e., a large intercept implies a large boundary layer.[55,59] The Bangham plot shown in Figure 13d was used to check the possibility of pore diffusion as the rate-limiting step. The plot was found to be linear with $R^2 > 0.9$ and $\chi^2 < 0.05$, implying pore diffusion governs the adsorption process. The Boyd plot (Figure 13e) was used to assess pore diffusion, and it shows multilinearity. The multilinearity represents succeeding adsorption processes.[57] Figure 13e can be described as two segments, the first between 60 and 180 min with an intercept close to zero; this indicates that adsorption in this period could be described by pore diffusion. In the second segment, the intercept suggests that other mechanisms described above have taken over the adsorption process.

https://doi.org/10.1021/acsomega.4c01150
ACS Omega 2024, 9, 37621−37635

Adsorption Thermodynamics. The Arrhenius equation, eq 15, was used to gain more insight into the type of adsorption:

$$\ln k = \ln A - \frac{E_a}{RT} \quad (15)$$

where k is the rate constant, A is the Arrhenius factor, E_a is the activation energy for the adsorption process, R is the gas constant (8.314 J/K.mol), and T is the temperature in Kelvin. The activation energies for physisorption are categorized between 5 and 40 kJ/mol and are between 40 and 800 kJ/mol for chemisorption.[60] The slope of Figure 14 was used to

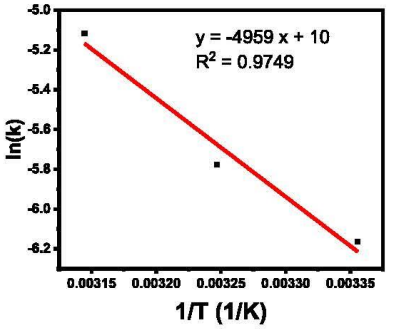

Figure 14. Plot of ln k vs T^{-1}: for the estimation of activation energy, E_a.

determine E_a, which was found to be 41.2 kJ/mol for the adsorption of MB on the adsorbent film, indicating chemisorption. Similar values have been observed for cellulose composites used for dye adsorption.[61]

Thermodynamic parameters which include standard entropy (ΔS°), standard enthalpy (ΔH°), and standard free energy (ΔG°) were determined to assess the thermal nature of MB adsorption on the adsorbent film according to previous reports.[51,57] ΔS° and ΔH° were calculated from the van't Hoff plot as depicted in Figure 15 according to eq 16:

$$\ln K_L = \frac{\Delta S^\circ}{R} - \frac{\Delta H^\circ}{RT} \quad (16)$$

ΔG° was determined using eq 17:

$$\Delta G^\circ = -RT \ln K_L \quad (17)$$

Table 2 shows thermodynamic parameters derived from Figure 15. The ΔG° values became less negative with increasing temperature, indicating the occurrence of saturation on the adsorbent surface at increased temperatures; however, the process was thermodynamically spontaneous at higher temperatures. Furthermore, ΔS° was negative, and ΔH° was negative, signifying an exothermic adsorption process.

Proposed Adsorption Mechanism and Reusability Studies. The interaction of MB molecules with CA-supported MOF-5/CNC can be understood by using Figure 16. The presence of functional groups on the adsorbent film guarantees intermolecular interactions with dye molecules. The proposed adsorption mechanism of MB on the surface of the adsorbent occurs through several ways. FTIR showed the presence of hydroxyl and carbonyl groups on the adsorbent film. These

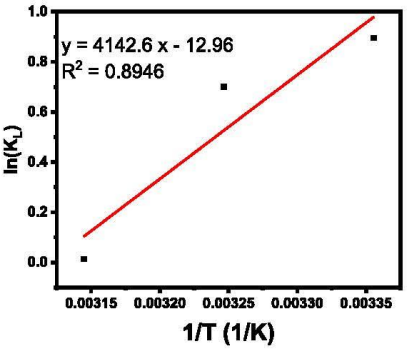

Figure 15. van't Hoff plot for MB adsorption on the CA-supported MOF-5/CNC adsorbent film.

Table 2. Thermodynamic Parameters for MB Adsorption on the CA-Supported MOF-5/CNC Adsorbent Film

T/K	ΔG° (kJ/mol)	ΔH° (kJ/mol)	ΔS° (J/K.mol^{-1})	activation energy (E_a) (kJ/mol)
298	−2.21838	−34.44158	−107.749	41.2
308	−1.05112			
318	−0.03525			

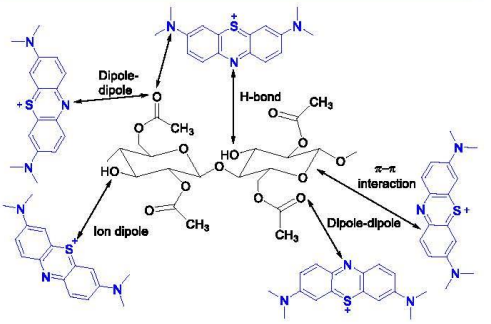

Figure 16. Adsorption mechanisms of CA-supported MOF-5/CNC to MB.

groups can interact electrostatically with MB.[62] The interactions include ion-dipole forces, dipole−dipole, hydrogen bonding, and $\pi-\pi$ interactions, similar mechanisms have been proposed in the literature for MB adsorption.[63] During adsorption, since pH > pH_{pzc}, the negatively charged adsorbent is electrostatically attracted to the cationic MB, and this favors adsorption. In addition, the hydrogen atom from the hydroxyl groups can form hydrogen bonds with the nitrogen from MB as illustrated in Figure 16. $\pi-\pi$ interactions can also occur between the cellulose polymer chain and the MB aromatic ring.[64]

Adsorption efficiency was evaluated, as seen in Figure 17. Cycle 1 represents MB adsorption with a fresh adsorbent and cycles 2−5 represents the times the adsorbent has been desorbed in methanol and readsorbed in fresh MB solution. A 7% drop in the adsorption capacity was observed from cycle 1 to cycle 2. A 13% decrease in adsorption capacity was observed

https://doi.org/10.1021/acsomega.4c01150
ACS Omega 2024, 9, 37621−37635

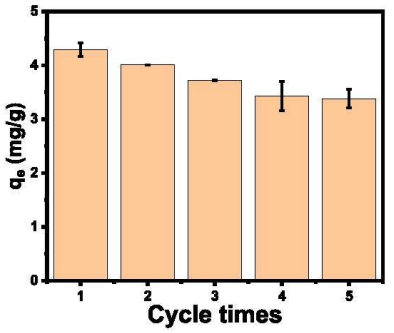

Figure 17. MB uptake over five adsorption/desorption cycles on CA-supported MOF-5/CNC.

for cycle 3 followed by a 20% decrease for cycle 4. These results support the thermodynamic data that allude to MB adsorption being driven by chemisorption resulting in reduced removal efficiency. There was no significant decrease after the fourth cycle (21% decrease for cycle 5), suggesting the binding sites were relatively fixed after the fourth cycle.

Simultaneous Adsorption of Methylene Blue and Methyl Orange (MO) and Treatment of Dye-Containing Wastewater. Dye-containing wastewater constitutes a complicated mixture of dyes, which include neutral, cationic, and anionic dyes. The simultaneous adsorption of anionic and cationic dyes is important for remediation hence the CA-supported MOF-5/CNC film was evaluated for the simultaneous adsorption for MB and MO at varied pH. As shown in Figure 18, MO had better adsorption under acidic conditions

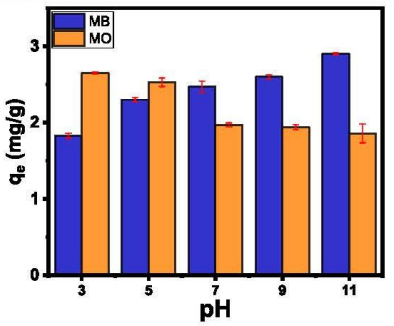

Figure 18. Simultaneous adsorption of MB and MO on the CA-supported MOF-5/CNC adsorbent film.

with the highest adsorption capacity of 2.65 mg/g obtained at pH 3. pH 11 remained the optimum pH for MB adsorption for the adsorbent film with an adsorption capacity of 2.9 mg/g, and MO had an adsorption capacity of 1.86 mg/g at this pH. The MB q_e values were lower than those reported without MO, this shows the influence of competing species for active sites.

The efficiency of the adsorbent film for wastewater treatment was examined by using domestic-industrial effluent spiked with MB. The pH of the wastewater sample was determined to be 8.35. Figure 19 shows a decrease in the absorption spectra for MB post adsorption. The % removal of

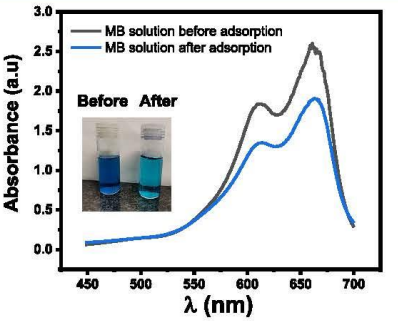

Figure 19. Adsorption of MB in domestic-industry effluent spiked with MB.

MB in the real water sample was determined to be 42%. The reduced efficiency was due to other contaminants interfering with the adsorption process.

Economic Assessment. In the development of any technological method applied in wastewater treatment, it is important to provide information about the cost of the treatment process. Depending on the treatment method, cost analysis is generally done by considering the costs of energy and material as major cost items.[65] For a material for which the purpose of the study is to investigate its efficiency in the removal of a dye, the simplified approach used in this study is considered sufficient.

In calculating the operating cost (OC), eq 18 was used:

$$\mathrm{OC}\left(\frac{\mathrm{USD}}{\mathrm{m}^3}\right) = aC_{\mathrm{energy}} + bC_{\mathrm{chemicals}} \tag{18}$$

where C_{energy} and $C_{\mathrm{chemicals}}$ are the energy consumed (in kWh/m^3) and the chemical consumption (in kg/m^3), respectively. The letter a is the electrical energy price USD 0.105 kWh for the South African market as of March 2024, and the letter b is the price of the chemicals used in the preparation of the adsorbent film material (USD/kg or USD/m^3).

In this study, the synthesized material could treat 0.030 L of wastewater in the first cycle; however, the calculated operating cost was done on the basis of treating 1 m^3 of the synthesized aqueous solution containing methylene blue following a reported approach.[66] The study considered the power rating in watts for all of the equipment used and the duration for which it was operated as well as the cost of the chemicals. Therefore, the total energy consumption was 110.8 kWh/m^3, which equates to USD 11.67/m^3, and the total chemical cost was USD 31.93/m^3. The operating cost was calculated to be USD 43.60. The operating cost for $C_{\mathrm{chemicals}}$ was 2.8 times more expensive than that of C_{energy}.

Comparison with Other Adsorbents. A comparison of the maximum adsorption capacities for MB adsorption of MOF-cellulose composite adsorbents is shown in Table 3. An adsorbent based on MOF-derived porous carbon (MOF-DPC) nanoparticles supported on CA had a q_e value of 41.36 mg/g at an initial MB concentration of 50 mg·L^{-1} at 65 °C.[42] A cellulose aerogel fabricated from CA and ZIF-8 had a q_e value

https://doi.org/10.1021/acsomega.4c01150
ACS Omega 2024, 9, 37621−37635

Table 3. MB Maximum Adsorption Capacity of MOF-Cellulose-Based Adsorbents

adsorbent	q_e (mg/g)	ref
CA/MOF-DPC	41.36	42
ZIF-8 (CA@ZIF-8)	90.18	67
C-BZ-1000	227	68
CA-supported MOF-5/CNC	4.29	this study

of 90.18 mg/g.[67] The MOF was grown in situ on the surface of the adsorbent. A q_e value of 227 mg/g was determined from nitrogen-doped carbon aerogels fabricated from the carbonization of bacterial cellulose@ZIF-8 composite aerogels.[68] While these adsorbents show better q_e values, the fabrication processes require extreme temperatures that may affect the overall cost-effectiveness of the adsorbent.

CONCLUSIONS

A CA-supported MOF-5/CNC adsorbent film was successfully fabricated by using solvothermal and ultrasonication methods for methylene blue adsorption in aqueous media. The film showed a porous morphology with a measured film thickness of 131.5 μm. The integration of CNC and MOF into the CA support was confirmed by FTIR, SEM-EDX, TGA, and XPS. The CNC provided the adsorbent with hydrolytic stability, while the CA support secured the MOF. Various factors that influence MB batch adsorption were assessed, and the maximum adsorption capacity and % removal were determined to be 4.29 mg/g and 77.4%, respectively, at 25 °C, at an initial concentration of 6 mg/L, at pH 11 and at 14.7 wt % MOF loading. The adsorption process was spontaneous and exothermic as indicated by negative ΔG° and ΔH° values. The Freundlich and pseudo-second-order models were the best-fit adsorption isotherm and kinetic models, respectively, and the activation energy was consistent with chemisorption. Electrostatic interactions, such as dipole−dipole, $\pi-\pi$ interactions, and hydrogen bonding, were proposed as chemical interactions between methylene blue and the film to influence adsorption. After being regenerated five times, the film maintained 79% activity, indicating its value for reusability. The cost analysis for the adsorption was established. There was a 42% removal of MB when the film was applied for the treatment of wastewater. Overall, this work established a simple synthetic route for a MOF adsorbent film for water remediation.

AUTHOR INFORMATION

Corresponding Author

Nolwazi Nombona − *Department of Chemistry, University of Pretoria, Pretoria 0002, South Africa;* orcid.org/0000-0002-9946-2568; Email: nolwazi.nombona@up.ac.za

Author

Lebogang Manamela − *Department of Chemistry, University of Pretoria, Pretoria 0002, South Africa*

Complete contact information is available at: https://pubs.acs.org/10.1021/acsomega.4c01150

Author Contributions

L.M. designed the project with the guidance of N.N. L.M. prepared the manuscript and N.N. proofread and made the contributions and suggestions to the structure and contents of the manuscript.

Notes

The authors declare no competing financial interest.

ACKNOWLEDGMENTS

The authors would like to acknowledge the University of Pretoria, Chemistry department for providing a conducive environment to conduct this study and the National Research Foundation for funding this study. We would like to thank the National Metrology Institute of South Africa for the XPS measurements, Tshwane Municipality for providing the industrial-domestic wastewater, and Dr Samuel A. Iwarere from the Department of Chemical Engineering at the University of Pretoria for the cost analysis calculations.

REFERENCES

(1) Al-Tohamy, R.; Ali, S.-S.; Li, F.; Okasha, K.-M.; Mahmoud, Y.-A.-G.; Elsamahy, T.; Jiao, H.; Fu, Y.; Sun, J. A critical review on the treatment of dye-containing wastewater: Ecotoxicological and health concerns of textile dyes and possible remediation approaches for environmental safety. *Ecotoxicol. Environ. Saf.* **2022**, *231*, No. 113160.
(2) Shathy, R.-A.; Fahim, S.-A.; Sarker, M.; Quddus, S.; Moniruzzaman, M.; Masum, S.; Molla, A.-I. Natural Sunlight Driven Photocatalytic Removal of Toxic Textile Dyes in Water Using B-Doped ZnO/TiO2 Nanocomposites. *Catalysts* **2022**, *12*, 308.
(3) Moyo, S.; Makhanya, B.-P.; Zwane, P.-E. Use of bacterial isolates in the treatment of textile dye wastewater: A review. *Heliyon* **2022**, *8*, No. e09632.
(4) Oladoye, P.-O.; Bamigboye, M.-O.; Ogunbiyi, O.-D.; Akano, M.-T. Toxicity and decontamination strategies of Congo red dye. *Groundw. Sustain. Dev.* **2022**, *19*, No. 100844.
(5) Khan, I.; Saeed, K.; Zekker, I.; Zhang, B.; Hendi, A.-H.; Ahmad, A.; Ahmad, S.; Zada, N.; Ahmad, H.; Shah, L.-A.; Shah, T.; Khan, I. Review on Methylene Blue: Its Properties, Uses, Toxicity and Photodegradation. *Water* **2022**, *14*, 242.
(6) Miao, G.; Li, F.; Gao, Z.; Xu, T.; Miao, X.; Ren, G.; Song, Y.; Li, X.; Zhu, X. Ag/polydopamine-coated textile for enhanced liquid/liquid mixtures separation and dye removal. *IScience* **2022**, *25*, No. 104213.
(7) Olas, B.; Białecki, J.; Urbanska, K.; Brys, M. The Effects of Natural and Synthetic Blue Dyes on Human Health: A Review of Current Knowledge and Therapeutic Perspectives. *Adv. Nutr.* **2021**, *12*, 2301−2311.
(8) Sunil, K.; Sherugar, P.; Rao, S.; Lavanya, C.; Geetha, R.; Balakrishna, G. R.; Arthanareeswaran, G.; Padaki, M. Prolific approach for the removal of dyes by an effective interaction with polymer matrix using ultrafiltration membrane. *J. Environ. Chem. Eng.* **2021**, *9*, No. 106328.
(9) Ihaddaden, S.; Aberkane, D.; Boukerroui, A.; Robert, D. Removal of methylene blue (basic dye) by coagulation-flocculation with biomaterials (bentonite and Opuntia ficus indica). *J. Water Process Eng.* **2022**, *49*, No. 102952.
(10) Qazi, U.-Y.; Iftikhar, R.; Ikhlaq, A. Application of Fe-RGO for the removal of dyes by catalytic ozonation process. *Environ. Sci. Pollut. Res.* **2022**, *29*, 89485−89497.
(11) Fu, Q.; Shi, D.; Mo, C.; Lou, J.; Zhou, S.; Zha, L.; Wang, J.; Yan, W.; Luo, J. Adsorption behavior of methylene blue on regenerable composite Cu-BTC@AG. *J. Solid State Chem.* **2022**, *311*, No. 123100.
(12) Nimbalkar, M.-N.; Bhat, B.-R. Simultaneous adsorption of methylene blue and heavy metals from water using Zr-MOF having free carboxylic group. *J. Environ. Chem. Eng.* **2021**, *9*, No. 106216.
(13) Ngulube, R.; Pillay, L.; Nombona, N. Synthesis and characterization of electrospun composite nanofibers from Moringa oleifera biomass and metal oxide nanoparticles as potential adsorbents for the removal of lead ions. *Chem. Pap.* **2024**, *78*, 599−611.
(14) Rashid, R.; Shafiq, I.; Akhter, P.; Iqbal, M.-J.; Hussain, M. A state-of-the-art review on wastewater treatment techniques: the

https://doi.org/10.1021/acsomega.4c01150
ACS Omega 2024, 9, 37621−37635

effectiveness of adsorption method. *Environ. Sci. Pollut. Res.* **2021**, *28*, 9050−9066.
(15) El-Bery, H.-M.; Saleh, M.; El-Gendy, R.-A.; Saleh, M.-R.; Thabet, S.-M. High adsorption capacity of phenol and methylene blue using activated carbon derived from lignocellulosic agriculture wastes. *Sci. Rep.* **2022**, *12*, 5499.
(16) Ali, J.; Bakhsh, E.-M.; Hussain, N.; Bilal, M.; Akhtar, K.; Fagieh, T.-M.; Danish, E.-Y.; Asiri, A.-M.; Su, X.; Khan, S.-B. A new biosource for synthesis of activated carbon and its potential use for removal of methylene blue and eriochrome black T from aqueous solutions. *Ind. Crops Prod.* **2022**, *179*, No. 114676.
(17) Hamad, H.-N.; Idrus, S. Recent Developments in the Application of Bio-Waste-Derived Adsorbents for the Removal of Methylene Blue from Wastewater: A Review. *Polymers* **2022**, *14*, 783.
(18) Sharma, G.; Sharma, S.; Kumar, A.; Lai, C.-W.; Naushad, M.; Shehnaz; Iqbal, J.; Stadler, F.-J. Activated Carbon as Superadsorbent and Sustainable Material for Diverse Applications. *Adsorpt. Sci. Technol.* **2022**.
(19) Alves, A.-T.; Lasmar, D.-J.; de Andrade Miranda, I.-P.; da Silva Chaar, J.; dos Santos Reis, J. The Potential of Activated Carbon in the Treatment of Water for Human Consumption, a Study of the State of the Art and Its Techniques Used for Its Development. *Adv. Biosci. Biotechnol.* **2021**, *12*, 143−153.
(20) Mohamed, F.; Shaban, M.; Zaki, S.-K.; Abd-Elsamie, M.-S.; Sayed, R.; Zayed, M.; Khalid, N.; Saad, S.; Omar, S.; Ahmed, A.-M.; Gerges, A.; El-Mageed, H.-R.; Soliman, N.-K. Activated carbon derived from sugarcane and modified with natural zeolite for efficient adsorption of methylene blue dye: experimentally and theoretically approaches. *Sci. Rep.* **2022**.
(21) El Messaoudi, N.; El Khomri, M.; El Mouden, A.; Bouich, A.; Jada, A. Regeneration and reusability of non-conventional low-cost adsorbents to remove dyes from wastewaters in multiple consecutive adsorption−desorption cycles: a review. *Biomass Convers. Biorefin.* **2022**, *14*, 1−18.
(22) Duan, Y.; Li, L.; Shen, Z.; Cheng, J.; He, K. Engineering Metal-Organic-Framework (MOF)-Based Membranes for Gas and Liquid Separation. *Membranes* **2023**, *13*, 480.
(23) Naser, S.-A.-E.; Badmus, K.-O.; Khotseng, L. Synthesis, Properties, and Applications of Metal Organic Frameworks Supported on Graphene Oxide. *Coatings* **2023**, *13*, 1456.
(24) Zhang, S.; Wang, J.; Zhang, Y.; Ma, J.; Huang, L.; Yu, S.; Chen, L.; Song, G.; Qiu, M.; Wang, X. Applications of water-stable metal-organic frameworks in the removal of water pollutants: A review. *Environ. Pollut.* **2021**, *291*, No. 118076.
(25) Al-Hazmi, G.-A.-A.; El-Zahhar, A.-A.; El-Desouky, M.-G.; El-Bindary, M.-A.; El-Bindary, A.-A. Adsorption of industrial dye onto a zirconium metal-organic framework: synthesis, characterization, kinetics, thermodynamics, and DFT calculations. *J. Coord. Chem.* **2022**, *75*, 1203−1229.
(26) Wang, X.; Zang, M.; Yang, J.; Yang, J.; Duan, H. Efficient removal of dyes from water by zirconium-based metal-organic cages with varying functional groups. *J. Mol. Stuct.* **2023**, *1291*, No. 136018.
(27) Chen, P.; Wang, Y.; Zhuang, X.; Liu, H.; Liu, G.; Lv, W. Selective removal of heavy metals by Zr-based MOFs in wastewater: New acid and amino functionalization strategy. *J. Environ. Sci.* **2023**, *124*, 268−280.
(28) Flores-Cervantes, D.-X.; Medina-Montiel, C.; Ramirez-Corona, N.; Navarro-Amador, R. Zirconium Based MOFs and Their Potential Use in Water Remediation: Current Achievements and Possibilities. *Air Soil Water Res.* **2022**, *15*, 1−15.
(29) Xue, W.; Wang, J.; Huang, H.; Mei, D. Structural and Hydrolytic Stability of Coordinatively Unsaturated Metal−Organic Frameworks $M_3(BTC)_2$ (M = Cu, Co, Mn, Ni, and Zn): A Combined DFT and Experimental Study. *J. Phys. Chem. C* **2021**, *125*, 5832−5847.
(30) An, Y.; Lv, X.; Jiang, W.; Wang, L.; Shi, Y.; Hang, X.; Pang, H. The stability of MOFs in aqueous solutions—research progress and prospects. *Green Chem. Eng.* **2024**, *5*, 187.
(31) Mosca, L.-P.-L.; Gapan, A.-B.; Angeles, R.-A.; Lopez, E.-C.-R. Stability of Metal−Organic Frameworks: Recent Advances and Future Trends. *Eng. Proc.* **2023**, *56*, 146.
(32) Li, Z.; Wang, L.; Qin, L.; Lai, C.; Wang, Z.; Zhou, M.; Xiao, L.; Liu, X.; Zhang, M. Recent advances in the application of water-stable metal-organic frameworks: Adsorption and photocatalytic reduction of heavy metal in water. *Chemosphere* **2021**, *285*, No. 131432.
(33) Ding, M.; Jiang, H.-L. Improving Water Stability of MOFs by a General Surface Hydrophobic Polymerization. *CCS Chem.* **2021**, *2*, 2740−2748.
(34) Yang, S.; Karve, V.-V.; Justin, A.; Kochetygov, I.; Espín, J.; Asgari, M.; Trukhina, O.; Sun, D.-T.; Peng, L.; Queen, W.-L. Enhancing MOF performance through the introduction of polymer guests. *Coord. Chem. Rev.* **2021**, *427*, No. 213525.
(35) He, Y.; Wang, Y.; Shi, J.; Lu, X.; Liu, Q.; Liu, Y.; Zhu, T.; Wang, D.; Yang, Q. Incorporating metal−organic frameworks into substrates for environmental applications. *J. Chem. Eng.* **2022**, *446*, No. 136866.
(36) Yu, B.; Liu, Y.; Li, Z.; Liu, Y.; Rao, P.; Li, G. Durable substrates incorporated with MOFs: Recent advances in engineering strategies and water treatment applications. *J. Chem. Eng.* **2023**, *455*, No. 140840.
(37) Yu, S.; Pang, H.; Huang, S.; Tang, H.; Wang, S.; Qiu, M.; Chen, Z.; Yang, H.; Song, G.; Fu, D.; Hu, B.; Wang, X. Recent advances in metal-organic framework membranes for water treatment: A review. *Sci. Total Environ.* **2021**, *800*, No. 149662.
(38) Dehghankar, M.; HmtShirazi, R.; Mohammadi, T.; Tofighy, M.-A. Synthesis and modification methods of metal-organic frameworks and their application in modification of polymeric ultrafiltration membranes: A review. *J. Environ. Chem. Eng.* **2023**, *11*, No. 109954.
(39) Salahuddin, N.; Akelah, A.; Elnagar, M.; Abdelwahab, M.-A. Antibacterial and cytotoxicity of methylene blue loaded-cellulose nanocarrier on breast cancer cell line. *Carbohyd. Polym. Technol. Appl.* **2024**, *2*, No. 100138.
(40) Peedikakkal, A.-M.-P.; Aljundi, I.-H. Upgrading the Hydrogen Storage of MOF-5 by Post-Synthetic Exchange with Divalent Metal Ions. *Metal Ions. Appl. Sci.* **2021**, *11*, 11687.
(41) Matebie, B.-Y.; Tizazu, B.-Z.; Kadhem, A.-A.; Prabhu, S.-V. Synthesis of Cellulose Nanocrystals (CNCs) from Brewer's Spent Grain Using Acid Hydrolysis: Characterization and Optimization. *J. Nanomater.* **2021**, *2021*, 10.
(42) Tahazadeh, S.; Karimi, H.; Mohammadi, T.; Motejadded, H.-B.; Tofighy, M.-A. Fabrication of biodegradable cellulose acetate/MOF-derived porous carbon nanocomposite adsorbent for methylene blue removal from aqueous solutions. *J. Solid State Chem.* **2021**, *299*, No. 122180.
(43) Fiaz, M.; Kashif, M.; Fatima, M.; Batool, S.-R.; Asghar, M.-A.; Shakeel, M.; Athar, M. Synthesis of Efficient TMS@MOF-5 Catalysts for Oxygen Evolution Reaction. *Catal. Lett.* **2020**, *150*, 2648−2659.
(44) Asadevi, H.; Prasannakumaran, P.; Kumari, N.-C.; Amma, R.-P.; Khadar, S.-A.; Sasi, S.-C.; Raghunandan, R. ZnO@MOF-5 as a Fluorescence "Turn-Off" Sensor for Ultrasensitive Detection as well as Probing of Copper(II) Ions. *ACS Omega* **2022**, *7*, 13031−13041.
(45) Hu, Y.; Yang, H.; Wang, R.; Duan, M. Fabricating Ag@MOF-5 nanoplates by the template of MOF-5 and evaluating its antibacterial activity. *Colloids Surf. A: Physicochem. Eng.* **2021**, *626*, No. 127093.
(46) Imiete, I.-E.; Giannini, L.; Tadiello, L.; Orlandi, M.; Zoia, L. The effect of sulfate half-ester groups on the mechanical performance of cellulose nanocrystal-natural rubber composites. *Cellulose* **2023**, *30*, 8929−8940.
(47) Leong, S.-L.; Tiong, S.-I.-X.; Siva, S.-P.; Ahamed, F.; Chan, C.; Lee, C.-L.; Chew, I.-M.-L.; Ho, Y.-K. Morphological control of cellulose nanocrystals via sulfuric acid hydrolysis based on sustainability considerations: An overview of the governing factors and potential challenges. *J. Environ. Chem. Eng.* **2022**, *10*, No. 108145.
(48) Zhu, W.; Han, M.; Kim, D.; Zhang, Y.; Kwon, G.; You, J.; Jia, C.; Kim, J. Facile preparation of nanocellulose/Zn-MOF-based catalytic filter for water purification by oxidation process. *Environ. Res.* **2022**, *205*, No. 112417.

https://doi.org/10.1021/acsomega.4c01150
ACS Omega 2024, 9, 37621−37635

(49) Azam, R.-S.; Almasri, D.-A.; Alfahel, R.; Hawari, A.-H.; Hassan, M.-K.; Elzatahry, A.-A.; Khaled, A. MXene (Ti3C2Tx)/Cellulose Acetate Mixed-Matrix Membrane Enhances Fouling Resistance and Rejection in the Crossflow Filtration Process. *Membranes* **2022**, *12*, 406.
(50) Şendal, K.; Özgür, M.-U.; Gülen, J. Biosynthesis of ZnO photocatalyst and its application in photo catalytic degradation of methylene blue dyestuff. *J. Disper. Sci. Technol.* **2023**, *44*, 2734−2747.
(51) Gülen, J.; Gezerman, A.-O. A novel biosorbent for remediation of colored waste water. *Biomass Conv. Bioref.* **2023**, *13*, 3227−3235.
(52) Melese, H.; Tsade, H. Cellulose based adsorbent for cationic methylene blue dye removal. *Discovery Appl. Sci.* **2024**.
(53) Amrutha; Jeppu, G.; Girish, C.-R.; Baakrishna, P.; Mayer, K. Multi-component Adsorption Isotherms: Review and Modeling Studies. *Environ. Process* **2023**, *10*, 38.
(54) Khatri, M.; Ahmed, M.-E.; Al-Juboori, R.-A.; Khanzada, N.-K.; Hilal, N. Reusable environmentally friendly electrospun cellulose acetate/cellulose nanocrystals nanofibers for methylene blue removal. *J. Environ. Chem. Eng.* **2024**, *12*, No. 111788.
(55) Wang, J.; Guo, X. Rethinking of the intraparticle diffusion adsorption kinetics model: Interpretation, solving methods and applications. *Chemosphere* **2022**, *309*, No. 136732.
(56) Gülen, J.; Akın, B.; Özgür, M. Ultrasonic-assisted adsorption of methylene blue on sumac leaves. *Desalin. Water Treat.* **2016**, *57*, 9286.
(57) Gülen, J.; İskeçeli, M. Removal of methylene blue by using porous carbon adsorbent prepared from carbonized chestnut shell. *Materials Testing* **2017**, *59*, 188−194.
(58) Mekuria, D.; Diro, A.; Melak, F.; Asere, T.-G. Adsorptive Removal of Methylene Blue Dye Using Biowaste Materials: Barley Bran and Enset Midrib Leaf. *J. Chem.* **2022**, *2022*, 1.
(59) Gülen, J.; Zorbay, F. Methylene Blue Adsorption on a Low Cost Adsorbent—Carbonized Peanut Shell. *Water Environ. Res.* **2017**, *89*, 805.
(60) Alharby, N.-F.; Almutairi, R.-S.; Mohamed, N.-A. Adsorption behavior of methylene blue dye by novel cross-linked O-CM-Chitosan hydrogel in aqueous solution: kinetics, isotherm and thermodynamics. *Polymers* **2021**, *13*, 3659.
(61) Zaman, A.; Orasugh, J.-T.; Banerjee, P.; Dutta, S.; Ali, M.-S.; Das, D.; Bhattacharya, A.; Chattopadhyay, D. Facile one-pot in-situ synthesis of novel graphene oxide-cellulose nanocomposite for enhanced azo dye adsorption at optimized conditions. *Carbohydr. Polym.* **2020**, *246*, No. 116661.
(62) Wu, Z.; Liao, Q.; Chen, P.; Zhao, D.; Huo, J.; An, M.; Li, Y.; Wu, J.; Xu, Z.; Sun, B.; Huang, M. Synthesis, characterization, and methylene blue adsorption of multiple-responsive hydrogels loaded with Huangshui polysaccharides, polyvinyl alcohol, and sodium carboxyl methyl cellulose. *Int. J. Biol. Macromol.* **2022**, *215*, 157−171.
(63) Yang, T.; Li, Z.; Wei, W.; Wang, X.; Liu, F.; Xu, X.; Liu, Z. Structure and Properties of Lignin Extracted from Cotton Stalk by Non-polluting Ethanol-Assisted Hot Water Pretreatment and its High-Value Utilization for Methylene Blue Removal. *Waste Biomass Valor.* **2023**, *14*, 2085−2101.
(64) Rana, J.; Goindi, G.; Kaur, N.; Krishna, S.; Kakati, A. Synthesis and application of cellulose acetate-acrylic acid-acrylamide composite for removal of toxic methylene blue dye from aqueous solution. *J. Water Process Eng.* **2022**, *49*, No. 103102.
(65) Kobya, M.; Delipinar, S. Treatment of the baker's yeast wastewater by electrocoagulation. *J. Hazard. Mater.* **2008**, *154*, 1133−1140.
(66) Bayramoglu, M.; Kobya, M.; Can, O.-T.; Sozbir, M. Operating cost analysis of electrocoagulation of textile dye wastewater. *Sep. Purif. Technol.* **2004**, *37*, 117−125.
(67) Wu, G.; Zhou, C.; Li, H.; Xia, S.; Zhu, Y.; Han, J.; Xing, W. Controlled fabrication of the biomass cellulose aerogel@ZIF-8 nanocomposite as efficient and recyclable adsorbents for methylene blue removal. *Ind. Crop. Prod.* **2023**, *193*, No. 116169.
(68) Ma, X.; Xu, Y. Three-dimensional porous nitrogen-doped carbon aerogels derived from cellulose@mof for efficient removal of dye in water. *J. Environ. Chem. Eng.* **2022**, *10*, No. 108385.

https://doi.org/10.1021/acsomega.4c01150
ACS Omega 2024, 9, 37621−37635

CHAPTER 4

4.0 ADSORPTION OF METHYLENE BLUE ON WATER-STABLE CU-BDC MOF/CELLULOSE COMPOSITE FILM

Lebogang Manamela and Nolwazi Nombona

University of Pretoria, Department of Chemistry, Private Bag X20, Hatfield 0028, Gauteng, South Africa

4.1 Abstract

We report the synthesis of an effective and economical adsorbent film using a solvothermal process, aimed at removing methylene blue (MB) from water. The adsorbent uses cellulose acetate (CA) as a substrate for a composite material consisting of Cu-based MOF (Cu-BDC) and crystalline nanocellulose (CNC). The film is water-stable, recyclable, and customizable for selective adsorption through pH adjustment. Characterization techniques, including X-ray diffraction (XRD), thermal gravimetric analysis (TGA), scanning electron microscopy (SEM), X-ray photoelectron spectroscopy (XPS), Brunauer-Emmett-Teller (BET) analysis, and Fourier transform infrared spectroscopy (FTIR), confirmed the successful synthesis of the film. The Cu-BDC adsorbent showed rapid adsorption within the first 2 hours, reaching equilibrium by 5 hours with a maximum adsorption capacity of 3.60 mg/g and a dye removal efficiency of 84%. Experimental data closely fitted the Langmuir isotherm and pseudo-second-order kinetic models, with thermodynamic studies indicating exothermic and feasible adsorption. The adsorbent was applied to real industrial dye effluent where it achieved 20% effluent removal. The adsorbent film showed good regeneration capability, emphasizing its cost-effectiveness. The selectivity and versatility of the CA-supported Cu-BDC/CNC film make it practical for wastewater treatment applications.

4.2 Introduction

Dyes are the most common pollutants released from industries and are often an indicator of contamination in aquatic environments [1–3]. Organic dyes are made of auxochromes that make them water-soluble. Most organic dyes are classified as carcinogenic and are a risk to aquatic and human life [1, 4–7]. The adsorptive removal of toxic pollutants from aquatic systems is regarded as an efficient decontamination process [8–10]. Zeolites, porous carbons, bio-adsorbents, and metal nanoparticles have been commonly used for the adsorption of pollutants from water [11–14]. However, over the past decade, metal-organic frameworks (MOFs) have gained popularity as adsorbent materials due to their high surface area, porosity, tuneable chemical properties, and customizable structure [15–18]. MOFs are organic-inorganic hybrid materials consisting of a metal ion, or a cluster, bridged by organic linkers to form 1D, 2D or 3D network arrays. The tuneable structure of MOFs allows for functionalized forms which include hybridization or coating of the pristine MOF leading to the development of novel materials with enhanced and preferable characteristics [18–22].

MOF composites such as MOF/organic polymers, MOF/metal oxide, and carbon/MOFs are materials that have shown improved performance compared to individual materials when used as adsorbents [23]. They achieve enhanced performance by leveraging unique properties brought by individual materials in the composite. In most MOF-based composites, MOFs remain the integral material for selectivity and adsorption, and the other materials provide mechanical support and promote their handling for improved recyclability.

Cellulose derivatives have emerged as potentials to form composites with MOFs for several reasons [24–27]. These materials improve the hydrolytic stability of MOFs, as hydrophilic cellulose behaves favourably in water. Cellulose chains, as observed from plant cell walls, are very stable in water and will enhance the composite's overall stability. Zhou *et al.* (2023) showed that nanocellulose (NC) materials in MOF@NC composites act as support structures to improve strength and promote recyclability [28]. The study further revealed that cellulose materials can effectively prevent agglomeration of MOF materials. Hou *et al.* (2021) demonstrated that CNC was the dispersing agent for the core-shell magnetic Fe_3O_4/CNC@MOF catalyst [29]. Zang *et al.* (2021) showed the ZIF-67/cellulose hybrid had good structural stability in aqueous environments when employed for the degradation of MB in water [30]. Additionally, cellulose has adsorption active sites, -OH groups, on its surface that can contribute positively to the adsorption process [31 – 32].

The choice of MOF is crucial for every intended application. Copper-based MOFs offer advantages in organic dye adsorption due to their high surface area and versatile coordination chemistry. The

copper ion center of the MOF acts as an adsorption active site, forming stronger interactions with organic dyes in aqueous solutions, leading to higher affinities and enhanced adsorption efficiencies [33 – 34].

In this work, Cu-BDC was embedded into cellulose-based supports. CNC was used to form a composite with Cu-BDC, to impart hydrolytic stability. CA was used to provide mechanical support and aid in the recyclability of the Cu-BDC/CNC composite. The absorption behaviour of MB on the CA-supported Cu-BDC/CNC adsorbent film was investigated.

4.3 Methods and materials

4.3.1 Materials

Ethanol (99.9 %), N, N-Dimethylformamide (DMF, 99.9 %), chloroform (CH_3Cl, 99 %), and sulfuric acid (H_2SO_4, 98 %) were procured from Radchem. Copper nitrate trihydrate ($Cu(NO_3)_2 \cdot 3H_2O$, 98%), microcrystalline cellulose (MCC, 11 wt %), cellulose acetate (CA, 39.3 % - 40.3 %), methylene blue (MB, 98%) and terephthalic acid (BDC, 99 %) were bought from Sigma-Aldrich.

4.3.2 Synthesis of 18 wt% CA-supported Cu-BDC/CNC

Cu-BDC MOF was synthesized using a previously reported procedure with modifications [35]. Initially, 1 g of terephthalic acid and 4 g of $Cu(NO_3)_2 \cdot 3H_2O$ were dissolved in a 2:1 ratio of DMF and ethanol mixture (50 mL:25 mL) and the mixture was stirred for 1 hour, followed by sonication for 30 minutes. The resulting solution was transferred to a Teflon-lined autoclave and kept in an oven at 120 ^oC, for 12 hours. The obtained solid product was washed with DMF and water, and vacuum dried at 80 ^oC, yielding powdered Cu-BDC MOF.

The preparation of the Cu-BDC/CNC composite was done by the addition of 0.1 g of Cu-BDC to 100 mL of distilled H_2O followed by stirring for 30 minutes then sonication for 30 minutes. In a separate reaction vessel, 0.1 g crystalline nanocellulose synthesized through H_2SO_4 hydrolysis [36], was added to 100 mL of distilled H_2O and stirred for 30 minutes. The CNC solution was added to the Cu-BDC mixture followed by stirring for 1 hour, then 30 minutes of sonication, to yield a homogeneous solution. The resulting solution was vacuum-dried at 70 ^oC overnight, yielding a powdered Cu-BDC/CNC composite.

CA-supported Cu-BDC/CNC adsorbent was synthesized by stirring 18 wt% Cu-BDC/CNC in DMF for 30 minutes followed by 30 minutes of sonication. In a separated reaction vessel, 4 g of CA was dissolved in 40 mL DMF and stirred overnight. The CA solution was degassed with N_2 gas for 12 hours. The CA solution (3.3 mL) was added to the Cu-BDC/CNC solution and the mixture was stirred and sonicated for 1 hour. The resulting mixture was drop-cast on a glass slide, submerged in a water bath to facilitate phase inversion for 4 hours. The resulting film was air-dried to yield CA-supported Cu-BDC/CNC adsorbent film.

4.3.3 Adsorption of MB by CA-supported Cu-BDC/CNC film

The adsorption process was conducted using batch experiments. The CA-supported Cu-BDC/CNC adsorbent mats of dimensions 7 mm x 15 mm (3 mg) were immersed in 3 mL MB solutions with initial concentrations ranging from 1 mg/L to 6 mg/L which were agitated in a bath shaker for 6 hours. The varied parameters also include contact time, solution pH, and solution temperature. The MB removal percentage was calculated using equation (4.1), and the equilibrium adsorption capacity, q_e, was calculated using equation (4.2):

$$\%\ MB\ Removal\ = \frac{C_i - C_e}{C_i} \times 100 \qquad (4.1)$$

$$q_e = \frac{C_i - C_e}{m} \times V \qquad (4.2)$$

where C_i is the initial concentration of MB solution (mg/L), C_e is the equilibrium concentration of MB solution (mg/L), q_e is the equilibrium adsorption capacity (mg/g), V is the volume of the solution (L), and m is the mass of the adsorbent (g).

Reusability experiments were conducted such that after each adsorption cycle, the adsorbent film was removed from the MB solution, placed in 10 mL methanol, and shaken for 4 hours to desorb the MB dye. The film was then taken out and air-dried for 1 hour and ready for the next adsorption cycle.

4.3.4 Adsorption isotherms

Adsorption isotherms are used to describe the interactions between the adsorbent and the adsorbates. The data acquired from the adsorption process in this study was expressed using Langmuir and Freundlich isotherms. Langmuir isotherm assumes the adsorption process follows a monolayer coverage on a homogeneous adsorption surface, whereas Freundlich isotherm assumes adsorption follows multilayer coverage on a heterogeneous surface. The two isotherms were used to model the adsorption process using their linearised equations, equations (4.3) and (4.4)

$$\frac{1}{q_e} = \frac{1}{K_L q_{max}} X \frac{1}{C_e} + \frac{1}{q_{max}} \quad (4.3)$$

$$log(q_e) = log(K_F) + (\frac{1}{n}) log(C_e) \quad (4.4)$$

where q_{max} is the maximum adsorption capacity of the adsorbent (mg/g), and K_L is a Langmuir constant related to adsorption energy. When K_L is high, the interaction between the adsorbent and adsorbate is strong. K_F is the Freundlich isotherm constant. The heterogeneity factor, $\frac{1}{n}$ is a function of the strength of the adsorption process. Normal adsorption occurs when $0 < \frac{1}{n} < 1$ and when $\frac{1}{n} > 1$, cooperative adsorption is taking place. R_L is the separation factor and is calculated using equation (4.5):

$$R_L = \frac{1}{1 + K_L C_i} \quad (4.5)$$

where C_i is the initial adsorbate concentration. The adsorption process is unfavorable when $R_L > 1$ linear when $R_L = 1$, favorable when $0 < R_L < 1$ and irreversible when $R_L = 0$.

4.3.5 Adsorption kinetics

Kinetic studies are important as they assist in understanding adsorption Behaviour and mechanisms such as mass transfer and chemical reactions. In this work, the kinetic data obtained were analyzed using the pseudo-first-order and pseudo-second-order rate equations, represented by equation (4.6) and equation (4.7):

$$ln(q_e - q_t) = ln(q_e) - k_1 t \quad (4.6)$$

$$\frac{1}{q_t} = \frac{1}{k_2 q_e^2} + \frac{1}{q_e} t \quad (4.7)$$

where q_e is the equilibrium adsorption capacity, q_t is the adsorption capacity at time t, t is the contact time, k_1 is the first-order equilibrium constant, and k_2 is the second-order equilibrium constant. To investigate intraparticle diffusion, the experimental data was fitted to the Webber-Morris model using equation (4.8):

$$q_t = k_{id} t^{1/2} + I \quad (4.8)$$

where, k_{id} is the intraparticle diffusion rate constant (mg/g·min$^{-1/2}$), and I is the thickness of the boundary layer. The Bangham diffusion model was studied to investigate the adsorption mechanism using equation (4.9):

$$loglog\left(\frac{C_i}{C_i - q_t}\right) = log\left(\frac{k_b m}{2.303V}\right) + \alpha log(t) \quad (4.9)$$

where k_b and α are constants. The Boyd model, a pore diffusion model, was investigated to identify the rate-limiting step using equation (4.10):

$$B_t = -0.4977 - ln(1 - F) \quad (4.10)$$

where F represents the fraction of MB adsorbed at time t (min) determined by equation (4.11):

$$F = \frac{q_t}{q_e} \quad (4.11)$$

4.3.6 Statistical tests

To find the best model fit for the experimental data, a nonlinear chi-square (χ^2) statistical test was performed in addition to the correlation coefficient (R^2). When the model and experimental data closely match, the χ^2 value is low; when it is greater, there is a disagreement. Equation (4.12) was utilized in the computation of χ^2.

$$\chi^2 = \Sigma \frac{(q_e - q_{ecal})^2}{q_{ecal}} \quad (4.12)$$

From equation (4.12), q_e is the experimental equilibrium adsorption capacity and $q_{e,cal}$ is the model equilibrium adsorption capacity.

Characterization techniques

X-ray diffraction (XRD) was conducted on a Bruker D2 PHASER-e diffractometer using Cu-Kα radiation (0.15418 nm). Scanning electron microscopy (SEM) was conducted using a crossbeam 540 FEG SEM microscope from Zeiss. Energy-dispersive X-ray spectroscopy (EDX) was carried out on a crossbeam 540 FEG SEM microscope from Zeiss. UV-vis absorption measurements were carried out on a CARY 100 BIO UV-Vis spectrophotometer. FTIR spectroscopy was carried out using Brunker Alpha Fourier transform spectroscopy with platinum attenuated total reflectance (ATR) sampling accessory, 4 cm^{-1} resolution. Thermal gravimetric analysis was carried out using SDT Q600 V20.9 Build 20 Module DSC-TGA Standard. Brunauer–Emmett–Teller (BET) analysis. N_2 adsorption/desorption isotherms were obtained using the Autosorb iQ model:7, ASiQWin version 5.2x, at -196 °C, covering a relative pressure (P/P_o) range from 0 to 1.0. Before the measurement, the samples underwent pre-degassing at 130 °C for 18 hours under vacuum. The BET and Barrett–Joyner–Halenda (BJH) models were employed to determine the pore volume and surface area. X-ray photoelectron spectroscopy (XPS) was carried out on a Thermo model: ESCAlab 250Xi using monochromatic Al kα X-ray source.

4.4 Results and Discussion

4.4.1 Materials Characterisation

X-ray diffraction (XRD)

Figure 4.1 displays the XRD patterns of the synthesized materials. Figure 4.1a shows the reference diffraction pattern of Cu-BDC and figure 4.1b shows the synthesized Cu-BDC pattern, exhibiting peaks that correspond to those observed in the reference pattern [37]. The diffraction pattern of Cu-BDC aligns with prior studies, featuring peaks at 2-theta values at 8.5°, 10.5°, 12.4°, 17.3°, and 19.9°, confirming the successful formation of Cu-BDC [37–38]. The crystallite size of Cu-BDC was determined using the Scherrer equation, presented in Equation (4.13).

$$D = \frac{K\lambda}{\beta Cos\theta} \qquad (4.13)$$

From this equation, D is the crystallite size, K is the Scherrer constant with a value of 0.9, β is the full width at half maximum (FWHM), and θ is the peak position. The crystallite size was calculated to an average of 15.8 nm using peaks at 2θ positions 8.5º, 10.5º, 12.4º, 17.3º, 19.9º and 25º.

Figure 4.1c shows the diffraction pattern of CNC with peaks at 2θ values at 15.2°, 16.7°, 22.6°, and 34.4°, indexed as (110), (110), (102), (200), and (004) respectively. These indices are consistent with previous reports and match the JCPDS file number 03-0226, confirming the successful synthesis of CNC [39–40]. The XRD pattern of Cu-BDC/CNC (figure 4.1d), shows a combination of peaks from Cu-BDC and CNC, indicating the preservation of their respective structures in the composite material. Peaks corresponding to Cu-BDC are observed at 8.5°, 17.3°, and 25°, while those of CNC appear at 15.2° and 22.6°. This suggests that the crystal structures of both materials were retained during the formation of the composite. The XRD pattern of CA (figure 4.1e), showed no distinct peaks, indicative of its amorphous nature. Figure 4.1f shows the diffraction pattern of CA-supported Cu-BDC/CNC revealing several peaks from the composite with reduced sharpness and quality, indicating the successful preparation of the CA-supported Cu-BDC/CNC adsorbent film.

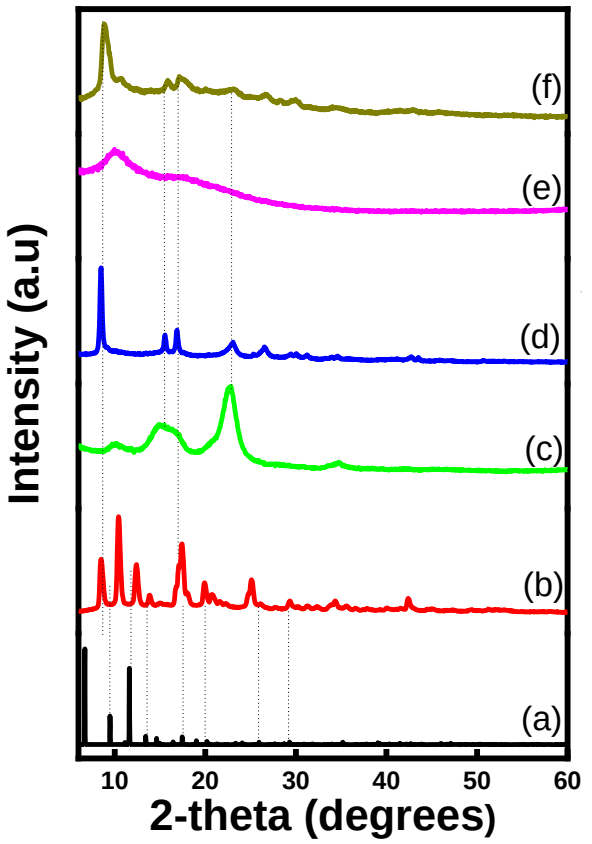

Figure 4.1: XRD patterns of (a) reference Cu-BDC, (b) Cu-BDC, (c) CNC, (d) Cu-BDC/CNC composite, (e) CA and (f) CA-supported Cu-BDC/CNC adsorbent film.

Fourier-transform infrared spectroscopy (FTIR)

The FTIR analysis of the prepared materials is presented in figure 2.2. The Cu-BDC MOF (figure 2.2a) exhibited characteristic peaks at 3600 cm^{-1}, 1640 cm^{-1}, 1500 cm^{-1}, 1390 cm^{-1}, and 1010 cm^{-1} corresponding to O–H stretching, C=O stretching, –C=O– stretching, C–C stretching, and C–O stretching vibrations, consistent with prior findings [37–38, 41]. Bands between 766 cm^{-1} and 663 cm^{-1} are attributed to the terephthalic acid ring, while bands at 730 cm^{-1} and 488 cm^{-1} arise from Cu–O bending and stretching, respectively.

The CNC spectrum shown in figure 2.2b was consistent with literature [36, 39–40]. A band at 3300 cm^{-1} represents the O–H stretching of hydroxyl groups on the CNC surface as well as adsorbed moisture. The band at 1634 cm^{-1} corresponds to C=O stretching within the molecule, and bands at 1430 cm^{-1}, 1374 cm^{-1}, 1313 cm^{-1}, and 1163 cm^{-1} correspond to CH_2 scissoring, C-H bending, CH_2 rocking, and anti-symmetrical bridge C-O stretching, respectively. The glycosidic C_1–H deformation within the ring, characteristic of glycosidic linkages between glucose molecules in cellulose, is represented by the band at 892 cm^{-1}.

The Cu-BDC/CNC spectrum (figure 2.2c) presents bands from both Cu-BDC and CNC, indicating successful composite synthesis and preservation of each material's structural integrity. Figure 2.2d illustrates the FTIR spectrum of CA, showing characteristic bands at 1738 cm^{-1}, 1370 cm^{-1}, 1232 cm^{-1}, and 1049 cm^{-1}, corresponding to C=O stretching, C-H vibration, C-O stretching, and C-O stretching vibration, respectively.

Figure 2.2e shows the spectrum of the adsorbent, CA-supported Cu-BDC/CNC, with main bands arising from CA. These bands appear shifted, likely due to hydrogen bonding between the CA substrate and the Cu-BDC/CNC composite. The band at 1736 cm^{-1} for the CA substrate is shifted to 1738 cm^{-1} for the adsorbent film. Similar findings have been reported previously [42 – 44].

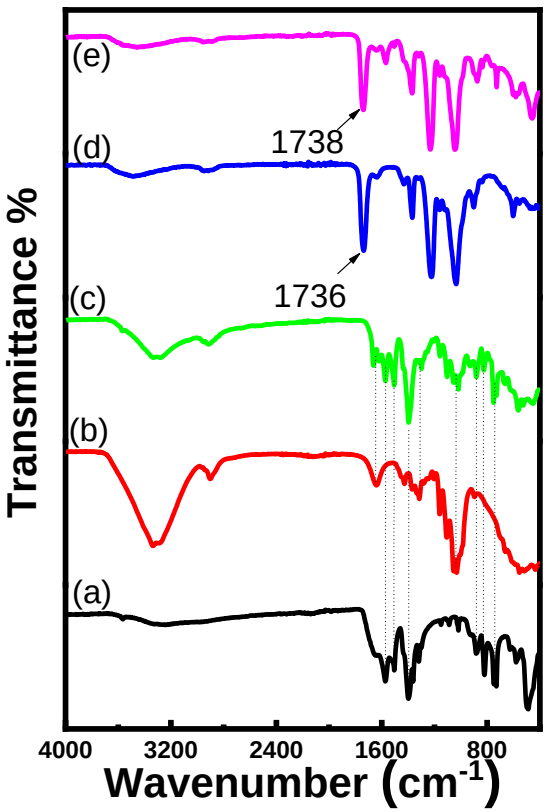

Figure 4.2: FTIR spectra of (a) Cu-BDC MOF, (b) CNC, (c) Cu-BDC/CNC composite, (d) CA, and (e) CA-supported Cu-BDC/CNC adsorbent film.

Scanning electron microscopy (SEM)

Figure 4.3a shows Cu-BDC as well-defined spherical particles with diameters between 500 nm – 900 nm. The walls of the MOF spheres are composed of closely packed Cu-BDC nanoparticles. Spherical morphology has been previously reported for Cu-BDC [45 – 46]. The SEM image of CNC (figure 4.3b) depicts the material with nanowhisker morphology similar to previous reports [39 – 40]. The nanowhiskers have diameters between 2 nm and 20 nm, and lengths of 100 nm to 500 nm. The SEM micrograph of the Cu-BDC/CNC composite, figure 4.3c, displays clustered Cu-BDC nanoparticles on the CNC nanowhiskers. Surface and cross-section micrographs of CA-supported Cu-BDC/CNC are shown in figure 4.3d and figure 4.3e, respectively. The surface of the adsorbent film is a flat highly porous sheet with pore channels running through the cross-section. The pore sizes range between 200 nm and 1 μm. The EDX spectrum of the adsorbent is shown in figure 4.3f with copper and oxygen detected on the material.

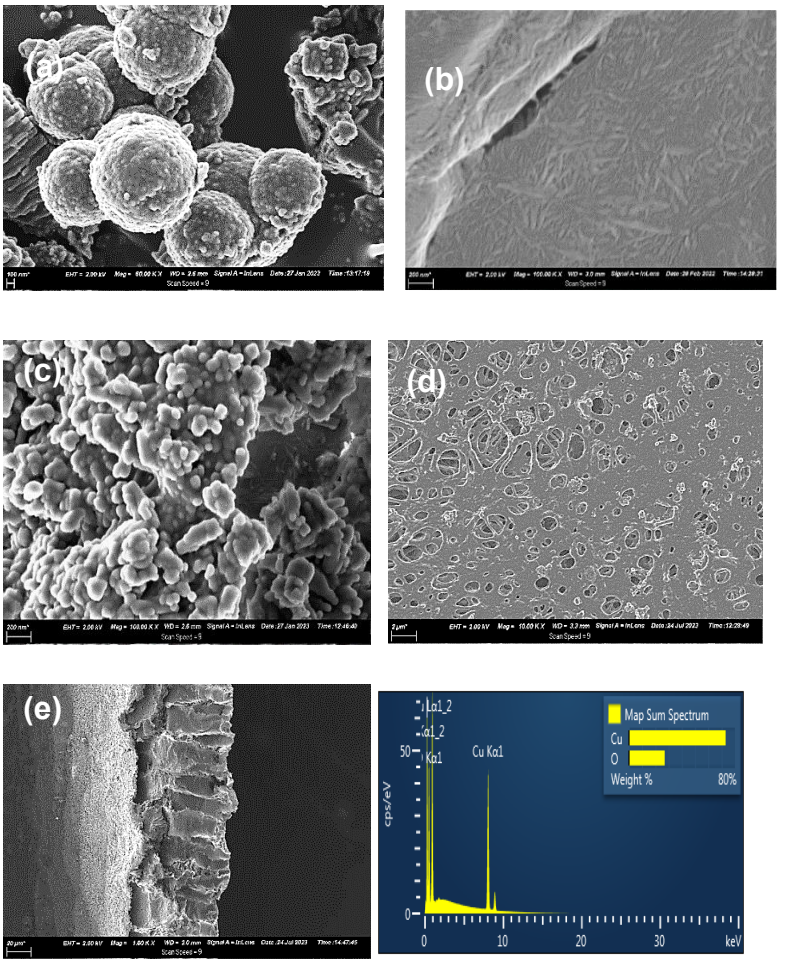

Figure 4.3: SEM images of a) Cu-BDC MOF, b) CNC, c) Cu-BDC/CNC composite, (d) surface of CA-supported Cu-BDC/CNC film, and (e) the cross-section of CA-supported Cu-BDC/CNC. (f) EDX spectrum of CA-supported Cu-BDC/CNC.

Thermal Gravimetric Analysis (TGA)

Figure 4.4 shows the thermal properties of the synthesized materials. All the materials experienced a weight loss at 100 ºC, due to adsorbed moisture. The loss of adsorbed DMF occurred between 170 ºC - 260 ºC. The 43 % weight loss for Cu-BDC (figure 4.4a) between 260 ºC - 390 ºC corresponds to the decomposition of the BDC organic linker collapsing the metal-organic framework and leaving behind Cu metal at temperatures above 390 ºC, which constitutes 49 % of the MOF. Figure 4.4b shows the CNC TGA curve which is characterized by further weight loss between 260 ºC - 320 ºC owing to the pyrolysis of cellulose and hemicellulose. The weight loss between 320 ºC and 340 ºC is due to the breakdown of intermediates until the complete degradation of CNC. The Cu-BDC/CNC composite (figure 4.4c) experienced a further weight loss of 50 % at 360 ºC due to the degradation of the organic components. Above 440 ºC, 32 % of the

total mass of the composite was maintained, which was the Cu metal. Thermal degradation observed for the adsorbent film between 330 ^{o}C - 390 ^{o}C (figure 4.4d) shows the decomposition of cellulose, resulting in the formation of intermediates. These intermediates were further broken down as the temperature increased to 520 ^{o}C, leaving behind copper which constitutes 6 % of the adsorbent film.

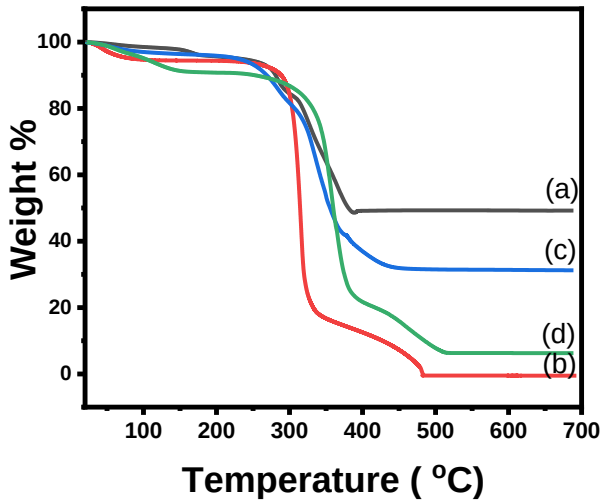

Figure 4.4: TGA plots of (a) Cu-BDC, (b) CNC, (c) Cu-BDC/CNC, and (d) CA-supported Cu-BDC/CNC.

Brunauer-Emmett-Teller (BET) and X-ray photoelectron spectroscopy (XPS)

Figure 4.5 shows the adsorbent film exhibits a type I adsorption/desorption isotherm, suggesting a uniform pore structure, characteristic of microporous material. The reversible adsorption process, as evidenced by the mirroring adsorption and desorption curves, further supports this conclusion. The BET surface area for the adsorbent film was measured at 19.99 m²/g, significantly lower than that of Cu-BDC MOF. This decrease is due to composite formation, where CNC nanowhiskers may obstruct the pores of the MOF, compounded by the embedding of the composite in the polymeric matrix of CA [47]. Consequently, the adsorption capacity of the adsorbent film is anticipated to be low. The determined pore diameter of 1.75 nm confirms the microporous nature of the adsorbent film, with pore diameters below 2 nm. Additionally, the pore volume of 0.22 cm³/g reflects the total pore volume per gram of the sample.

Figure 4.6 presents the XPS analysis of the adsorbent film, which is crucial for gaining insights into its surface elemental composition and chemical bonding states. In figure 4.6a, the presence of oxygen (O) and carbon (C) atoms on the film's surface is evident. The deconvolution of the carbon peak is shown in figure 4.6b, revealing five peaks attributed to sp^3-hybridized C-C, C-O, and C=O bonds, detected at 281.9, 283.7, 285.2, 286.3 eV, respectively. This deconvolution confirms the presence of the ester group characteristic of CA, indicated by the C-O and C=O bonds. Figure 4.6c shows the deconvolution of oxygen, demonstrating three peaks at 530.9, 530.0, and 529.1 eV, assigned to C=O, C-O, and O-H bonds, respectively.

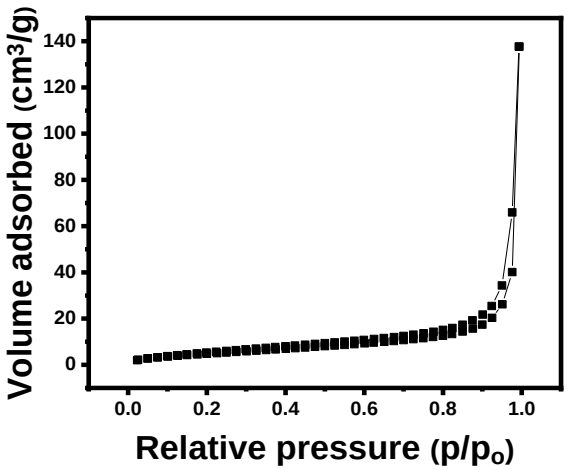

Figure 4.5: N_2 adsorption/desorption isotherm for CA-supported Cu-BDC/CNC film.

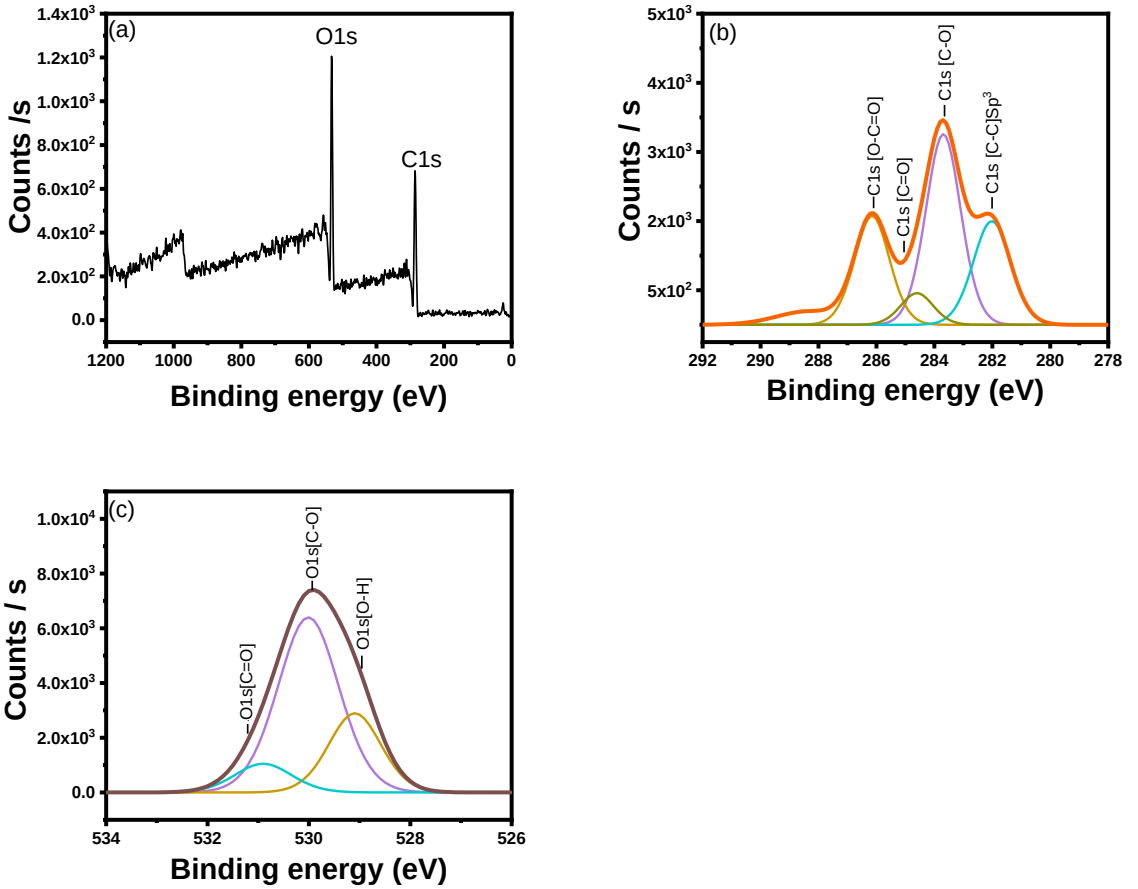

Figure 4.6: (a) XPS survey of the CA-supported MOF-5/CNC. High-resolution XPS spectra of (b) C1s and (c) O1s.

Point of zero charge (pH_{pzc})

The pH at which the adsorbent film's net surface charge is zero, the point of zero charge (pH_{pzc}), was determined. Figure 4.7 plots ΔpH vs. pH_i for the adsorbent. The data point indicates that the film's pH_{pzc} is 7.0 meaning that at acidic pH, the adsorbent film's surface has a net positive charge, and in alkaline pH, a net negative charge. At extreme pH values (pH=1 and pH=13) there is no change in pH because at these levels there are more H^+ or OH^- ions, respectively, in the solution and the adsorbent film does not influence the acidity/alkalinity of the solution.

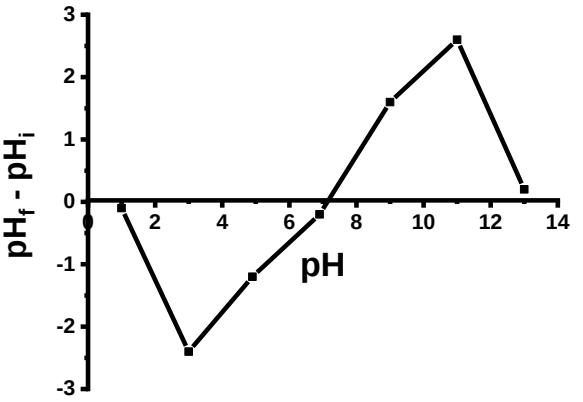

Figure 4.7: Plot of pH_f – pH_i vs pH_i

4.4.2 Adsorption studies

Effect of solution pH

Figure 4.8a and figure 4.8b show the effect of pH on equilibrium adsorption capacity (q_e) and % MB removal, respectively, at an initial concentration of 6 mg/L. The degree of electrostatic charges on the adsorbent film surface changes at different pH conditions. The adsorption capacity increases with an increase in pH, from 0.07 mg/g to 3.60 mg/g, as pH increases from 1 to 11, with the highest adsorption efficiency observed at pH 11. MB % removal increased to 60 %, as pH was increased to 11. At acidic pH, the surface of the adsorbent film is positively charged, this impedes the adsorption of cationic MB dye which is electrostatically repelled by the cationic surface of the adsorbent. Adsorption efficiency was enhanced when the solution pH was alkaline due to electrostatic attraction between the negatively charged surface of the adsorbent and the cationic MB dye. This makes the adsorbent capable of adsorbing either cations or anions, depending on the solution pH. In this work, the highest adsorption efficiency occurred at pH 11.

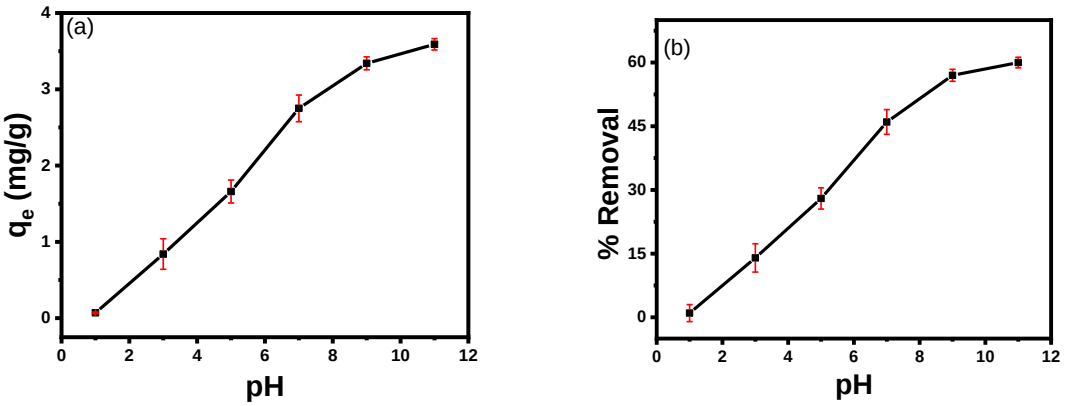

Figure 4.8: The effect of solution pH on a) equilibrium adsorption capacity and (b) % MB removal efficiency.

Effect of contact time

Figure 4.9 demonstrates the effect of contact time on MB adsorption capacity and % removal. The adsorption process takes place in three phases. The first phase occurs during the first 2 hours of the adsorption process and is characterized by a rapid increase in adsorption capacity owing to the availability of the maximum amount of adsorption active sites as well as the maximum amount of MB species in the bulk solution. The second phase occurs between 2 hours – 4 hours. At this stage, the adsorption rate gradually slows down as fewer adsorption active sites are available for adsorption. The last phase is observed between 5 hours – 6 hours as indicated by minimal change in adsorption efficiency. This occurs because equilibrium has been reached. The maximum adsorption capacity occurring at equilibrium at pH 11 is 3.60 mg/g and it corresponds to 84 % MB removal.

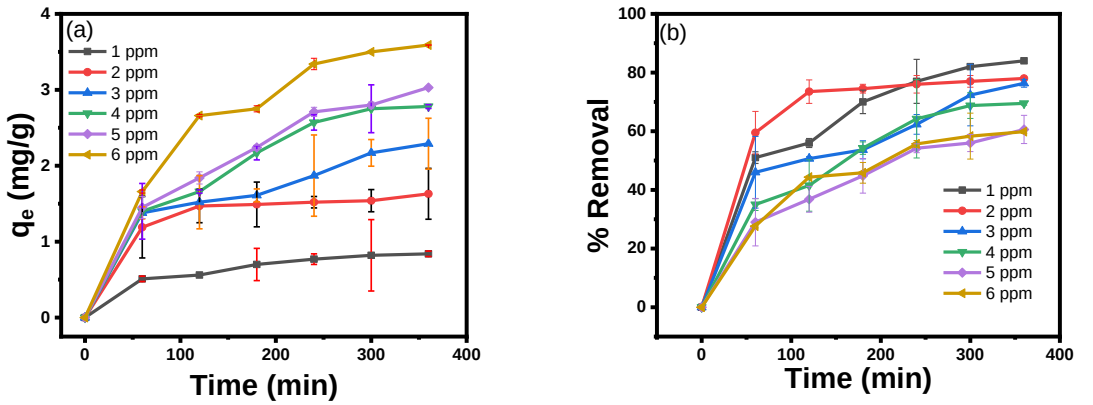

Figure 4.9: The effect of contact time on (a) qe and (b) % MB removal.

Effect of initial concentration

The effect of initial concentration on the adsorption process was investigated under optimum conditions as shown in figure 4.10. Figure 4.10a illustrates the equilibrium adsorption capacity (q_e) experiences a linear increase, from 0.84 mg/g to 3.60 mg/g, with increasing initial concentration. Conversely, as depicted in figure 4.10b, the % MB removal decreases from 84% to 59%. The increased adsorption of methylene blue at higher initial concentrations was attributed to mass transfer effects. However, under these conditions, the saturation of active sites leads to a reduction in percentage removal. Based on these findings, an initial concentration of 6 mg/L was identified as the optimal concentration.

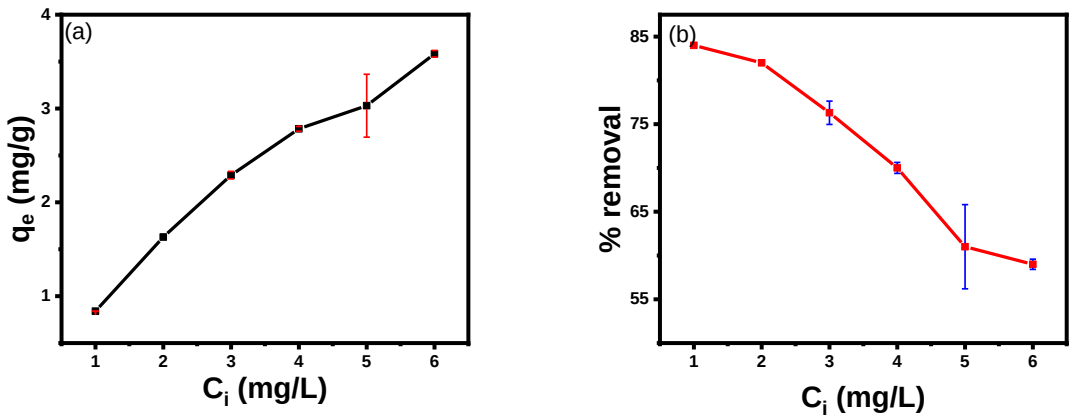

Figure 4.10: The effect of initial concentration on (a) equilibrium adsorption capacity and (b) % MB removal.

The effect of temperature on adsorption

Temperature is a significant factor in the adsorption process. The effect of temperature on q_e and % MB removal is shown in figure 4.11. A decrease in q_e from 3.60 mg/g to 3.01 mg/g was observed in figure 4.11a and a decrease from 60 % to 50 % was observed when the temperature was increased from 298 K to 318 K, as shown in figure 4.11b. This shows that the adsorption process is exothermic as confirmed under thermodynamics studies.

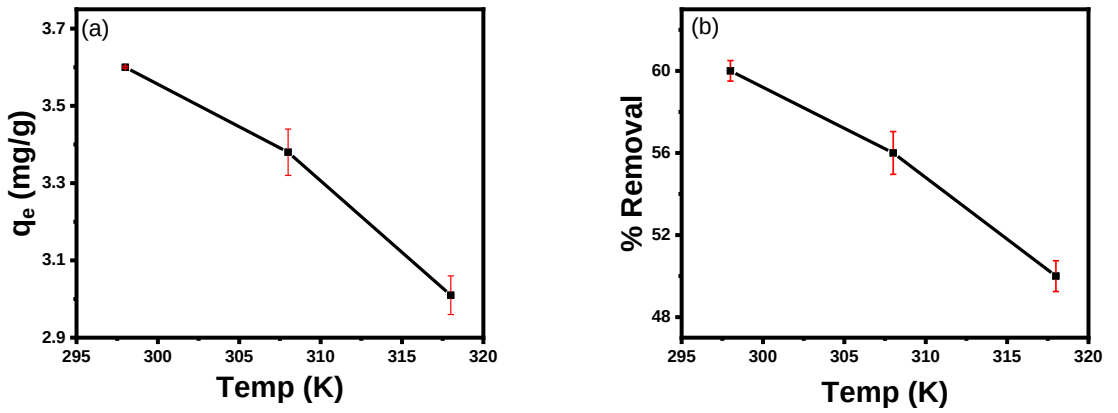

Figure 4.11: Effect of temperature on (a) equilibrium adsorption capacity and (b) % MB removal.

Adsorption isotherms

Adsorption isotherms describe the adsorption process and investigate adsorption mechanisms. The Langmuir and Freundlich adsorption isotherm models were employed to determine the adsorption parameters governing the adsorption process. Figure 4.12 displays the linear plots, and table 4.1 presents the derived parameters with correlation coefficients (R^2) and nonlinear chi-square (χ^2) values. The Langmuir isotherm model, shown in figure 4.12a, operates on the assumption of a homogeneous surface of the adsorbent, where maximum adsorption occurs upon achieving monolayer coverage [48]. The isotherm exhibited an R^2 value of 0.9972 and a χ^2 value of 0.021. The Langmuir constant, K_L, which is dimensionless, signifies the affinity between the adsorbent and the adsorbate. In this study, the K_L value was 0.40, indicating a relatively strong interaction between the adsorbate and the adsorbent surface, implying a favorable adsorption process. The calculated maximum adsorption capacity, q_{max}, was 4.34 mg/g vs the experimentally obtained q_e of 3.60 mg/g. The separation factors, R_L, observed across all initial concentration values (figure 4.12c), ranged between 0 and 1, signifying a favorable adsorption process.

The Freundlich isotherm model, figure 4.12b, assumes adsorption takes place on heterogeneous active sites with varying surface energies and follows a multilayer coverage. The isotherm displayed an R^2 value of 0.9572 and a χ^2 value of 0.045. From this curve, the heterogeneity factor, 1/n, ranged between 0 and 1, indicating favorable adsorption. The Freundlich constant, K_F, was determined to be 2.4. The adsorption capacity measured from the Freundlich isotherm was calculated to be 3.71 mg/g, calculated from the non-linearised form of the Freundlich isotherm. The adsorption process showed a better fit to the Langmuir isotherm model because its R^2 value

is closer to 1 and its calculated q_{max} is comparable to the experimental q_e, meaning adsorption of MB on the surface of CA-supported Cu-BDC/CNC may be a monolayer coverage.

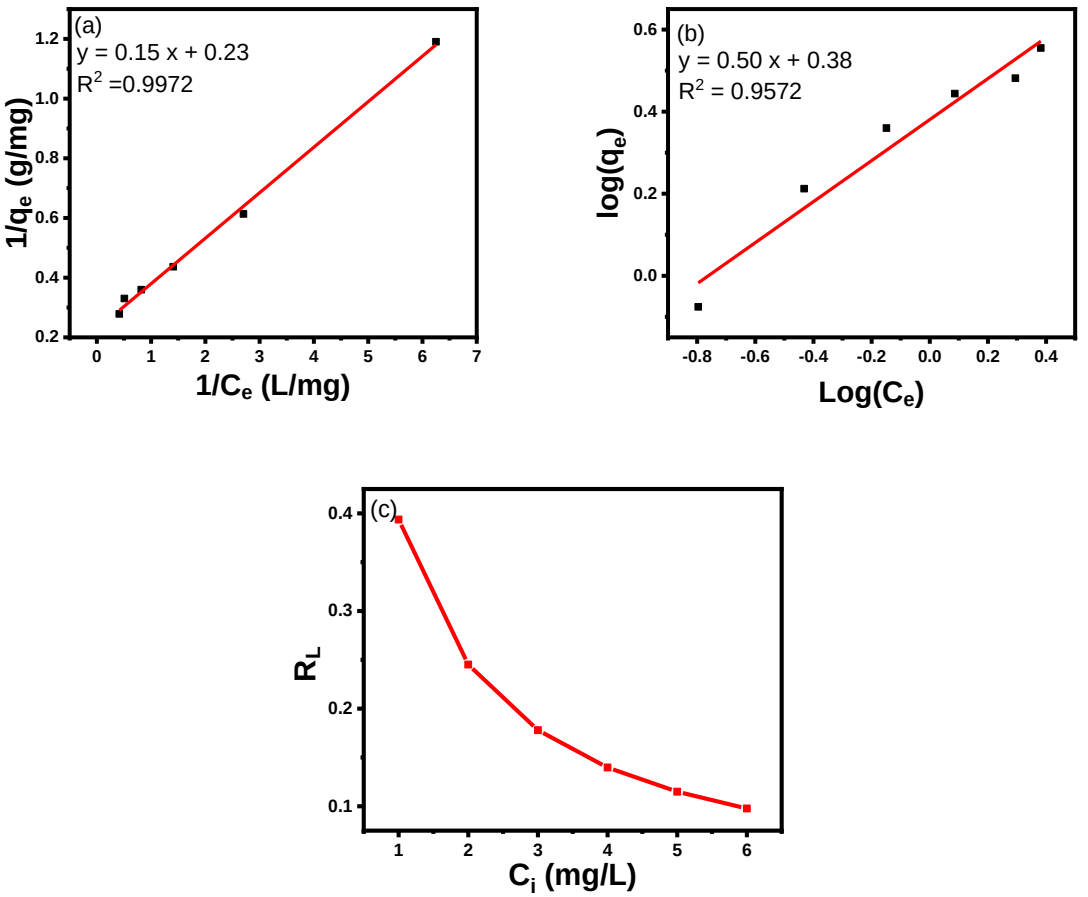

Figure 4.12: Langmuir and (b) Freundlich isotherm for the adsorption of MB by CA-supported Cu-BDC/CNC. (c) R_L values for all initial concentrations.

Adsorption kinetics

Kinetic studies were carried out to determine the primary step governing the rate and adsorption mechanism. The experimental data was analyzed using pseudo-first order and pseudo-second order kinetic models, shown in figures 13a and 13b respectively. The parameters and correlation coefficients are shown in table 1. Notably, the pseudo-second-order kinetic model exhibited a superior fit to the experimental data as indicated by the higher R^2 value of 0.9879 compared to the R^2 value of 0.9003 for the pseudo-first-order kinetic model. Furthermore, the pseudo-second-order

model yielded a q_e value of 4.34 mg/g, which is closer to the experimentally obtained q_e value of 3.60 mg/g, in contrast to the 8.33 mg/g calculated for the pseudo-first-order kinetic model. Since the experimental data fits the pseudo-second kinetic model better than the pseudo-first-order model, it indicates that the adsorption process is most likely controlled by chemical interactions between the adsorbate and adsorbent, such as chemisorption [49]. Kinetic studies can only explain the interactions between solute and surface during adsorption processes, but they cannot explain the diffusion mechanism between solutes and particles, hence this study used the Weber-Morris intraparticle diffusion model, Bangham model, and Boyd model to study the diffusion models and their plots are shown in figure 4.13c-e, respectively, and their parameters listed in table 4.1.

The diffusion models are useful in establishing the rate-limiting step. The Weber-Morris plot displays a straight line that has an $R^2 > 0.9$ and its $\chi^2 < 0.05$. The curve does not pass through the origin and has a y-intercept, C, value of 0.55, which is a reflection of the boundary layer, meaning that the intraparticle diffusion step is not the only rate-determining step and the external diffusion additionally controls the rate-determining step [50 – 51]. The Bangham model has a better correlation with the experimental data as its $R^2 > 0.9$ and its $\chi^2 < 0.05$, indicating that diffusion of MB in the pores of the adsorbent film contributes to the rate-limiting step [52]. The Boyd model displayed a graph that had 2 segments between t = 60 – 180 and t = 240 – 300 minutes. Both curves are not passing through the origin, indicating that film diffusion is involved in the adsorption mechanism. The first curve has an intercept closer to 0, meaning that within that period in the adsorption process, the pore diffusion mechanism may be the dominating step, and during the period of the second segment, the dominating mechanism may be film diffusion [53].

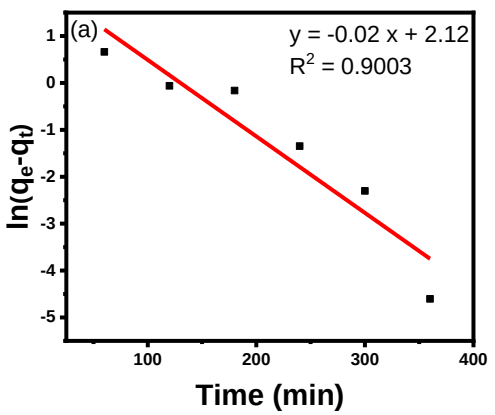

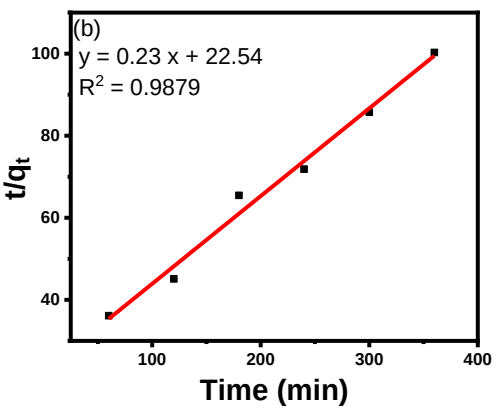

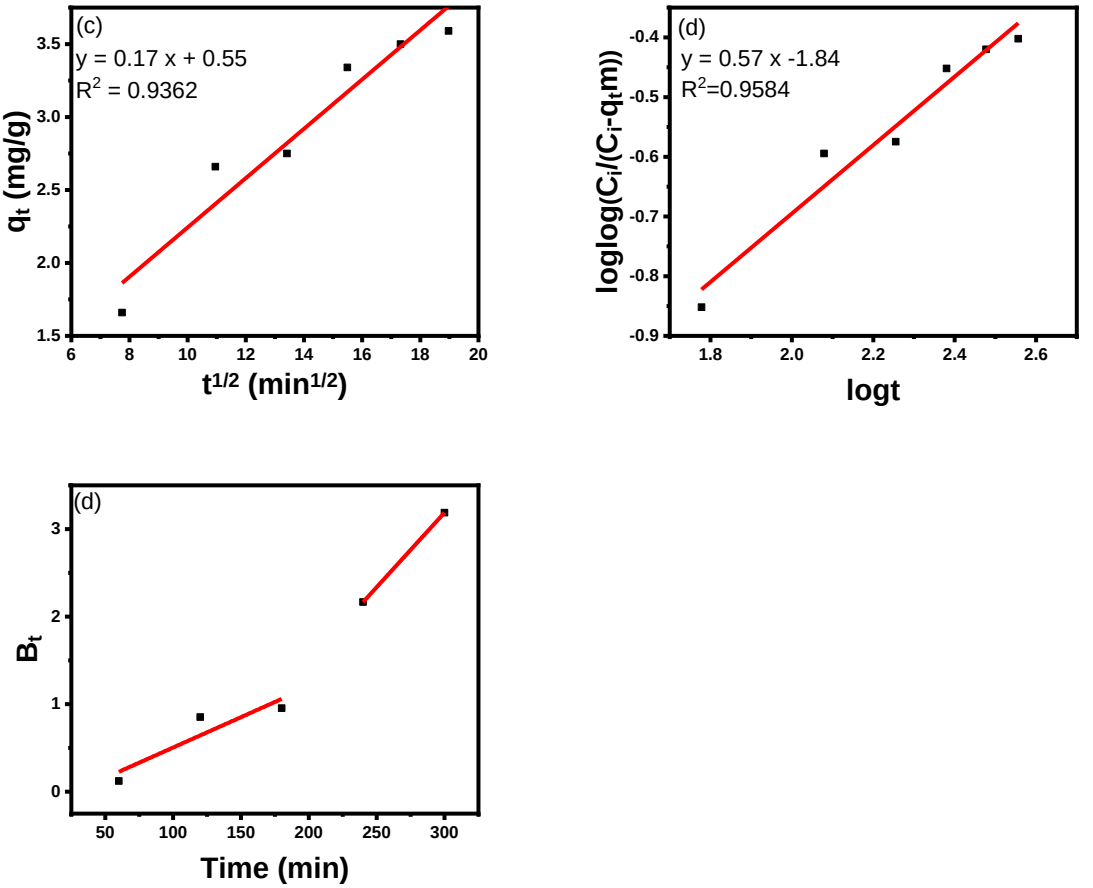

Figure 4.13: (a) Pseudo-first order, (b) pseudo-second order, (c) intraparticle (d) pore diffusion, and (e) Boyd model plots for the adsorption process.

Table 4.1: Parameters of pseudo-first order and pseudo-second order kinetic models for the adsorption of MB by CA-supported Cu-BDC/CNC.

Langmuir	**Freundlich**	**Pseudo first-order**	**Pseudo second order**	**Intraparticle diffusion model**	**Bangham Model**	**Pore diffusion**
q_{max} (mg/g) 4.34	q_e (mg/g) 3.72	q_e (mg/g) 8.33	q_e (mg/g) 4.34	k_{id} 0.17	K_B 0.10	1st segment slope 0.007 2nd segment slope 0.017
K_L (L/mg) 0.40	K_F (mg/g) 2.4	k_1 0.00005	k_2 0.0024	C 0.55		1st Intercept -0.19
R^2 0.9972	R^2 0.9572	R^2 0.9003	R^2 0.9879	R^2 0.9362	R^2 0.9584	2nd Intercept -1.92
X^2 0.021	X^2 0.045	X^2 0.025	X^2 0.020	X^2 0.042	X^2 0.036	

Adsorption thermodynamics

The Arrhenius equation was employed to understand the nature of the adsorption process, and it is expressed as equation (4.14):

$$ln\, k = lnA\ - \frac{E_a}{RT} \qquad (4.14)$$

were k is the rate constant, A the Arrhenius factor, E_a is the activation energy for the adsorption process, and it indicates the nature of the adsorption process between MB and the adsorbent film, R is the gas constant (8.314 J/K.mol), and T is the temperature in Kelvin. Activation energies for physisorption typically fall within the range of 5-40 kJ/mol, while for chemisorption, they range

between 40-800 kJ/mol. The slope of figure 4.14 was used to calculate the activation energy (E_a) and was determined to be 42.3 kJ/mol for the adsorption of methylene blue (MB) on the adsorbent film, suggesting chemisorption. This further verifies the kinetic studies as they indicated that the adsorption process occurs *via* chemisorption.

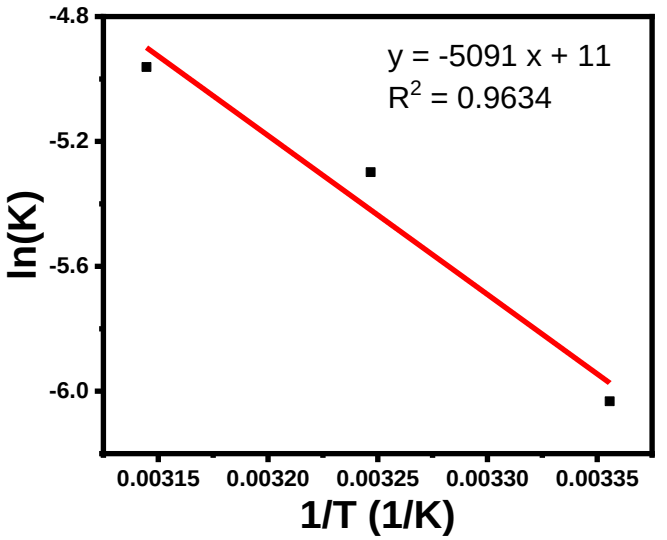

Figure 4.14: Plot of lnk vs T^{-1}: for the estimation of activation energy, E_a.

Thermodynamic parameters, encompassing standard entropy (ΔS°), standard enthalpy (ΔH°), and standard free energy (ΔG°), were calculated to evaluate the thermal characteristics of MB adsorption on the adsorbent film. ΔS° and ΔH° were derived from the van't Hoff plot, as illustrated in figure 4.15, using equation (4.15).

$$lnK_L = \frac{\Delta S^\circ}{R} - \frac{\Delta H^\circ}{RT} \qquad (4.15)$$

ΔG° was determined using equation (4.16):

$$\Delta G^\circ = -RT\ lnK_L \qquad (4.16)$$

Table 4.2 shows the thermodynamic parameters obtained from figure 4.15. As the temperature increased, the ΔG^o values became less negative, suggesting saturation on the adsorbent surface at elevated temperatures. The overall negative values of ΔG^o imply that the adsorption process is feasible. Nonetheless, the process remained thermodynamically spontaneous at higher temperatures. The negative value of ΔH^o indicates that the adsorption process is exothermic. The

ΔS^o was recorded to be negative suggesting a high degree of order at the interface between MB and CA-supported Cu-BDC/CNC.

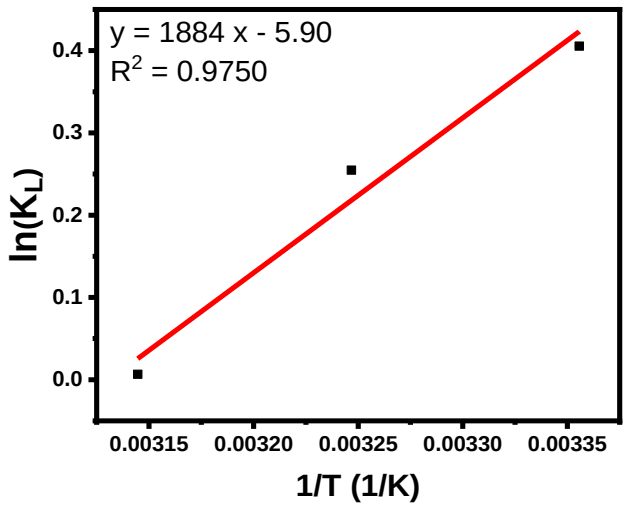

Figure 4.15: Van Hoff plot illustrating the thermodynamics of adsorption of MB on CA-supported Cu-BDC/CNC from water.

Table 4.2: Thermodynamic parameters for adsorption of MB by CA-supported Cu-BDC from water.

T/K	**Δ Gº (kJ/mol)**	**Δ Hº (kJ/mol)**	**Δ Sº (J/K.mol^{-1})**	**E_a (kJ/mol)**
298	-1.00	-15.66	-49.05	42.3
308	-0.65			
318	-0.02			

Proposed adsorption mechanism

The manner in which MB molecules interact with CA-supported Cu-BDC/CNC can be explained using figure 4.16. Functional groups present on the adsorbent film ensure intermolecular interactions with dye molecules. The proposed adsorption mechanism of MB onto the adsorbent surface operates through multiple pathways. FTIR analysis revealed hydroxyl and carbonyl groups on the adsorbent film, capable of electrostatic interaction with MB. These interactions include ion-dipole forces, dipole-dipole interactions, hydrogen bonding, and $\pi - \pi$ interactions, similar to

mechanisms proposed in existing literature for MB adsorption [54]. At a pH higher than the pH_{pzc}, the negatively charged adsorbent is electrostatically drawn to the cationic MB, facilitating adsorption. Furthermore, hydrogen atoms on the hydroxyl groups can engage in hydrogen bonding with nitrogen atoms from MB, as depicted in figure 4.16. The $\pi - \pi$ interactions may occur between the cellulose polymer chain and the aromatic ring of MB.

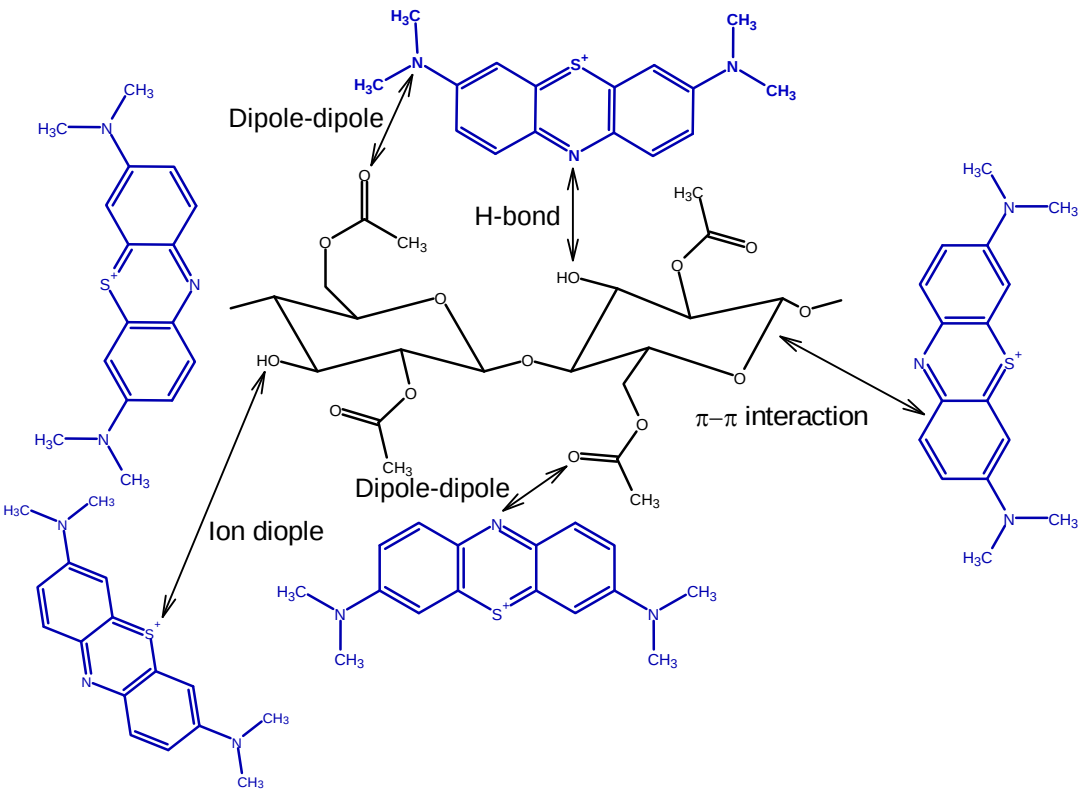

Figure 4.16: Adsorption mechanisms of CA-supported Cu-BDC/CNC to MB.

Reusability studies

The regeneration of an adsorbent is important in its practical applicability and its economic feasibility. The reusability of the CA-supported Cu-BDC/CNC adsorbent film was evaluated, and the results are shown in figure 4.17. The adsorption capability was observed to be reduced with an increase in the number of adsorption cycles. The adsorbent film was observed to be effective after five adsorption cycles, maintaining 73 % of the equilibrium adsorption capacity observed after the first cycle, which is a reduction from 3.6 mg/g to 2.64 mg/g. This decrease in the adsorption efficiency may occur due to the obstruction of the adsorbent's pores by the MB chemisorbed on the adsorbent film which may have not been completely desorbed during the washing process.

Overall, this study confirms that CA-supported Cu-BDC/CNC can be used multiple times for the adsorptive removal of MB from water.

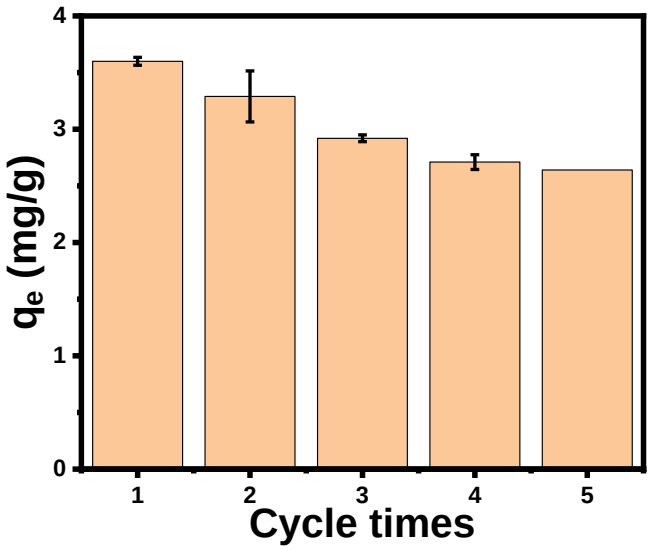

Figure 4.17: Reusability studies.

Simultaneous adsorption of methylene blue and methyl orange (MO) and treatment of industrial effluent

CA-supported Cu-BDC/CNC film was assessed for the simultaneous adsorption of MB and MO across varying pH. Figure 4.18 shows that at acidic pH, the adsorbent had a high affinity for anionic MO, whereas a high affinity for cationic MB is observed under alkaline conditions. This supports the pH_{pzc} observation studies, as it was established that under acidic conditions, the adsorbent film has a positive surface charge, making it have a high affinity for negatively charged species (such as MO), and under alkaline conditions, the adsorbent will have a net negative surface charge and will have a high preference for cationic species such as MB. This shows that the adsorbent film exhibits a pH-dependent selectivity of cationic and anionic species. At pH 3, the adsorbent film showed better adsorption for MO with a q_e of 2.65 mg/g while it was determined to be 1.70 mg/g for MB. At pH 11, a better adsorption for MB was observed with a q_e of 2.9 mg/g compared to 1.9 mg/g for MO. At neutral pH, the adsorbent exhibited good adsorption efficiency for both MB and MO, with q_e values of 2.2 mg/g and 2.49 mg/g, respectively, as the surface was neutral, and the adsorbent was not involved in selective electrostatic adsorption and no antagonistic effect during

simultaneous adsorption. This study showed that the adsorbent is versatile, and its surface can be tailored to be selectively attracted to a desired group of substances.

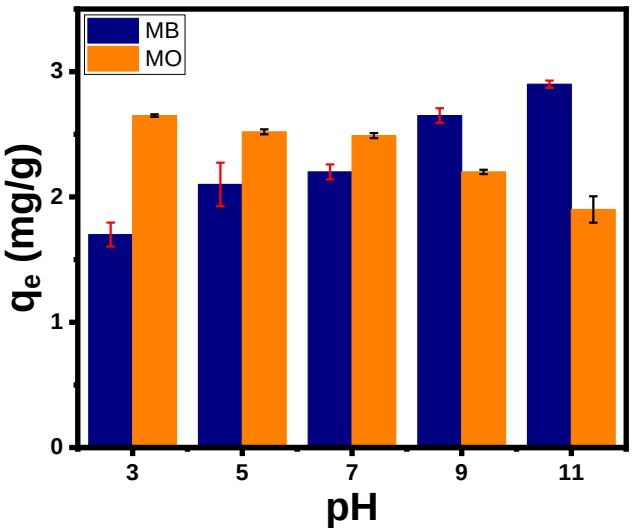

Figure 4.18: Simultaneous adsorption of MB and MO on CA-supported Cu-BDC/CNC adsorbent film.

The adsorbent was employed for the adsorptive remediation of real textile industry effluent to assess the adsorbent's practical applicability. Figure 4.19 shows the adsorption spectra of the effluent and it can be seen that 20 % of the textile dyes were removed. The dye wastewater contains a mixture of dyes that are competing for the same number of adsorption active sites on the adsorbent.

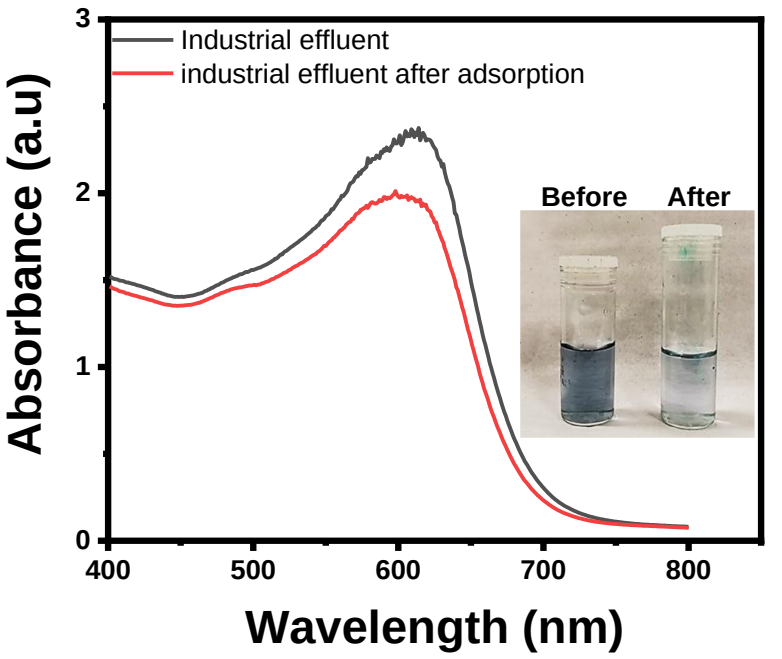

Figure 4.19: Adsorption of industrial MB solution by CA-supported Cu-BDC/CNC.

4.5 Economic assessment

The cost analysis was calculated using equation (4.17):

$$\text{Operation cost (OC)} \left(\frac{\text{USD}}{\text{m}^3}\right) = aC_{\text{energy}} + bC_{\text{chemicals}} \qquad (4.17)$$

where C_{energy} and $C_{chemicals}$ are the energy consumed (in kWh/m^3) and the chemical consumption (in kg/m^3) respectively. The symbol *a* represents the cost of electrical energy, which is USD 0.19 kWh for the South African market as of June 2024 and the symbol *b* denotes the price of the chemicals utilized in creating the adsorbent film material, measured in USD per kilogram (USD/kg) or per cubic meter (USD/m^3).

For each run of the adsorption process, the adsorbent treats 0.003 L of MB aqueous solution, however, the calculation of OC is based on the adsorbent treating 1 L of the MB solution. Furthermore, all the equipment used were calculated based on their power ratings in watts and their total operation duration. The cost of the adsorbent was calculated per kg.

Consequently, the total energy consumption amounted to 110.8 kilowatt-hours per cubic meter (kWh/m³), equivalent to USD 20.43 per cubic meter, while the overall chemical cost totaled USD 32.34 per cubic meter. Thus, the operating cost was calculated to be USD 52.77 per cubic meter.

4.6 Conclusions

This study focused on the solvothermal synthesis of CA-supported Cu-BDC/CNC film and its use as an adsorbent for the removal of MB from aqueous solutions. The adsorbent film was characterized as a semicrystalline flat porous sheet possessing pore channels through the cross-section, consisting of carbonyl and hydroxyl functional groups on its surface responsible for the adsorption of MB. The adsorption process followed the pseudo-second-order and the Langmuir isotherm models implying that MB adsorbs on the surface of the adsorbent to form a monolayer through chemisorption. The activation energy was determined to be 42.3 kJ/mol confirming that adsorption is taking place through chemisorption. The adsorption kinetics were used to determine the rate-determining step of the adsorption process. Electrostatic attractions were determined to be the primary adsorption mechanism. The adsorption was feasible, spontaneous, and exothermic, with the efficiency decreasing with increasing temperature. The maximum adsorption capacity and % MB removal were 3.60 mg/g and 84 %, respectively, at 25 °C, at an initial concentration of 6 mg/L, at pH 11, and at 18 wt% Cu-BDC loading. The adsorbent film showed a pH-dependent selectivity for cationic MB and anionic MO, indicating better adsorption of MO at acidic pH and better adsorption of MB at alkaline pH. Recyclability studies showed the adsorbent can be used multiple times, maintaining 73% of the adsorption efficiency after 5 cycles. The operation cost was calculated, and the adsorbent film was tested for the removal of dyes from industrial effluent. This study provides a new, recyclable, versatile, and cost-effective MOF-based adsorbent for the removal of organic dyes from aqueous solutions.

4.7 References

1. Oladoye, P. -O.; M. O. Bamigboye, O. D. Ogunbiyi, and M. T. Akano, “Toxicity and decontamination strategies of Congo red dye” *Groundw. Sustain. Dev.* 2022, DOI:10.1016/j.gsd.2022.100844.

2. Dalari, B.-L.-S.-K.; Giroletti, C.-L.; Malaret, F.-J.; Skoronski, E.; Hallett, J.-P.; Matias, W.-G.; Puerari, R.-G.; Nagel-Hassemer, M.-E. Application of a phosphonium-based ionic liquid for reactive textile dye removal: Extraction study and toxicological evaluation.” *J. Environ. Manage.* 2022, DOI:10.1016/j.jenvman.2021.114322.

3. Al-Tohamy, R.; Ali, S.-S.; Li, F.; Okasha, K.-M.; Mahmoud, Y.-A.-G.; Elsamahy, T.; Jiao, H.; Fu, Y.; Sun, J. A critical review on the treatment of dye-containing wastewater: Ecotoxicological and health concerns of textile dyes and possible remediation approaches for environmental safety. *Ecotoxicol. Environ. Saf.* 2022, DOI: 10.1016/j.ecoenv.2021.113160.

4. Lanjwani, M.-F.; Tuzen, M.; Khuhawar, M.-Y.; Saleh, T.-A. Trends in photocatalytic degradation of organic dye pollutants using nanoparticles: A review. *Inorg. Chem. Commun.* 2024, DOI: 10.1016/j.inoche.2023.111613.

5. Verma, N.; Chundawat, T.-S.; Chandra, H.; Vaya, D. An efficient time reductive photocatalytic degradation of carcinogenic dyes by TiO_2-GO nanocomposite. *Mater. Res. Bull*. 2023, DOI:10.1016/j.materresbull.2022.112043.

6. Jia, J.; Wu, H.; Xu, L.; Dong, F.; Jia, Y.; Liu, X. Removal of Acidic Organic Ionic Dyes from Water by Electrospinning a Polyacrylonitrile Composite MIL101(Fe)-NH_2 Nanofiber Membrane. *Molecules* 2022, DOI:10.3390/molecules27062035.

7. Uddin, M.-J.; Ampiaw, R.-E.; Lee, W. Adsorptive removal of dyes from wastewater using a metal-organic framework: A review. *Chemosphere*, 2021, DOI:10.1016/j.chemosphere.2021.131314.

8. Mohammed N.; Lian, H.; Islam, M.-S.; Strong, M.; Shi, Z.; Berry, R.-M.; Yu, H.; Tam, K.-C. Selective adsorption and separation of organic dyes using functionalized cellulose nanocrystals. *Chem. Eng. J.* 2021, DOI:10.1016/j.cej.2021.129237.

9. Ngoc, P.-K.; Mac, T.-K.; Nguyen, H.-T.; Viet, D.-T.; Thanh, T.-D.; Vinh, P.-V.; Phan, B.-T.;

Duong, A.-T.; Das, R. Excellent organic dye adsorption capacity and recyclability of hydrothermally synthesized α-Fe2O3 nanoplates and nanorices. *J. Sci. Adv. Mater. Devices* 2021, 6.

10. El-Bery, H.-M.; Saleh, M.; El-Gendy, R.-A.; Saleh, M.-R.; Thabet, S.M. High adsorption capacity of phenol and methylene blue using activated carbon derived from lignocellulosic agriculture wastes. *Sci. Rep.* 2022, 12.

11. Ngulube, R.; Pillay, L.; Nombona, N. Synthesis and characterization of electrospun composite nanofibers from Moringa oleifera biomass and metal oxide nanoparticles as potential adsorbents for the removal of lead ions. *Chem. Pap.* 2023, DOI: 10.1007/s11696-023-03115-5.

12. Vaddi, D.-R.; Malla, R.; Geddapu, S. Magnetic activated carbon: A promising approach for the removal of methylene blue from wastewater. *Desalin. Water Treat*. 2024, DOI:10.1016/j.dwt.2024.100146.

13. Kenawy, R.; Tenhu, H.; Khattab, S.-A.; Eldeeb, A.-A.; Azaam, M.-M. Highly efficient adsorbent material for removal of methylene blue dye based on functionalized polyacrylonitrile. *Eur. Polym. J.* 2022, DOI:10.1016/j.eurpolymj.2022.111138.

14. Pérez-Botella, E.; Valencia, S.; Rey, F. Zeolites in Adsorption Processes: State of the Art and Future Prospects. *Chem. Rev.* 2022, 122.

15. Tchinsa, A.; Hossain, M.-F.; Wang, T.; Zhou, Y. Removal of organic pollutants from aqueous solution using metal organic frameworks (MOFs)-based adsorbents: A review. *Chemosphere*, 2021, DOI:10.1016/j.chemosphere.2021.131393.

16. Beydaghdari, M.; Saboor, H.-F.; Babapoor, A.; Karve, V.-V.; Asgari, M. Recent Advances in MOF-Based Adsorbents for Dye Removal from the Aquatic Environment. *Energies* 2022, DOI:10.3390/en1506202.

17. Darabdhara J.; Ahmaruzzaman, M. Recent developments in MOF and MOF based composite as potential adsorbents for removal of aqueous environmental contaminants. *Chemosphere*, 2022, DOI: 10.1016/j.chemosphere.2022.135261.

18. Zadehahmadi. F.; Eden, N.-T.; Mahdavi, H.; Konstas, K.; Mardel, J.; Shaibani, M.; Banerjee, P.-C.; Hill. M.-R. Removal of metals from water using MOF-based composite adsorbents.

Environ. Sci. Water Res. Technol. 2023, 9.

19. Koppula, S.; Jagasia, P.; Babu, S.; Surya, M. MOF (M=Zr, Zn, Co)@COFs hybrid composite as a potential adsorbent for UO_2^{2+} and Methylene blue (MB) from solutions. *Mater. Today Commun.* 2023, DOI:10.1016/j.mtcomm.2023.105336.

20. Rivadeneira-Mendoza, B.-F.; Filho, O.-A.-E.; Fernández-Andrade, K.-J.; Curbelo, F.; Fred da Silva, F.; Luque, R.; Rodríguez-Díaz, J.-M. MOF@biomass hybrids: Trends on advanced functional materials for adsorption. *Environ. Res.* 2023, DOI:10.1016/j.envres.2022.114424.

21. Gebremariam, S.-K.; Dumée, L.-F.; Llewellyn, P.-L.; Alwahedi, Y.-F.; Karanikolos, G.-N. Metal-organic framework hybrid adsorbents for carbon capture - A review. *J. Environ. Chem. Eng.* 2023, DOI: 10.1016/j.jece.2023.109291.

22. Lee, H.; Lee, H.; Ahn, S.; Kim, J. MIL-100(Fe)-Hybridized Nanofibers for Adsorption and Visible Light Photocatalytic Degradation of Water Pollutants: Experimental and DFT Approach. *ACS Omega*, 2022, 7.

23. Poonia, K.; Patial, S.; Raizada, P.; Ahamad, T.; Parwaz, K.-A.-A.; Van, L.-Q.; Nguyen, V.-H.; Hussain, C.-M.; Singh, P. Recent advances in Metal Organic Framework (MOF)-based hierarchical composites for water treatment by adsorptional photocatalysis: A review. *Environ. Res*. 2023, DOI:10.1016/j.envres.2023.115349.

24. Lu, Y.; Liu, C.; Mei, C.; Sun, J.; Lee, J.; Wu, Q.; Hubbe, M.-A.; Li, M. Recent advances in metal organic framework and cellulose nanomaterial composites. *Coord. Chem. Rev.* 2022, DOI:10.1016/j.ccr.2022.214496.

25. Tu, K.; Ding, Y.; Keplinger, T. Review on design strategies and applications of metal-organic framework-cellulose composites. *Carbohydr. Polym.* 2022, DOI:10.1016/j.carbpol.2022.119539.

26. Zhang, X.-F.; Wang, Z.; Ding, M.; Feng, Y.; Yao, J. Advances in cellulose-metal organic framework composites: Preparation and applications. *J. Mater. Chem. A* 2021, 9.

27. Abdelhamid, H.-N.; Mathew, A.-P. Cellulose–metal organic frameworks (CelloMOFs) hybrid materials and their multifaceted Applications: A review. *Coord. Chem. Rev.* 2022, DOI:10.1016/j.ccr.2021.214263.

28. Zhou, J.; Song, M.; Hu, X.; Zhang, W.-X.; Deng, Z. Environmental applications of nanocellulose scaffolded metal organic frameworks (MOFs@NC). *Crit. Rev. Environ. Sci. Technol.* 2023, 53.

29. Hou, C.; Fu, L.; Wang, Y.; Chen, W.; Chen, F.; Zhang, S.; Wang. J. Core–shell magnetic Fe3O4/CNC@MOF composites with peroxidase-like activity for colorimetric detection of phenol. *Cellulose* 2021, 28.

30. S. Zhang, M. Zhao, H. Li, C. Hou, and M. Du, "Facile in situ synthesis of ZIF-67/cellulose hybrid membrane for activating peroxymonosulfate to degrade organic contaminants," *Cellulose*, vol. 28, no. 6, 2021, doi: 10.1007/s10570-021-03717-w.

31. Shahnaz, T.; Bedadeep, D.; Narayanasamy, S. Investigation of the adsorptive removal of methylene blue using modified nanocellulose. *Int. J. Biol. Macromol.* 2022, 200.

32. Xue, J.; Zhu, E.; Zhu, H.; Liu, D.; Cai, H.; Xiong, C.; Yang, Q.; Shi,Z. Dye adsorption performance of nanocellulose beads with different carboxyl group content. *Cellulose* 2023, 30.

33. Hamid Raza, Ibrahim Yildiz, Farhat Yasmeen, Khurram S. Munawar, Muhammad Ashfaq, Muzafar Abbas, Maqsood Ahmed, Hussein A. Younus, Shiguo Zhang, Nazir Ahmad, Synthesis of a 2D copper(II)-carboxylate framework having ultrafast adsorption of organic dyes, *Journal of Colloid and Interface Science*, 602, 2021.

34. Lin, C.; Guo, X.; Mo, F.; Sun, D. Different Dimensional Copper-Based Metal-Organic Frameworks with Enzyme-Mimetic Activity for Antibacterial Therapy. *Int. J. Mol. Sci.* 2023, DOI:10.3390/ijms24043173.

35. Nayak, A.; Viegas, S.; Dasari, H.; Sundarabal. N. Cu-BDC and Cu_2O Derived from Cu-BDC for the Removal and Oxidation of Asphaltenes: A Comparative Study. *ACS Omega* 2022 7.

36. Xiaoshan, Y.; Yu, J.; Qitang, W.; Zebin, W.; Xianke, L.; Yangmei. C. Preparation and Characterization of Cellulose Nanocrystal Extraction From Pennisetum hydridum Fertilized by Municipal Sewage Sludge via Sulfuric Acid Hydrolysis. *Front. Energy Res.* 2021, DOI:10.3389/fenrg.2021.774783.

37. Mao, J.; Qin, L.; Tian, L.; He, L.; Zhu, Y.; Meng, Q.; Zhang, G. Hierarchical N-Doped CuO/Cu Composites Derived from Dual-Ligand Metal-Organic Frameworks as Cost-

Effective Catalysts for Low-Temperature CO Oxidation. *ACS Omega* 2021, 6.

38. Huang, Y.; Fan, X.; Zhou, Y.; Liu, S.; Li, Y. In situ growth of Cu(BDC) on microscale Cu-based carboxymethylcellulose fibers: A new strategy for constructing efficient catalysts for A3-coupling reactions. *Appl. Organomet. Chem.* 2023, 37.

39. Zhang, L.; Jia, X.; Ai, Y.; Huang, R.; Qi, W.; He, Z.; Klemeš, J.-J.; Su, R. Greener production of cellulose nanocrystals: An optimised design and life cycle assessment. *J. Clean. Prod.* 2022, DOI:10.1016/j.jclepro.2022.131073.

40. Raza, M.; Abu-Jdayil, B.; Banat, F.; Al-Marzouqi, A.-H. Isolation and Characterization of Cellulose Nanocrystals from Date Palm Waste. *ACS Omega* 2022, 7.

41. Taheri, S.; Mollabagher, H.; Mousavi, S.-A.-H. Metal Organic Framework Cu-BDC as an Efficient and Reusable Catalyst for One-Pot Synthesis of Benzophenazine Derivatives. *Polycycl. Aromat. Comp.* 2021, 42.

42. Azam, R.S.; Almasri, D.A.; Alfahel, R.; Hawari, A.H.; Hassan, M.K.; Elzatahry, A.A.; Mahmoud, K.A. MXene ($Ti_3C_2T_x$)/Cellulose Acetate Mixed-Matrix Membrane Enhances Fouling Resistance and Rejection in the Crossflow Filtration Process. *Membranes* 2022, 12, DOI:10.3390/membranes12040406.

43. Tahazadeh, S.; Karimi, H.; Mohammadi, T.; Emrooz, H.-B.-M.; Tofighy. M.-A. Fabrication of biodegradable cellulose acetate/MOF-derived porous carbon nanocomposite adsorbent for methylene blue removal from aqueous solutions. *J. Solid State Chem.* 2021, DOI:10.1016/j.jssc.2021.122180.

44. Hashemian, H.; Ghaedi, M.; Dashtian, K.; Mosleh, S.; Hajati, S.; Razmjoue, D.; Khan, S. Cellulose acetate/MOF film-based colorimetric ammonia sensor for non-destructive remote monitoring of meat product spoilage. *Int. J. Biol. Macromol.* 2023, DOI:10.1016/j.ijbiomac.2023.126065.

45. Hamdalla, T.-A.; Alfadhli, S.; Khasim, S.; Darwish, A.-A.-A.; ElZaidia, E.-F.-M.; Al-Ghamdi, S.-A.; Aljohani, M.-M.; Mahmoud, M.-E.; Seleim. S.-M. Synthesis of novel Cu/Fe based benzene Dicarboxylate (BDC) metal organic frameworks and investigations into their optical and electrochemical properties. *Heliyon* 2024, DOI:1016/j.heliyon.2024.e25065.

46. Varmazyari, M.; Khani, Y.; Bahadoran, F.; Shariatinia, Z.; Soltanali, S. Hydrogen production employing Cu(BDC) metal–organic framework support in methanol steam reforming process within monolithic micro-reactors. *Int. J. Hydrogen Energ.* 2021, 46.

47. Eze, E.; Omer, A.-M.; Hassanin, A.-H. Eltaweil, A.-S.; El-Khouly, M.-E. Cellulose acetate nanofiber modified with polydopamine polymerized MOFs for efficient removal of noxious organic dyes. *Environ. Sci. Pollut. Res.* 2024, 31.

48. Assafi, A.; El Hadj Ali, Y.-A.; Almufarij, R.-S.; Hejji, L.; Raza, N.; Villarejo, L.-P.; Souhail, B.; Azzouz, A.; Abdelrahman, E.-A.; Rodríguez-Castellón, E. Ultrasound-assisted adsorption of organic dyes in real water samples using zirconium (IV)-based metal-organic frameworks UiO-66-NH_2 as an adsorbent. *Heliyon* 2023, DOI: 10.1016/j.heliyon.2023.e22001.

49. Dawei Guo, Jiabo Wu, Dongdong Feng, Yalong Zhang, Xishan Zhu, Zhen Luo, Yunkun Kang, Yijun Zhao, Shaozeng Sun, Mechanism of efficient magnetic biochar for typical aqueous organic contaminant combined-adsorption removal, *Fuel Processing Technology*, 247, 2023, DOI:10.1016/j.fuproc.2023.107795.

50. Wang, J.; Guo, X. Rethinking of the intraparticle diffusion adsorption kinetics model: Interpretation, solving methods and applications. *Chemosphere*. 2022, DOI: 10.1016/j.chemosphere.2022.136732.

51. Gulen, J.; Zorbay, F. Methylene Blue Adsorption on a Low Cost Adsorbent—Carbonized Peanut Shell. *Water Environ. Res.* 2017, DOI:10.2175/106143017X14902968254836.

52. Hashem, A.; Aniagor, C.-O.; Farag, S.; Fikry, M.; Aly, A.-A.; Amr, A. Evaluation of the adsorption capacity of surfactant-modified biomass in an aqueous acid blue 193 system. *Waste Management Bulletin* 2024, 2.

53. Siti, A.-S.; Foo, K.-Y. Sodium salt-assisted low temperature activation of bentonite for the adsorptive removal of methylene blue. *Sci. Rep*. 2022, DOI:10.1038/s41598-022-06254-z.

54 Khatri, M.; Ahmed, F.-E.; Al-Juboori, R.-A.; Khanzada, N.-K.; Hilal, N. Reusable environmentally friendly electrospun cellulose acetate/cellulose nanocrystals nanofibers for methylene blue removal. *J. Environ. Chem. Eng.* 2024, DOI:10.1016/j.jece.2023.111788.

CHAPTER 5

5.0 NI-BDC AND CRYSTALLINE NANOCELLULOSE-BASED ADSORBENT FILMS FOR METHYLENE BLUE REMOVAL

Lebogang Manamela and Nolwazi Nombona

University of Pretoria, Department of Chemistry, Private Bag X20, Hatfield 0028, Gauteng, South Africa

5.1 Abstract

Several industries pollute the environment by discharging organic dyes into waterbodies, which negatively affect humans, animals and plants. This study investigates the use of a solvothermally synthesized adsorbent film composed of a Ni-based metal-organic framework (MOF) and crystalline nanocellulose (CNC), supported on a cellulose acetate (CA) substrate (CA-supported Ni-BDC/CNC) for the adsorptive removal of methylene blue (MB) from aqueous solutions. The synthesis of the adsorbent film was verified using standard techniques such as X-ray diffraction (XRD), Fourier transform infrared spectroscopy (FTIR), scanning electron microscopy (SEM), energy dispersive X-ray (EDX), thermogravimetric analysis (TGA), Brunauer-Emmett-Teller (BET) analysis and X-ray photoelectron spectroscopy (XPS). A batch-type adsorption method was used, and the adsorbent achieved an equilibrium adsorption capacity (q_e) of 2.78 mg/g and an MB removal efficiency of 85 %. The adsorption results were better fitted to the Langmuir isotherm and pseudo-second-order kinetic model. The adsorption activation energy (E_a) was determined to be 50 kJ/mol, confirming that MB forms a monolayer on the surface of the adsorbent film through chemical adsorption. The adsorption process was exothermic, and the adsorbent film demonstrated good recyclability. The adsorbent showed simultaneous cationic MB and anionic MO adsorption while also treating real textile industry effluent, highlighting its practical applicability. The CA-supported Ni-BDC/CNC demonstrated potential to be used as an adsorbent for wastewater remediation.

5.2 Introduction

The development of advanced materials is important in addressing the growing demands for sustainability, efficiency, and functionality across various industries. Among these materials, cellulose and MOFs (metal-organic frameworks) have gained significant attention due to their unique properties and broad applications. Cellulose, the most abundant biopolymer on Earth, offers advantages such as biodegradability, renewability, and good mechanical properties [1 – 3]. MOFs are gaining popularity as versatile materials in catalysis, gas storage, and separation technologies due to their high surface area, high, porosity, and diverse chemical properties [4 – 6]. Recent advancements have enabled the creation of composites that synergistically combine cellulose (or its derivatives) and MOFs, leveraging the structural integrity and environmental benefits of cellulose with the functional versatility and high performance of MOFs. These composites open up new possibilities in various applications including environmental remediation, energy storage, and biomedical engineering.

Organic dyes are essential compounds in industries including textile, pharmaceutical, plastic, and leather [7 – 9]. However, the uncontrollable discharge of dye-containing wastes from these industries into the environment poses a substantial health hazard to both aquatic and terrestrial life, with human exposure reported to result in dizziness, nausea, and cancer, [10 – 11]. This highlights the urgent need to decontaminate organic dyes before their release into the environment. Methylene blue (MB), a cationic, bulky molecule, is one of the most widely used dyes in industries and serves as a model contaminant in this study.

Adsorption, the adhesion by which molecules (contaminants) adhere to the surface of a solid material is one of the best technologies for the removal of dyes from water due to efficiency, ease of operation, and cost-effectiveness [12 – 13]. The properties of MOFs are beneficial in adsorptive water purification technologies. Ni-BDC, a MOF composed of nickel, and terephthalic acid as the organic linker, has demonstrated high adsorption capacities for organic dyes, good selectivity, and high affinity for organic molecules [14 – 15], making it a good candidate for the adsorption of MB from water. Mohammadi *et al.* (2022) highlighted the use of Ni-based MOF for the removal of organic dyes and inorganic contaminants from water [16].

Cellulose, a linear single chain composed of thousands of D-glucose units can be treated further to obtain more versatile cellulose derivatives [17]. Crystalline nanocellulose (CNC) obtained by treating cellulose with acid resulting in crystalline rod-like materials of diameters between 5-70 nm and lengths of 100 – 500 nm [18 – 19], was noticed to have potential in dye removal due to

chemical and mechanical stability, high surface area, hydrophilicity, and high surface area [20 – 21]. Their incorporation in composites improves adsorption efficiency, wetting, mechanical stability, and promotes dispersion [22 - 23].

Composites play a significant role in adsorption as they take advantage of properties presented by both materials. As demonstrated above, Ni-BDC and CNC both show great potential for the removal of MB from water. Therefore, it is hypothesized that the formation of a composite from these materials will yield an adsorbent with a high surface area and high porosity to facilitate and maximize the adsorption process. The resulting adsorbent will further demonstrate good stability in aqueous applications. Furthermore, the hydrophilic nature of CNC will promote the dispersion of MOF particles, maximizing the surface area.

In this study, a Ni-BDC/CNC crystalline powdered composite was supported on cellulose acetate (CA) substrate to promote easy handling and mitigate potential secondary contamination that can occur with powdered adsorbents. The adsorbent, CA-supported Ni-BDC/CNC, was tested for adsorptive removal of MB from water. The effects of pH, initial concentration, contact time, and temperature on the adsorbent process were studied as well as the adsorption isotherms, kinetics, and thermodynamics.

5.3 Experimental

5.3.1 Materials

N'N'-dimethylformamide (DMF, 99.9 %), sulfuric acid (H_2SO_4, 98 %), sodium hydroxide pellets (NaOH, 97 %), and chloroform (CH_3Cl, 99 %) were purchased from Radchem. Nickel (II) nitrate hexahydrate ($Ni(NO_3)_2 \cdot 6H_2O$, 99.99 %), methylene blue (MB, 98%), cellulose acetate (CA, 39.3 % - 40.3 %), microcrystalline nanocellulose (MCC, 11 wt %), and terephthalic acid (BDC, 99 %) were purchased from Sigma-Aldrich.

5.3.2 Synthesis of CA-supported Ni-BDC/CNC adsorbent film

The method used to prepare Ni-BDC was reported by Cheng *et al.* (2022) with modifications [24]. In this procedure, 1.5 g of terephthalic acid and 6.7 g of nickel nitrate hexahydrate were dissolved in 60 mL of DMF followed by stirring for 1 hour at room temperature. To the mixture, 10 mL of 2 M sodium hydroxide was added, and the mixture was stirred for 2 hours. Afterwards, the mixture was

transferred to an autoclave and heated at 130 ^{o}C for 36 hours and the solid product obtained was washed with DMF and water, followed by vacuum drying, to yield Ni-BDC MOF.

CNC was synthesized through hydrolysis of microcrystalline cellulose by H_2SO_4 [25]. The procedure involved a slow addition of 1 g microcrystalline cellulose into 0.1 M H_2SO_4 solution under vigorous stirring at 45 ^{o}C. The sample was quenched with iced deionized water and subsequently centrifuged to separate the newly synthesized CNC from the acidic solution. Multiple centrifugation steps with deionized water was the process used to wash the sample until all the acid was removed. The synthesized pellet was freeze-dried at 72 hours to yield powdered CNC.

Ni-BDC/CNC composite was synthesized by adding 100 mg of Ni-BDC in 20 mL deionized water, followed by sonication and vigorous stirring of the mixture. In a separate reaction vessel, 50 mg of CNC was added to 20 mL of deionized water, which was stirred, and sonicated until a solution resulted. The resulting CNC solution was added into the reaction vessel of Ni-BDC and stirring was continued for an hour, followed by sonication. The mixture was centrifuged to isolate the solid product, which was Ni-BDC/CNC, and was dried at 70 ^{o}C in an oven for 24 hours.

CA-supported Ni-BDC/CNC was synthesized by dissolving 0.12 g of Ni-BDC/CNC in DMF under vigorous stirring and sonication [26]. In another reaction vial, 4 g of CA was dissolved in 40 mL of DMF, stirred for 24 hours, and subsequently degassed using N_2. In the stirring Ni-BDC/CNC mixture, 3.3 mL of the CA sludge was added, and stirring was continued for another hour. The resulting sludge was drop-casted on a glass slide, submerged in an ice bath for 4 hours, then air-dried for 24 hours to form CA-supported Ni-BDC/CNC adsorbent film.

5.3.3 Adsorption of MB by CA-supported Ni-BDC/CNC adsorbent film

This study investigated the effect of pH, contact time, initial concentration, and temperature on the adsorption of MB on CA-supported Ni-BDC/CNC. In batch-type adsorption experiments, 7 mm × 15 mm (3 mg) adsorbent films were immersed in 3 mL MB solutions with initial concentrations between 1 mg/L – 6 mg/L, pH values between 3 – 11, contact times from 60 minutes – 360 minutes, and temperature from 298 K to 318 K. The solutions were agitated under specified conditions and the absorbance before and after agitation were recorded on the UV/vis spectrophotometer to determine the % MB removal and adsorption capacity using equations (5.1) and (5.2), respectively:

$$\% \, MB \, removal = \frac{C_i - C_e}{C_i} \times 100 \, \% \quad (5.1)$$

$$q_e = \frac{C_i - C_e}{m} \times V \quad (5.2)$$

where C_i is the initial concentration of MB solution (mg/L), C_e is the equilibrium concentration of MB solution (mg/L), q_e is the equilibrium adsorption capacity (mg/g), V is the volume of the solution (mL), and m is the mass of the adsorbent (g).

In order to desorb the MB dye, reusability tests were carried out in which the adsorbent film was taken out of the MB solution, submerged in 10 mL methanol, and shaken for four hours following each adsorption cycle. After an hour of air drying, the film was removed and prepared for the subsequent adsorption cycle.

5.3.4 Adsorption isotherms

To analyze the adsorption isotherms, the experimental data were fitted to the Langmuir and the Freundlich isotherm models. The Langmuir isotherm model assumes monolayer adsorption on a homogenous surface while the Freundlich isotherm assumes multilayer adsorption on a heterogeneous surface. Langmuir and Freundlich isotherm models were used to model the adsorption process using their linearised equations, equations (5.3) and (5.4), respectively.

$$\frac{1}{q_e} = \frac{1}{K_L q_{max}} \times \frac{1}{C_e} + \frac{1}{q_{max}} \quad (5.3)$$

$$log(q_e) = log(K_F) + (\frac{1}{n}) log(C_e) \quad (5.4)$$

From the equations, q_{max} is the maximum adsorption capacity of the adsorbent (mg/g), and K_L is a Langmuir constant (mg/g) related to adsorption energy. High K_L values suggest stronger interactions between the adsorbent and adsorbate. K_F is the Freundlich isotherm constant (mg/g). The gradient of the linear form of the equation, $\frac{1}{n}$, is a function of the strength of the adsorption process referred to as the heterogeneity factor. Normal adsorption occurs when $\frac{1}{n} < 1$. When $\frac{1}{n} > 1$, cooperative adsorption is taking place. R_L is a separation factor and is calculated using equation (5.5):

$$R_L = \frac{1}{1 + K_L C_i} \quad (5.5)$$

where K_L is the Langmuir constant, and C_i is the initial adsorbate concentration. Adsorption is unfavorable when $R_L > 1$, linear when $R_L = 1$, favorable when $0 < R_L < 1$ and irreversible when $R_L = 0$.

5.3.5 Adsorption kinetics

Adsorption kinetics provide insight into mechanisms such as mass transfer and chemical reactions during adsorption. To study adsorption kinetics, experimental data was fitted to linearised forms of the pseudo-first-order and the pseudo-second-order rate equations, represented by equation (5.6) and equation (5.7), respectively:

$$ln(q_e - q_t) = ln(q_e) - k_1 t \quad (5.6)$$

$$\frac{1}{q_t} = \frac{1}{k_2 q_e^2} + \frac{1}{q_e} t \quad (5.7)$$

where q_e is the adsorption capacity at equilibrium, q_t is the adsorption capacity at time t, t is the contact time, k_1 is the first-order equilibrium constant, and k_2 is the second-order equilibrium constant.

Pore diffusion mechanisms were studied by fitting experimental data to the Webber-Morris intraparticle-diffusion model, Bangham model, and Boyd model, represented by equation (5.8) – (5.10), respectively:

$$q_t = k_{id} t^{1/2} + I \quad (5.8)$$

$$loglog\left(\frac{C_i}{C_i - q_t}\right) = log\left(\frac{k_b m}{2.303V}\right) + \alpha log(t) \quad (5.9)$$

$$B_t = -0.4977 - ln(1 - F) \quad (5.10)$$

where k_{id} is the intraparticle diffusion rate constant (mg/g·min$^{-1/2}$) and I is the thickness of the boundary layer. The k_b and α are Bangham equation constants, F is the fraction of MB adsorbed at any time t (min) and is calculated by equation (5.11):

$$F = \frac{q_t}{q_e} \quad (5.11)$$

5.3.6 Statistical tests

Statistical studies were used to determine the best-fitting model using a nonlinear chi-square (χ^2) statistical test and the linear correlation coefficient (R^2). The R^2 and χ^2 values for different models were compared to determine the best fit for the experimental data. Models with higher R^2 and lower χ^2 values were considered to be better representations of the adsorption process. Equation (5.12) was used to calculate χ^2.

$$\chi^2 = \Sigma \frac{(q_e - q_{ecal})^2}{q_{ecal}} \qquad (5.12)$$

Thermodynamic studies

The temperature dependence of the adsorption process was evaluated using thermodynamics. Thermodynamic parameters such as standard entropy (ΔS°), standard enthalpy (ΔH°), and standard free energy (ΔG°) were determined using the Van Hoff plot, which provides the basis for the calculation of (ΔS°) and (ΔH°) according to equations (5.13) and (5.14):

$$lnK_L = \frac{\Delta S^\circ}{R} - \frac{\Delta H^\circ}{RT} \qquad (5.13)$$

$$\Delta G^\circ = -RT\ lnK_L \qquad (5.14)$$

where K_L is the equilibrium constant, R is the universal gas constant and T is temperature.

5.3.7 Characterization techniques

X-ray diffraction (XRD) analysis was conducted on a Bruker D2 PHASER-e diffractometer using Cu-Kα radiation (0.15418 nm). Scanning electron microscopy (SEM) and Energy-dispersive X-ray spectroscopy (EDX) were carried out on a crossbeam 540 FEG SEM microscope from Zeiss. UV-vis absorption measurements were taken using a CARY 100 BIO UV-Vis spectrophotometer. FTIR spectroscopy was conducted on a Brunker Alpha Fourier transform spectroscopy with platinum attenuated total reflectance (ATR) sampling accessory, 4 cm^{-1} resolution. Thermogravimetric analysis was done using SDT Q600 V20.9 Build 20 Module DSC-TGA Standard. The Brunauer-Emmett-Teller (BET) and Barrett–Joyner–Halenda (BJH) models' analysis was conducted on the

Autosorb iQ model:7, ASiQWin version 5.2x. X-ray photoelectron spectroscopy (XPS) was carried out on a Thermo model: ESCAlab 250Xi using a monochromatic Al kα X-ray source.

5.4 Results and Discussion

5.4.1 Material characterization

X-ray diffraction (XRD)

Figure 5.1a shows the XRD pattern of Ni-BDC MOF displaying peaks at 9.16º, 14.44º, 16.01º, 18.14º, and 25.4º. The obtained diffraction pattern corresponds to previously reported XRD patterns for Ni-BDC and aligns well with JCPDS file number 035.1677 [27 – 28], confirming the synthesis of the MOF. The crystallite size was calculated to be 12.67 nm using the Scherrer equation, presented in equation (5.15):

$$D = \frac{K\lambda}{\beta Cos\theta} \qquad (5.15)$$

where D is the crystallite size, K is the Scherrer constant with a value of 0.9, β is the full width at half maximum (FWHM), and θ is the peak position. Figure 5.1b shows the XRD pattern of CNC characterized by peaks at 14.5º, 16.5º, 20.6º, 22.6º, and 34.4º, indexed (110), (110), (102), (200), and (004), respectively. The diffraction pattern is consistent with previously reported XRD results of CNC and corresponds with the JCPDS file number 03-0226 [29 – 30]. Ni-BDC and CNC were combined to form a composite, Ni-BDC/CNC, which was confirmed through XRD characterization, as shown in figure 5.1c. The diffraction pattern exhibited peaks from both Ni-BDC and CNC observed at 9.16 º, 14.44 º, 18.14 º, 25.4 º, and 15.01 º, 22.6 º, and 34.4 º, respectively, verifying the formation of the composite. The diffraction pattern of CA shown in figure 5.1d, has no distinct peaks, characteristic of the amorphous material. The diffraction pattern of CA-supported Ni-BDC/CNC shown in figure 5.1e is more comparable to the XRD pattern of amorphous CA as it constitutes most of the adsorbent film.

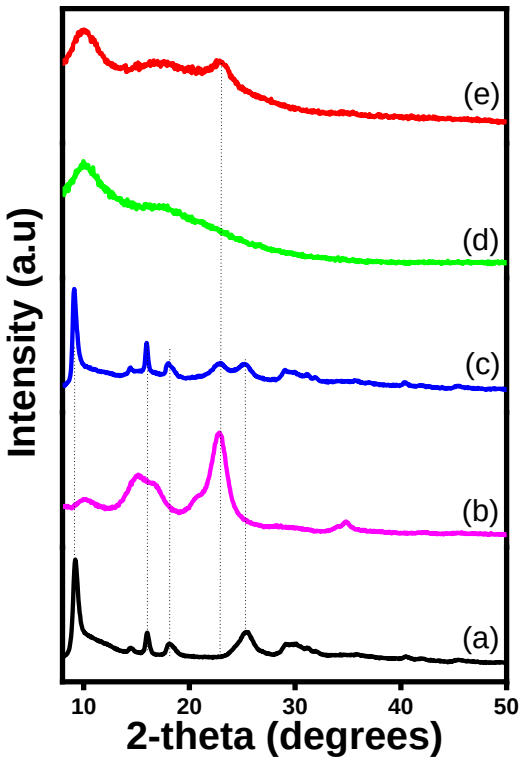

Figure 5.1: XRD patterns of (a) Ni-BDC, (b) CNC, (c) Ni-BDC/CNC, (d) CA, and (e) CA-supported Ni-BDC/CNC.

Fourier-transform infrared spectroscopy (FTIR)

To confirm the structure of the synthesized materials, FTIR spectroscopy was used as illustrated in figure 5.2. Figure 5.2a shows the IR spectrum of Ni-BDC characterized by several peaks at 3600 cm^{-1},1578 cm^{-1} and 1372 cm^{-1} correspond to O-H stretching, O=C stretching, and C=C vibration, respectively. The peaks occurring at 814 cm^{-1} and 740 cm^{-1} are assigned to the in-plane bending vibration of Ni-O and the stretching vibrations of Ni-O, respectively. A similar spectrum for Ni-BDC has been reported elsewhere [31].

Figure 5.2b shows the spectrum of CNC with peaks at 3600 cm^{-1} and 1634 cm^{-1} corresponding to O-H stretching and C=O stretching vibration. Peaks at 1430 cm^{-1}, 1374 cm^{-1} and 1313 cm^{-1} are due to C–O vibrations of the pyranose ring structure, and the reflection occurring at 892 cm^{-1}, represents the glycosidic C_1–H deformation within the ring, characteristic of the glycosidic bonds within the cellulose chain. This spectrum is consistent with previous reports [32].

Figure 5.2c shows the FTIR spectrum of the Ni-BDC/CNC composite displaying peaks from both Ni-BDC and CNC. Peaks at 1578 cm^{-1}, 1372 cm^{-1}, and 814 cm^{-1} correspond to Ni-BDC, while CNC peaks occur at 1634 cm^{-1} and 1000 cm^{-1}. CA spectrum is shown in figure 5.2d and is consistent

with previous reports. Figure 5.2e shows the spectrum of CA-supported Ni-BDC/CNC adsorbent film showing great similarities with the spectrum of CA, consistent with reports where CA has been used as a substrate material [26, 33]. The peak displayed at 1736 cm^{-1} for CA is shifted to 1738 cm^{-1} for the adsorbent film. The distortion verifies the hydrogen bond interaction between the composite and the CA substrate, confirming that the Ni-BDC/CNC composite is embedded within the CA matrix.

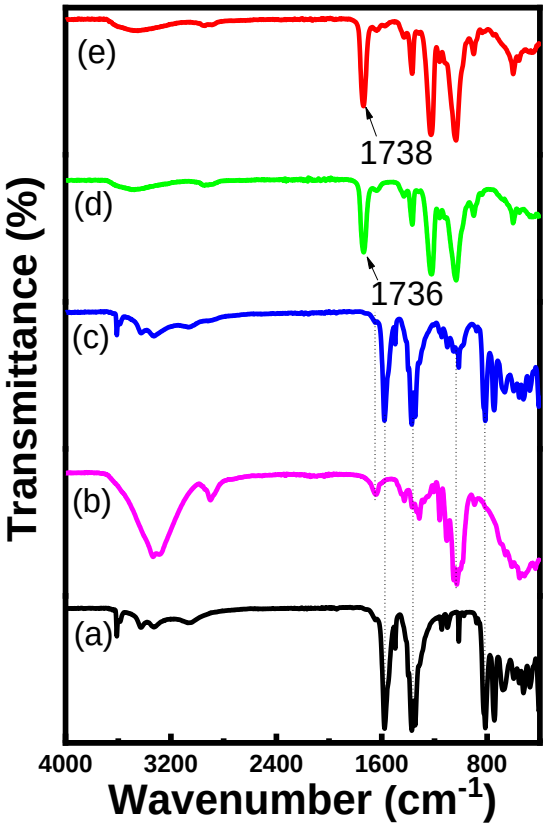

Figure 5.2: FTIR spectra of (a) Ni-BDC, (b) CNC, (c) Ni-BDC/CNC, (d) CA, and (e) CA-supported Ni-BDC/CNC.

Scanning electron microscopy (SEM)

Figure 5.3a shows the SEM image of Ni-BDC as layered flakes, consistent with previous reports [31, 34 – 35]. The CNC shows nanowhisker morphology, with the material having rod-like particles, with lengths between 100 nm - 500 nm and diameters in the range of 2 nm - 20 nm, also consistent with previous findings [36 – 38]. The Ni-BDC/CNC composite (figure 5.3c) shows a layered structure decorated by grain-like particles. The surface morphology and the cross-section of the

CA-supported Ni-BDC/CNC adsorbent film are shown in figures 5.3d and 5.3e, respectively. The adsorbent film exhibits a flat, perforated sheet-like morphology with pore channels running through the cross-section of the film. The EDX spectrum of CA-supported Ni-BDC/CBC (figure 5.3f) shows the detection of oxygen and nickel confirming the presence of Ni-BDC MOF within the adsorbent film.

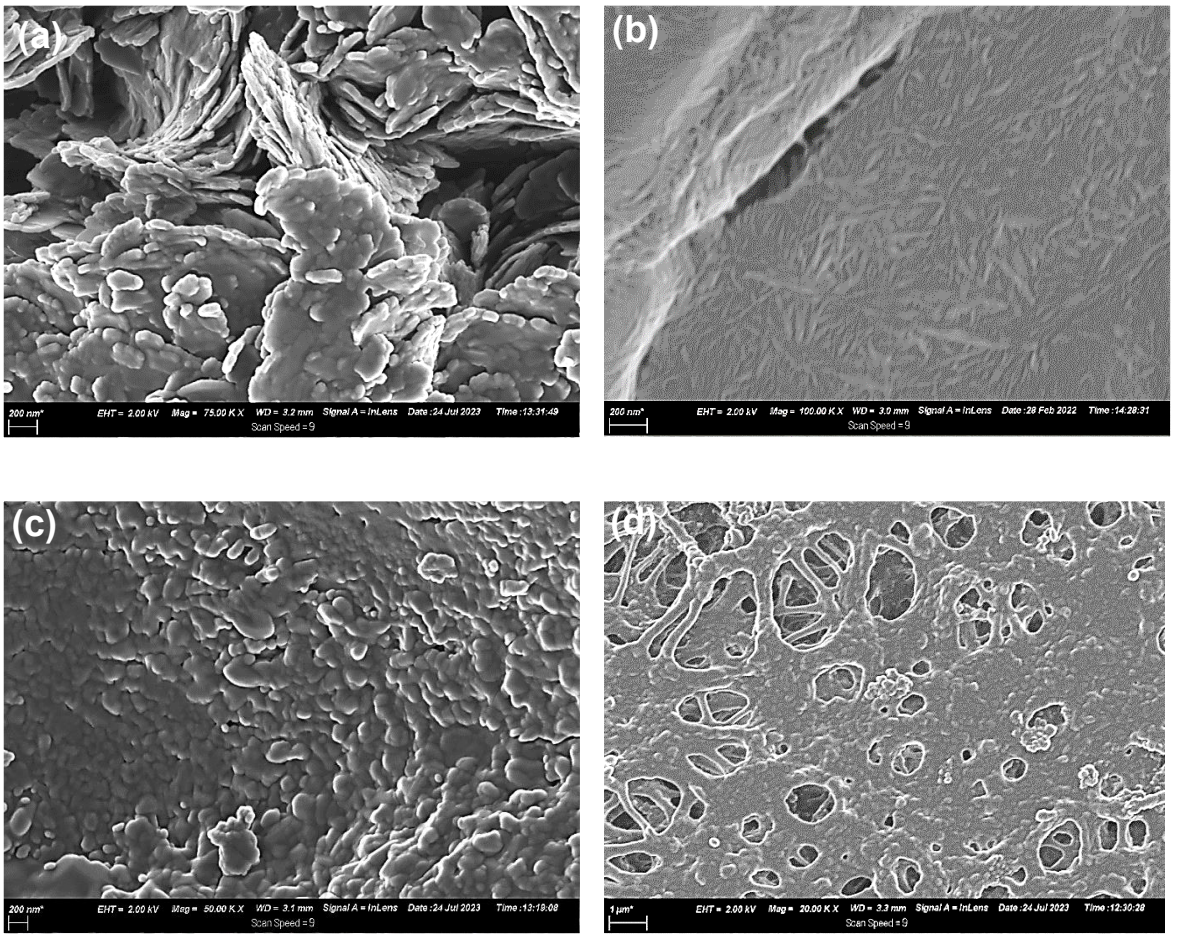

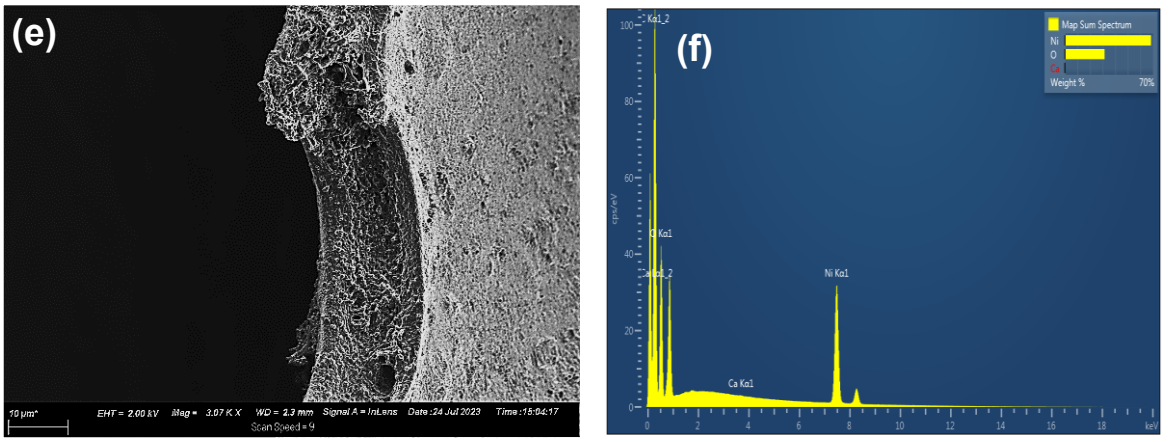

Figure 5.3: SEM micrographs of (a) Ni-BDC, (b) CNC, and (c) Ni-BDC/CNC. (d) The surface morphology and the (e) cross-section of CA-supported Ni-BDC/CNC. (f) The EDX spectrum of CA-supported Ni-BDC/CNC.

Thermal Gravimetric Analysis (TGA)

TGA studies the thermal stability of materials by monitoring percentage weight change as temperature increases and the results are shown in figure 5.4. All the materials showed a weight loss at 100 ^{o}C associated with the removal of physically adsorbed moisture and gases. The weight loss observed between 150 ^{o}C and 250 ^{o}C occurred due to the removal of adsorbed DMF, the solvent used during synthesis. Ni-BDC, shown in figure 5.4a, displays a third weight loss of 52 % between 380 ^{o}C and 480 ^{o}C indicating the degradation of Ni-BDC through the breakdown of the framework and the decomposition of terephthalic acid, leaving nickel metal which constitutes 39 % of the MOF. CNC showed the pyrolysis of cellulose and hemicellulose resulting in intermediates when the temperature increased from 260 ^{o}C to 320 ^{o}C, as depicted in figure 5.4b and this was accompanied by 70 % weight loss. A temperature increase from 320 ^{o}C to 480 ^{o}C resulted in 24 % weight loss, which occurred due to a further breakdown of the intermediates signifying a total decomposition of CNC. Figure 5.4c shows the TGA plot of the Ni-BDC/CNC composite and its total decomposition was observed at 480 ^{o}C, the 27 % that remained was the nickel metal. The adsorbent film experiences a total decomposition at 515 ^{o}C, with the 5 % remaining being the nickel metal.

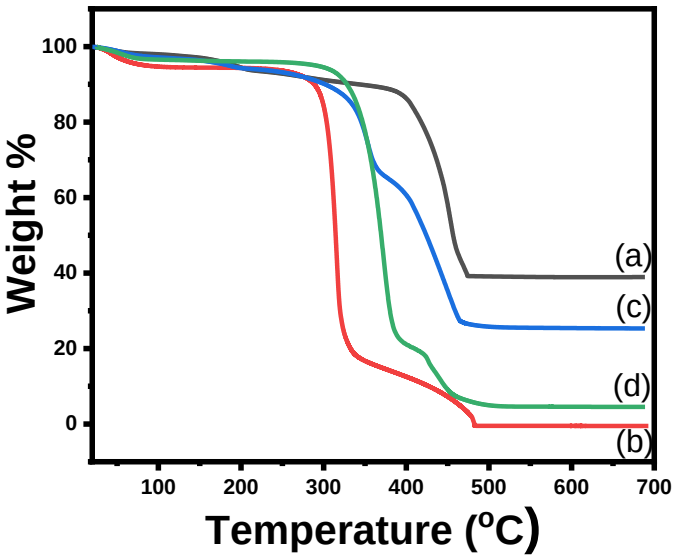

Figure 5.4: TGA curves of (a) Ni-BDC, (b) CNC, (c) Ni-BDC/CNC, and (d) CA-supported Ni-BDC/CNC.

Brunauer-Emmett-Teller (BET) and X-ray photoelectron spectroscopy (XPS)

The BET measurement for the adsorbent film shown in figure 5.5, represents a type I isotherm N_2 adsorption/desorption curve characteristic of microporous materials [39]. The analysis showed the adsorbent film has a specific surface area of 19.986 m^2/g, significantly lower than the expected surface area, possibly due to the blocking of pores of the MOF during composite formation and by the CA substrate. Consequently, the adsorption capacity of the adsorbent is expected to be lower, however, with eliminated secondary contamination, recyclability, and water stability. The pore geometry was analyzed using BJH analysis, demonstrating a pore diameter of 1.2 nm which is microporous, and a pore volume of 0.264 cm^3/g.

XPS was used to examine the surface chemical composition and bonding states. Figure 5.6a shows the surface of CA-supported Ni-BDC/CNC consisting of oxygen and carbon as shown by the C1s and O1s peaks. The high-resolution XPS spectra enabled the deconvolution of the C1s and O1s, as demonstrated in figure 5.6b and 5.6c, respectively. The high-resolution spectrum of C1s shows the presence of four sub-peaks at 287.5 eV, 286.2 eV, 284.9 eV, and 283.4 eV, assigned to O–C=O, C=O, C-O, and C-C, respectively. The deconvoluted O1s peak is characterized by three peaks at 531.9 eV, 530.9 eV, and 529.6 eV, corresponding to C=O, C–O, and O–H, respectively. Failure to detect Ni might be because the adsorbent has the Ni-BDC/CNC embedded within the CA matrix.

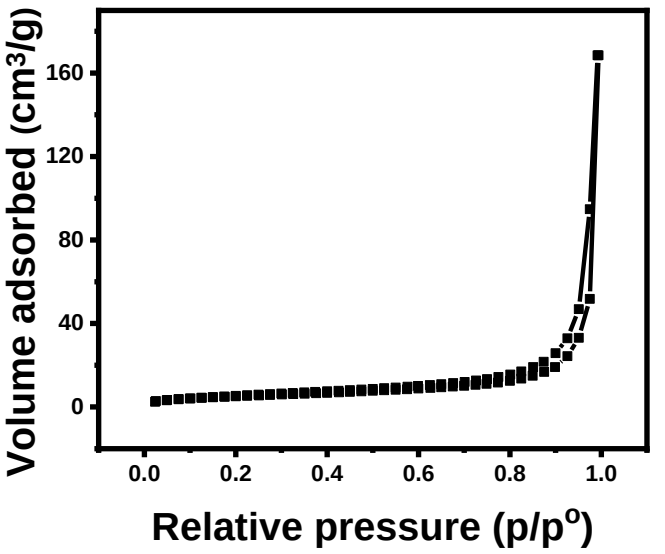

Figure 5.5: N_2 adsorption/desorption isotherm of CA-supported Ni-BDC/CNC

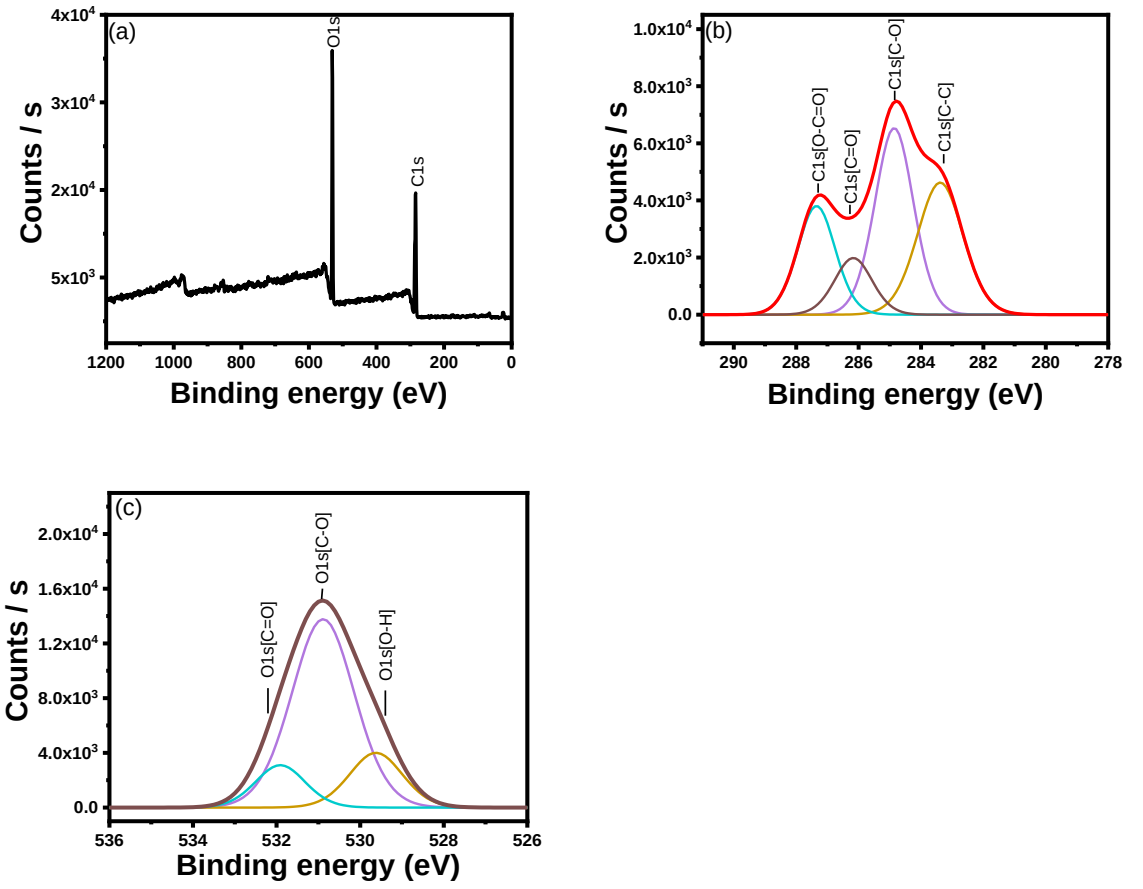

Figure 5.6: (a) XPS survey spectrum of CA-supported Ni-BDC/CNC adsorbent and the corresponding high-resolution spectra of (b) C1s and (c) O1s.

Point of zero charge (pH_{PZC})

The point of zero charge, represented by pH_{pzc}, is the pH at which the adsorbent's surface has a net zero charge. The pH_{pzc} was determined by comparing the pH of the NaCl solution before CA-supported Ni-BDC/CNC was submerged and agitated and the resulting pH after the process. The resulting plot of Δ pH against initial pH is shown in figure 5.7. The adsorbent film's pH_{pzc} was determined to be 6.1, implying that at pH above 6.1; the adsorbent's surface is deprotonated by excess OH^- groups in the solution resulting in a net negative surface charge. At pH below the pH_{pzc}, the adsorbent's surface is protonated by excess H^+ in the solution, rendering the net surface charge to be positive. At extreme pH values of 1 and 13, there are more H^+ and OH^- ions in the solution, respectively, resulting in the adsorbent film having no influence on pH, hence there is little to no change in pH.

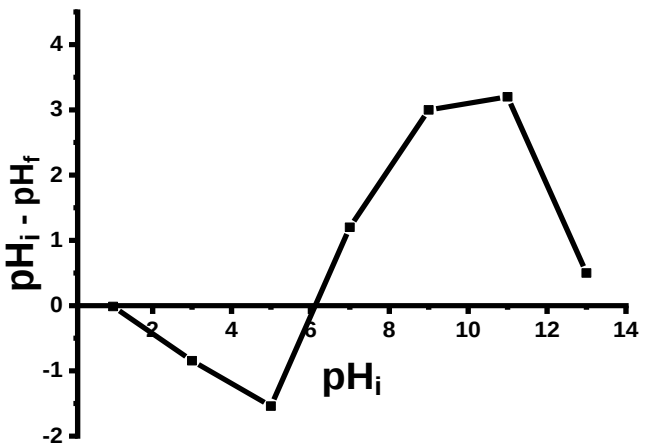

Figure 5.7: The point of zero charge of CA-supported Ni-BDC/CNC.

5.4.2 Adsorption studies

Effect of pH on adsorption

Figure 5.8a shows the effect of pH on equilibrium adsorption capacity, q_e, and figure 5.8b shows the effect of pH on % MB removal. From figure 5.8 it can be concluded that adsorption efficiency increases with an increase in pH, consistent with the pH_{pzc} studies as at lower pH values, the surface of the adsorbent film has a net positive charge and will be electrostatically repelled by the cationic MB dye, limiting MB adsorption. As pH is increased well above the pH_{pzc}, the adsorbent's

surface becomes negatively charged, and this is evidenced by a steady increase in the adsorption efficiency of the cationic dye due to electrostatic attractions. This study shows that pH affects the surface chemistry of CA-supported Ni-BDC/CNC adsorbent film, and therefore, affects the adsorption efficiency of MB by the adsorbent film. The highest adsorption efficiency was recorded at pH 11.

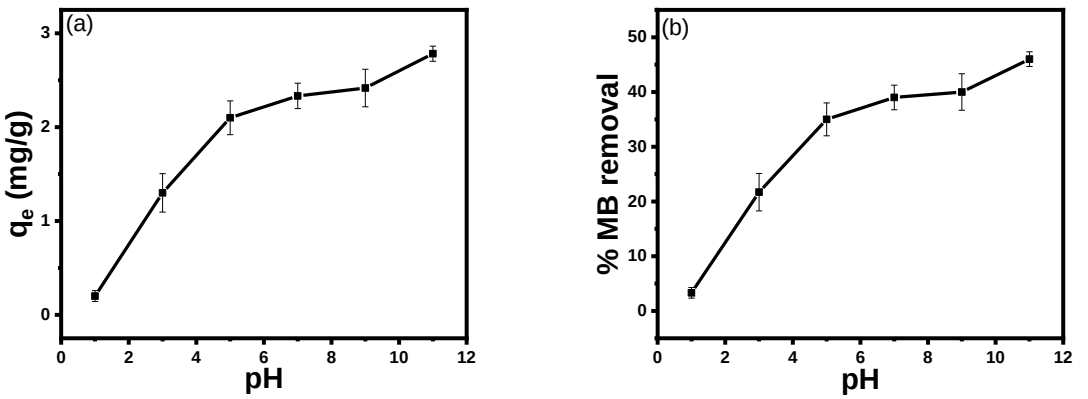

Figure 5.8: The effect of pH on (a) equilibrium adsorption efficiency and (b) % MB adsorption.

Effect of contact time on adsorption

The effect of contact time on the adsorption efficiency was studied and the resulting plots were shown in figure 5.9. The contact time was 6 hours at initial MB concentrations of 1 mg/L to 6 mg/L. Adsorption occurs in three stages during this period, the first stage is a rapid increase in capacity within the first hour as a result of available adsorption active sites on the adsorbent film. The second stage takes place between the second hour to the fifth hour where adsorption capacity occurs at a slower rate due to few adsorption active sites on the adsorbent film and fewer MB dye molecules in the solution. The flat curve observed during the last hour demonstrates equilibrium where there is little to no change in the adsorption capacity. The adsorption capacity during this stage is the equilibrium adsorption capacity, q_e. The % MB removal plots in figure 5.9b follows a similar trend. The highest equilibrium adsorption capacity was 2.78 mg/g and the highest % MB adsorption was 85 %.

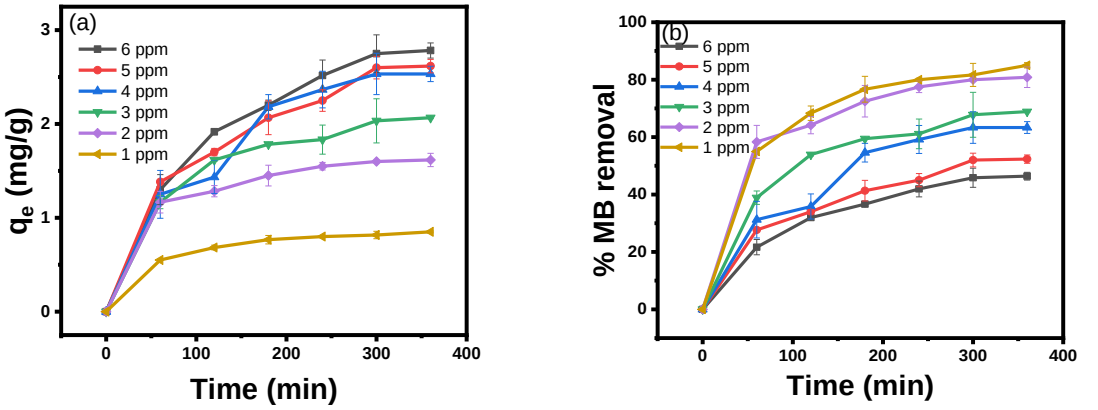

Figure 5.9: The effect of contact time on (a) adsorption capacity and (b) % MB removal.

Effect of initial concentration

Figure 5.10 shows the effect of initial concentration on the adsorption of MB onto CA-supported Ni-BDC/CNC. The initial MB concentrations studied were 1 mg/L – 6 mg/L at pH 11 and the area of the adsorbent films used was 7 mm x 15 mm. Figure 5.10a shows an increase in equilibrium adsorption capacity with increasing initial concentration of MB solution. This trend is observed due to the adsorptive removal of MB by the adsorbent film being concentration-dependent, meaning the MB concentration provides the driving force to overcome the mass transfer barrier between the adsorbent surface and the adsorbate. Therefore, at higher initial concentrations of MB, the adsorption capacity increased. The effect of initial concentration on % MB removal is represented by figure 5.10b showing a decrease in the % removal with increasing initial concentration of MB since at lower initial MB concentrations, the adsorbent's available surface area and active sites were higher, leading to more MB molecules being adsorbed. As the initial concentration of MB is increased and the number of active sites remains constant and limited, the % MB removal decreases as fewer MB molecules are taken by the adsorbent film from the solution.

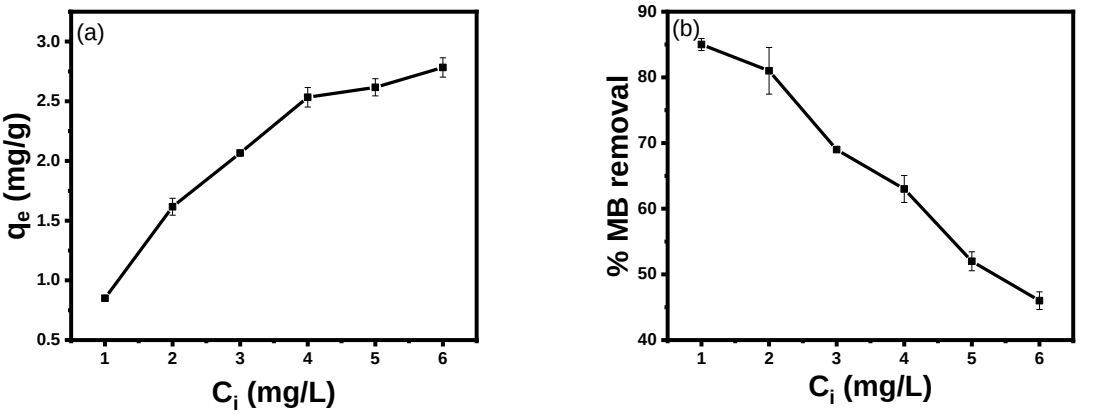

Figure 5.10: The effect of initial concentration on (a) equilibrium adsorption efficiency and (b) % MB removal.

Adsorption isotherms

Adsorption isotherms are necessary in adsorption studies as they explain adsorption. The equilibrium adsorption data was analyzed using Langmuir and Freundlich isotherm models to determine the isotherm model that better describes the adsorption process. The adsorption isotherm plots are shown in figure 5.11 and their corresponding parameters are listed in table 5.1. The correlation coefficients (R^2) are 0.9956 and 0.9314 for the Langmuir and the Freundlich isotherm, respectively, indicating the adsorption process better agrees with the Langmuir isotherm model. Moreover, the determined maximum adsorption capacity, q_{max}, from the Langmuir isotherm model was 3.13 mg/g, which is closer to the experimentally obtained q_e, 2.78 mg/g compared to 4.39 mg/g determined by the Freundlich model. The separation factor, R_L, values at all the initial MB concentrations, were between 1 and 0, as illustrated in figure 5.11c, indicating that the adsorption process was favourable. From the Freundlich isotherm, the heterogeneity factor, 1/n, was determined to be 0.37 ($0 < \frac{1}{n} < 1$) further confirming the favourable adsorption. The Langmuir isotherm has a lower χ^2 than the Freundlich isotherm. As such, it can be concluded that the adsorption of MB onto CA-supported Ni-BDC/CNC adsorbent film can be described to closely follow the Langmuir isotherm, meaning that MB molecules form a monolayer on the surface of the adsorbent film and similar results have been reported for the adsorption of Azo dyes [40 – 42].

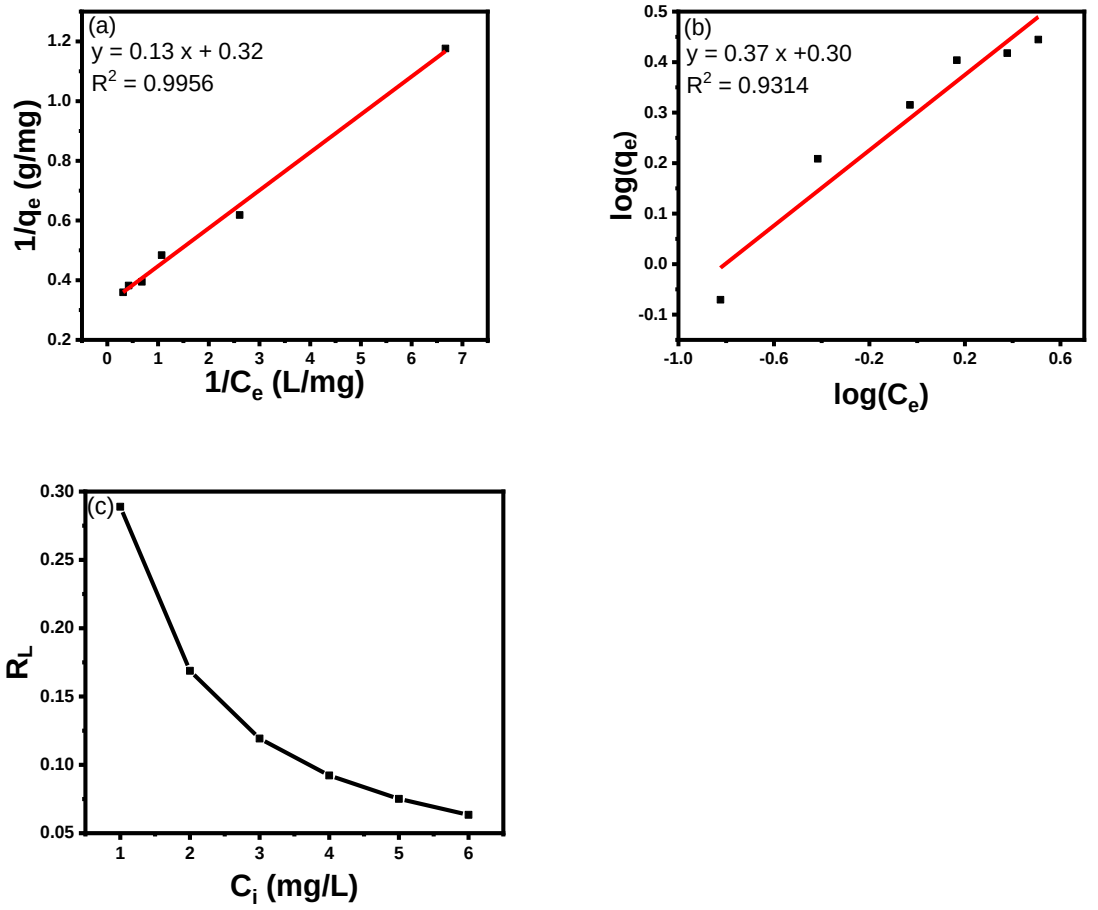

Figure 5.11: (a) Langmuir isotherm model, (b) Freundlich isotherm model, and (c) Separation factor values obtained against the initial MB concentration.

Adsorption kinetics

The kinetic studies in adsorption processes are important as they assist in identifying the rate of an adsorption process and contribute to analyzing the adsorption mechanisms. This study also sheds light on the rate-determining step. The adsorption of MB by CA-supported Ni-BDC/CNC was subjected to kinetic studies using pseudo-first order and pseudo-second order kinetic models, shown in figure 5.12a and 5.12b, respectively. Their respective kinetic parameters are listed in table 5.1. The adsorption process closely fits the pseudo-second-order kinetic model as the R^2 value was 0.9966, compared to the pseudo-first-order kinetic model with an R^2 value of 0.9075. Further confirmation lies in the pseudo-second-order kinetic model demonstrating a q_e value of 3.7 mg/g, which is closer to the experimental q_e of 2.78 mg/g, compared to 7.77 mg/g exhibited by the pseudo-first-order kinetic model. Furthermore, the χ^2 of the pseudo-second kinetics was calculated to be lower than the value obtained for the pseudo-first-order and similar observations have been

reported [43 – 45]. This implies that the adsorption of MB on CA-supported Ni-BDC/CNC takes place through chemical adsorption, which might be contributing to the rate-limiting step.

Pore diffusion mechanisms were studied by fitting experimental data to the Webber-Morris intraparticle diffusion model, Bangham model, and the Boyd model, and the results are shown in figure 5.12c, 5.12d, and 5.12e, respectively. The intraparticle diffusion model demonstrates a straight-line curve having an R^2 value of 0.9729, which is close to unity, and a χ^2 value > 0.05, indicating that this model is valid for the adsorption process. The plot has a positive y-intercept, I, of 0.35, which is an indication of the boundary layer. If the plot does not pass through the origin, the intraparticle diffusion model alone does not account for the rate control step [46]. The Bangham model has an R^2 value of 0.9875 and a χ^2 value > 0.05 indicating that the diffusion of MB in the pores of CA-supported Ni-BDC/CNC contributes to the rate-determining step [47]. The Boyd model displays two straight line segments which occur at 60 – 120 minutes and 240 – 300 minutes, labelled segment 1 and segment 2 respectively. Both segments do not pass through the origin, indicating that film diffusion is involved in the rate-determining step, but it is not solely responsible [48].

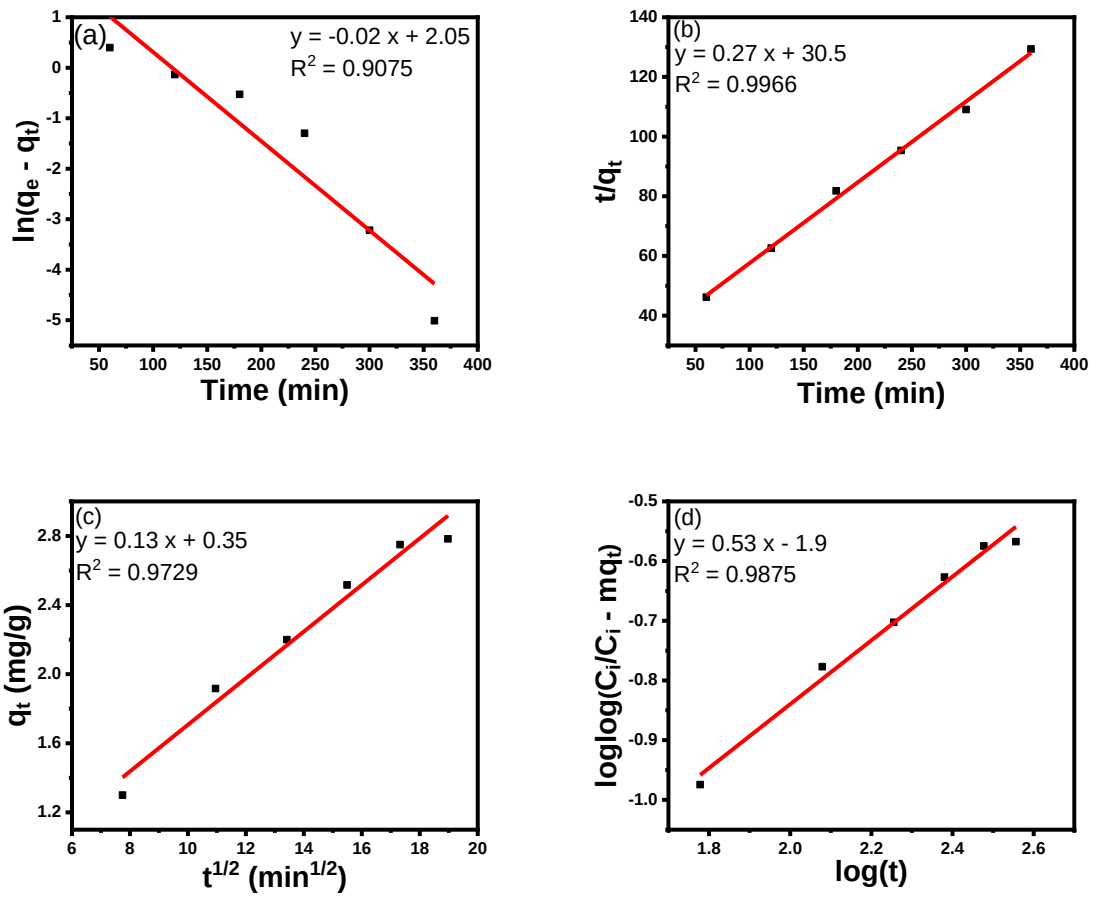

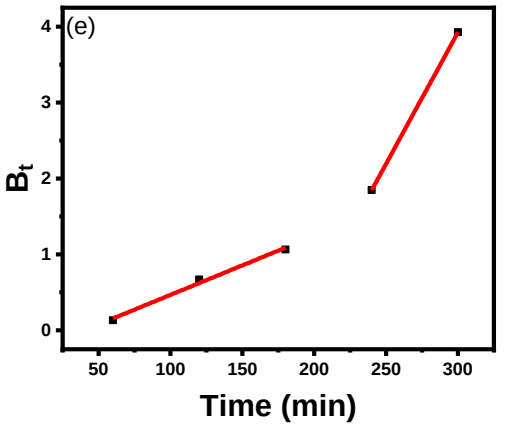

Figure 5.12: (a) The pseudo-first-order kinetic model, (b) the pseudo-second-order kinetic model, (c) the Weber-Morris intraparticle diffusion model, (d) Bangham kinetic model, and (e) the Boyd kinetic model.

Table 5.1: Kinetic parameters of pseudo-first-order kinetic model, pseudo-second-order kinetic model, and Weber-Morris intraparticle diffusion model.

Langmuir	**Freundlich**	**Pseudo first-order**	**Pseudo second order**	**Intraparticle diffusion model**	**Bangham Model**	**Pore diffusion**
q_{max} (mg/g) 3.13	q_e (mg/g) 4.39	q_e (mg/g) 7.77	q_e (mg/g) 3.70	k_{id} 0.13	K_B 0.09	1st segment slope 0.08 2nd segment slope 0.035
K_L (L/mg) 2.46	K_F (mg/g) 2	k_1 0.02	k_2 0.0024	C 0.35		1st Intercept -0.31
R^2 0.9965	R^2 0.9314	R^2 0.9075	R^2 0.9966	R^2 0.9729	R^2 0.9875	2nd Intercept -6.5
χ^2 0.00757	χ^2 0.043	χ^2 0.0068	χ^2 0.0027	χ^2 0.011	χ^2 0.0085	

Activation energy

The activation is energy (E_a) provides insights on the nature and strength of the adsorption of MB on CA-supported Ni-BDC/CNC and it is expressed by equation (5.16):

$$ln\, k = lnA\ - \frac{E_a}{RT} \qquad (5.16)$$

where k is the pseudo-second-order rate constant, A is the Arrhenius constant, E_a is the activation energy, R is the ideal gas constant (8.314 J/K.mol) and T is the temperature in K. The E_a is calculated from the slope of the Arrhenius plot shown in figure 5.13 and was calculated to be 50 kJ/mol, supporting the observation made in the kinetic studies that the adsorption of MB onto the surface of the adsorbent film occurs through chemisorption. This is guided by the fact that for

chemisorption, E_a ranges between 40 - 800 kJ/mol, while for physisorption, activation energy ranges between 5 - 40 kJ/mol [49].

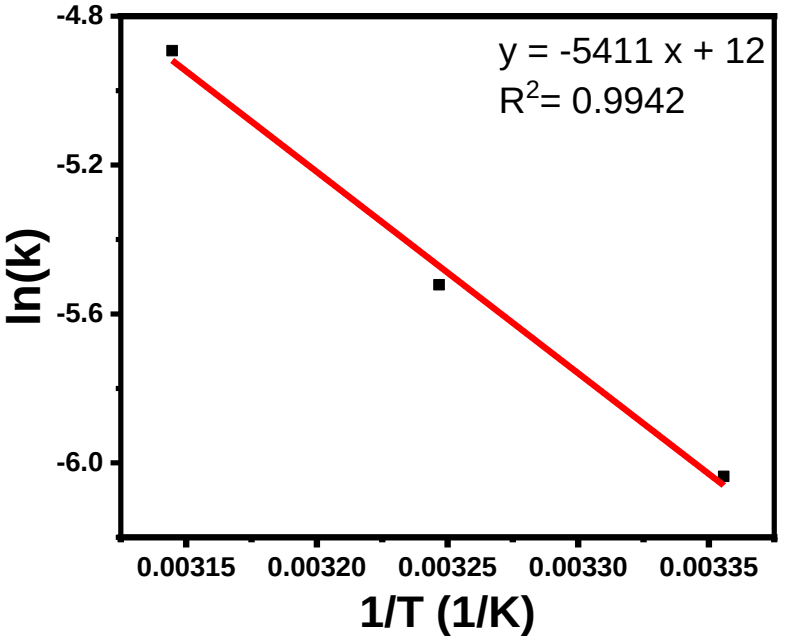

Figure 5.13: Plot of lnk vs T^{-1} for the estimation of activation energy, E_a.

Adsorption thermodynamics

The effect of temperature on the adsorption efficiency of MB onto CA-supported Ni-BDC/CNC adsorbent film was studied, and the results are presented in figure 5.14. The temperature was increased from 298 K to 318 K, the initial concentration used was 6 mg/L, at pH 11, at a contact time of 6 hours and the area of the adsorbent kept at 7 mm x 15 mm. Figure 5.14a shows the effect of temperature on the equilibrium adsorption capacity, and figure 5.14b shows the effect of temperature on % MB removal. Both curves follow a similar trend, which is the reduction in adsorption efficiency with increasing temperature. This indicates that the adsorption process is exothermic.

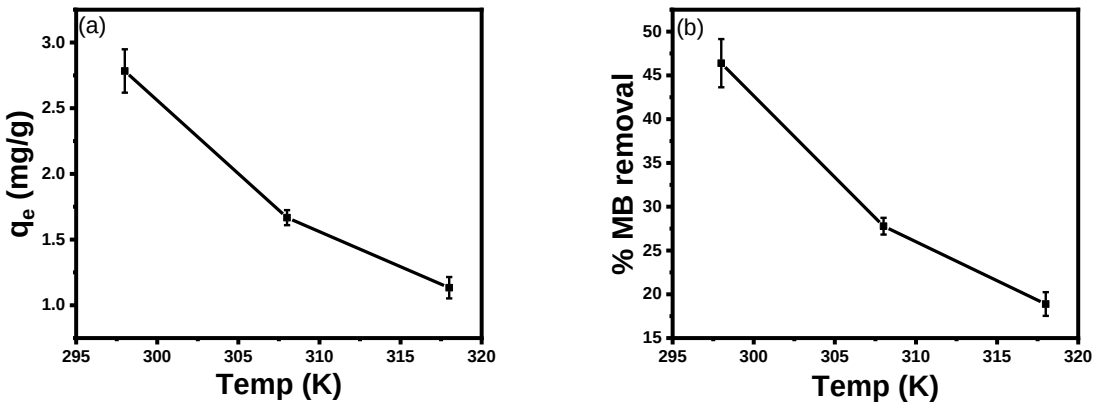

Figure 5.14: The effect of temperature on (a) equilibrium adsorption capacity and (b) % MB removal.

The thermodynamic study illustrated by the Van 't Hoff plot is shown in figure 5.15, and the corresponding thermodynamic parameters are listed in table 5.2. The ΔG^o values at all the temperatures are positive, indicating that the adsorption process was non-spontaneous within the temperature range of this study. The value of ΔH^o was determined to be negative, implying that the adsorption process was exothermic in nature. The ΔS^o value was determined to be negative, showing that the adsorption process results in the adsorbed MB being more orderly than in the bulk solution [50 – 51]. This means that the mobility of MB onto the adsorbent film is restricted as compared to the mobility in aqueous solutions. Similar results have been reported elsewhere [52].

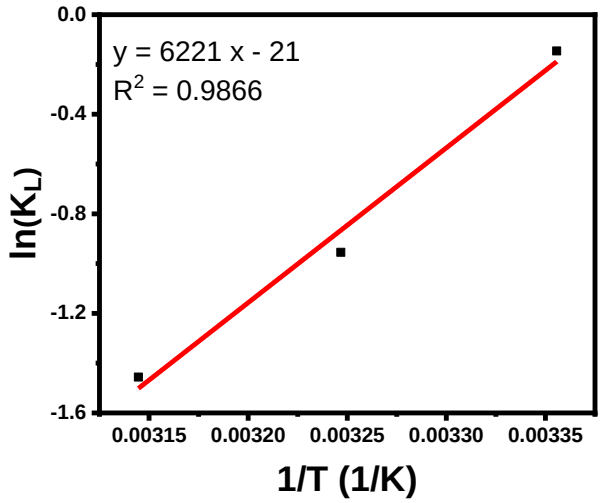

Figure 5.15: Van't Hoff plot for the adsorption of MB by CA-supported Ni-BDC/CNC.

Table 5.2: Thermodynamic parameters for adsorption of MB by CA-supported Ni-BDC/CNC.

T/K	Δ G° (kJ/mol)	Δ H° (kJ/mol)	Δ S° (J/K.mol^{-1})	E_a (kJ/mol)
298	0.361084	-51.7	-175.15	50
308	2.444966			
318	3.84935			

Reusability

The reusability of CA-supported Ni-BDC/CNC was assessed to understand the stability of the adsorbent film, results are shown in figure 5.16. After the fifth cycle of MB adsorption, the adsorbent achieved a q_e of 1.11 mg/g, which is 67 % of the q_e obtained after the first cycle. The reduced efficiency may be due to adsorbed MB molecules still occupying active sites. This shows that the adsorbent film has the capacity to be used multiple times for the removal of MB and that the adsorbent is stable in aqueous solutions. This makes the film sustainable with reduced environmental impact and economically efficient as it does not require constant replacing.

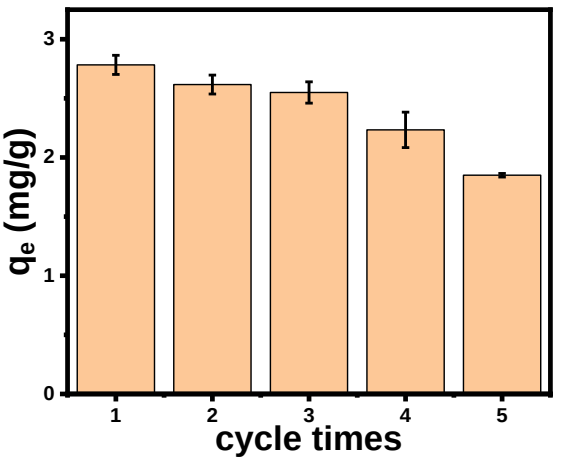

Figure 5.16: Reusability of CA-supported Ni-BDC/CNC adsorbent film.

Adsorption mechanisms

Figure 5.17 displays the proposed mechanisms of the adsorption of MB onto CA-supported Ni-BDC/CNC adsorbent film. Adsorption can occur through multiple pathways because of the hydroxyl and carbonyl groups present on the surface of the adsorbent film, confirmed by FTIR spectrum and XPS. These include ion-dipole, dipole-dipole, hydrogen bonding and $\pi - \pi$

interactions. Similar mechanisms have been reported elsewhere for CA-based adsorbents for MB removal [53]. At the optimum pH (pH 11), the adsorbent film has a net negative surface charge and is attracted to cationic MB through electrostatic attractions. Moreover, hydrogen bonding occurs between the hydroxyl groups on the adsorbent film and the nitrogen atoms on the MB structure, and $\pi - \pi$ interactions contribute to the adsorption process.

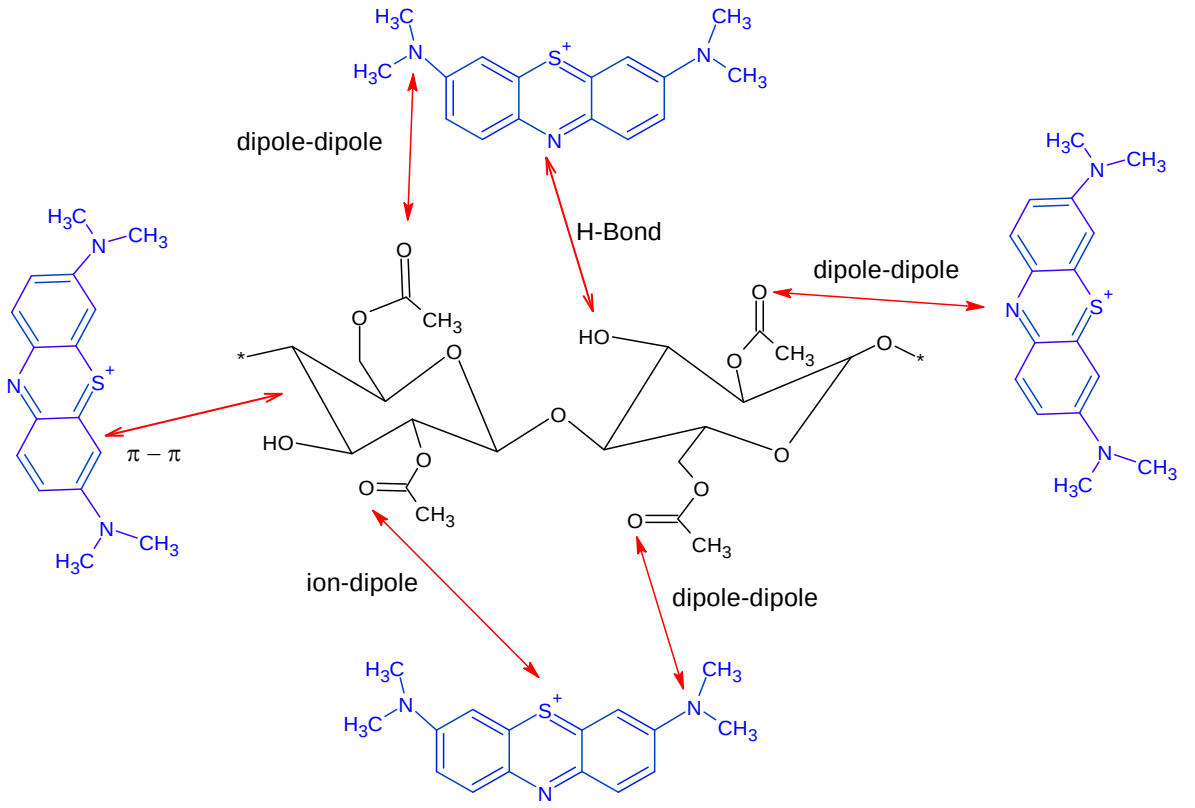

Figure 5.17: Adsorption mechanisms of MB onto CA-supported Ni-BDC/CNC.

Simultaneous adsorption of MB and methyl orange (MO)

CA-supported Ni-BDC/CNC adsorbent film was tested for the simultaneous adsorption of cationic MB and anionic methyl orange (MO), to assess the practical applicability of the adsorbent film. Figure 5.18 shows that simultaneous adsorption was conducted between pH 3 -11. It was observed that under acidic conditions, the adsorbent film had a high affinity for MO, while at alkaline pH conditions, the film demonstrated high adsorption of MB. This is in line with the observation of pH_{pzc} that at pH below 6.1, the adsorbent film's surface charge is positive hence the high affinity for anionic MO. At pH values above 6.1, the adsorbent's surface charge is negative, leading to a higher affinity for cationic MB. At pH 3 the adsorbent achieved the highest q_e of 1.63 mg/g for MO compared to 1 mg/g for MB. At pH 11, the film achieved a q_e of 2.3 mg/g for MB, compared to 1.18 mg/g for MO. At neutral pH, the q_e values of the two dyes were comparable. This is observed as a

result of the electrostatic interactions between the adsorbent and the dyes. This study shows the adsorbent film has a pH-dependent selectivity for MO and MB dyes.

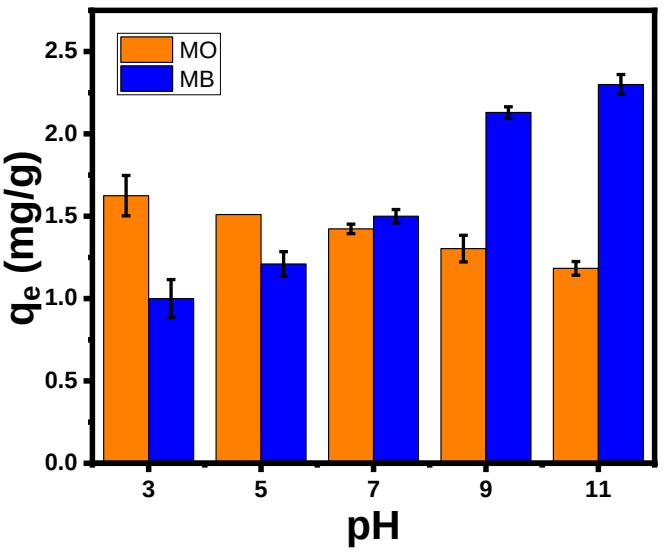

Figure 5.18: The effect of pH on the simultaneous adsorption of MB and MO by CA-supported Ni-BDC/CNC.

Adsorption of real textile effluent

The CA-supported Ni-BDC/CNC adsorbent film was tested for its potential in adsorptive purification of real textile industry wastewater and the results are shown in figure 5.19. The film removed 45 % of the textile effluent. The adsorbent performed relatively well despite the industrial effluent containing a mixture of dyes and many other species competing for adsorption active sites.

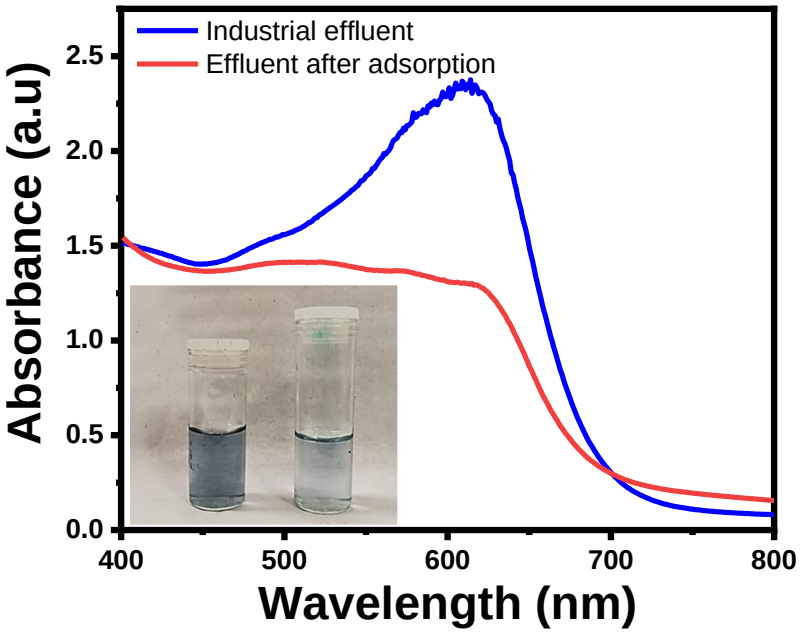

Figure 5.19: Adsorption of the industrial textile effluent by CA-supported Ni-BDC/CNC.

5.5 Economic assessment

The cost assessment of the adsorption process is important as it highlights the economic feasibility of the process. To assess the cost of the adsorption process, equation (5.17) was employed:

$$\text{Operation cost (OC)} \left(\frac{\text{USD}}{\text{m}^3}\right) = aC_{\text{energy}} + bC_{\text{chemicals}} \qquad (17)$$

where C_{energy} and $C_{chemicals}$ are the energy consumed (in kWh/m^3) and the chemical consumption (in kg/m^3), respectively, the symbol *a* represents the cost of electrical energy in the South African market (USD 0.19 kWh) as of July 2024, while the symbol *b* signifies the cost of chemicals used to manufacture the adsorbent film measured, in USD per kilogram (USD/kg) or per cubic meter (USD/m^3).

In this study, 0.003 L of the MB aqueous solution is treated by the adsorbent, and the OC calculation is based on the adsorbent treating 1 L of the MB solution. Additionally, the equipment was calculated based on their power ratings in watts and the total duration of operation. The cost of the adsorbent was calculated per kilogram. The total energy consumption reached 110.8 kilowatt-hours per cubic meter (kWh/m^3), which is equivalent to USD 20.43 per cubic meter, while

the total chemical cost amounted to USD 32.57 per cubic meter. Therefore, the operating cost was determined to be USD 53 per cubic meter.

5.6 Conclusions

The Ni-BDC/CNC composite was successfully synthesized through a solvothermal procedure followed by embedding in a CA matrix via drop-casting to yield CA-supported Ni-BDC/CNC. The film was characterized using XRD, FTIR, SEM, EDX, TGA, BET, and XPS. The synthesized adsorbent film was tested for the adsorptive removal of MB from aqueous solutions reaching the highest adsorption capacity of 2.78 mg/g and the highest % MB removal of 85 % at solution pH 11, 6 mg/L initial concentration, contact time of 6 hours at 25 ^{o}C. The adsorption process was better described by the Langmuir isotherm and pseudo-second-order kinetic models, demonstrating an E_a of 50 kJ/mol, implying a monolayer chemisorption process of MB onto the surface of the film. The adsorption process was exothermic in nature, and the film demonstrated good recyclability and pH-dependent selectivity for both cationic and anionic contaminants. The practical applicability of the adsorbent film was further demonstrated by a 45 % removal efficiency of industry dye effluent from water. The CA-supported Ni-BDC/CNC shows it is a promising adsorbent for the adsorptive removal of contaminants from aqueous solutions.

5.7 References

1. Abdelhamid, H.-N.; Mathew, A.-P. Cellulose-Based Materials for Water Remediation: Adsorption, Catalysis, and Antifouling. *J. Environ. Chem. Eng.* 2021, DOI: 10.3389/fceng.2021.790314.
2. Etale, A.; Onyianta, A.-J.; Turner, S.-R.; Eichhorn, S.-J. Cellulose: A Review of Water Interactions, Applications in Composites, and Water Treatment. *Chemical Reviews* 2023, 123, 2016-2048.
3. Cheng, W.; Zhu, Y.; Jiang, Cao, K.; Zeng, S.; Chen, W.; Zhao, D.; Yu, H. Sustainable cellulose and its derivatives for promising biomedical applications, *Prog. Mater. Sci.* 2023, DOI: 10.1016/j.pmatsci.2023.101152.
4. Phan, P.T.; Hong, J.; Tran, N.; Le, T.H. The Properties of Microwave-Assisted Synthesis of Metal–Organic Frameworks and Their Applications. *Nanomaterials* 2023, 352, https://doi.org/10.3390/nano13020352
5. Ghosh, A.; Fathima Thanutty Kallungal, S.; Ramaprabhu, S. 2D Metal-Organic Frameworks: Properties, Synthesis, and Applications in Electrochemical and Optical Biosensors. *Biosensors* 2023, 123. https://doi.org/10.3390/bios13010123
6. Li, D.; Yadav, A.; Zhou, H.; Roy, K.; Thanasekaran, P.; Lee, C. Advances and Applications of Metal-Organic Frameworks (MOFs) in Emerging Technologies: A Comprehensive Review. *Global challenges* 2023, DOI: 10.1002/gch2.202300244.
7. Oladoye, P.-O.; Bamigboye, M.-O.; Ogunbiyi, M.-O.; Akano, M.-T. Toxicity and decontamination strategies of Congo red dye. *Groundw. Sustain. Dev.* 2022, DOI: 10.1016/j.gsd.2022.100844.
8. Al-Tohamy, R.; Ali, S.-S.; Li, F.; Okasha, K.-M.; Mahmoud, Y.A.-G.; Elsamahy, T.; Jiao, H.; Fu, Y.; Sun, J. A critical review on the treatment of dye-containing wastewater: Ecotoxicological and health concerns of textile dyes and possible remediation approaches for environmental safety. *Ecotoxicol. Environ. Contam.* 2022, DOI: 10.1016/j.ecoenv.2021.113160.
9. Alsukaibi, A.K.-D. Various Approaches for the Detoxification of Toxic Dyes in Wastewater. *Processes* 2022, DOI:10.3390/pr10101968.
10. Islam, T.; Repon, M.-R; Sarwar, Z. Mohammed M. Rahman7. Impact of textile dyes on health and ecosystem: a review of structure, causes, and potential solutions. *Environ. Sci. Pollut. Res.* 2023, 30, 9207–9242.
11. Mehra, S.; Singh, M.; Chadha, P. Adverse Impact of Textile Dyes on the Aquatic Environment as well as on Human Beings. *Toxicol. Int*. 2021, 28.

12. Badran, A.-M.; Utra, U.; Yussof, N.-S.; Bashir, M.-J.-K. Advancements in Adsorption Techniques for Sustainable Water Purification: A Focus on Lead Removal. *Separations* 2023, 10, DOI:10.3390/separations10110565.
13. Algarni, T.-S.; Al-Mohaimeed, A.-M. Water purification by adsorption of pigments or pollutants via metaloxide. *J. King Saud Univ. Sci.* 2022, DOI: 0.1016/j.jksus.2022.102339.
14. Cheng, P.; Wang, X.; Markus, J.; Wahab, A.; Chowdhury, S.; Xin, R.; Alshehri, S.-M.; Bando, Y.; Yamauchi, Y.; Kaneti, Y.-V. Carbon nanotube-decorated hierarchical porous nickel/carbon hybrid derived from nickel-based metal-organic framework for enhanced methyl blue adsorption. *J. Colloid Interface Sci.* 2023, 638.
15. Zheng, Y.; Cheng, B.; Fan, J.; Yu, J.; Ho, W. Review on nickel-based adsorption materials for Congo red. *J. Hazard. Mater.* 2021, DOI:10.1016/j.jhazmat.2020.123559.
16. Mohammadi, A.-A.; Niazi, Z.; Heidari, K.; Afarinandeh, A.; Kazemi, M.-S.; Haghighat, G.-A.; Vasseghian, Y.; Rezania, S.; Barghi, A. Nickel and iron-based metal-organic frameworks for removal of organic and inorganic model contaminants. *Environ. Res.* 2022, DOI: 10.1016/j.envres.2022.113164.
17. Seddiqi, H.; Oliaei, E.; Honarkar, H.; Jin, J.; Geonzon, L.-C.; Bacabac R.-G.; Klein-Nulend, J. Cellulose and its derivatives: towards biomedical applications. *Cellulose* 2021, 28.
18. Jing, S.; Wu, L.; Siciliano, Chen, C.; Li, T.; Hu, L. The Critical Roles of Water in the Processing, Structure, and Properties of Nanocellulose. *ACS Nano.* 2023, 17.
19. Qi, Y.; Wang, S.; Liza, A.-A.; Li, J.; Yang, G.; Zhu, W.; Song, J.; Xiao, H.; Li, H.; Guo, J. Controlling the nanocellulose morphology by preparation conditions. *Carbohydr. Polym.* 2023, DOI: 10.1016/j.carbpol.2023.121146.
20. Bai, L.; Ding, A.; Li, G.; Liang, H. Application of cellulose nanocrystals in water treatment membranes: A review. *Chemosphere* 2022, DOI: 10.1016/j.chemosphere.2022.136426.
21. Whba, F.; Mohamed, F.; Idris, M.-I.; Yahya, M.-S. Surface Modification of Cellulose Nanocrystals (CNCs) to Form a Biocompatible, Stable, and Hydrophilic Substrate for MRI. *Appl. Sci.* 2023, DOI:10.3390/app13106316.
22. Lu, Y.; Liu, C.; Mei, C.; Sun, J.; Lee, J.; Wu, Q.; Hubbe, M.-A.; Li, M. Recent advances in metal organic framework and cellulose nanomaterial composites. *Coord*. *Chem*. *Rev*. 2022, DOI: 10.1016/j.ccr.2022.214496.

23. Tao, Y.; Du, J.; Cheng, Y.; Lu, J.; Min, D.; Wang, H. Advances in Application of Cellulose-MOF Composites in Aquatic Environmental Treatment: Remediation and Regeneration. *Int*. *J*. *Mol*. *Sci*. 2023, DOI: 10.3390/ijms24097744.
24. Cheng, J.; Shao, Y.; Guo, H.; Zhang, Z.; Mao, Y.; Qian, L.; Xin, K.; Yang, W. Ni-based metal–organic frameworks prepared with terephthalic acid hydroxylation converted methyl palmitate into jet-fuel range hydrocarbons in CO_2 atmosphere. *Fuel* 2022, DOI: 10.1016/j.fuel.2022.123679.
25. Xiaoshan, Y.; Yu, J.; Qitang, W.; Zebin, W.; Xianke, L.; Yangmei, C. Preparation and Characterization of Cellulose Nanocrystal Extraction From Pennisetum hydridum Fertilized by Municipal Sewage Sludge via Sulfuric Acid Hydrolysis. *Front. Energy Res.* 2021, 9, DOI:10.3389/fenrg.2021.774783.
26. Tahazadeh, S.; Karimi, H.; Mohammadi, T.; Motejadded, H.-B.; Tofighy, M.-A. Fabrication of biodegradable cellulose acetate/MOF-derived porous carbon nanocomposite adsorbent for methylene blue removal from aqueous solutions. *J. Solid State Chem.* 2021, DOI: 10.1016/j.jssc.2021.122180.
27. Huang, W.; Peng, C.; Tang, J.; Diao, F.; Yesibolati, M.-N.; Sun, H.; Engelbrekt, C.; Zhang, J.; Xiao, X.; Molhave, K. Electronic structure modulation with ultrafine Fe3O4 nanoparticles on 2D Ni-based metal-organic framework layers for enhanced oxygen evolution reaction. *J. Energy Chem.* 2021, 65. DOI:10.1016/j.jechem.2021.05.030.
28. Wu, F.; Li, Q.; Guo, H.; Wang, S.; Hao, G,; Hu, Y.; Zhang, G.; Jiang, W. Modulating crystal and electronic structure of NiFe-MOFs by inorganic acid for highly efficient electrochemical water oxidation. *Dalton Trans.* 2023, 52.
29. Doan, T.-K.-Q.; Chiang, K.-Y. Characteristics and kinetics study of spherical cellulose nanocrystal extracted from cotton cloth waste by acid hydrolysis. *Sustain. Environ. Res.* 2022, 32, DOI:10.1186/s42834-022-00136-9
30. Risite, H.; Salim, M.-H.; Oudinot, B.-T.; Ablouh, E.; Joyeux, H.-T.; Sehaqui, H.; Razafimahatratra, J.-H.-A.; Qaiss, A.-E.-K.; El Achaby, M.; Kassab, Z. Artemisia annua Stems a New Sustainable Source for Cellulosic Materials: Production and Characterization of Cellulose Microfibers and Nanocrystals. *Waste Biomass Valor* 2022, 13.
31. Azhar, M.-H.; Noor, T.; Iqbal, N.; Zaman, N.; Farrukh, S. CO_2 adsorption properties of Ni-BDC MOF and its 1–8 wt% g-C_3N_4/Ni-BDC MOF. *Mater. Sci. Eng. B* 2024, DOI: 10.1016/j.mseb.2023.117043.

32. Ogunjobi, J.-K.; Adewale, A.-I, Adeyemi, S.-A. Cellulose nanocrystals from Siam weed: Synthesis and physicochemical characterization. *Heliyon* 2023, DOI:10.1016/j.heliyon.2023.e13104.
33. Chandran, A.-M.; Tayal, E.; Mural, P.-K.-S. Polycaprolactone-blended cellulose acetate thin-film composite membrane for dairy waste treatment using forward osmosis. *Environ. Sci. Pollut. Res.* 2022, 29.
34. Dong, Q.; Shuai, C.; Mo, Z.; Guo, R.; Liu, N.; Liu, G.; Wang, J.; Liu, W.; Chen, Y.; Liu, J.; Jiang, Y.; Gao, Q. The in situ derivation of a NiFe-LDH ultra-thin layer on Ni-BDC nanosheets as a boosted electrocatalyst for the oxygen evolution reaction. *CrystEngComm.* 2021, 23.
35. Mao, Y.; Cheng, J.; Shao, Y.; Guo, H.; Qian, L.; Yang, W. Highly Active Ni Nanocatalysts Derived from Metal–Organic Framework (Ni-BDC) Boosted Deoxygenation and Cracking of Fatty Acid Methyl Esters. *Ind. Eng. Chem. Res*. 2023, 62.
36. Surov, O.V.; Afineevskii, A.V.; Voronova, M.I.; Sulfuric acid alcoholysis as a way to obtain cellulose nanocrystals. *Cellulose* 2023, 30.
37. Ma, T.; Hu, X.; Lu, S.; Cui, R.; Zhao, J.; Hu, X.; Song, Y. Cellulose nanocrystals produced using recyclable sulfuric acid as hydrolysis media and their wetting molecular dynamics simulation. *Int. J. Biol. Macromol.* 2021, 184.
38. Wang, H.; Du, H.; Liu, K.; Liu, H.; Xu, T.; Zhang, S.; Chen, X.; Zhang, R.; Li, H.; Xie, H.; Zhang, X.; Si, C. Sustainable preparation of bifunctional cellulose nanocrystals via mixed H_2SO_4/formic acid hydrolysis. *Carbohydr. Polym*. 2021, DOI: 10.1016/j.carbpol.2021.118107.
39. Rupam, T.-H.; Tuli, F.-J.; Jahan, I.; Palash, M.-L.; Chakraborty, A.; Saha, B.-B.; Isotherms and kinetics of water sorption onto MOFs for adsorption cooling applications. *TSEP*, 2022, DOI: 10.1016/j.tsep.2022.101436.
40. Sarvalkar, P.-D.; Vadanagekar, A.-S.; Karvekar, O.-S.; Kumbhar, P.-D.; Terdale, S.-S.; Thounaojam, A.-S.; Kolekar S.-S.; Vhatkar, R.-S.; Patil, P.-S.; Sharma, K.-K.-K.; Thermodynamics of Azo Dye Adsorption on a Newly Synthesized Titania-Doped Silica Aerogel by Cogelation: A Comparative Investigation with Silica Aerogels and Activated Charcoal. *ACS Omega* 2023, 8.
41. Zaman, H.-G.; Baloo, L.; Kutty, S.-R.; Aziz, K.; Altaf, M.; Ashraf, A.; Aziz, F. Insight into microwave-assisted synthesis of the chitosan-MOF composite: Pb(II) adsorption. *Environ. Sci. Pollut. Res*. 2023, 30.

42. Nassef, H.-M.; Al-Hazmi, G.-A.-A.-M.; Alayyafi, A.-A.; El-Desouky, M.-G.; El-Bindary, A.-A. Synthesis and characterization of new composite sponge combining of metal-organic framework and chitosan for the elimination of Pb(II), Cu(II) and Cd(II) ions from aqueous solutions: Batch adsorption and optimization using Box-Behnken design. *J. Mol. Liq.* 2024, DOI: 10.1016/j.molliq.2023.123741.
43. Mohamed, N.-S.; Abbas, M.; Trari, M. Understanding the rate-limiting step adsorption kinetics onto biomaterials for mechanism adsorption control. *Prog. React. Kinet. Mec.* 2024, DOI:10.1177/14686783241226858.
44. Hasani, N.; Selimi, T.; Mele, A.; Thaçi, V.; Halili, J.; Berisha, A.; Sadiku, M. Theoretical, Equilibrium, Kinetics and Thermodynamic Investigations of Methylene Blue Adsorption onto Lignite Coal. *Molecules* 2022, DOI:10.3390/molecules27061856.
45. Sellak, S.; Bensalah, J.; Ouaddari, H.; Safi, Z.; Berisha, A.; Draoui, K.; Barrak, I.; Guedira, T.; Bourhia, M.; Ibenmoussa, S.; Okla, M.; Dauelbait, M.; Habsaoui, A.; Harcharras, M. Adsorption of Methylene Blue Dye and Analysis of Two Clays: A Study of Kinetics, Thermodynamics, and Modeling with DFT, MD, and MC Simulations. *ACS Omega* 2024, 9.
46. Saeed, T.; Naeem, A.; Din, I.-U.; Farooq, M.; Khan, I.-W.; Hamayun, M.; Malik, T. Synthesis of chitosan composite of metal-organic framework for the adsorption of dyes; kinetic and thermodynamic approach, *J. Hazard. Mater.* 2022, DOI: 10.1016/j.jhazmat.2021.127902.
47. Belmabrouk, H.; Selmi, M.; Alshahrani, T.; Bajahzar, A.; Jabli, M. Experimental and theoretical study of methylene blue biosorption using a new biomaterial Pergularia tomentosa L. fruit. *Int. J. Environ. Sci. Technol*. 2022, 19.
48. Çelebi, M.; Söğüt, E.-G. High-efficiency removal of cationic dye and heavy metal ions from aqueous solution using amino-functionalized graphene oxide, adsorption isotherms, kinetics studies, and mechanism. *Turk. J. Chem.* 2022, DOI: 10.55730/1300-0527.3462.
49. Mustapha, L.-S.; Yusuff, A.-S. Dim, P.-E. RSM optimization studies for cadmium ions adsorption onto pristine and acid-modified kaolinite clay. *Heliyon*, 2023, DOI: 10.1016/j.heliyon.2023.e18634.
50. Alsohaimi, I.-H.; Alhumaimess, M.-S.; Alqadami, A.-A.; Alshammari, G.-T.; Al-Olaimi, R.-F.; Abdeltawab, A.-A.; El-Sayed, M.-Y.; Hassan, H.-M. Adsorptive performance of aminonaphthalenesulfonic acid modified magnetic-graphene oxide for methylene blue dye: Mechanism, isotherm and thermodynamic studies. *Inorg. Chem. Commun.* 2023, DOI: 10.1016/j.inoche.2022.110261.

51. Malima, N.-M.; Owonubi, S.-J.; Lugwisha, E.-H.; Mwakaboko A.-S. Thermodynamic, isothermal and kinetic studies of heavy metals adsorption by chemically modified Tanzanian Malangali kaolin clay. *Int. J. Environ. Sci. Technol.* 2021, 18.
52. Saima, N.; Safa, I.; Sobhy, M.-I.; Kusuma, H.-S.; Arif, N.; Yaseen, M.; Khan, M.-I.; Iqbal, M. ZnO, CuO and Fe_2O_3 green synthesis for the adsorptive removal of direct golden yellow dye adsorption: kinetics, equilibrium and thermodynamics studies. *Z Phys. Chem*. 2021, 253.
53. Khatri, M.; Ahmed, F.-E.; Al-Juboori, R.-A.; Khanzada, N.-K.; Hilal, N. Reusable environmentally friendly electrospun cellulose acetate/cellulose nanocrystals nanofibers for methylene blue removal. *J. Environ. Chem. Eng.* 2024, DOI:10.1016/j.jece.2023.111788.

CHAPTER 6

6.0 GENERAL CONCLUSIONS AND FUTURE WORK

6.1 General Conclusions

In this study, CA-supported MOF-5/CNC (**1**), Cu-BDC/CNC (**2**), and Ni-BDC/CNC (**3**) adsorbent films were successfully fabricated through solvothermal and drop-casting techniques. The films were characterized using X-ray diffraction (XRD), Fourier transform infrared spectroscopy (FTIR), scanning electron microscopy (SEM), energy dispersive X-ray (EDX), thermogravimetric analysis (TGA), Brunauer-Emmett-Teller (BET) analysis and X-ray photoelectron spectroscopy (XPS). XRD measurements showed the MOF/CNC composites as crystalline materials embedded in amorphous CA. FTIR and XPS confirmed the presence of O-H and C=O functional groups on the surface of the adsorbent films, while EDX detected metals on the surface of the adsorbent films confirming the presence of the MOFs within the matrices of CA substrates. These characterization techniques verified the successful synthesis of the adsorbent films.

The adsorbent films were successfully evaluated for the adsorptive removal of cationic MB from aqueous solutions under various conditions. The optimum adsorption conditions were determined at pH 11, at a contact time of 360 minutes, at an initial concentration of 6 mg/L, and at 25 ^{o}C. The adsorption capacities ranged from 2.78 – 4.29 mg/g, with a maximum % MB removal between 77 – 85 %. The adsorption of MB on film **1** followed the Freundlich isotherm model, whereas adsorption on films **2** and **3** followed the Langmuir isotherm model. Adsorption kinetics showed chemisorption as the likely process of adsorption. Through the proposed mechanisms, electrostatic interactions between the films and MB were identified according to the functional groups determined through FTIR and XPS analysis.

The practical applicability of the adsorbent films was successfully demonstrated, with results showing the adsorbents can be recycled by desorbing MB through methanol washing. After five cycles of MB adsorption, the adsorbent films maintained between 67-79% of their initial adsorption capacities, showing that the adsorbent films are stable, recyclable, and cost-effective with minimal environmental impacts associated with disposal. Furthermore, the adsorbent films exhibited a pH-dependent selectivity for anionic and cationic organic contaminants, highlighting versatility and practical applicability. The adsorbent films showed affinity for anionic methyl orange (MO) at acidic pH and showed affinity for cationic MB at alkaline pH during simultaneous adsorption. At neutral pH, the adsorbent films attained comparable adsorption efficiencies for both MO and MB

adsorption. When applied for the treatment of real textile industry wastewater, the adsorbent films achieved a % removal of the effluent between 20 - 45 % with a calculated cost of the adsorption process for each film between USD 43.60-53.00.

Film **1** exhibited the highest adsorption capacity (4.29 mg/g), followed by Film **2** (3.60 mg/g) and Film **3** (2.78 mg/g). Kinetic studies showed that all the films reached equilibrium after 4 hours of adsorption. Film **1** demonstrated the highest recyclability, retaining 79% of its initial capacity after five cycles, compared to 73% for Film **2** and 67% for Film **3**. Film **1** also exhibited the lowest estimated cost at USD 43.60 per unit, compared to USD 52.77 for Film **2** and USD 53.00 for Film **3**. Based on these results, Film **1** is recommended as the most suitable composite film for practical applications.

This work established a cost-effective, recyclable, and versatile easy to synthesize cellulose-based adsorbent films incorporated with metal-organic frameworks that show great potential for the adsorptive removal of organic dyes from aqueous solutions.

6.2 Future work and Recommendations

This study utilized celluMOF-based films as adsorbents through batch adsorption methods. The films were found to be porous; suggesting that they can be further explored as potential filters in membrane technologies. Filtration and rejection performance, along with pure water permeability tests can be conducted to evaluate the effectiveness of these films in membrane technology.

To expand the applicability of the celluMOF-based films, their potential use as photocatalytic membranes should be explored. The combination of these process will allow for the separation and oxidative degradation contaminants. In addition to MOF-5, other MOFs with strong photocatalytic properties such ZIF-67, MIL-101 and bimetallic MOFs could also be incorporated into the cellulose matrix.

To enhance desorption, a Soxhlet extraction method is recommended. This continuous solvent flow over the adsorbent films will greatly improve MB removal and potentially allow for the recovery of methanol. The adsorption capacities of the films can be further improved by grafting additional functional groups onto the surface, which would strengthen the interaction with organic dyes. To gain deeper insights into the films structural properties, transmission electron microscopy (TEM)

can be used to characterize the films. This will provide information on the morphology and porosity which will assist in understanding the role of porosity in influencing adsorption capacity.

APPENDICES

APPENDIX A

Nonlinear isotherm and kinetic curves of CA-supported MOF-5/CNC film

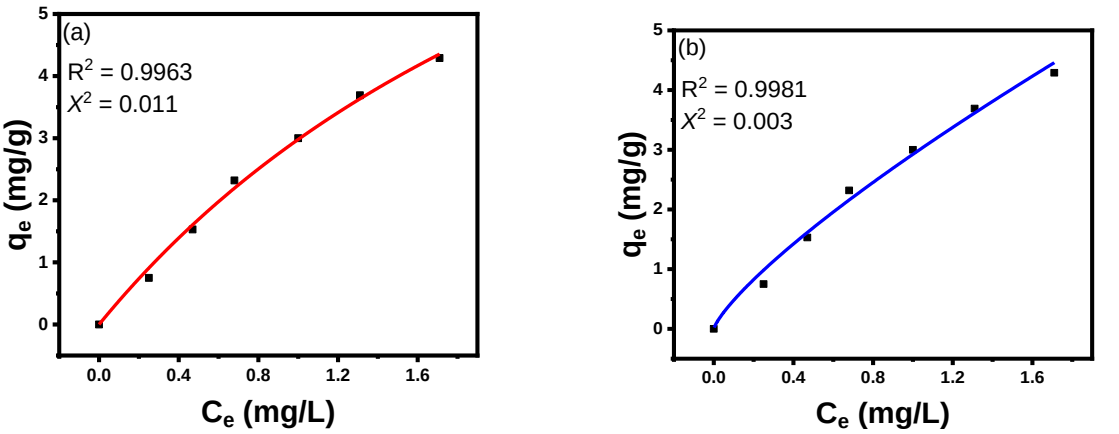

Figure A 1: (a) Langmuir and (b) Freundlich non-linear isotherm curves.

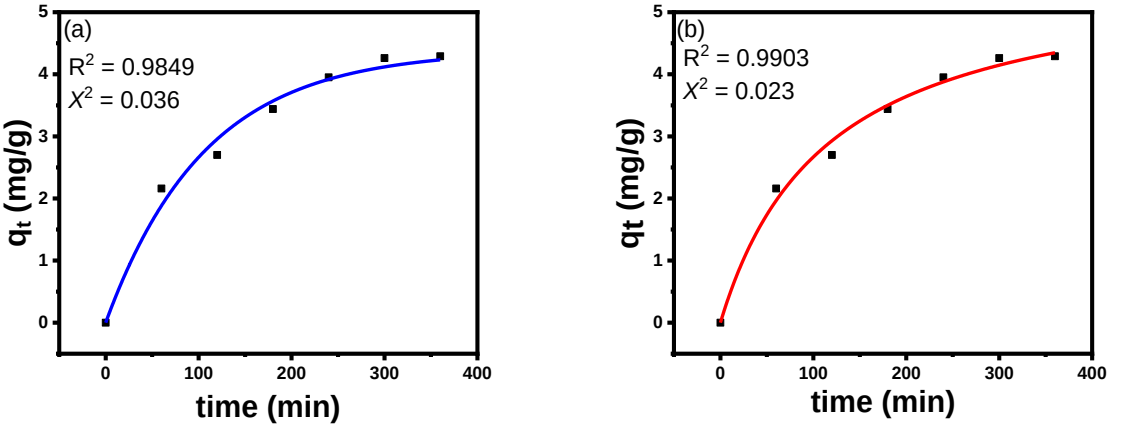

Figure A 2: Non-linear (a) pseudo-first-order and (b) pseudo-second-order kinetic models.

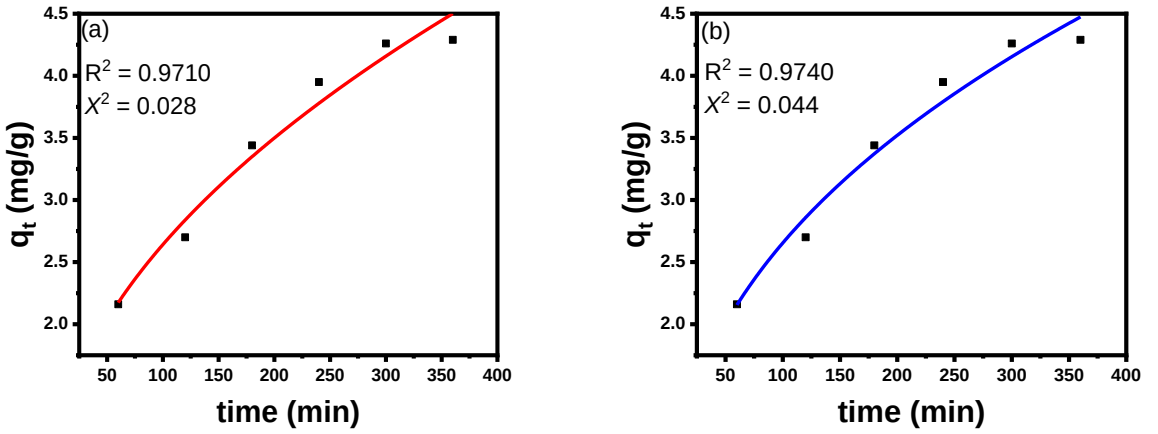

Figure A 3: Non-linear (a) intraparticle diffusion and (b) Bangham models.

APPENDIX B

Nonlinear isotherm and kinetic curves of CA-supported Cu-BDC/CNC film

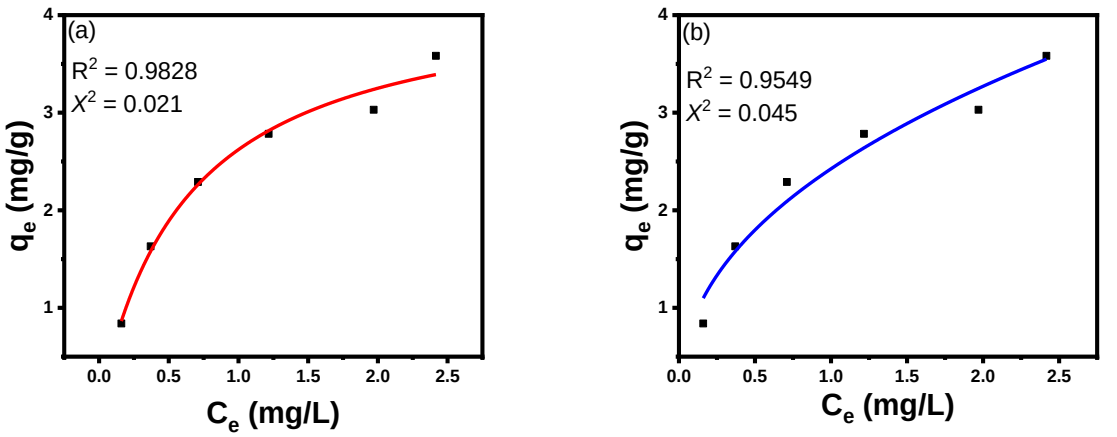

Figure B 1: (a) Langmuir and (b) Freundlich non-linear isotherm curves.

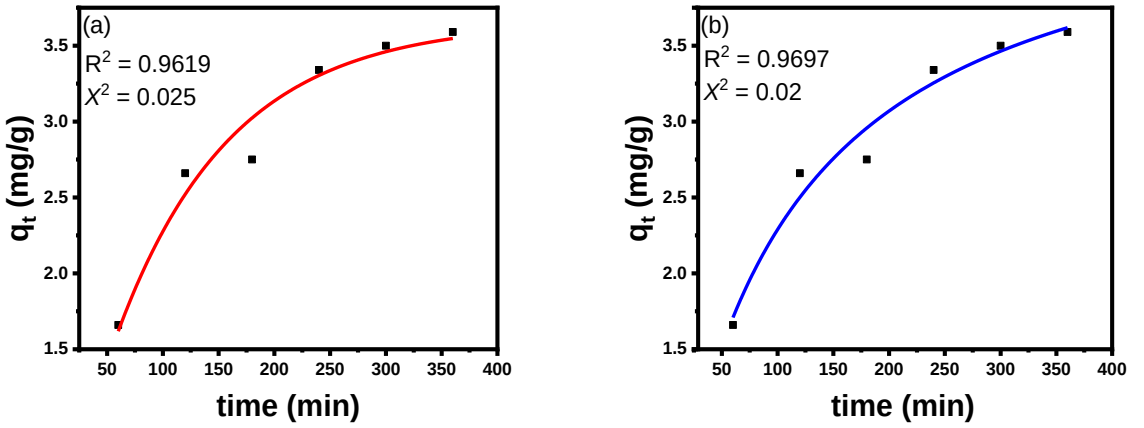

Figure B 2: Non-linear (a) pseudo-first-order and (b) pseudo-second-order kinetic models.

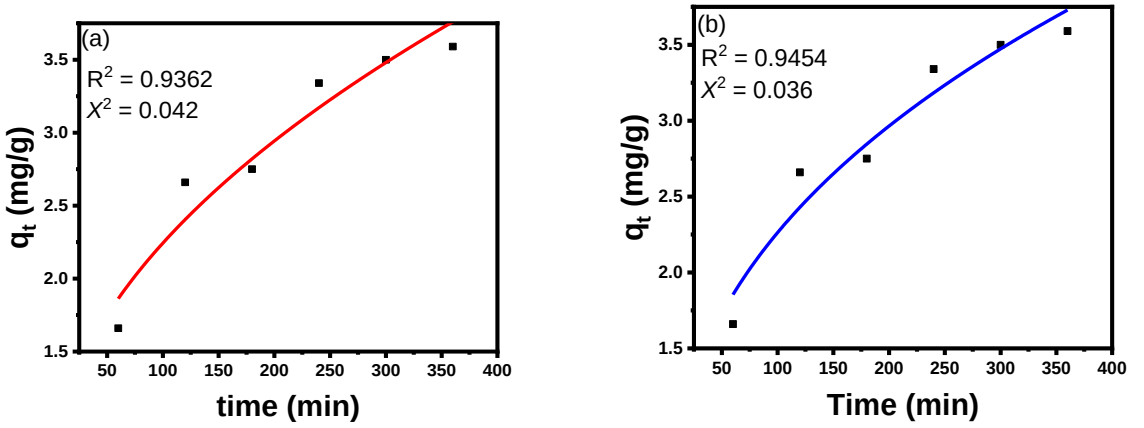

Figure B 3: Non-linear (a) intraparticle diffusion and (b) Bangham models.

APPENDIX C

Nonlinear isotherm and kinetic curves of CA-supported Ni-BDC/CNC film

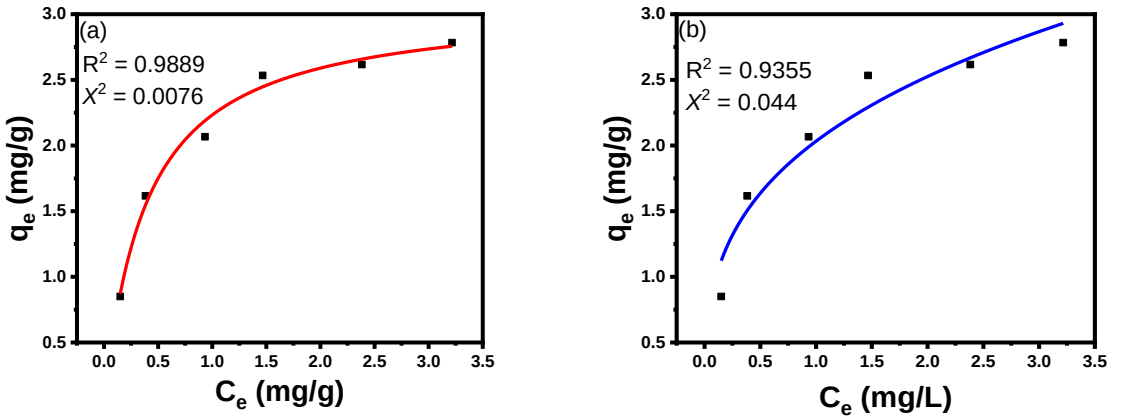

Figure C 1: (a) Langmuir and (b) Freundlich non-linear isotherm curves.

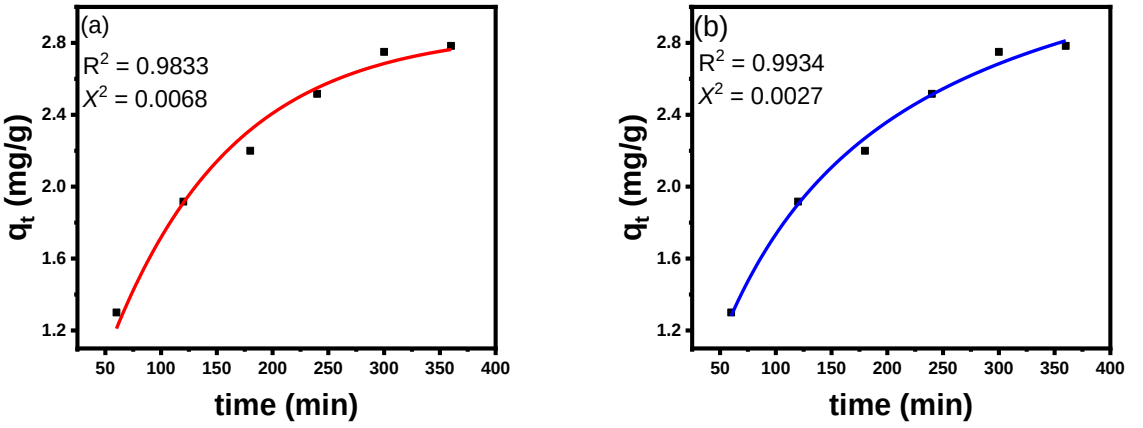

Figure C 2: Non-linear (a) pseudo-first-order and (b) pseudo-second-order kinetic models.

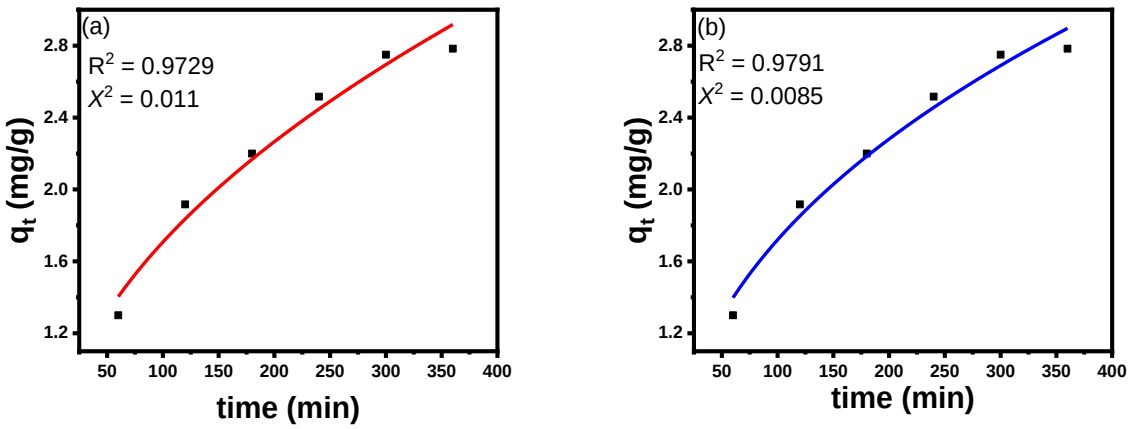

Figure C 3: Non-linear (a) intraparticle diffusion and (b) Bangham models.